Study on Fibre Optic Sensors Embedded into Metallic Structures by Selective Laser Melting

Dirk Havermann

A dissertation submitted for the degree of Doctor of Philosophy

Heriot-Watt University

School of Engineering and Physical Sciences

December 2015

Abstract

Additive Manufacturing, which builds components layer by layer, opens up exciting possibilities to integrate sophisticated internal features and functionalities such as fibre optic sensors directly into the heart of a metal component. This can create truly smart structures for deployment in harsh environments. The innovative and multidisciplinary study conducted in this thesis demonstrates the feasibility to integrate fibre optics sensors with thin, protective nickel coatings (outer diameter ~350 µm) into stainless steel (SS 316) coupons by Selective Laser Melting technology (SLM).

Different concepts for fibre embedment by SLM are investigated. The concepts differ in which way the fibre is positioned and how the powder is deposited and solidified by the laser in respect to the optical fibre. Only one approach is found suitable to reliably and repeatable encapsulate fibres whilst preserving their structural integrity and optical properties. In that approach SS 316 components are manufactured using SLM, incorporating U-shaped grooves with dimensions suitable to hold nickel coated optical fibres. Coated optical fibres containing Fibre Bragg Gratings (FBG) for strain and temperature sensing are placed in the groove. Melting subsequent powder layers on top of the FBGs fuses the fibre's metallic jacket to the steel and completes the integration of the fibre sensor into the steel structure.

Cross-sectional microscopy analysis of the fabricated components, together with analysis of fibre optic sensors' behaviour during fabrication, indicates proper stress and strain transfer between coated fibre and added SS 316 material. During the SLM process embedded Fibre Bragg grating (FBG) sensors provide in-situ temperature measurements and potentially allow measuring the build-up of residual stresses.

Subsequently, FBG sensors embedded into SS 316 structures using our approach follow elastic and plastic deformations of the SS 316 component, with a resolution of better than 3 $pm*\mu\varepsilon^{-1}$. Temperature measurements are also conducted with a precision of 3 $pm*K^{-1}$. Such embedded fibre sensors can also be used to high temperatures of up to ~400 °C.

However, at elevated temperatures issues arise from the significantly larger thermal expansion coefficient of SS 316, leading to delamination of the more rapidly expanding metal from the glass. Rapid thermal expansion of the metal also leads to high axial stresses within the glass exceeding the fibres tensile strength and ultimately leading to structural damage of the optical fibre.

Acknowledgements

First of all, I would like to thank my supervisors Professor Duncan Hand and Dr Robert Maier for the opportunity of a PhD within the Applied Optics and Photonics Group. Their supervision and guidance throughout the course of this PhD is very much appreciated.

Special thank goes to Professor Bill MacPherson and particularly, to (again) Dr Robert Maier for their support and academic and practical contribution. The list of practical things I have learnt from them is endless, ranging from splicing optical fibres to dissembling a notorious vacuum chamber, making this PhD truly worthwhile.

Also, I would like to say thank you to all the members of the Applied Optics and Photonics research group, to other colleagues, and the technical and support staff at Heriot-Watt University.

Big thanks to Paul Harrison. He instigated the idea of me moving to Scotland and doing a PhD at Heriot-Watt. Furthermore, I would like to thank Andrew, Jianyong and Dimitrios for the good laughs we had in the office, making the time just flying by. Particularly big thanks to Andrew, for not only correcting my poor grammar but also providing a car for lunchtime excursions.

Most special thanks must go to my parents Roswitha and Bernd, my brothers Jens and Andreas, and little Henrik. I am extremely grateful for their unwavering and unconditional support given me throughout the whole period of my studies.

Mein allerherzlichster Dank gilt meinen Eltern Roswitha und Bernd, meinen Brüdern Jens und Andreas und natürlich auch dem kleinen Henrik. Ich bin äußerst dankbar für die bedingungslose Unterstützung die ich von euch erfahren habe. Ohne euch wäre diese Arbeit nicht möglich gewesen.

Thank you! *Danke !*

ACADEMIC REGISTRY
Research Thesis Submission

Name:	**Dirk Havermann**		
School/PGI:	**School of Engineering and Physical Sciences [EPS]**		
Version: *(i.e. First, Resubmission, Final)*	**Final submission**	Degree Sought (Award **and** Subject area)	**PhD**

Declaration

In accordance with the appropriate regulations I hereby submit my thesis and I declare that:

1) the thesis embodies the results of my own work and has been composed by myself
2) where appropriate, I have made acknowledgement of the work of others and have made reference to work carried out in collaboration with other persons
3) the thesis is the correct version of the thesis for submission and is the same version as any electronic versions submitted*.
4) my thesis for the award referred to, deposited in the Heriot-Watt University Library, should be made available for loan or photocopying and be available via the Institutional Repository, subject to such conditions as the Librarian may require
5) I understand that as a student of the University I am required to abide by the Regulations of the University and to conform to its discipline.

* *Please note that it is the responsibility of the candidate to ensure that the correct version of the thesis is submitted.*

Signature of Candidate:		Date:	**08/12/2015**

Submission

Submitted By *(name in capitals):*	**Dirk Havermann**
Signature of Individual Submitting:	
Date Submitted:	**08/12/2015**

For Completion in the Student Service Centre (SSC)

Received in the SSC by *(name in capitals):*			
Method of Submission *(Handed in to SSC; posted through internal/external mail):*			
E-thesis Submitted (mandatory for final theses)			
Signature:		Date:	

Table of Contents

List of Publications by the Candidate

Journal Publications

D. Havermann, J. Mathew, W.N. Macpherson, R. R. J. Maier, D. P. Hand, *"Temperature and Strain Measurements with Fibre Bragg Gratings embedded in Stainless Steel"*, Journal of Lightwave Technology, Vol. 33 (12), pp. 2574- 2579, 2015.

J. Mathew, O. Schneller, D. Polyzos, D. Havermann, W.N. Macpherson, D. P. Hand, R. R. J. Maier, *"In-Fiber Fabry–Perot Cavity Sensor for High-Temperature Applications"*, Journal of Lightwave Technology, Vol. 33 (12), pp. 2419- 2425, 2015.

Conference contributions

R.R.J. Maier, D. Havermann. W.N. Macpherson, R. R. J. Maier, D. P. Hand, *"Embedding metallic jacketed fused silica fibers into stainless steel using additive layer manufacturing technology"*, Proceedings and poster presented at European Workshop on Fibre Sensors (EWOFS) 2013, Krakow, Poland.

D. Havermann, W.N. Macpherson, R. R. J. Maier, D. P. Hand, *"Embedding Optical Sensors into Metallic Structures using Laser Additive Manufacturing"*, Talk presented at the Industrial Laser Applications Symposium (ILAS) 2013, Nottingham, UK.

D. Havermann, W.N. Macpherson, R. R. J. Maier, D. P. Hand, *"Embedding fibre optic sensors using laser additive manufacturing"*, Talk presented at the 2nd Manufacturing the Future Conference, 2014, Cranfield, UK.

D. Havermann, W.N. Macpherson, R. R. J. Maier, D. P. Hand, *"Embedding Optical Sensors into Metallic Structures using Laser Additive Manufacturing"*, Proceedings and Talk presented at the International Congress on Applications of Lasers & Electro-Optics (ICALEO), 2013, Miami, USA.

D. Havermann, W.N. Macpherson, R. R. J. Maier, D. P. Hand, *"Embedding Optical Sensors into Metallic Structures using Laser Additive Manufacturing"*, Poster presented at the EPSRC Centre for Innovative Manufacturing Launch Event, 2013, Edinburgh, UK.

R.R.J. Maier, D. Havermann, J. Mathew, W.N. Macpherson, R. R. J. Maier, D. P. Hand, *"Optical Fibre Sensing in Metals by Embedment in 3D Printed Metallic Structures"*, Proceedings and Talk presented at Optical Fibre Conference (OFS) 23, Santander, Spain.

D. Havermann, J. Mathew, W.N. Macpherson, R. R. J. Maier, D. P. Hand, *"In-situ Measurements with Fibre Bragg Gratings embedded in Stainless Steel"*, Proceedings and Poster presented at Optical Fibre Conference (OFS) 23, 2013, Santander, Spain.

D. Havermann, J. Mathew, W.N. Macpherson, R. R. J. Maier, D. P. Hand, *"In-situ Measurements with Fibre Bragg Gratings embedded in Stainless Steel"*, Talk presented at Photon 14, 2014, London, UK.

D. Havermann, J. Mathew, W.N. Macpherson, R. R. J. Maier, D. P. Hand, *"In-situ Strain Measurements with Fiber Optic Sensors Embedded in Stainless Steel"*, Proceedings and Poster presented at SPIE Smart Structures, 2015, San Diego, USA.

D. Havermann, W.N. Macpherson, R. R. J. Maier, D. P. Hand, *"Embedding Optical Sensors into Stainless Steel by Selective Laser Melting"*, Talk presented at the Industrial Laser Applications Symposium (ILAS), 2015, Coventry, UK.

D. Havermann, J. Mathew, W.N. Macpherson, R. R. J. Maier, D. P. Hand, *"Measuring Residual Stresses in metallic components manufactured with Fibre Bragg Gratings embedded by Selective Laser Melting"*, Talk presented at Optical Fibre Conference 24, Curitiba, Brazil.

Chapter 1

Introduction

This chapter provides the background information for this thesis. The key technologies that are being used and combined in this thesis are introduced. Following from there the motivation of this thesis is developed.

1.1 Background

Additive Manufacturing (AM) technologies offer novel and exciting possibilities when constructing and fabricating components in polymers and metals [1]. Where conventional manufacturing technologies such as CNC milling, turning or drilling reduce solid components to a specific design, AM technologies work in reverse by building up components one layer at a time. Potentially, AM is being amongst the most innovative and disruptive manufacturing technologies currently available, decoupling the' manufacturing costs of a part from its complexities [2] and revolutionising supply chains ("Time-to-Market", "Direct Digital Manufacturing") or component design processes ("Design for Manufacturability") [3].

By overcoming the accessibility constraints of CNC processes (machining tool is typically on a spindle), AM opens up exciting possibilities to fabricate sophisticated free form components with complex geometries and integrated internal features (Figure 1-1)[4]. Consolidated designs for components optimised for lightweight functionality deploy material only where the functionality requires specific strengths [5], resulting often in hollow or porous structures potentially leaving room for the integration of sensors at points of interest.

In one of the key laser-based AM technologies for metal materials (Selective Laser Melting - SLM) pure metal material in form of powder is solidified layer-by-layer using focused laser beams. The physical properties of SLM fabricated components exhibit the properties of conventionally manufactured components [6]. A wide range of metals material can be processed using SLM including stainless steels such as SS 316 or nickel-based super alloys for high temperature operations IN738LC [7].

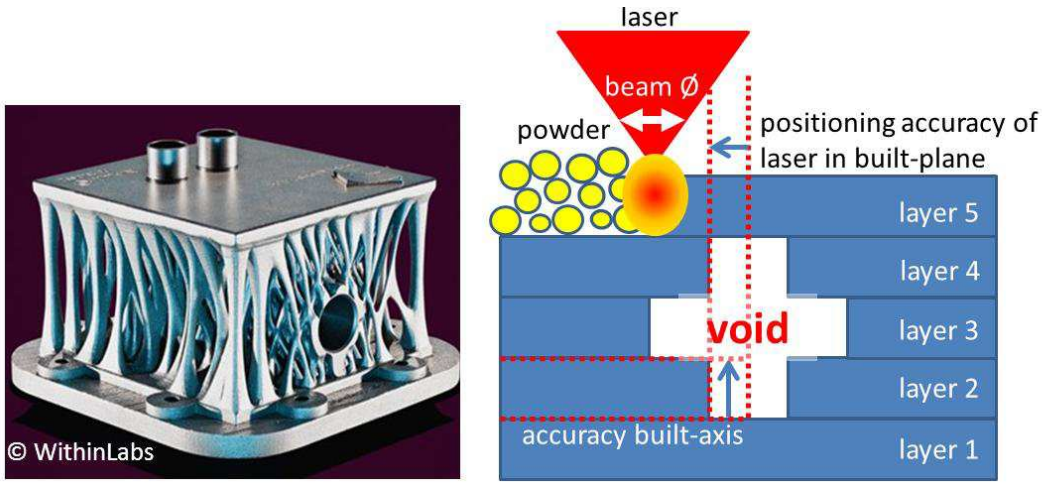

Figure 1-1 Photographic image (from WithinLabs) of SLM fabricated part showing the geometric freedom SLM technology offers (left). Schematic illustration of SLM process highlighting the mechanisms involved defining the process's accuracy (right).

A major problem when fabricating components by AM is the occurrence of significant residual stresses particularly for materials with high melting temperatures and large thermal expansion coefficients such as metals [8]. High melting temperatures cause large temperature gradients between the molten material and the solid surround, leading to steep gradients in volume expansion. Rapid cool-down freezes the volumes in their expanded states, leading to residual stresses within the component once it has cooled down. In SLM fabricated parts, the distribution of residual stresses is typically in a highly complex 3-D pattern [9]. Residual stresses can cause delamination between layers, cracking, in-accuracy in the dimensions of the fabricated parts and unacceptable surface morphology. Another problem that can arise in AM manufactured components is the occurrence of anisotropies of the component's physical properties. Research shows that changing the position where a component is built within the AM machine, different physical properties such as Yield strength or Young modulus are exhibited [10]. Due to the huge potential of AM technology, it is highly desirable to investigate and understand the mechanism for the generation and accumulation of residual stresses and anisotropies within SLM-fabricated components [6, 11].

The accuracy and resolution of the SLM process are determined by three fundamental process characteristics, (i) layer thickness in direction of the built axis; (ii) positioning accuracy of the laser over the build plane; (iii) and seam width of the solidified material which is dependent on the laser beam diameter spot size (Figure 1-1; right). Using 2-axis beam deflection systems such as galvanometer scanners, the positioning of the laser

beam over the build plane is an order of magnitude more precise that the resolution due to layer thickness and beam diameter. Available galvanometer scanners achieve high resolutions (e.g. < 12 µrad [12]) and in combination with low distortion f-theta lenses exhibit high precision (e.g. < 3 µm for f = 160 mm). The minimum layer thickness is determined by the average powder particle size, minimally one powder particle is solidified at a time (e.g. commercially available powders for SS 316 ~ 10 – 40 µm). The excellent beam quality of commercially available high brightness laser systems such as fibre lasers allows power delivery with small spot sizes of a few tens of micrometers in diameter [13]. Small spot sizes are beneficial because they lead to smaller melt pools of similar dimension and furthermore, less heat conduction into surrounding material and minimised heat affected zones occur [14]. Hence, using SLM in combination with high brightness lasers, metal components can be relatively precisely (few 10 µm resolution) fabricated, containing consolidated internal geometries such as hollow channels. These internal geometries offer further potential to integrate dissimilar materials such as sensing elements in a minimised manner directly into the heart of the component.

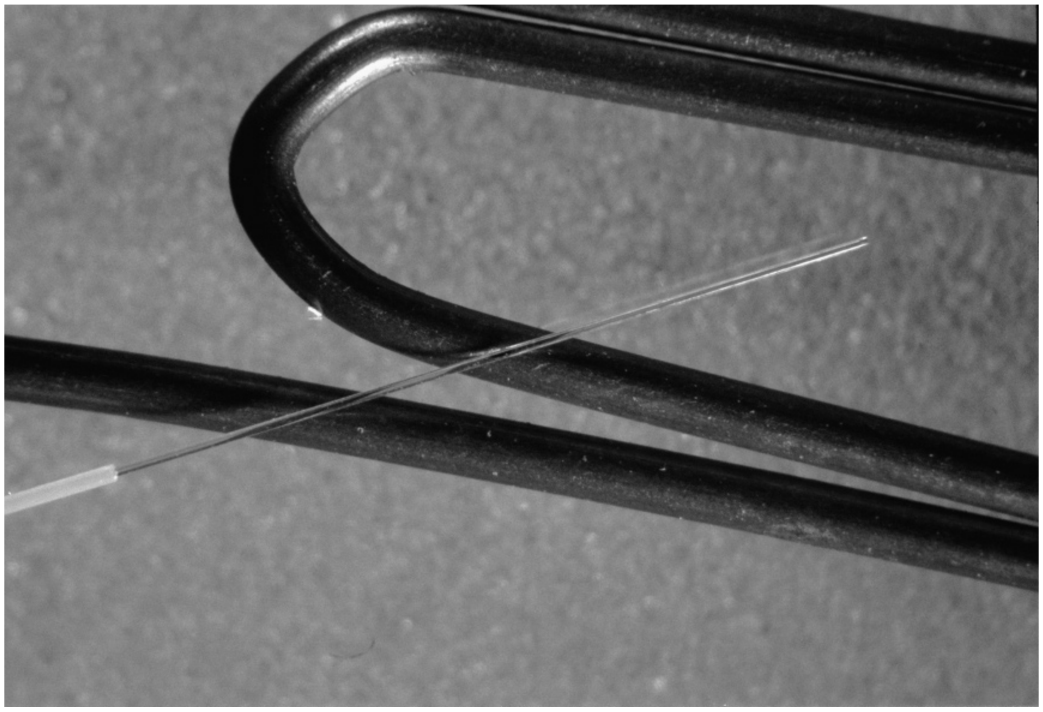

Figure 1-2 Comparison between single mode fibre and a paper clip highlighting the compact dimensions of a optical fibre sensor. (picture from [15])

Fibre optic sensors offer the advantages of light and compact design (OD 125 µm for uncoated SMF-28 single mode fibre; Figure 1-2), providing huge potential for savings in space and weight e.g., in vehicles, in particular in aircraft or spacecraft [15]. Information is measured intrinsically within the dimensions of the optical fibre itself. Wavelength encoding of the measurand offers the possibility of several sensors along a single fibre or multiplexing of several fibres into optical networks, allowing compact lightweight distributed intrinsic sensing grids, something not yet accomplished with conventional electrical sensors [16].

For continuously monitoring strain and temperature of metal components at elevated temperatures exceeding 1000 °C, appropriate sensor technologies are required. Electrically based sensors suffer from limited reliability at high temperatures and are likely to be disturbed by electromagnetic fields. Optical sensors based on silica fibres overcome these limitations [17]. The softening temperature of fused silica is almost 1200 °C which means that fibre optic sensors are highly suitable for high temperature applications in the aerospace and energy industry [18-20]. Generally, optical fibres withstand high temperatures better than electrical cables and are more robust in the presence of aggressive chemicals. Moreover, optical fibres are insulators and provide perfectly separated electrical potentials, highly desirable, e.g., in petrochemical installations [15].

1.2 Motivation – combining Selective Laser Melting and fibre optic sensing

The inclusion of an optical sensor by SLM into metal components is ideal for structural health monitoring [21]. The precision of SLM processes with high brightness lasers is appropriate for the dimensions of optical fibres. During the SLM process, the optical sensor will provide temperature and stress measurements from close proximity to the SLM process zone, helping to understand the occurrence of residual stresses or anisotropies and potentially providing valuable information for future standardisation of SLM processes.

Once integrated, the optical sensor is protected from the potentially hazardous environment by the component itself offering the possibility of in-situ measurements in harsh environments from the heart of the component, creating intelligent and smart structures. In-situ measurements offer potential for enhanced asset management,

including lifetime monitoring, and the safe use of components closer to their design limits of mechanical stability [22].

The overall motivation of the research conducted in this thesis is therefore to demonstrate the feasibility of integrating fibre optic sensors into metallic SLM fabricated components suitable for commercial processes and for high temperature sensing applications, ideally capable of measuring elastic or plastic straining and temperature changes of the component. This will lead to the fabrication of truly smart metal structures, highly desirable for high temperature and or harsh environment applications in e.g. in petrochemical (oil wells) and energy industries (turbines) or in aircraft and space applications.

1.3 Thesis outline

The chapters of the thesis are outlined below:

- **Chapter 2** provides the theoretical background for various technologies involved in the embedding of fibres into metals by SLM. The technologies involved are fibre optic sensors, applying metal jacketing to such sensors and SLM technology. Previously reported concepts for fibre embedding are studied and following from there the objectives of this thesis are specified.

- In **Chapter 3** techniques for coating optical fibres with metal jackets are developed, suitable for high temperature operations.

- **Chapter 4** describes the development of a home-built experimental setup for laser-based sintering processes (SLM) for stainless steel powder materials.

  Chapter 3 and Chapter 4 only reproduce technologies from literature and hence they add only limited new insights to both technologies. However, it was necessary to allocate a substantial percentage of this PhD work into developing and evaluating both technologies. In-depth empirical knowledge for metal jacketing of fibres and SLM processes with metal powder materials was not available within the research group at the start of the PhD studies.

- **Chapter 5** focuses on the key novelty of this work in which high brightness laser-based SLM processes are used to integrate optical fibres into metal components. The best practices for fibre inclusion are identified and parameters are incrementally changed to test the process boundaries. Potential means for further improvements for fibre integration are experimentally tested.

- Following from this, SS 316 coupons with embedded fibre sensors are fabricated and strain and temperature tested in **Chapter 6**. The fibre sensor behaviour during the SLM encapsulation process is monitored by high-speed interrogation providing new insights into the temperature in SLM processes. The build-up of residual stresses in SLM fabricated components is monitored. Strain and temperature measurements of SLM embedded fibre sensors are investigated.

- **Chapter 7** summarises the conducted work followed by a discussion of the main findings and also providing an outlook for future work.

Chapter 2

Literature Review and Background

This chapter reviews existing technologies and procedures, providing important background for integrating optical fibres into SS 316 by SLM. Background about fibre optics is provided and is followed by a more detailed review on Fibre Bragg Gratings and their behaviour as sensing elements. A review of SLM is provided, focussing on aspects important to achieve the objective of incorporating fibre optic sensors. Ultimately, after reviewing previously reported concepts for fibre embedment into metal components, the objectives of the following experimental work are outlined.

2.1 Optical fibres

Optical fibres consist of a core surrounded by a cladding. The cladding has a lower refractive index ($\Delta n = 10^{-3}$). A ray of light coupled into an optical fibre is guided through the fibre's core according to the total internal reflection mechanism (Figure 2-1). Optical fibres are made from a wide range of materials, such as fluoride glasses, chalcogenide glass or crystalline sapphire, but for applications in telecommunication and fibre optic sensing, fibres are predominately made from silica-dioxide glass, which is normally referred to as fused silica glass [15].

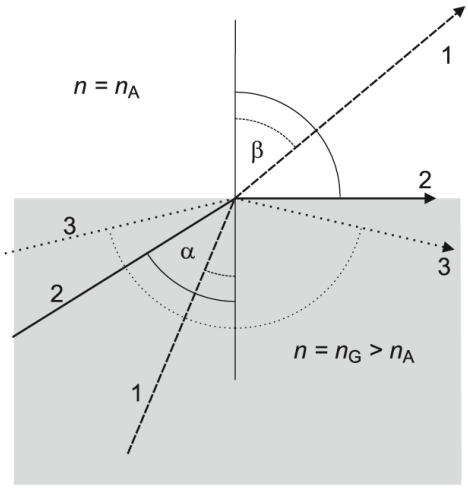

Figure 2-1 Schematic illustration of internal reflection mechanism. At the boundary between two transparent materials with different refractive indexes, light is totally reflected (path #3) for angles larger than the critical angle (α) at the boundary. (from [15])

Silicon based glasses have an extremely low thermal expansion coefficient (~ $5.5*10^{-7}$) allowing it to undergo large and rapid temperature changes without cracking [15]. Silicon is ubiquitous and is, after oxygen, the second most frequent element in the earth's crust. Making silica based optical fibres is cheap and extensive expertise making such fibres has been acquired. Most common way to fabricate silica fibres is by drawing them from preforms. Thereby, preforms which inner compositions represent the different refractive indexes of the finished fibre are drawn to longer aspect ratios (Figure 2-2). The preform composition can also be doped to further change the silica's optical and physical characteristics. Germanium doped fibre core for example exhibit a higher photosensitivity, beneficial for laser based Bragg Grating inscription.

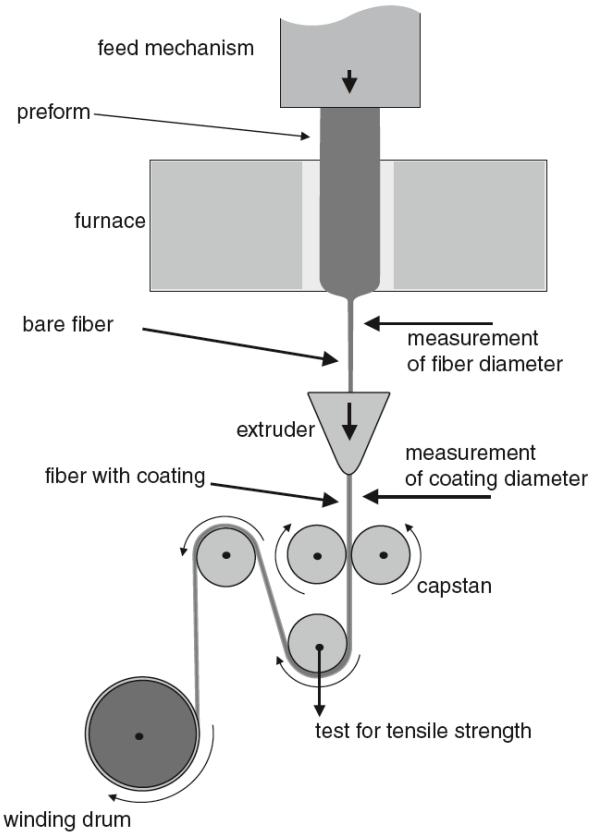

Figure 2-2 Schematic illustration for the drawing process of optical fibres. The fibre is drawn from a preform. Thereby the properties of the preform is a scaled-up version of the final composition of the fibre with different refractive indexes in core and cladding. (from [15])

Silica optical fibres do not plastically deform, they respond to stresses purely by elastic deformation. The Young Modulus for amorphous silica-dioxide is about 72 GPa. If stresses exceed the strength of the fibre, the material cracks. Under ideal conditions, fibres can endure tensile stresses of about 20 GPa [15]. For standard

telecommunications fibres (SMF-28; OD 125 µm) this implies that in theory critical tensile forces of about 245 N can be applied. In reality these values are significantly lower, since endurable stresses are highly dependent on the fibre surface quality. Findings indicate an inverse proportion between strength and scratch size on the fibre's surface [15]. Cracks of less of a few nanometres reduce the fibre strength to about 5 GPa. From this it follows that bare optical fibres have to be treated with utmost care to avoid the creation of small scratches. Any manual handling, such as mechanically and chemically stripping the fibre from its polymer coating will significantly reduce its strength [23]. High temperatures can also significantly impact the strength [24]. Empirical studies of fibres annealed at high temperatures show that annealing at 530 °C can reduce the strength to less than 0.5 GPA which is less than 3 % of the strength under ideal conditions.

2.1.1 Propagation of light through silica fibre optics

Light propagating through silica glass is attenuated by three fundamental mechanisms (Figure 2-3), absorption in the ultraviolet due to electronic transitions, absorption in the infrared due to excitation of molecules, and Rayleigh scattering due to the amorphous structure [15]. The lowest losses in silica-dioxide fibres occur at a wavelength of 1550 nm. At that wavelength the theoretical minimum losses are about 0.12 $dB*km^{-1}$ whereas in practice losses of about 0.2 $dB*km^{-1}$ are widely obtained in commercially available fibres [15].

Additional losses in transmission occur when optical fibres are bent either macroscopically or microscopically. Losses due to macro-bending occur when fibres are bent with radii greater than the fibre diameter up to a few cm. In this regime small radii lead to propagation of light into the cladding due to the occurrence of low incidence angles (Figure 2-1) hence losses in transmitted intensity occur.

Losses due to micro-bending can be simply explained by the fibres deviation from a straight line, leading to small changes of the claddings refractive index [25] causing local failure of the total internal reflection mechanism (Figure 2-4). Smallest perturbations (0.1 – 1 µm) on the fibre's surface change the fibre's loss characteristics by superimposing a loss spectrum [26]. With increased amount of micro-bends along the fibre, increased losses in transmission occur.

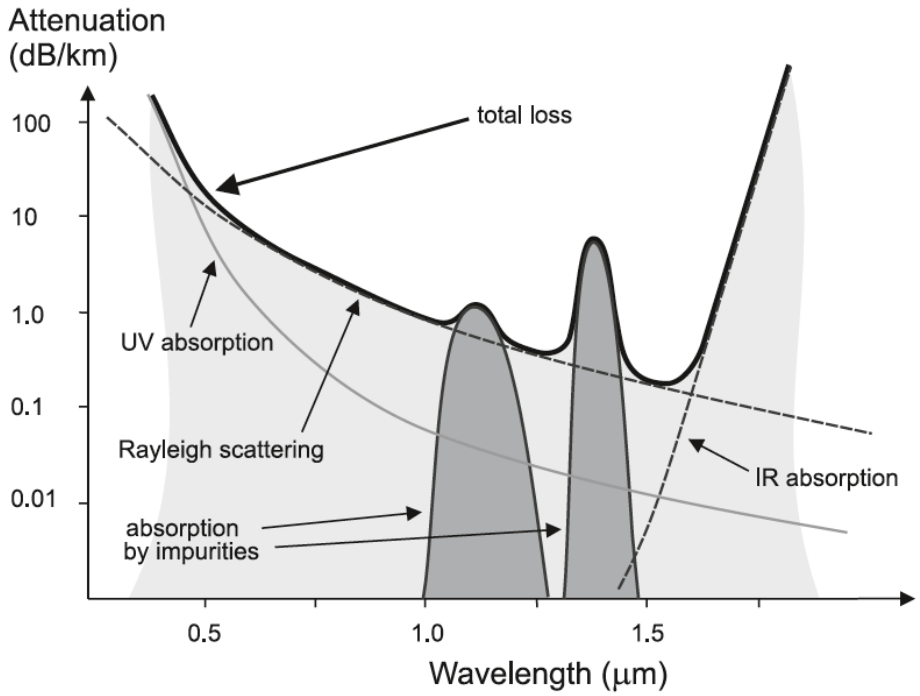

Figure 2-3 Plot losses as a function of wavelength in silica-dioxide fibres. Lowest absorption occurs at around a wavelength of 1550 nm. (from [15])

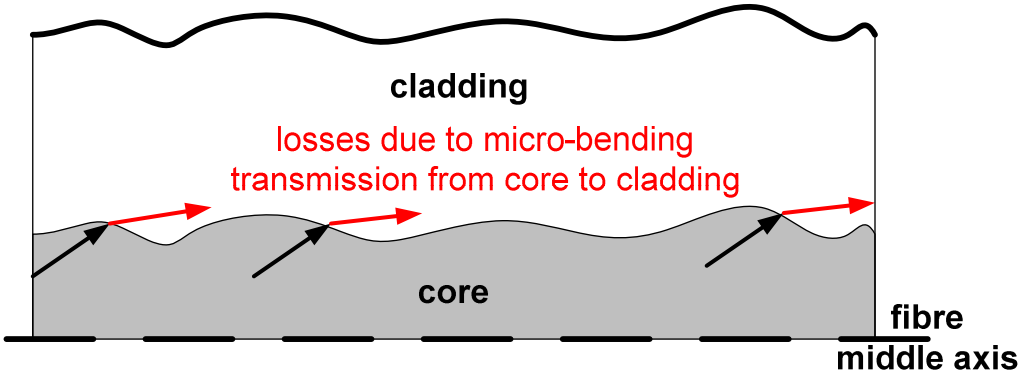

Figure 2-4 Schematic illustration showing mechanism leading to micro-bending losses. Perturbations in the fibres surface leads to perturbation at the core-cladding interface locally modifying the internal reflection mechanism leading to coupling of light into the cladding and therefore to losses.

Losses due to micro-bending can be exploited for sensing applications e.g. pressure sensing, where light transmitted through optical fibres embedded into concrete is gradually more attenuated with increased forces applied onto the concrete [27]. With

increased pressure the concrete's rough surface causes increased micro-bending of the fibre, reducing fibre transmission. Periodic micro-bends along the fibre can form gratings and as a result, specific wavelengths injected into the fibre are reflected according to the periodicity of the micro-bends [28].

2.1.2 Fibre optic sensors

Fibre optic sensors can be broadly split between intrinsic and extrinsic sensors [16]. In extrinsic applications optical sensors that are mounted close to the fibre end, quantify the measurand and couple a corresponding light signal into the fibre. The fibre acts only as a transmission medium. In contrast, intrinsic sensors use the fibre itself or part of it to directly read the measurand. The fibre is both the sensor and transmission medium, thus minimising the size of the sensor.

Further distinction is possible when taking into account the actual dimensions of the sensing element. If the measurand is only taken at a particular point, this is typically referred to as point sensing. Most electrical sensors work on this basis (e.g. thermocouples, strain gauges) and no further information about the spatial resolution of the measurand is provided. Also, most extrinsic fibre optic sensors, such as fibre cantilever sensors, dip-in ends for measurements in liquids or mounting of the fibre to resonant structures (transducers, e.g. hydrophones) work on this basis.

The full potential of fibre optic sensors is realised if used in so called distributed sensing arrangements [17]. The fibre acts as a series of sensing elements providing information as a function over its length. Thereby arrangements must be differentiated between fully distributed sensing and quasi-distributed sensing (Figure 2-5). In fully-distributed sensing arrangements information is discriminated in spatial mode, widely applied in fibre optics using Raman or Brillion scattering. The fibres used are often similar to standard telecommunication optical fibres and are therefore low cost, however the additional equipment necessary for interrogating these fibres in a fully distributed manner is very costly especially in cases where high spatial resolution is necessary. A high spatial resolution of about 10 cm is achieved in Raman scattering using picosecond laser pulses, leading to a resolution of the measurand of about 1 °C or 25 με [29] but costs remain high (> 100k GBP for the interrogation system (year 2015))

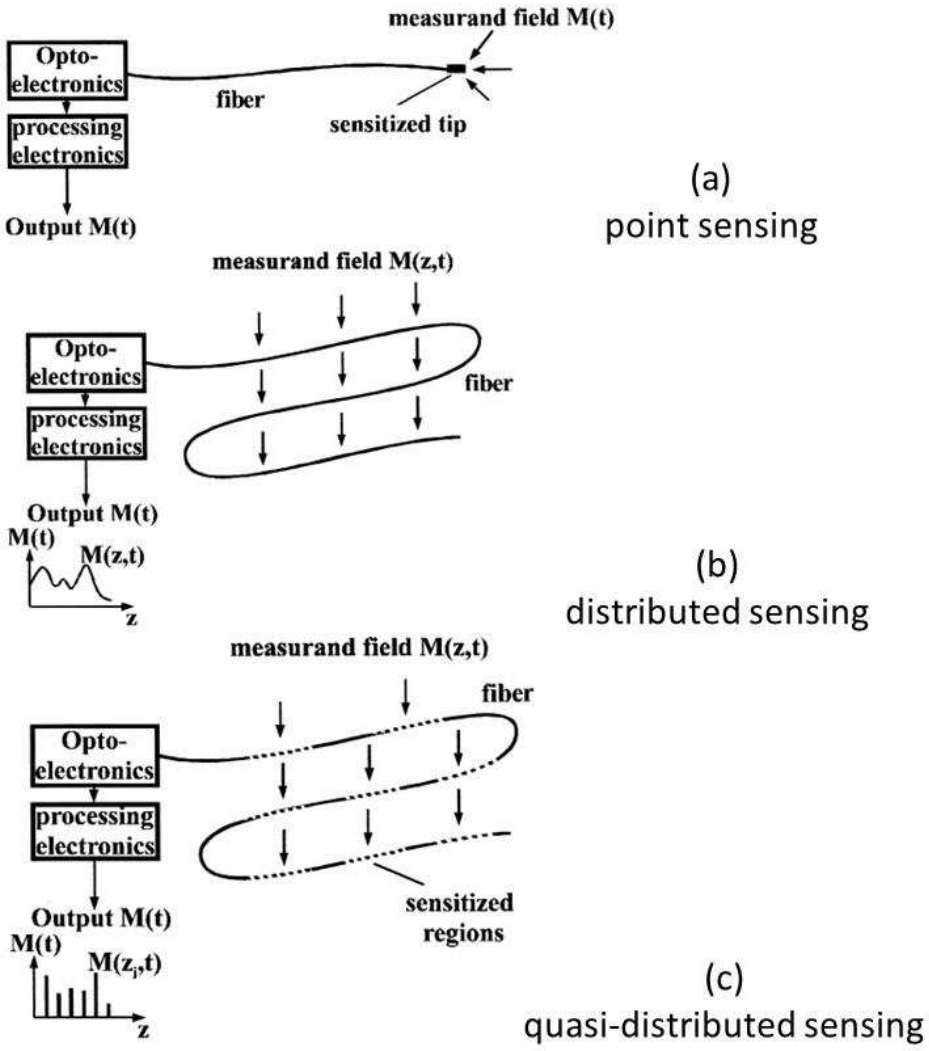

Figure 2-5 Schematic illustration for fibre sensing arrangements, point sensing (a) distributed sensing (b), and quasi-distributed sensing (c). (from [17])

More efficient in terms of cost and practicality are quasi-distributed sensors where the measurand information is obtained at particular and pre-determined points along the length of a fibre network. Fabry-Perot based sensors or Fibre Bragg Gratings (FBG) are such sensors. E.g. numerous FBGs can be placed along optical fibres and independently interrogated using techniques such as wavelength-multiplexing [30]. These sensors are mainly based on standard telecommunications fibres and are therefore low cost, and extensive knowledge is available. Therefore, research reported in this thesis concentrates on Fibre Bragg Gratings. However, it is worth highlighting that once optical fibres can be integrated into metals using SLM, all the other measurement

techniques such as Raman or Brillion scattering can be applied since these techniques are all based on similar optical fibres.

2.1.3 Photosensitivity of fused silica and inscription of Bragg Gratings

The high absorptivity of silica-dioxide for UV-light (λ = 100 nm – 400 nm) can be exploited to cause changes in the refractive index of the glass when exposed to such UV light. In the literature, this effect is often referred to as photosensitivity of glass [16, 31-34]. When using a one dimensional spatially modulated illumination with UV-light and high intensities, this leads to a one dimensional spatially modulated refractive index changes along the core of the fibre, creating a FBG ().

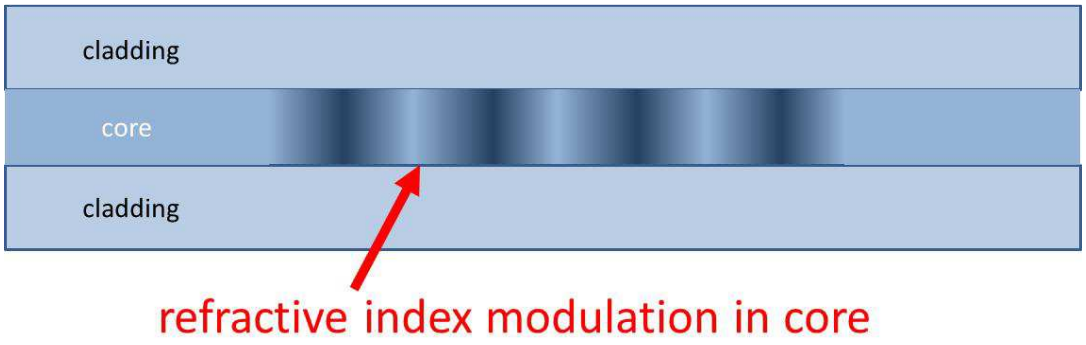

Figure 2-6 Schematic illustration for optical fibre with cladding and core. Refractive index modulation of the core is creating a FBG.

One technique to write such a spatially modulated illumination is to use a phase mask. Phase masks are one of the most effective methods for FBG inscription [35]. The excitation laser beam is spatially modulated by a diffractive optical element, the phase mask [33, 34]. The surface of the phase mask is formed from a one-dimensional periodic-relief pattern which is etched with a period (Λ_{PM}). The profile of this surface-relief grating is designed that the incident laser beam is diffracted into different orders (Figure 2-7).

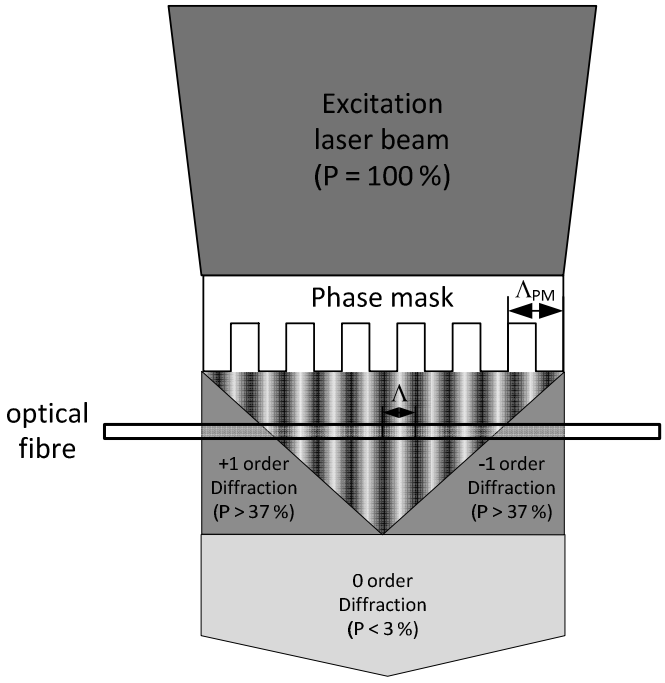

Figure 2-7 Scheme of a setup for FBG inscription by using a phase mask. (derived from [35])

By irradiating the phase mask perpendicular to its surface, the zero-order, un-diffracted beam is almost suppressed (< 3 % of the incident laser power) due to destructive interference. Each of the two (±) first order diffracted fractions of the incident laser beam contains more than 37 % of the incident laser power. Overlapping these two beams results in a near-field fringe pattern, resulting from the interference of the (±) first-order diffracted beams. The periodicity of this fringe-pattern is one and a half times the periodic-relief pattern of the phase mask, generating a refractive index modulation in the core of a photosensitive optical fibre. Thereby the fibre is typically placed in close proximity (less than 100 µm) to the phase mask [33, 34].

The phase mask technique requires a laser source with good spatial coherence. Higher coherences allow the fibre to be placed at greater distances from the phase mask due to the larger spatial dimensions of the interference pattern [33, 34].

2.1.4 Properties of Fibre Bragg Gratings

The basic operation principle of FBG-based sensor systems is the monitoring of the shift in Bragg wavelength (λ_B) [34]. A typical interrogation system for a FBG system is shown schematically in Figure 2-8 [36]. The system includes a broadband source, an optical spectrum analyser (OSA) and the FBG itself. The light of the broad-band source

is coupled into the optical fibre with FBG. The FBG acts as a reflector for a specific wavelength, the Bragg wavelength. Light with wavelengths around the Bragg wavelength λ_B is reflected by the FBG with intensities in accordance to the FBG's reflectivity. The selective reflectivity of the FBG causes the appearance of a loss band at the Bragg wavelength in the transmission spectrum.

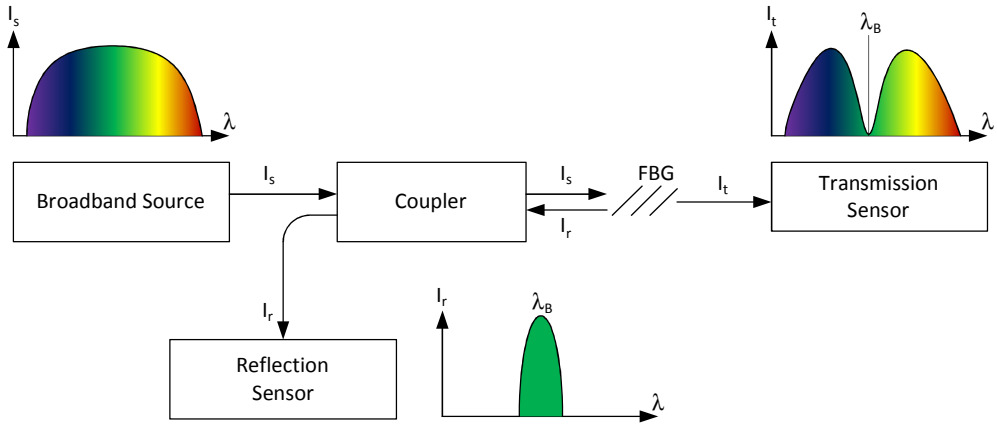

Figure 2-8 Scheme of a FBG sensor layout. Light from broadband source is injected into optical fibre containing a FBG. According to Braggs Law, light at the Bragg wavelength λ_B is reflected by the grating. (derived from [36])

Using a coupler directs the back reflected light of the FBG to a detector or spectrum analyser to allow the measurement of the wavelength λ_B of the back reflected light [32]. The measured Bragg wavelength does not depend on the light intensity of the emitter or losses which might occur at the interfaces of different components, which is a particular advantage of FBG sensors [32].

The reflectivity of a FBG can be calculated by using solutions of coupled mode theory [37]. The reflection R of a FBG at the Bragg wavelength λ_B is a function of the grating length l and the optical fibre constant K and the refractive index modulation Δn:

$$R = \tanh^2\left(\frac{\pi \cdot \Delta n \cdot l}{\lambda_B} \cdot \left(1 - \left(\frac{2 \cdot \pi}{\lambda_B} \cdot K\right)^{-2}\right)\right) \qquad \text{EQN 1}$$

Whereby the optical fibre propagation constant K is determined by the material and geometrical properties of the fibre, namely the refractive index of core (n_{co}) and cladding (n_{cl}) and also the core diameter (d_c).

The reflectivity of a FBG is in literature is often referred to as its strength. This strength is dependent on the refractive index modulation and is thus strongly dependent on the fluence, the accumulated energy per area, of the inscription process. High peak fluencies during pulsed inscription processes lead to the occurrence of type II damage gratings if the fluence of each laser pulse is above the damage threshold of fused silica [38]. These type II gratings provide a large refractive index modulation and hence a high strength. However, this is compromised by a large signal width and significantly developed losses in the spectrum for wavelengths shorter than the Bragg wavelength compared to type I gratings. FBG inscription by laser pulses below the damage threshold increases the refractive index modulation accumulative to the irradiated fluence of the laser source until a level of saturation is achieved [39].

The reflectivity of a Fibre Bragg Grating is increased by larger grating lengths [40]. However, achieving strong FBGs with good spectral properties such as a small spectral width or overall spectral signal quality is a compromise. The signal quality of the gratings is decreased by longer grating lengths due to arising sidelobes next to the Bragg wavelength [40]. These sidelobes and large grating widths are not suitable for multiplexing many gratings into a network. More ideal are gratings with a narrow spectrum and high reflectivity [33, 34]. A refractive index modulation of at least 1×10^{-4} should be obtained in a standard optical fibre (SMF-28) to achieve a high reflectivity of the grating. To overcome the sidelobes arising with longer grating lengths, apodization is used which modulates the fluence over the grating length [41].

2.1.5 Sensitivity of Fibre Bragg Gratings to external factors

FBG are based on periodic refractive index modulation of an optical fibre over a specific length [34]. This index perturbation is comparable to a stop-band filter. A narrow part of the incident spectrum of light is reflected by successive coherent scattering from the index modulation and the strongest interaction occurs at the Bragg wavelength (λ_B). The Bragg wavelength (λ_B) is dependent on the periodicity of the

index modulation (Λ) and the effective refractive index (n_{eff}) of the fibre core[33, 34] :

$$\lambda_B = 2 \cdot n_{eff} \cdot \Lambda \qquad \text{EQN 2}$$

Differentiating EQN 2 leads to the Bragg wavelength shift:

$$\Delta\lambda_B = 2 \cdot \Delta n \cdot \Lambda + 2 \cdot n \cdot \Delta\Lambda \qquad \text{EQN 3}$$

The shift of the Bragg wavelength $\Delta\lambda_B$ is sensitive to changes in strain and temperature [31]. A FBG sensor is sensitive to temperature changes due to the temperature dependency of the refractive index n and the elongation of the grating pitch (Λ) due to thermal expansion. The variation of grating pitch length with temperature ($\Delta\Lambda * \Delta T^{-1}$) is equals the thermal expansion coefficient (α), a specific material constant. The dependence of the Bragg wavelength shift ($\Delta\lambda_B$) to a temperature change (ΔT) is:

$$\frac{\Delta\lambda_B}{\Delta T} = \lambda_B \cdot \left(\alpha + \frac{1}{n}\frac{dn}{\Delta T} \right) \qquad \text{EQN 4}$$

For bare uncoated silica-dioxide fibres the thermal expansion coefficient $\alpha = \sim 5.5 \times 10^{-7}$ (at ambient temperature) is an order of magnitude smaller than typical values for the refractive index temperature sensitivity $dn * \Delta T^{-1} \sim 5 \times 10^{-6}$. At higher temperatures the refractive index temperature sensitivity significantly increases. At room temperature the sensitivity of Bragg wavelength to temperature is about 7 $pm * C^{-1}$ (@ wavelength $\lambda_B \approx 1.5$ µm) and shows an exponential increase to about 11.5 $pm * C^{-1}$ for temperatures above 150 °C (Figure 2-9) [34, 42, 43].

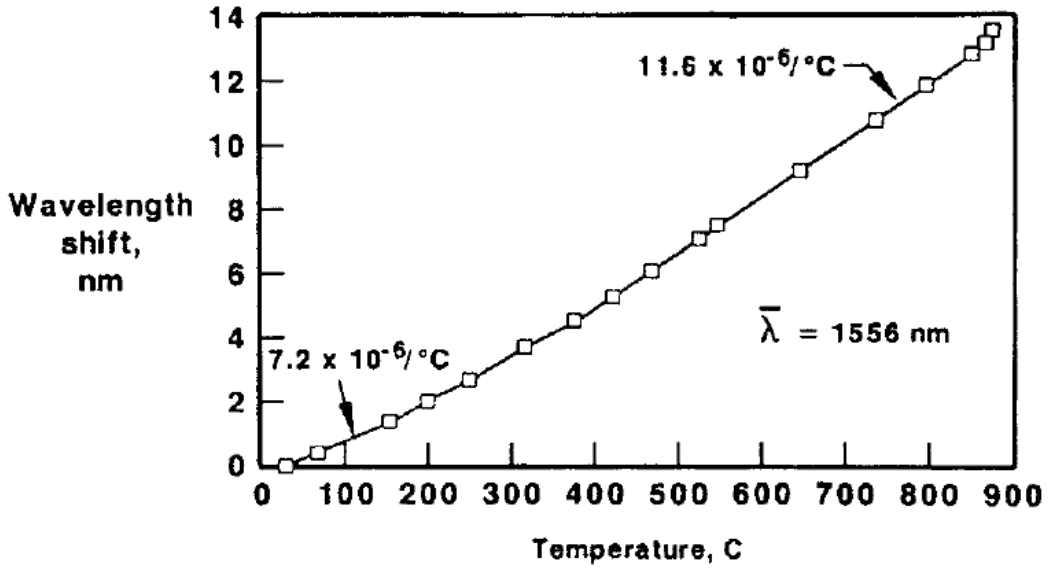

Figure 2-9 Bragg wavelength shift as a function of temperature for an uncoated FBG sensor. The FBG tracks temperature changes with a sensitivity of about 11.6 pm*C^{-1} for temperatures above 150 °C. (from [16])

If the fibre is jacketed or embedded into materials, the thermal expansion coefficient is influenced by the surrounding material and hence the grating temperature sensitivity also changes. Assuming a model of two parallel springs, the thermal expansion of a nickel jacketed FBG ($OD_{fibre} \approx 125$ µm) is dominated by the thermal expansion of nickel provided that the coating thickness exceeds about 50 µm [43].

The fibre also responds to strain, via the physical elongation of the sensor and therefore the elongation of the grating period Λ and the change in the average refractive fibre index due to the photo elastic effect [33, 34, 42]. The dependency of the Bragg wavelength shift $\Delta\lambda_B$ to the relative physical elongation (ε) induced by strain is given by:

$$\Delta\lambda_B = \lambda_B \cdot \varepsilon\left(\frac{\Delta n}{n} + 1\right) \qquad \text{EQN 5}$$

Whereby the term $\Delta n*n^{-1}$ is dependent on the photo elastic effect and contains material constants such as the Poisson constant and the Pockels coefficient. Using standard parameters for standard silica fibres, the wavelength shift is in the range of 1 pm*(µε)$^{-1}$ for axial straining [36, 44]. If straining is not isotropically applied

(axial ε_a: transversal: ε_t) further derivation of the photo elastic term ($\Delta n * n^{-1}$) leads to incorporation of the direction dependent Pockel's coefficients p_{xy}:

$$\frac{\Delta\lambda_B}{\lambda_B} = \varepsilon_a - (\frac{n^2}{2}) \cdot (p_{11} \cdot \varepsilon_t + p_{12}(\varepsilon_a + \varepsilon_t)$$ EQN 6

From this it follows that in presents of transversal straining ε_t of the FBG the shift in Bragg wavelengths for axial straining is mitigated. The spectral response of an FBG for different strain modes is displayed in (Figure 2-10). Applying only longitudinal stresses (axial straining) the grating spectrum shifts whilst the reflection width remains constant. Applying additional transverse stresses onto the FBG causes a negative wavelength shift, but also the grating spectrum can be significantly widened with two double peaks clearly evident [45].

This phenomenon occurring when transversally stressing FBGs is also often referred to as birefringence. The double-peaking is highly sensitive to the polarisation of the light propagating through the fibre. If the polarisation angle matches the direction of the applied transverse load, double peaking occurs. For other polarisation states some broadening remains but the spectral response of the grating is more complex.

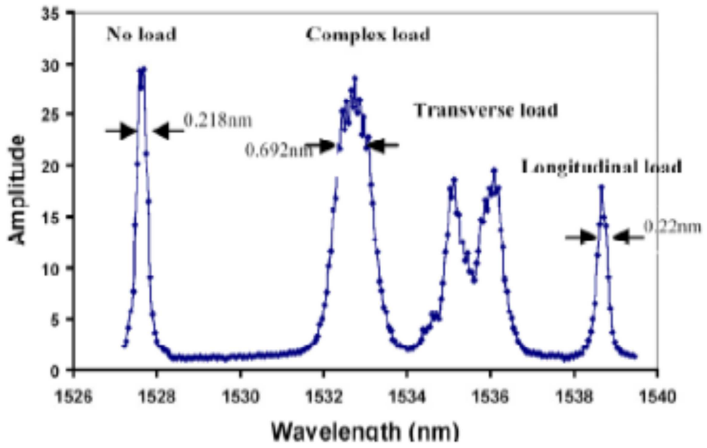

Figure 2-10 Spectral response for FBGs with different load cases. In case longitudinal tensile load is applied the Bragg wavelength simply shifts to longer wavelengths. Applying loads with transversal elements the spectral response of the grating is distorted. (from [45])

A thorough study on birefringence in single-mode FBGs is conducted in [46]. A fibre is squeezed between two plates and the force is incrementally increased and spectra are recorded (Figure 2-11).

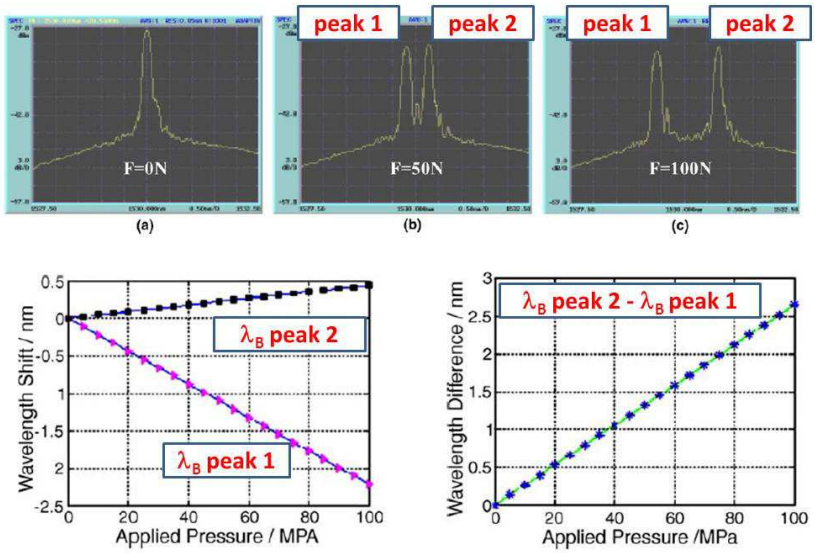

Figure 2-11 Spectra of FBG recorded under different transverse loads (top). The higher the transverse load, the greater the widening of the grating, leading to pronounced double-peaks. Plot (bottom) displays the differences in centre wavelength of peaks as a function of transverse force. (all from [46])

The whole reflection spectrum shifts negatively with increased transversal load. Thereby, the peak with the higher Bragg wavelength remains almost constant and the second occurring peak at lower wavelengths shifts negatively.

2.1.6 Fibre Bragg Gratings at elevated temperatures

FBG sensors inscribed into standard germanium doped telecommunications silicon fibres with UV laser excitation (Type I gratings) at a first glance are not suited for applications at high temperatures [16, 33, 34]. Temperatures above 80°C lead to bleaching out of the defects causing the refractive index change and hence to incremental losses in grating strength. Temperatures of more than 300 °C cannot be endured for longer periods (>hrs) [47].

Doping fibres with Selenium stabilises the FBGs temperature range up 650 °C [48]. Gratings written into hydrogen loaded phosphor-silicate fibres are capable of enduring

temperatures up 500 °C without showing any sign of decay in reflectivity over time [49]. Type IIA gratings which are produced by long exposure times can operate up to 800 °C depending on preparation in terms of hydrogen loading and heat treatment recipes [50, 51], Type II gratings inscribed with laser irradiation above the damage threshold survive even higher temperatures up to 1000 °C .

However, the problem with all these approaches is that they compromise the excellent properties achieved with standard type I gratings written into germanosilicate fibres. FBGs other than type I are accompanied by low refractive index modulations, degradation of the signal profiles, oscillations in reflectivity or large diffractive losses such as those observed with type II damage gratings [52].

It has been shown that by pre-annealing FBGs written into germanosilicate fibres with temperatures up to 745 °C and 20 min of total annealing time, type I FBG temperature survivability can be increased significantly. Canning et al describes this recipe [47, 52, 53] for boron co-doped and hydrogen-loaded standard germanium silicate optical fibres. The FBGs are written with an ArF excimer laser at wavelength of 193 nm. In subsequent annealing processes these gratings show no decay in signal strength over time for temperatures up to 600 °C and furthermore the loss in signal strength at 700 °C is slightly less than 3 dB. For temperatures greater than 700 °C the refractive index modulation and therefore the reflectivity of the grating starts to decay exponentially and vanishes at about 800 °C. Further trials demonstrate [52], that this kind of heat treatment enables both hydrogen-loaded as well as non-hydrogen-loaded germanium silicate fibres to survive temperatures up to 500 °C over long periods without showing any sign of decay in reflectivity.

Regenerated FBGs (RFBG) can be produced by annealing the fibre with even larger temperatures in a subsequent annealing step [47]. At a temperature of about 800°C no sign of the former type I FBG is detected (Figure 2-12). If the temperature is further increased, however a new grating emerges with the same Bragg wavelength and similar spectral properties. These gratings are called RFBG. The former type I FBGs produced by the pre-annealing recipe are called seed gratings due to their role as a source for the regenerated Bragg gratings. The strength of this regenerated Grating is usually about 20% of the original seed grating. Regenerated gratings endure temperatures up to the softening temperature of fused silica and achieve signal qualities comparable to type I

gratings. Unlike other high temperature gratings such as type II damage gratings they can also preserve the complex functionality, like apodization, of an advanced type I grating making them to appear a ideal choice for high temperature applications [47]. A disadvantage is that the refractive index modulation is an order of magnitude less than that of the original type I seed grating.

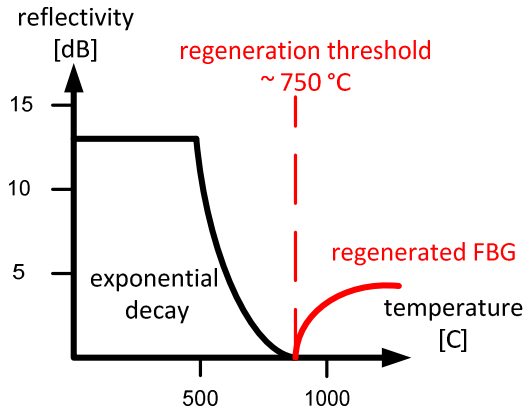

Figure 2-12 Schematic illustration for germano-silicate single mode-grating reflectivity over temperature. The grating is stabilised to temperatures up to 500 °C by pre-annealing with a temperature of 650 °C for 20 mins. When temperatures exceed 500 °C the grating continues to exponentially decay until it vanishes at around 750 °C. Further increases in temperature cause reappearance of the grating, a Regenerated Fibre Bragg grating is formed. (derived from [47])

The reflectivity of the regenerated FBG is strongly dependent on the fluence of the seed grating inscription process [39]. The regeneration factor, the ratio between the maximum reflectivity during the regeneration process and the reflectivity at room temperature before the regeneration process is almost tripled to 1 by doubling the fluence for seed grating inscription. The doping concentration of the fibre also influences the reflectivity and the regeneration temperature for the RFBG [54]. An increase of the germanium concentration in fibres significantly increases the reflectivity and lowers the temperature threshold for the regeneration process. For example the reflectivity of a FBG in a fibre with a germanium concentration of 10 % is almost twice that of a FBG in a standard telecommunications fibre with a germanium concentration of 3 %. The regeneration temperature for achieving the regeneration process is lowered by about 100 °C to 850 °C.

Regeneration of gratings written into germanosilicate optical fibres holds great promise for high temperature applications. Germanosilicate fibres are ubiquitous and can be readily commercially obtained with written gratings at low cost. This and their good spectral properties make gratings written into such fibres with high fluencies the first choice for investigating embedment of such FBGs into metals by SLM and subsequent high temperature applications.

2.2 Metal fibre coatings

For integrating optical fibres into metals by SLM and subsequent strain and temperature measurements a fibre coating is necessary to attach the fibre to the metal and protect the fibre from the energy of the SLM process. Common standard telecommunications fibres typically use ultraviolet (UV)-curable polymers as coating materials. These materials have advantages in terms of very high coating speeds and low micro bending losses [55]. Polymer coating materials are however unsuited for embedding of fibres in metallic structures by SLM. The melting temperature of commonly used polymers is usually below 200 °C and moreover polymers are not able to integrally join with metals [55]. Polymer-epoxy adhesion can be used to glue optical fibres for sensing purposes to metal components. But epoxies can only be used up to relatively low temperatures, even high temperature epoxies cannot sustain temperatures exceeding 350 °C and are therefore not an viable option for applications in high temperature environments [56]. Additionally, fibre optic sensors attached by epoxy adhesion suffer from non-linear strain transfer because adhesive layers consume shear energy due to shear deformation [57].

Barrera [19] describes a technique for packaging regenerated Bragg gratings on the base of a ceramic protection tube with an outer metallic layer. The two-bore ceramic protection tube holds the fibre grating straight by having just a slightly larger bore diameter (130 µm) than the diameter of the optical fibre (125 µm). Trials show that the response to temperature changes of the packaged and not packaged regenerated Fibre Bragg grating is unchanged. Furthermore no hysteresis behaviour is detected in the sensor signals. Despite these advantages, no proper attachment between fibre and jacketing exists. Strain and thermal expansion of the jacketing material is therefore not measured by the fibre.

Applying metals directly onto the fibre is more desirable. However, when coating optical fibres with metal materials, it is important to minimise energy inputs during the process to protect the fragile optical fibre. Therefore, recipes for coating optical fibres with metals found in literature have in common that the process temperature is limited to low temperatures to protect the fibre from heat and residual stresses [19, 55, 58]. Low temperature coating techniques of metal jacketed optical fibres are based on dip coating [55, 58], sputtering [44, 59] and plating [44, 58, 59].

Coating approaches based on drawing through or dipping into molten metal materials can be used with a wide range of materials with significant differences in melting temperatures. Drawing fibres containing FBGs through molten tin is described by Seo [55]. The melting temperature of tin is only about 230 °C. Different drawing speeds are analysed. Results show that with specific drawing speeds void free coatings can be achieved. The signal quality of FBGs inscribed into the fibre is not influenced by residual stresses, which can occur during the process. Tin readily bonds with iron atoms but also tin has a very low melting temperature (~230 °C) and therefore large quantities of Tin inside a component deployed in high temperature applications are not desirable. The concept of embedding fibre optic sensors into aluminium by casting is reported in [60]. The fibre is positioned in a casting form which is subsequently filled with molten aluminium (~ 660 °C). Stainless steel tubes are used to protect the fibre at the interface between molten aluminium and air. Using one of such approaches for drawing bare fibres through molten metals was not a viable option for the PhD studies described in this thesis. The objective of the research is to open up possibilities for temperature and strain sensing at temperatures that are close to the softening point of silica-dioxide (T_s ~ 1195 °C). Any metal material suitable for this temperature regime will have a higher melting temperature and inflict structural damage to a bare optical fibre drawn through the molten material. E.g. IN738LC at 850 °C still exhibits two-thirds of its ambient temperature tensile strength whilst the melting point is about 1400 °C [61].

Sandlin [58] describes a technique to apply thin silver layers (T_m ~ 960 °C) of 1 µm thickness onto fibres by a technique called mirror making. The purpose of the thin silver layer is to enable electrical conductivity for subsequent electroplating of nickel onto the fibre. The thin silver interlayer is applied to the fibre by the reduction of a silver ammonium complex with glucose in strongly alkaline conditions. In the

subsequent electroplating process nickel layers of up to 25 µm thickness are deposited on to the fibre. Nickel has a high melting point and readily integrates into iron-based alloys.

An alternative approach to applying a conductive layer is to use RF sputtering [10, 14]. A titanium layer with 1 µm thickness is sputtered onto the optical fibre to enhance the adhesion of the fibre to nickel. Subsequently a film of about 2 µm thickness of nickel is sputtered on top of the titanium layer. Finally the nickel layer is increased by low temperature electroplating to a total thickness of up to 1 mm. Another paper [59] describes a two-step technique for plating nickel onto optical fibres using electro-less plating by applying an initial electrical conductive keying layer and subsequently electroplating (higher deposition rates) for rapid deposition of much thicker coating thicknesses. The nickel layer is deposited by reduction of a nickel sulphate complex with sodium phosphate, ionic acid and boric acid. In a subsequent electroplating process the thickness of the nickel coating is increased to different thicknesses in the range of 2 – 335 µm by varying the time of the electroplating process.

It is clear that applying metal jackets using low temperature processes such as mirror-making, rf-magnetron sputtering and electroplating is the best route for jacketing optical fibres. The mirror-making technique is not ideal due to the comparatively low melting temperature of silver. It was decided to concentrate on a rf-magnetron sputtering approach to provide an electrical conductive metal keying layer and subsequent electroplating of nickel. For both processes facilities are available within the research group.

2.3 Melting metals with lasers

In laser processing of metals, the laser beam energy is absorbed at the material surface, resulting in an increase in temperature. The amount of energy (ΔQ) necessary to increase the temperature (ΔT) of a specific material volume (c_p = specific heat capacity; ρ = density; V = volume) is expressed by the following adiabatic equation [62]:

$$\Delta Q = \Delta T \cdot c_p \cdot \rho \cdot V \qquad \text{EQN 7}$$

For temperatures exceeding the material melting temperature (T_m) an additional term for the melt enthalpy (H_m) is added. Differentiating the equation over time (d/dt) allows expressing the power ($P_{process}$) which is necessary to achieve the desirable temperature change for a beam moving across the specimen's surface with a speed V/t:

$$\frac{d}{dt}\Delta Q = P_{process} = \frac{d}{dt}\Delta T \cdot c_p \cdot \rho \cdot V = \Delta T \cdot c_p \cdot \rho \cdot \frac{V}{t} \qquad \text{EQN 8}$$

The laser radiation is only absorbed at the material's surface according to the materials absorption coefficient (A_m), which is dependent on wavelength.

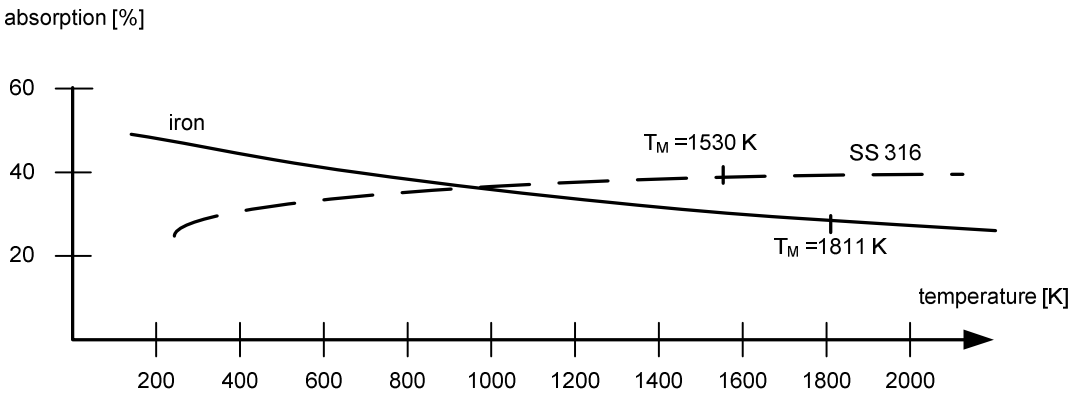

Figure 2-13 Absorption coefficient for solid iron and SS 316 material as a function of substrate temperature. For both materials in average only 40 % of the incident laser energy is absorbed (@ 1 µm wavelength). The remaining energy is reflected back into the environment and is lost. (from [63, 64])

For solid SS 316 material the absorption is about 30 % at ambient temperature and slightly increases to about 40 % at melting temperature, as shown in Figure 2-13, together with data for pure iron [64]. Therefore, it is assumed that for processing of iron-based steel alloys only about 40 % of the energy provided by the light source is utilised for the actual melt process, the remaining energy is reflected into the environment and is lost.

When processing materials with large thicknesses compared to the beam diameter, the width of the melt pool approximates the beam diameter, since only the laser beam delivers energy and no energy is "reflected" from the materials bottom surface into the process zone [65]. Provided that temperatures do not exceed vaporisation temperature

heat is transferred due to heat conduction and convection within the fluid melt pool leading to half-spherical melt pools [66]. Approximating the volume of molten material by the laser beams diameter (d) and in case of a moving laser beam the speed (v_f) by which the beam is travelling across the specimen delivers dV/dt. In combination these assumptions lead to the power P_{laser} which the laser needs to provide to achieve melting of the material [66, 67]:

$$P_{process} = A_m \cdot P_{laser} = \left(H_m + c_p(T_m - T_\infty)\right) \cdot \rho \cdot \left(\pi \cdot \frac{d_f^2}{8} \cdot v_f\right) \qquad \text{EQN 9}$$

Quadratic increases in light intensity (P_{laser}/d_f^2) occur with smaller spots and therefore with significantly less laser power, intensities can be high enough for with high brightness laser sources and small spot diameters. The necessary intensities for laser processes of iron are displayed as a function of interaction times in Figure 2-14. In continuous laser processes, the interaction time is defined by spot size over speed (d_f/v_f).

From this it follows that in order to embed optical fibres, high brightness lasers are the ideal choice. The small spot size is up to a factor of ten smaller than the optical fibre itself. Small-spot sizes enable high intensities and the higher the intensity, the quicker melting temperature is reached, minimising the interaction time which is advantageous because the energy input into the optical fibre needs to be minimised. Putting this into perspective with existing laser sources in our research group, a high brightness fibre laser with a maximum intensity ~2.5x 10^{-5} W*mm^{-2} reaches melting in interaction times of a few microseconds (Figure 2-14). A diode laser which was also available has an intensity of only 4x 10^{-3} W*mm^{-2} requires four orders of magnitude more interaction time (~tens of milliseconds) to achieve a similar result.

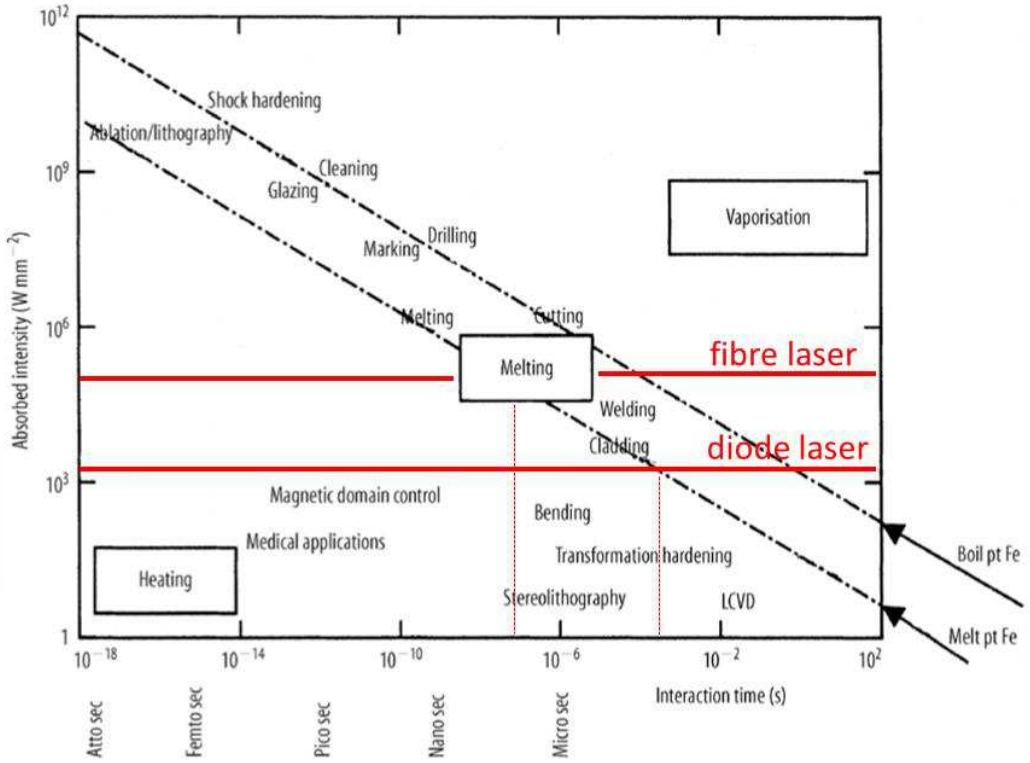

Figure 2-14 Estimates for necessary intensities to achieve laser material processing of solid iron material as a function of interaction time (from [67]). Using values for the available equipment in our research group the fibre laser system (100 W) due to its higher intensity achieves melting of the material four orders of magnitude faster than the available high power diode laser system (200 W) with small maximal intensity.

During the process, energy dissipates from the melt pool into the surrounding material, not contributing to the process and over time leading to power loss from the process [14].

$$P_{loss} = 4 \cdot \alpha \cdot d_f \left(T_m - T_\infty\right) \cdot \left(\frac{d_f \cdot v_f}{\alpha}\right)^{0.3} \qquad \text{EQN 10}$$

These losses are dependent on the thermal diffusity of the material and the spot size. Smaller spots lead to less heat conduction into the surrounding material. The thermal diffusity α is a material constant

$$\alpha = \frac{\lambda}{\rho \cdot c_p} \qquad \text{EQN11}$$

Where λ is thermal conductivity, c_p heat capacity and ρ density. Processing materials with high thermal diffusity such as copper or aluminium larger amounts of energy are necessary to overcome losses, since the energy readily diffuses into the environment [68]. Once a melt pool is created, melt pool dimensions are also typically larger, since high diffusity results in smaller temperature gradients. Steels are characterised by comparatively lower thermal diffusity compared to other, non-iron based metal alloys. Melt pools hence are locally defined and typically approximate beam diameter [68].

The total power P_{total} needed for the stationary melting process is the sum of the power for melting and the power for replacing lost energy due to conductivity. Estimates for P_{total} as a function of feeding speed for SS 316 are displayed in Figure 2-15. Two cases are presented representing the two different light sources available of this work in our research group, a high brightness fibre laser (100W) and a diode laser (200 W) with comparatively larger spot size.

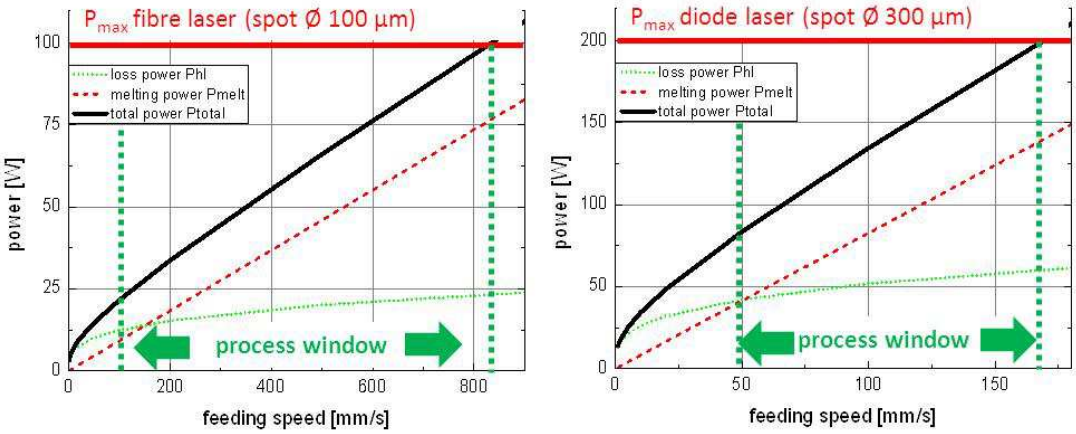

Figure 2-15 Calculated laser power required for melting as a function of feeding speeds The fibre laser offers a significantly wider process window.

With increasing feeding speeds the power required for melting rises more rapidly than the power losses, increasing the efficiency of the laser melting process at higher speeds. For feeding speeds where is $P_{hl} > P_{melt}$ processes are inefficient, more energy dissipates into the environment than is used for melting [65]. Furthermore processing metals with small feeding speeds is disadvantageous for the mechanical properties of the metal. When laser processing austenitic steel materials such as SS 316, slow speeds lead to

long interaction times and therefore long cool down times leading to weaker mechanical properties in areas remote to the process zone in which the material is annealed. In combination with the available output power of the laser source therefore a potential process window can be estimated. For SS 316 the high brightness fibre laser with smaller spot leads to significantly larger process windows, offering more potential to achieve melting process with high efficiencies and low heat conduction into surrounding material volumes.

At high intensities or long interaction times vaporisation can occur [67] (Figure 2-14). This results in the formation of a vapour filled "key-hole" inside the melt pool. The key-hole is kept open by the vapour pressure. The formation of the key-hole leads to a significant increase in laser absorption and melt penetration.

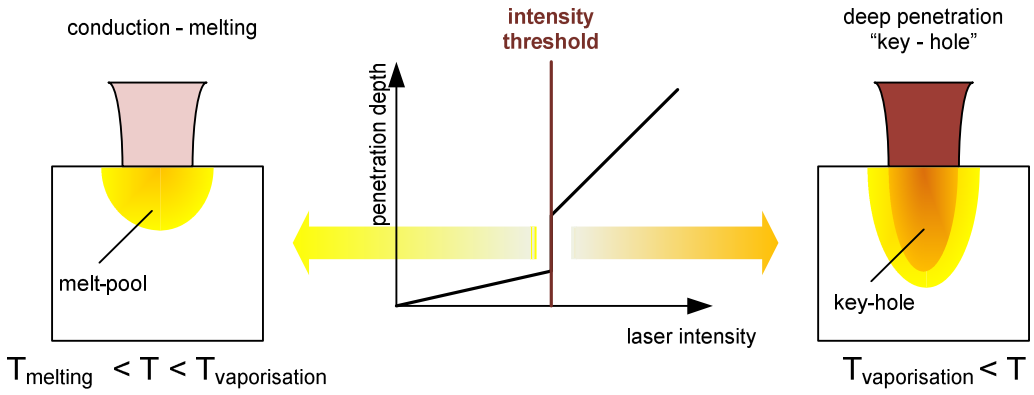

Figure 2-16 Schematic illustration for transition from conduction melting regime to vaporisation. Increasing laser intensity just above the vaporisation threshold leads to significantly deeper penetration depths. The incident laser light is better absorbed in the formed key-hole due to multiple-reflections, leading to more efficient use of the laser power.

The increase in melting depth happens rather rapidly, particularly for materials with comparatively low thermal diffusity such as SS 316. Once the intensity is sufficient to cause vaporisation the amount of absorbed energy is significantly increased since the incident laser light is absorbed inside the key-hole by multiple reflections. For steel materials then the absorption coefficient is rapidly increase from 40 % to almost full absorption leading to an increase of the melt pool volume of up 300 %. The melt pool width however almost stays constant and only the depth is increased leading to larger aspect ratios of the melt seam. Rays of the incident laser light are absorbed according to the materials absorption coefficient and propagate from the top to the bottom of the

keyhole due to multiple reflections inside the keyhole. Along their way to the bottom the rays incrementally lose their intensity. Therefore further increases in laser intensity lead mostly to deeper penetration depth into the work piece. Using very high power lasers (kW regime) with relatively small spot sizes (300 µm) aspect ratios of more than 40 are reported [69], therefore this regime of laser processes is often referred to as "deep penetration welding"

2.4 Selective Laser Melting

Abe was among the first to describe an experimental setup for SLM (Figure 2-17) [70]. A thin layer of powder is spread onto a base plate. A scanning laser is then used to melt particular areas of this powder which then fuse to the base plate. The base plate is then lowered and a further powder layer applied using a wiper. The scanning laser is used again to fuse selected areas of this second layer and join to the already solidified parts of the first layer. Oxidisation during the melting process is prevented by applying a low oxygen atmosphere either by implementing a vacuum or by using shielding gases to suppress the ambient oxygen. Setups similar to the one described by Abe can be found in the majority of commercial SLM systems, whereby most commonly used are galvanometer scanners for beam positioning instead of a scanning laser.

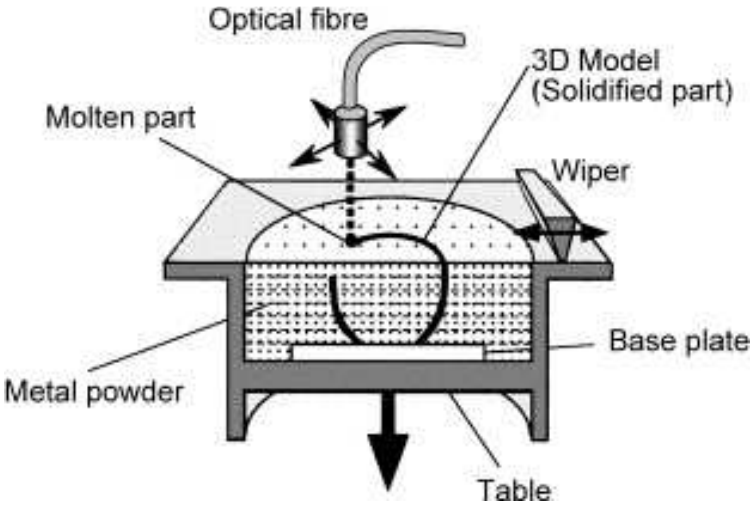

Figure 2-17 Experimental setup for Selective Laser Melting according to Abe. (from [70])

The physical mechanisms that are involved in such SLM processes are absorption and scattering of laser radiation by the powder material, heat transfer into surrounding powder and substrate material. Due to the heating, phase transformation occurs from solid to fluid and surface-tension gradients cause fluid flows within the melt pool. The

volume fraction of gases in the solidified powder layer decreases from a high value upon starting to nearly zero after process [71].

In SLM processes, the resulting characteristics of the fabricated components are dependent on various process parameters. Below, the most critical parameters will be discussed to ensure SLM manufactured solid metallic components have physical properties similar to components fabricated by other more conventional techniques such as casting.

2.4.1 Powder material

In SLM processes metallic powders of single composition are used. Therefore, pre-alloyed bulk material is atomised into particle thicknesses in the range of tens of micrometres. The two most commonly used ways are gas and water atomisation. Gas atomised powders particles typically possess a spherical shape (Figure 2-18 left) whereas water atomised powders possess a more irregular shape (Figure 2-18 right) [72].

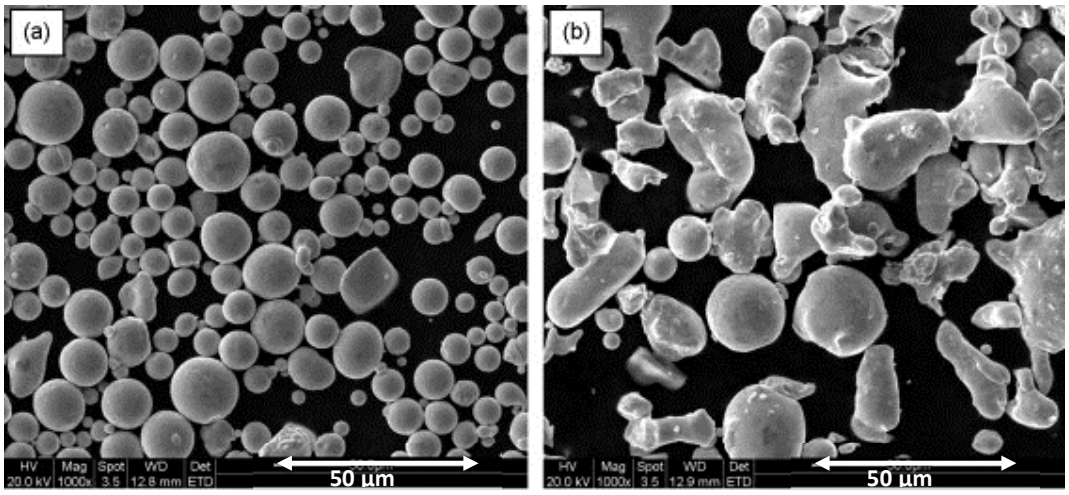

Figure 2-18 Microscopic analysis for gas (left) and water atomised SS 316 powder particle. (from [72])

Samples fabricated from gas atomised powder possess a denser structure compared to samples from water atomised powder. The spherical shape of gas atomised powders allows higher packing densities [72]. The smaller the powder particles size the smoother the resulting surface morphology. Ideally in 3D-SLM processes the ratio between particle size and layer thickness is less than one [73].

2.4.2 Atmosphere

Fabrication of iron based metal components with SLM, under the presence of oxygen, increases the melt volume formed during SLM process due to exothermic oxidation of iron. The presence of any oxygen within the sintering atmosphere and powder bed allows surface oxides and slags to form as the powder is heated and melted by the scanning laser beam. This leads to a deteriorated surface quality of single layers and also 3D components and is therefore undesirable [74]. Observing the growth and effects of these scales in differing atmospheric conditions has shown that elimination of all oxygen is required in order to reduce the melt volume allowing surface tension forces to become less dominant [75].

Therefore, SLM processes are either conducted under vacuum or inert-shielding gases such as argon or nitrogen. It was found that less porosity is obtained when sintering is carried out under an argon atmosphere. This could be attributed to the dissolution of nitrogen into the liquid iron during the course of laser sintering [76]. Murr investigated the influence of argon and nitrogen atmospheres during atomisation of the powder and the laser melting processes of stainless steel [77]. It was found that argon atmospheres during the SLM process more reliably conserve the used steels martensitic characteristics.

2.4.3 Single track formation - laser parameters

In SLM processes sufficient energy input by the laser source is required for melting both, powder and solid substrate, for intermixing them and ultimately form solid and strong components. Adding single tracks by SLM onto a substrate the most influential parameter for the resulting quality of in terms of shape, morphology and bonding of the added material is the energy input, which is typically defined by laser power over feeding speed.

In empirical studies of SLM processes, three different process regimes for the energy input in single-track formation can be differentiated. For specific material and experimental equipment therefore possible process windows for scanning speeds and laser powers can be determined, in which the SLM process delivers optimal results [71, 78] (Figure 2-19).

If the energy input is not sufficient to penetrate and melt the substrate, e.g. at high scanning speeds or low power levels, the molten powder material contracts due to surface tensions to spherical droplets and barely wets the substrate, a phenomenon often referred to as the balling effect [79] (Figure 2-19; bottom right). The height of the formed droplets can exceed the actual height of the deposited powder layers, potentially interfering with the powder delivery for subsequent layers. The balling effect can be overcome by adjusting the scanning speed and laser power depending on the thermal conductivity of the material. In general, high brightness laser with high intensities lead to a wider process windows for stable melting processes without occurrence of the balling effect [71].

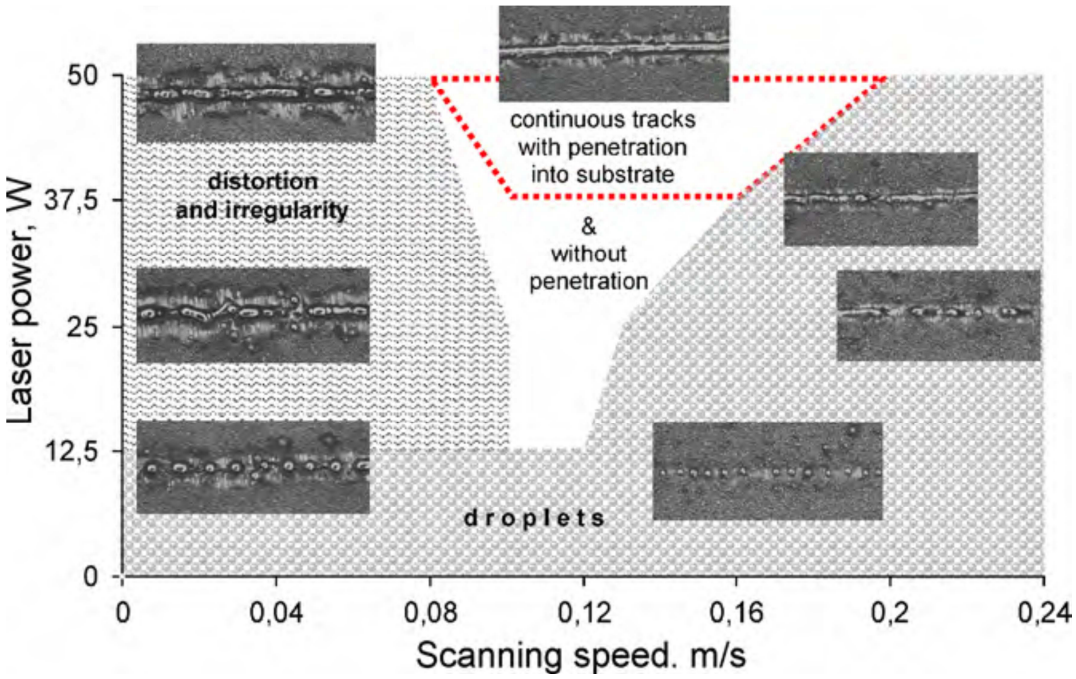

Figure 2-19 Single track process map for the first layer of SS grade 316L (−25µm) powder. Powder layer thickness is 50 µm. (from [71])

A study of SLM processes with SS 316 and a high brightness laser with similar characteristics to the laser in our research group was conducted by Li [72]. Figure 2-20 shows cross-section of single tracks conducted at different speeds. At a power of 60 W, the powder material is molten consistently over the length of the conducted track with no balling occurring. However, in this case the melt pool barely penetrates into the solid substrate. With increased laser power the melt pool extends further into the substrate. Ideally the penetration depth into the substrate is similar to the thickness of a

layer of powder material, guaranteeing good intermixing of the added powder material with the solid substrate [71].

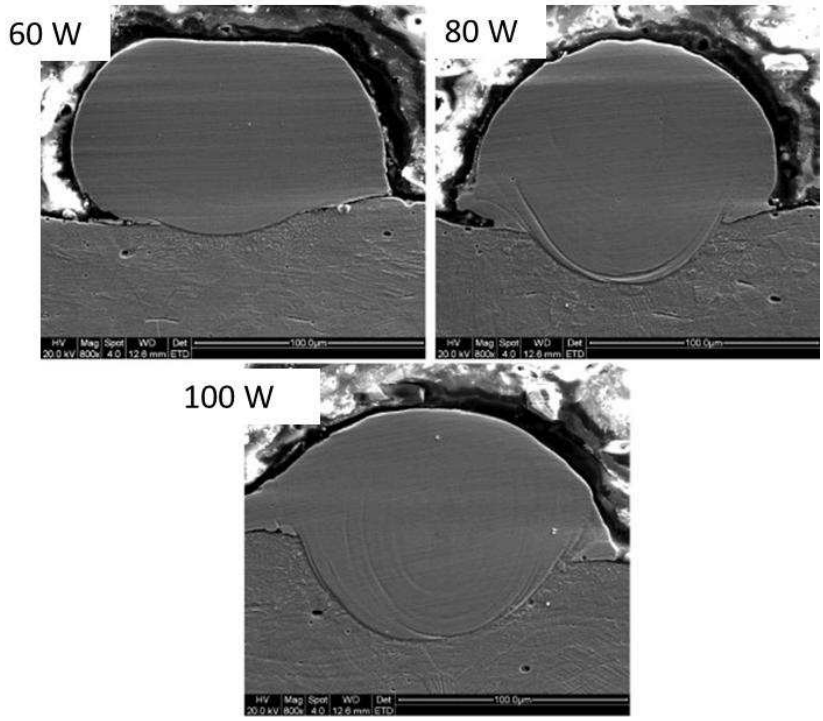

Figure 2-20 Cross-section analysis of SLM solidified SS 316 powder with different laser power. (speed 50 mm*s^{-1}; spot size: 80 µm) (from [72])

Generally larger laser powers lead to larger heat affected zones and if the laser power is too high other distortions and irregularities in the SLM process occur, such as spattering (Figure 2-19 left). Large amounts of energy deposited into the material leads to rapid expansion of heated material, propelling the material away from the process zone, and interrupting the single track formation. Thereby, at high powers surface roughness is negatively influenced by poor melt pool stability and sputtered particles [80]. Pulsing the laser source to allow the material to cool down is a feasible method for maintaining good surface quality in high intensity laser processes. However, using pulsed laser sources and low pulse-to-pulse overlap, built components suffer from porosity [81].

2.4.4 Scanning strategy – fabricating 3D components

Features that exceed the dimensions of single tracks are SLM fabricated by applying single lines in parallel to each other, applying patterns layer by layer which outer dimensions approximate the dimension of the to be fabricated component. In literature,

the distance between parallel lines, is typically referred to as line-to-line-spacing, -distance or simply hatching. The hatching parameter is highly influential for the resulting surface morphology and density of the SLM fabricated component [78].

The interaction of the laser light with the powder is different to the interaction that occurs with solid materials [82]. In solid metal materials the laser light is absorbed according to the Beer-Lambert law within several hundred nanometres of the surface. For highly reflective materials such as copper up to 90 % of the emitted laser light is back reflected and the absorbed energy is transferred by the heat conductivity into deeper depths. While processing powders the laser light penetrates the material much more deeply, up to several hundred micrometres, due to the voids and gaps between the powder particles as numerical estimates for single rays of light by Wang [82] show. A ray of light is scattered at a powder particle and the reflected part of the laser ray may subsequently hit another powder particle and so on. This cycle continues until either the initial laser ray is totally absorbed or the ray is reflected out towards the environment. Therefore the total absorption of laser energy when processing powder materials is significantly increased compared to solid materials, for example for copper and steel powders is as much as 80 % [82]. Because of the better energy absorption of steel powder at shorter wavelengths, the formerly widespread CO_2 –lasers have been replaced by solid state lasers ($\lambda \approx 1$ µm) or diode lasers ($\lambda \approx 0.8$ µm) to increase process efficiency [8]

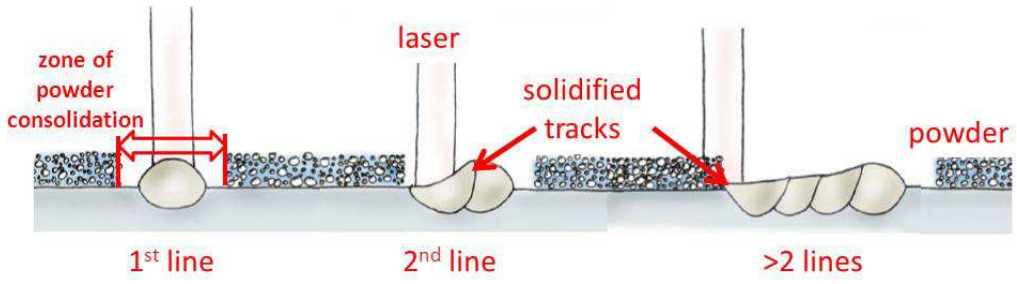

Figure 2-21 Schematic illustration for formation of zone for powder consolidation. (from [78]).

The first line solidified from freshly deposited powder material typically leads to larger dimensions than subsequent lines in close vicinity due to increased absorption of the laser energy by the powder materials compared to solid materials. More energy is available for the melting process, resulting in accumulation and densification of powder

material from a wider material. This leads to a zone of powder consolidation where for subsequent lines less powder material is available. Solidified metal materials have much lower absorption for light. From this it follows, if subsequent lines are placed in close vicinity to one of the initial lines, partially hitting either the previously solidified material or the zone of powder consolidation, less powder material and less energy for the melting process are available, ultimately leading to smaller dimensions of the lines [78].

The effect is mitigated by adjusting the scanning strategy so that for the first line with higher absorption less energy input is applied. Also, studies on the zone of powder consolidation show that with increased feeding speeds at constant energy input, the ratio between zone of powder consolidation and line width becomes smaller [78].

In cases where the line spacing exceeds the line width of single tracks, macro-porosity occurs. Studies on porosity behaviour of stainless steel SLM processes, for different scanning strategies indicate strong correlation between porosity and scanning strategy [83]. Figure 2-22 depicts microscopic analyses of SS 316 samples fabricated by SLM with different hatching parameters in a study conducted by Li [72].

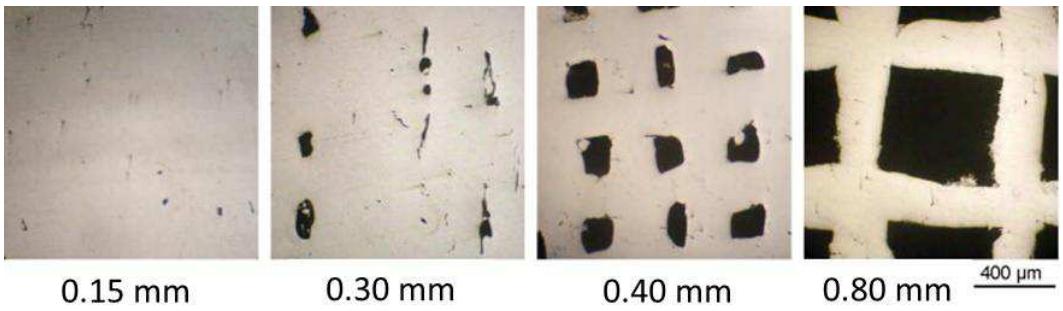

Figure 2-22 Microscopic images of SLM fabricated components with all similar parameters but varying hatching parameter. Provided that the hatching is less the single track width no porosity occurs, exceeding the single track width porosity scales with the hatching parameter (from [72]).

Provided that the hatching parameter does not exceed the width of the single tracks (compare to Figure 2-21) parts free of macro-porosity are fabricated. For hatching larger than the single track width, the porosity scales linearly with this hatching. The scanning strategy also has a strong influence on the surface morphology. Studies show

that the hatching distance should not exceed the average width of the individual lines in order to manufacture smooth surfaces [78].

The scan direction angle is the angle between laser scanning directions on consecutive layers. Changing the angle for subsequent layers mitigates the occurrence of anisotropy in SLM build components [10]. Currently, research is underway to understand the occurrence of anisotropy but preliminary results indicate that some variation of the angle in subsequent layers can significantly reduce the occurrence of anisotropy in SLM built components [84].

2.4.5 Residual stresses in SLM fabricated components

When fabricating with SLM large temperature gradients occur within the component. Locally confined to areas of similar dimension than laser spot, the material is heated up exceeding melting temperature, leading to temperature gradients which easily exceed 10^7 $K*m^{-1}$ [9, 85]. Rapid shrinking of the material induces residual stress into the component leading to deformation and in the worst possible cases cracking.

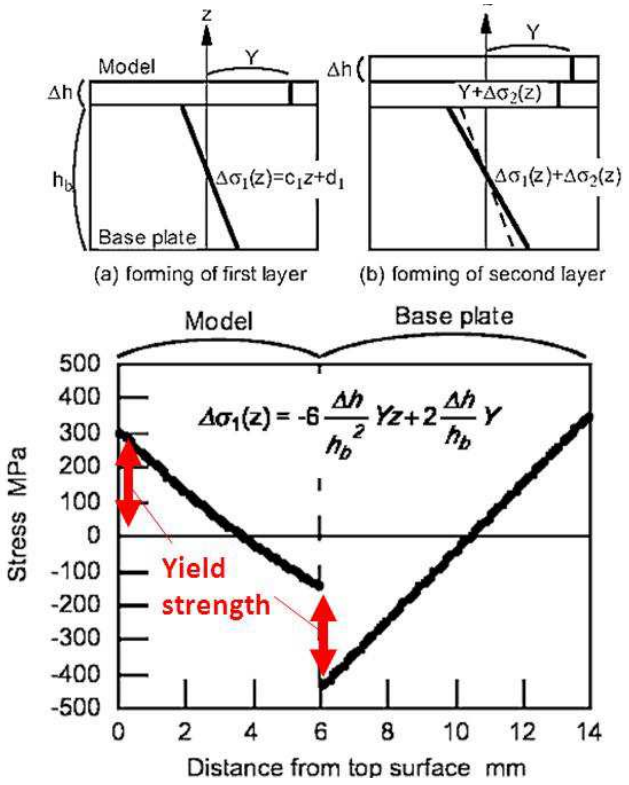

Figure 2-23 Model for residual stresses developing during SLM processes (top). Plot for modelled stresses for substrate (base plate) and SLM added material. (from [86])

Modelling residual stresses for substrates with SLM added materials illustrated in Figure 2-23. The model developed by Shiomi [86] assumes that each added layer contributes an incremental increase of stress into both substrate and SLM added material of the fabricated component. For stainless steel materials and typical values for layer thickness (0.1 mm) the model indicates significant tensile stresses in the components surface and compressive residual stresses within the component. Stress levels can easily exceed the Yield Strength of the material and cause plastic deformation (Figure 2-23).

Avoiding long track lengths mitigates residual stresses. Therefore, it is desirable to divide the SLM processed area into small segments, insular scanning [9]. Relaxation of residual stresses in casted or SLM fabricated components is achieved by subsequently annealing or hot isostatic pressing [87]. Residual stresses near the surface are relaxed by shot peening [88]. Residual stresses can be measured e.g. by X-ray techniques [89], neutron diffraction or hole drilling [90]. These measuring techniques are complicated and costly. Li [44] demonstrated the feasibility of measuring residual stresses of an AM fabricated (Fused Deposition Modelling, see section 2.5) part using embedded fibre optic sensors, however measurements where conducted only after applying the first layer on top of the fibre and not in real-time.

2.5 Embedded fibre sensors

Embedding of optical fibre sensors into composite materials has been widely reported and has seen extensive use across a wide range of applications for measuring strain and temperature from within components [91]. Fibre optics have also been embedded into plastics [92] and attached to metals by utilising epoxy adhesion [93]. However, all of these approaches limit the usable temperature range to below 350 °C due to the limited temperature stability of the involved polymer-based materials.

Three different concepts have been previously reported for incorporating optical sensors into metal components. In [94] the encapsulation of bare silica fibres into aluminium is described by using ultrasonic consolidation. However, ultrasonic consolidation of aluminium will limit the temperatures of possible application to below the melting temperature of aluminium (T_m ~ 680 ^{0}C). Furthermore, the bonding between subsequently consolidated layers is only due to atomic-level forces. A study conducted by Yang states that no localised melting and intermixing in ultrasonic consolidation

processes occurs, inherently limiting the physical properties (e.g. strength) of the fabricated components [95].

The other approaches work by metal jacketing the optical fibre prior embedding. These metal jackets are typically applied by low temperature processes such as electro-less plating [59] or a mixture of electroplating and magnetron sputtering [44]. Sandlin describes the embedment of such coated fibres into U-groove shaped steel materials by using brazing [58]. The brazing filler material is attaching the fibre to the steel component, however the brazing materials low melting temperature (~ 400 ^{0}C) will inherently limit the applicable temperature range.

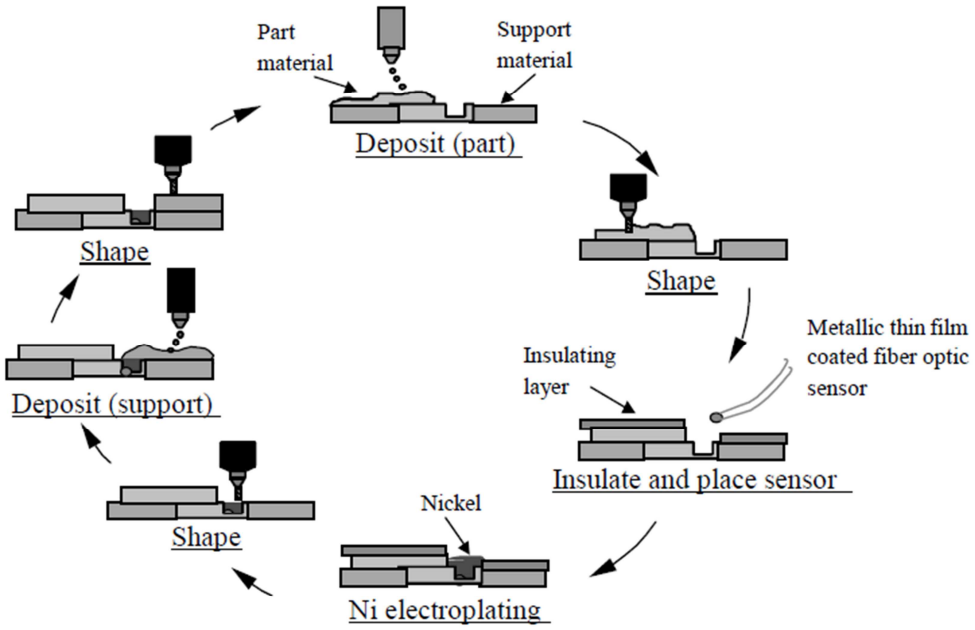

Figure 2-24 Approach for embedding optical fibres into metals by using Fused Deposition Modelling and electroplating of nickel. Nickel layers of significant thicknesses are necessary to protect the optical fibre from the energies of the laser cladding process. (from [44])

The only approach suitable for high temperature application is the embedding approach described by Li [44] (Figure 2-24). The method works by building U-shaped grooves of SS 316 material by laser cladding in combination with milling (net shape). Powder material is sprayed onto a substrate and solidified using a laser. Subsequently the added

material is machined down to its design shape using milling. After building the groove, the process is interrupted, the specimen is removed from the AM machine and a chromium rf-sputtered optical fibre sensor is placed into the groove. The fibre in the groove is electroplated with nickel with thicknesses of at least 1.5 mm, filling the groove. Subsequently the specimen is returned and placed into the AM machine and the build process is continued.

Li's work, dated 2001, is the state of the art for embedding optical sensors into metal components suitable for high temperature applications and therefore acts as a benchmark for this thesis. Li's thesis demonstrates the feasibility of embedding optical fibres sensors into SS 316 and shows that such embedded sensors are suitable for measuring strain and temperature from within the component. However, Li's approach suffers from several disadvantages:

- The increased volume of electroplated nickel to protect the fibre within the steel component is a significant distortion of the components physical properties. The reported cross-sectional areas of nickel within the steel component are typically about 3 mm x 1.5 mm, highly undesirable under aspects of minimisation (Figure 2-25).

- The poor beam quality of the laser used for the cladding process (2.4 kW cw laser, reported spot diameter: 2 mm). The large spot size leads to large melt pools an order of magnitude larger than the dimensions of the optical fibre sensor. Therefore, large nickel coatings to protect the fibre sensor during the cladding process are necessary. Li reports that when coating thicknesses of less than 1.5 mm are used significant attenuation of the transmitted light through the fibre occurs.

- Temperature measurements reported in the work are not exceeding 350 ^{0}C. A specific explanation why no tests with higher temperatures are conducted is not given (Figure 2-26).

- Strain testing was conducted in the elastic and plastic regime showing linear response to deformation in single strain cycles. Only single tests are reported

and no information about the long-term behaviour of the embedded fibre sensor is given (Figure 2-26).

Generally, the approach suffers from impracticalities and many aspects of the behaviour of such embedded sensors are not investigated. The AM process must be interrupted and the specimen removed from the AM machine in order to attach the fibre via electroplating. The metal powder melting is conducted with a laser of poor beam quality, resulting in large spot sizes and therefore large melt pool volumes, hence large nickel coatings are necessary to protect the fibre. In addition, prior to electroplating the surfaces of the steel component must be treated to improve adhesion of the electroplated nickel. Then, the component is returned into the AM machine to continue the build process and the fibre is encapsulated.

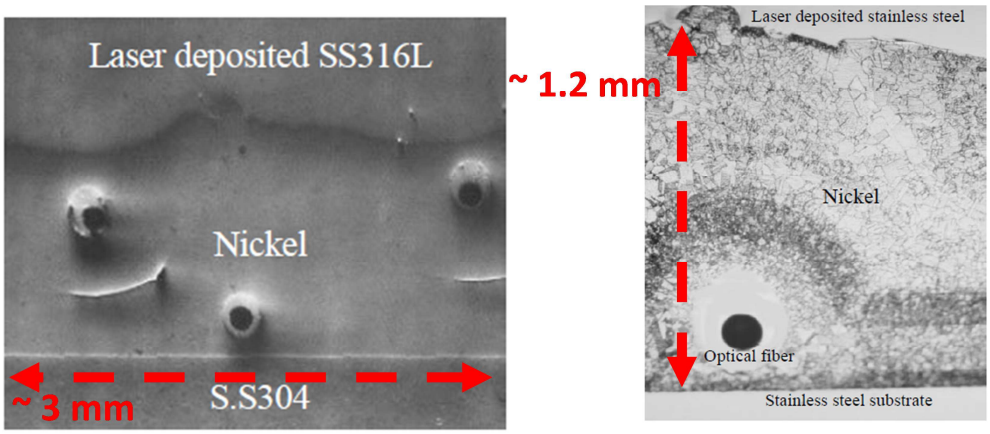

Figure 2-25 Cross-section analysis of fibres embedded into steel using nickel electroplating and laser cladding. Due to the large energy input of the cladding process (2.4 kW) significant nickel coating are necessary to protect the fibre during the embedding process. (from [44])

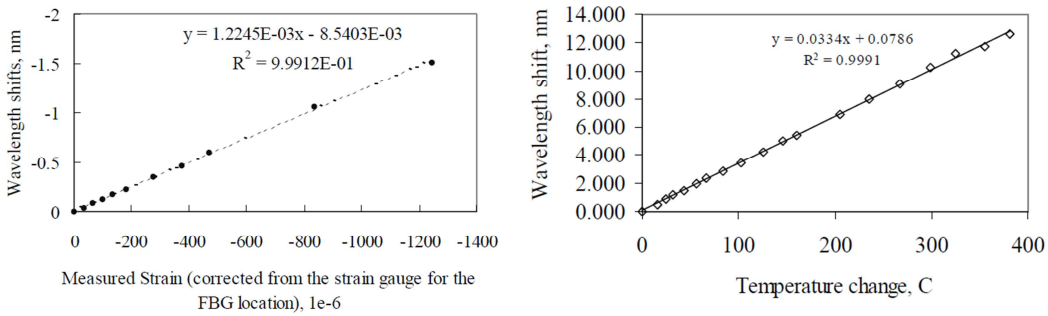

Figure 2-26 Change in Bragg wavelength as a function of applied strain (left) and temperature (right) for embedded FBG sensors into SS. For both loads the embedded FBG shows linear response. (from [44])

2.6 Thesis objective

Following from the review above, the objectives of the work presented in this thesis are outlined below. These are either incremental improvements (☐) to previous work, in particular that conducted by Li [44] or can be considered a novelty (■) in the sense that such research was not yet reported elsewhere:

- ☐ Reduce the physical size of the embedded sensing elements and therefore mitigate their influence on the physical properties of fabricated components. This is made possible by the high brightness laser systems, which are now used for the SLM processes. The high beam quality allows the volume of the melt pool to be precisely controlled reducing the likelihood of damage to the optical fibres being embedded and melt pool dimensions are an order of magnitude smaller than the optical fibre.

- ☐ Minimise interruption to the AM process. Ideally, the AM fabricated component remains in the AM machine for the whole fabrication process, rather than being taken out for sensor embedding, as described in Li's thesis. A minimal interruption is vital for a commercially viable process.

- ■ Identification of the minimum coating thickness for fusing the fibre metal jacket to the steel component using the high brightness laser.

- ■ Conduct temperature measurements in environments where temperatures exceed 1000 °C. Measurements of temperatures in this regime with metal embedded fibre optic sensors have not been demonstrated before.

- ■ Determine whether elastic straining and plastic deformation of the component is reliably tracked and measured by the SLM-embedded fibre optic sensor.

- ■ Demonstrate continuous interrogation of the fibre optic sensor during the SLM process. Commercially available interrogation systems for fibre optic sensors allow such sensors to be monitored at very high sampling rates (10 kHz), providing useful data about the temperature distribution in the component during the SLM process and also monitoring the development of residual stresses.

The experiments described in this thesis were mostly conducted using bespoke self-designed laboratory equipment, e.g. mounts for fibre coating or home-built setup for SLM processes. However, all these systems were designed to allow future transfer to commercially available equipment.

Given the limitations of the home-built SLM setup this research was carried out using SS 316 material, to demonstrate feasibility, even though, it is not an ideal material for long-term high temperature applications. However, SS 316 has the advantage of easy availability, low cost, significantly simplified handling and lower health and safety risks compared to more suitable high temperature materials, especially nickel-based alloys. Furthermore, in the scientific literature SLM fabrication of SS 316 components is extensively reported.

Chapter 3

Coating optical fibres

To embed optical fibres into metals by SLM, a protective layer around the fibre is required to protect the fibre and also to form a proper mechanical interface between silica fibre and metal component. Melt pool temperatures in steel sintering processes are typically several hundred degrees above the steel melting point (~1500 °C; [96]) to ensure that the localized melt zone extends beyond the focal volume of the laser beam to facilitate partial re-melting of the neighbouring materials and hence help to achieve a crack free solid component [97]. The softening point (where silica creeps under its own weight) of fused silica however is only about 1200 °C; [98]) Therefore, coating is essential to shield the fibre from the high temperatures of the embedding process not only to preserve the fibre's structural integrity but also to preserve FBGs that suffer from decay at elevated temperatures (Figure 3-1).

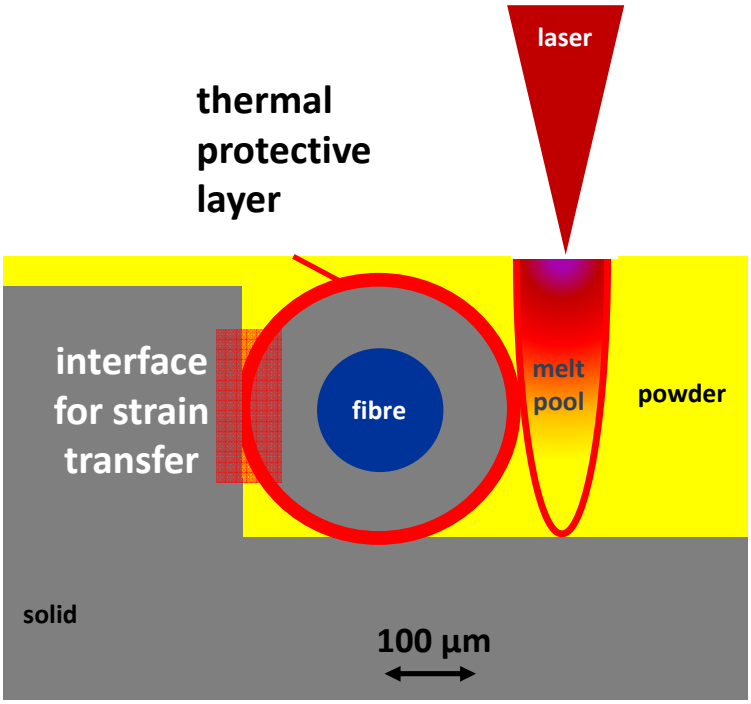

Figure 3-1 Schematic visualisation of the embedding process, highlighting the necessity of a fibre coating. A fibre coating is required that facilitates thermal protection during the SLM process and also bonds to SS 316.

For coating optical fibres a combination of RF sputtering and electroplating is proposed according to the recipe developed by Li [44]which describes sputtering of electrical conductive keying layers. This keying layer acts as both an adhesion layer and a conducting path for subsequent electroplating. Equipment is available to RF sputter substrates with various metals (Figure 3-2). Rf sputtering is a non-thermal vaporization process. Surface atoms are physically ejected from a solid surface ("target") by momentum transfer, typically by gaseous-ions accelerated from a plasma [99]. Sputtering is well established for thin film metallisation of semiconductor or glass materials.

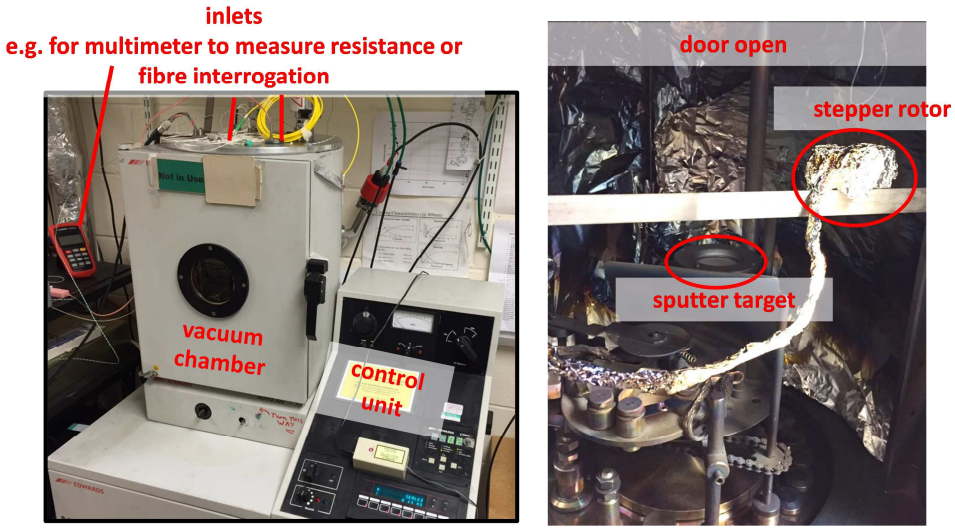

Figure 3-2 Image of the RF sputtering equipment. Setup consists of a vacuum chamber and its necessary control unit. Inlets at the top allow electrical wires and optical fibres to be fed into the vacuum chamber (e.g. for in-situ interrogation of an FBG during sputtering, electricity for stepper rotor). Inside the vacuum chamber are a stepper rotor and the sputter target.

The metals of interest are restricted to the high temperature sensing applications. Copper (melting point~1080 °C) and silver (~960 °C) often used for fibre coatings were hence not investigated and so the research reported here concentrates on coating fibres with chromium (~1910 °C), nickel (~1450 °C) and titanium (~1670 °C) which are also constituents of common stainless steel alloys and promise good intermixing with steel in the following embedding process (melting temperatures from [100]). For the electroplating process only a nickel plating facility was available.

3.1 Sputtering of keying layers

The RF sputtering characteristics of nickel, titanium and chromium were investigated. Preliminary tests indicated that sputtering relatively larger thicknesses (~ 1µm) of nickel using the available equipment is not feasible, due the nickel's magnetic behaviour. In combination with the limited power of the sputtering system (250 W), the nickel's magnetism leads to extremely low sputter yields since the dissolved nickel nuclei are drawn back to the magnetic sputter target. To facilitate deposition of thicker layers of nickel in reasonable times (> 1 µm thickness; < 1hr) extensive upgrades (power supply, adding counter magnets etc.) to the sputtering system would be necessary to mitigate the sputter target's magnetic characteristics [101].

For process evaluation rectangular glass plates are positioned 10 cm above the sputtering target. The glass substrates are partially covered by tape and after sputtering the tape is removed. To measure the difference in height between the sputtered and un-sputtered section of the specimen white light interferometry (Zygo) is used. Sputtering is conducted in high vacuum (10^{-8} bar) conditions. The sputter frequency is set to 13.56 MHz and argon is used as the plasma gas to facilitate highest sputter yields [99]. The measured thickness for RF sputtered chromium and titanium for different sputtering power and durations are plotted in (Figure 3-3) and (Figure 3-4) respectively. For both materials, the coating thickness increases linearly with sputter duration. Chromium achieves much higher sputter yields. Layer thicknesses of 1 µm are achieved after 15 min at 200 W or after 30 min at 133 W. Sputtering titanium of a similar thickness takes almost twice as long.

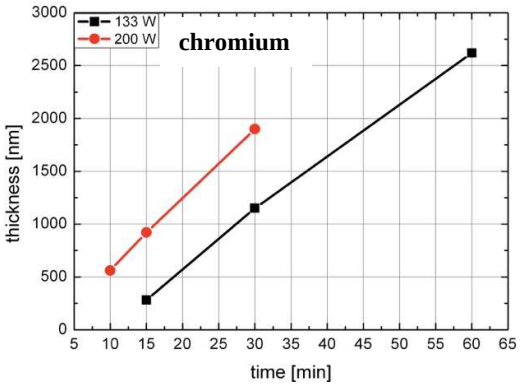

Figure 3-3 Deposition rates for chromium on microscopes slides as a function of time and sputtering power.

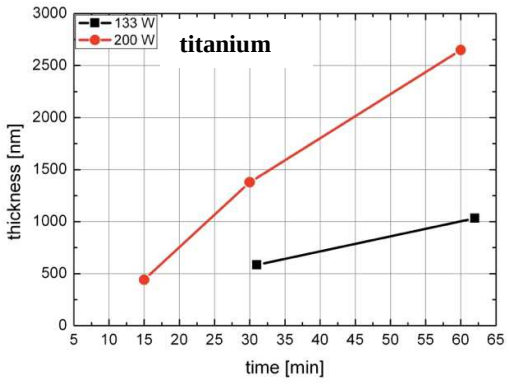

Figure 3-4 Deposition rates for titanium on microscope slides as a function of time and sputtering power.

Sputter yields for chromium are higher due to its lower sputter threshold [99]. For every material a specific sputter threshold exists which is dependent on many variables such as mass or molecular structure of the sputtering target. If the energy of the bombarding ions is below the threshold no sputtering occurs. Above the sputter threshold an increase in energy linearly increases the sputter yields.

The sputter coated fibres are subsequently electroplated. The available power-supply for the plating-process allowed the currents to be controlled to a precision of 1 mA for voltages up to 30 V. Therefore the resistance of the sputter-coated fibre has to be in the range of several hundred Ohms, to allow plating process to be controlled in a precise manner. The sheet resistance R of any electric conductive material is determined by the following equation [102]:

$$R = \rho \cdot \frac{L}{A} \qquad \text{EQN 12}$$

Increased lengths L or high specific resistance ρ increase the overall resistance R, whereby larger cross-sectional areas A lead to smaller resistance. Optical fibres are insulators. The cross-sectional area of the fibre coating is calculated by subtracting the area from the fibre OD_{fibre} from the outer diameter of the applied coating $OD_{coating}$:

$$A = \frac{(OD_{coating}^2 - OD_{fibre}^2)}{4} \cdot \pi \qquad \text{EQN 13}$$

The specific electrical resistance of Chromium is 125 nΩ*m whilst for titanium the specific resistance is 420 nΩ*m [103]. The calculated resistance of chromium and titanium as a function of coating thickness is plotted in Figure 3-5. The results indicate that for chromium a coating thickness of at least 200 nm and for titanium a thickness of 1 μm are desirable to achieve a resistance below 500 Ω.

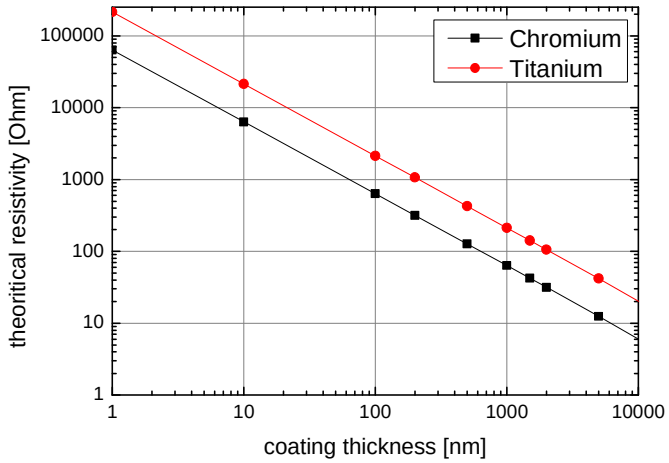

Figure 3-5 Plot for estimated resistance for chromium and titanium coatings over coating thickness applied onto an OD 125 µm optical fibre.

Both materials chromium and titanium bond equally well to oxide surfaces such as silica-dioxide [99]. Chromium achieves much higher sputter yields while having a lower specific resistance, making it the ideal choice for the RF sputtering process to provide an adhesive metallic jacket to the optical fibre and provide an electrical conductive path for subsequent electroplating.

The coatings are required to be uniform around the fibre's circumference. The available sputtering system could only provide one-directional sputtering, therefore it is necessary to rotate the fibres during the process. In order to provide a rotatable support, a glass tube of 5 mm diameter was fabricated as shown in Figure 3-6. A fibre is spanned freely across a length of about 8 cm, which is hence the maximum coating length. The glass-tubes' shape ensures that fibres are not shielded from the sputter target by rotating the glass tube, which is achieved by mounting the glass rod on a stepper-motor. The ends of the fibre were coiled up and taped to the ends of the glass tube, preventing accidental trapping whilst rotating.

Before taping onto the sputtering mount, the fibres are either mechanically or chemically stripped from the polymer jacketing. Stripping is applied over a length of about 6-7 cm, in order that a small section of the un-stripped fibre is also coated leading to a smooth transition from polymer coating to metal jacketing. The glass tube with fibre is attached to a stepper motor about 10 cm above the chromium target (Figure 3-7). The rotor is set to slow speeds of about 5 $r*min^{-1}$. Typically, the rotor is

set not to conduct whole revolutions. In case the glass rod is in-between sputter target and the fibre shielding occurs. Therefore, the rotor is set to only conduct half revolutions ensuring that the glass rod is not in-between fibre and sputter target. The fibre holder and the sections of the fibre that we do not wish to be coated are covered with tin foil to prevent deposition of material at these locations. This is important for the subsequent electroplating process, to minimise the area which is electrically conductive. Then, after sealing the sputtering unit and applying a high vacuum of less than $1x10^{-8}$ bar the sputtering process is started by inducing small amounts of argon (pressure at inlet $3x10^{-9}$ bar). Sputter power is set to 200 W and sputtering is conducted for approximately 60 min.

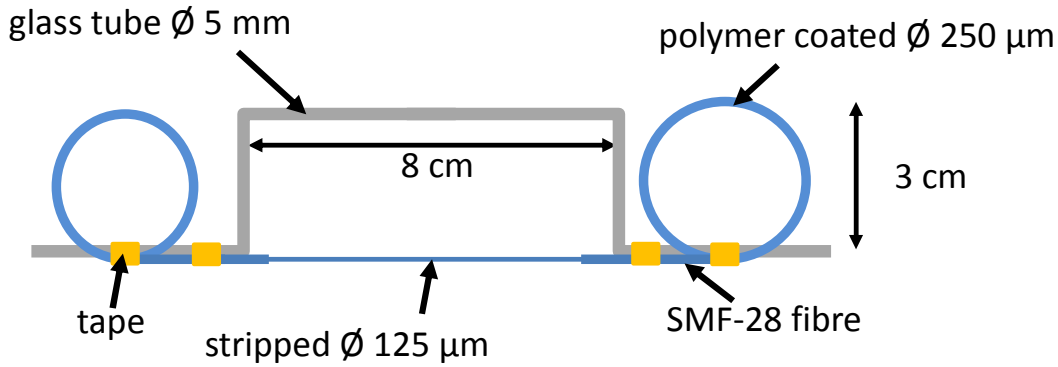

Figure 3-6 Mount to clamp stripped optical fibre in sputter unit. The fibre is stripped and taped to rectangular shaped glass tubes. The ends of fibre are coiled up to prevent interference with rotation when sputtered.

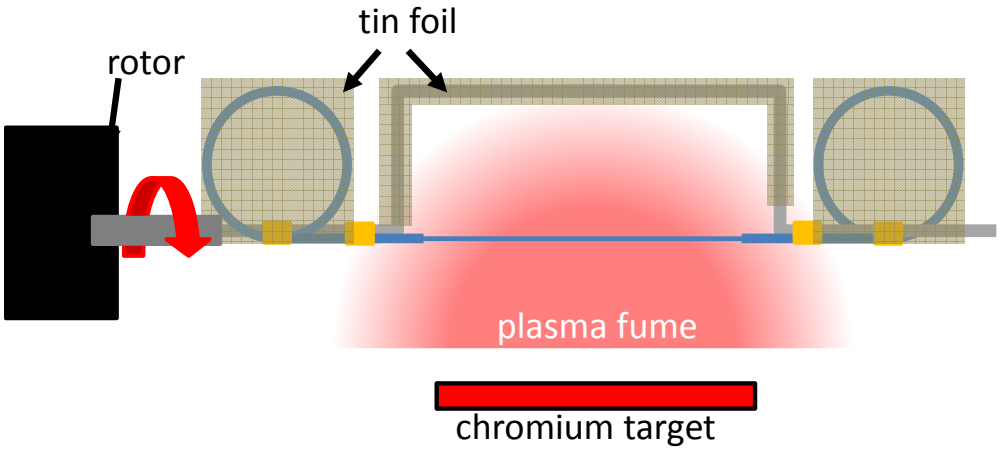

Figure 3-7 Fibre on mount attached to rotor in sputtering unit. Rotating the fibre over the chromium target allows uniform coatings to be applied by RF sputtering. Only half revolutions are conducted to prevent shielding of the fibre by the glass rod.

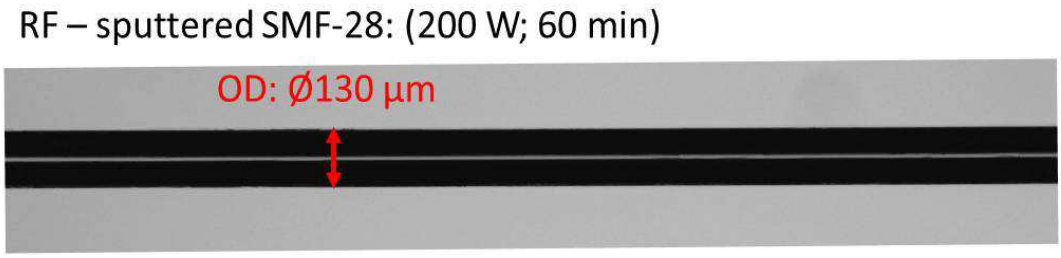

Figure 3-8 Chromium coated SMF – 28 fibre after 60 min of RF sputtering at 200 W sputter power.

After the process, the sample is taken out of the sputtering chamber and examined using microscopy. Sputtered fibres are uniformly coated with chromium (Figure 3-8) to outer diameters of typically around 130 µm, indicating that about 2.5 µm of chromium has been applied uniformly around the fibres circumference.

No obvious imperfections in the sputtered coating could be seen. The resistance of the applied coatings is well below 1kΩ, as predicted, low enough to facilitate the following electroplating process.

3.2 Electroplating

After RF-sputtering, the tin foil is removed from the sample holder. Electrical wiring is applied to the coated fibre just at the interface where the freely spanned fibre is attached to the sample holder (Figure 3-9). During the RF-sputtering process this area is not shielded by tin foil, making both, glass rod and fibre electrical conductive. It is difficult to determine the exact area that was coated after RF-sputtering, important to predict the optimum parameters of the subsequent electroplating process. However, over many experiments this approach was developed as best practice, since the partly coated sample holder provides additional surface area to apply the electrical wiring.

Using electrical conductive tape bridges an electrical conductive path from wire to fibre improving the electrical contact mechanism. Subsequent application of PTFE tape around the glass tube seals off unshielded ends of the electrical supply wires, preventing that the wires are permanently joint to the optical fibre by electroplated nickel.

For process evaluation rectangular glass plates are positioned 10 cm above the sputtering target. The glass substrates are partially covered by tape and after sputtering

the tape is removed. To measure the difference in height between the sputtered and un-sputtered section of the specimen white light interferometry (Zygo) is used. Sputtering is conducted in high vacuum (10^{-8} bar) conditions. The sputter frequency is set to 13.56 MHz and argon is used as the plasma gas to facilitate highest sputter yields [99]. The measured thickness for RF sputtered chromium and titanium for different sputtering power and durations are plotted in (Figure 3-3) and (Figure 3-4) respectively. For both materials, the coating thickness increases linearly with sputter duration. Chromium achieves much higher sputter yields. Layer thicknesses of 1 µm are achieved after 15 min at 200 W or after 30 min at 133 W. Sputtering titanium of a similar thickness takes almost twice as long.

The sample holder is then deployed for electroplating. A nickel-sulphamate bath is used that is kept at a constant temperature of 55 °C and a pH-level of about 4. Both electrical wires are connected to the power supply anode and the cathode is connected to the nickel source that is also deployed in the bath. The power control is set to a maximum current of 60 mA. At this current, a current density of about 15 A*dm^{-2} is achieved (length fibre: 8 cm, OD 130 µm) which is just at the higher end of the plating's bath specification (*from manual Lectro-Nic 10-03s:* 4 - 15 A*dm^{-2}), to deposit porosity free and smooth coatings. Coatings applied with such current densities also are also typically applied with little residual stresses [104, 105]. While in the bath, the deposition rate over time is decreasing (Figure 3-10).

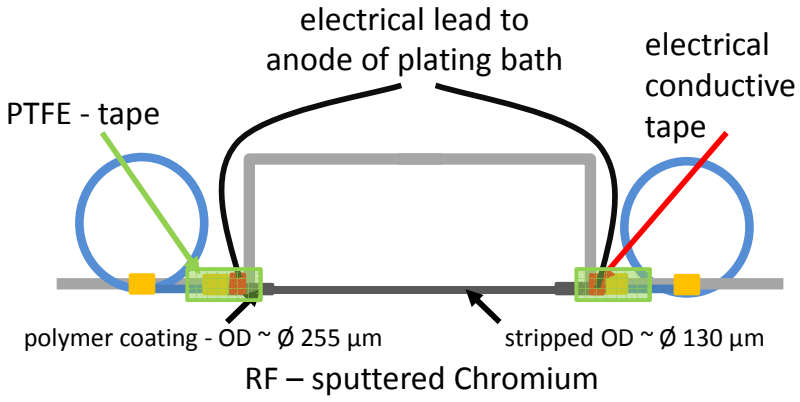

Figure 3-9 Schematic illustration for the sample holder of the electroplating setup. After RF-sputtering the electro plated fibre remains and the holder and electrical wiring is applied. PTFE tape and electrical conductive copper tape facilitates both, proper bonding between electrical wire and coated fibre and protection of their interface to prevent the wire and fibre from being permanently joint by the deposited nickel.

With increasing outer diameter, the current density on the coatings surface reduces, leading to lower deposition rates. As long as the coating thickness is not exceeding 400 µm, no further adjustments to the current settings are necessary since at this outer diameter the current density is still within specifications (ca. 5 A*dm^{-2}). The large spread of experimental results can be explained by uncertain contact mechanisms at the beginning of the process. In some cases, nickel is first electroplated onto one of the fibre ends and then bridges a connection to the other side, until the fibre is homogenously coated over its whole length. However, in subsequent measurements, no significant differences in coating thickness over the fibre length are observed. Once the material starts being deposited along the fibre's whole length, deposition rates are repeatedly following the curve plotted in Figure 3-10.

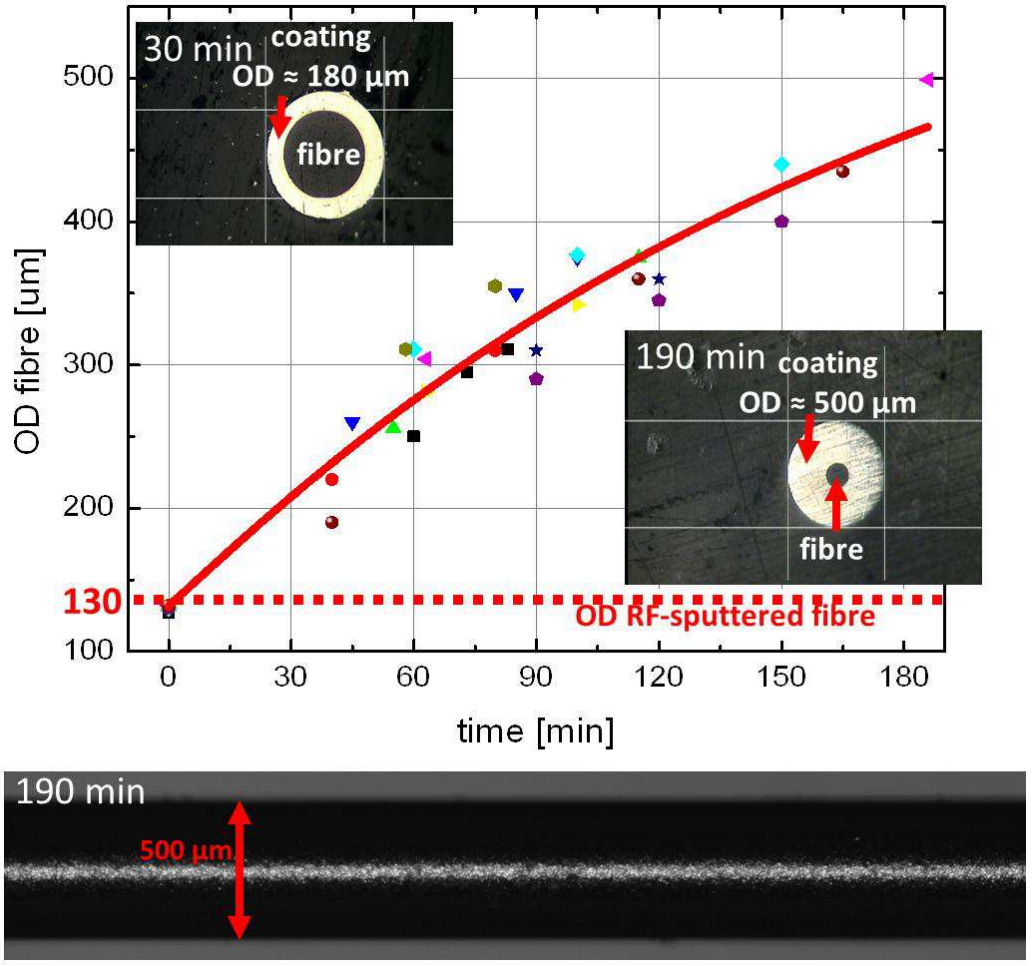

Figure 3-10 Increase in coating thickness in time for electroplating chromium coated fibres. Coating thickness increases as a function of time, decreasing current density at larger coating thicknesses leads to reduced deposition rates.

In order to obtain a fibre coating of particular thickness, it is necessary to periodically remove the fibre from the bath, in order to measure the outer diameter using microscopy. Then the specimen is returned into the plating bath and the remaining time necessary to achieve a certain coating thickness (± 5 µm) can be calculated. Cross-sectional analyses of the coatings show circular shaped coatings, with no porosity. No obvious imperfections are visible from the outside.

3.3 Chapter review

The techniques and procedures necessary to apply nickel coatings are reproduced and demonstrated. Thin chromium layers of thickness of about 2-3 µm applied by RF sputtering are found to be sufficient to act as an appropriate keying layer for the subsequent electroplating process. Using electroplating, homogenous nickel coatings up to large thicknesses (OD ≈ 1.5 mm demonstrated) can be applied. These nickel coatings have a circular cross-section and are porosity free with no other obvious imperfections. Provided that the coating process is properly monitored, coating thickness can precisely be estimated with a precision of about ± 3 µm.

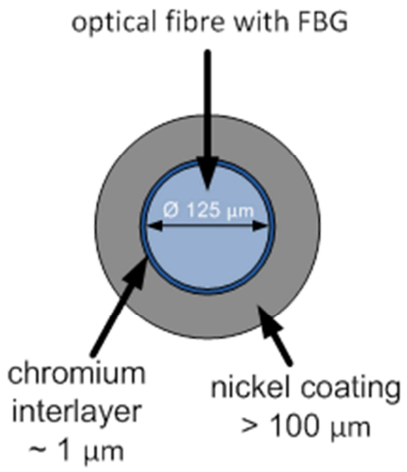

Figure 3-11 Concept for applying metal jacket to optical fibre sensors suitable for SLM embedment in SS 316.

The ability to coat optical fibres with nickel coatings is a fundamental step towards embedding these fibres in SS 316 by SLM. The precision with which the coating thickness can be selected (few µm) in combination with the precision of the SLM process (few ten µm) opens up potential for embedding such coated fibres in a minimised and precise manner. The melting temperature of nickel is similar to that of SS 316, potentially protecting the fibre during the SLM process if sufficient coating

material is present. Furthermore, nickel is a constituent of SS 316 capable of readily going in solution with iron-based steel alloys [106].

It is only the adhesion between fibre and metal coating that is considered to be a possible weak point. The thermal expansion coefficient of metal materials is typically an order of magnitude higher than the one of glass materials. This will induce thermal axial stresses via the bonding mechanism into the fibre. This is of concern, since the temperatures of desirable applications are in excess of 1000 °C, which leading to axial stresses in the fibre of up to 1.1 GPa ($\Delta CTE_{glass\text{-}nickel} = 15 * 10^{-6}$; Young Modulus glass = 72 GPa).

The adhesion between fibre and chromium is dependent on the sputtered chromium nuclei occupying troughs on the fibre's surface and hence the bonding's strength is highly dependent on the fibre surface characteristics [15]. Furthermore, at the interface between glass and chromium, the chromium forms bi-polar bonds with the oxygen present in the glass matrix, leading adhesion by chemisorption (atomic forces) promising strong bonds provided that the fibre's surface is clean [99]. The adhesive stresses σ_{shear} reported for such coatings are about 20 MPa and scratch tests indicate that shear forces of about 10 N can be tolerated, whereas a normal force of 0.15 N was applied [107].

To evaluate the adhesive strength of the glass to metal bond, a model for a cylindrical pressure joint from mechanical engineering applications is used. The required bonding strength p for obtaining a joint between an axially stressed and embedded cylinder and its surrounding can be estimated using [108]:

$$p \geq \frac{\sigma_{axial} \cdot d_{fibre}}{l \cdot \mu_{glass-chromium}} \qquad \text{EQN 14}$$

Apart from the axial stress σ_{axial} of the embedded cylinder, the equation takes into account the cylinder diameter d and length l and the friction coefficient of the two counter surfaces (sputtered chromium on glass in this case). No values for the friction coefficient of chromium sputtered on glass could be obtained from literature but using

the above values from the scratch test (F = 10 N, F_N = 0.15) a friction coefficient μ of 65 is estimated.

Applying this equation on the dimensions of an optical fibre, the coating length (~ cm) is at least two orders of magnitude longer than the diameter of the fibre (125 μm). Despite the relatively low adhesive strength of the chromium coating on the glass, using the derived friction coefficient from above, for a coating length of 5 cm the necessary adhesive strength for an axial stress of 1 GPa (as it would occur at 1000 °C) is less than 500 kPa, well below the 20 MPa of the adhesive strength. This indicates that the adhesive strength of the coating is sufficient for possibly occurring axial stresses for strain measurement applications at ambient temperatures, since the fibre strength is not more than 2 GPa and the strength of most metal materials does not exceed 1 GPa. Also, the adhesive strength is sufficient for the occurring axial stresses at elevated temperatures caused by differences in thermal expansion between metal and glass. However, the friction coefficient might be significantly reduced at elevated temperatures. The surrounding chromium cylinder will also expand laterally significantly more rapidly than the glass hence reducing the friction value.

Chapter 4

Selective Laser Melting

The use of a high brightness laser for laser melting processes provides very precise spatial and temporal control of the energy input into the process zone, allowing overall good control over the melt pool dimensions. By using such lasers to embed fibres, the amount of energy transferred into the fibre can be minimised, potentially reducing the thickness of the metal jacket required to protect the fibre during the embedding process. This in turn minimises the structural intrusion of the manufactured component created by the sensor element's incorporation.

The objective of this chapter is to characterise the SLM process appropriately, to identify parameters that allow the fabrication of features designed to precisely hold the fibre before over-coating with additional powder layers (Figure 4-1). In addition it is important to minimise the energy input close to the fibre whilst still achieving good bonding between subsequently deployed powder layers and no porosity.

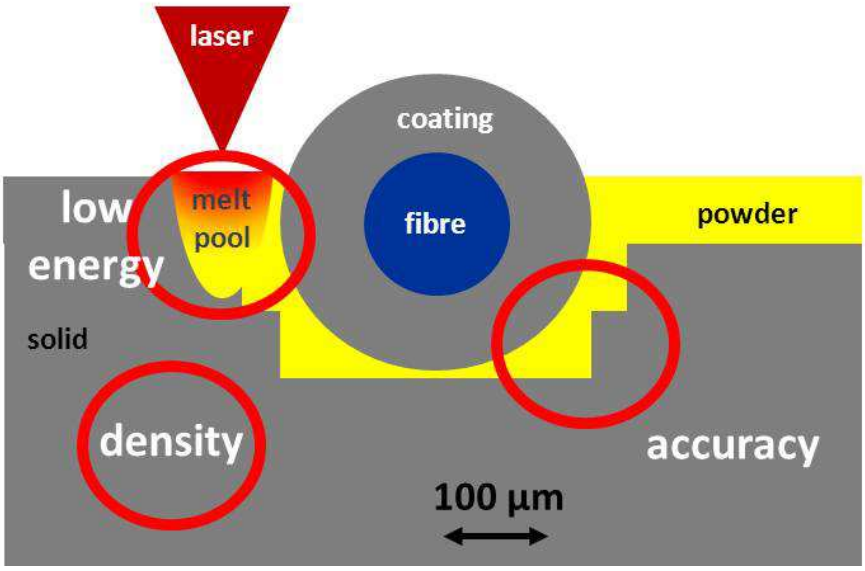

Figure 4-1 Requirements for the SLM process to embed coated optical fibres. The main objective is to fabricate SS 316 structures with high density, high precision and minimised melt pool dimensions.

4.1 Experimental setup laser melting

The optical system for SLM is shown in Figure 4-2. The laser beam is expanded before the galvanometer scan head in order to provide a sufficiently small focus spot at the work piece. The galvanometer scan-head is used to deflect and therefore move the laser light across the substrate's surface. F-theta optics attached to the scan-heads maintain the beam focus in a flat plane as it is scanned across.

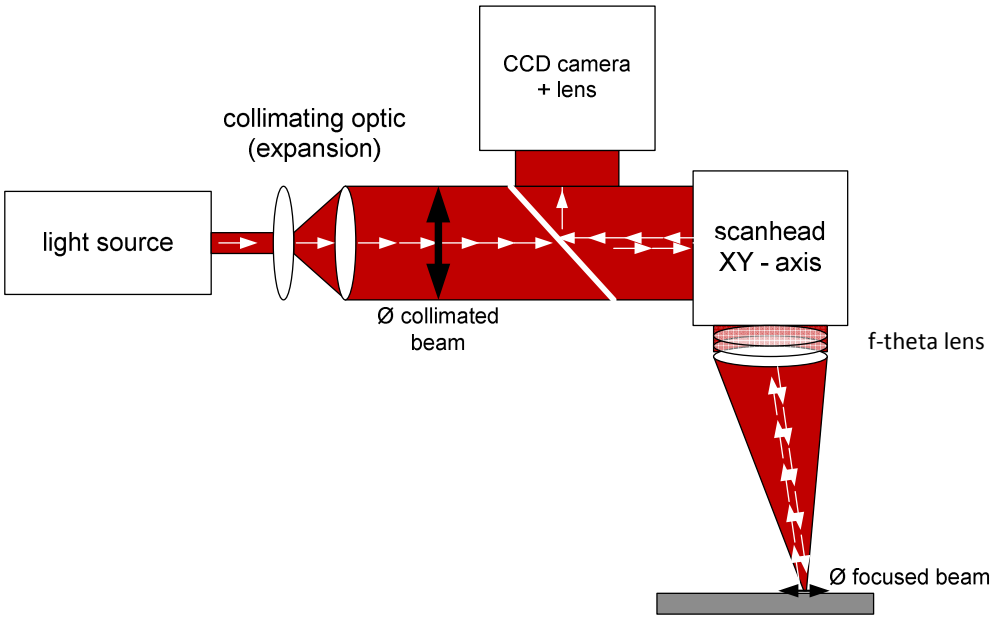

Figure 4-2 Optical setup for laser melting processes. Light from the source is expanded and the collimated beam is deflected by a two-axis mirror system (scan-head). On the substrate the collimated light is focused using an F-theta lens. Beam deflection across the substrate surface is achieved by movements of the mirror system.

To improve the alignment and targeting of the SLM system a CCD camera system is attached to the optical setup. A dichroic mirror is placed in the expanded collimated beam path to collect visible light from the substrate onto the CCD chip. By using the camera system, the positioning of the laser beam can be precisely aligned to features on the work piece. In combination with the scan system's accuracy, the position of the beam can be controlled to a precision of about ±5 μm.

Two suitable laser sources were available for SLM of SS 316, a diode laser and a high brightness fibre laser. The diode laser is an array of diodes, resulting in poor beam quality (~M^2 > 80) which means that the smallest focal spot that could be obtained was

255 µm providing a maximum intensity of 3.92 * 10^5 W*cm^{-2} (Table 4-1). The fibre laser meanwhile has an M^2 of ~1.1, providing a focal spot of 23 µm and intensities of 2.4 * 10^7 W*cm^{-2}. The intensity provided by the fibre laser is hence two orders of magnitude higher than that of the diode laser. Comparing these values with the findings from Steen (Figure 2-14;[67]) for laser material processing of solid iron, the fibre laser can melt of the materials in the ten microsecond regime, whereas the diode laser system requires millisecond timescales.

light source [-]	max power [W]	wavelength [nm]	f - focus [mm]	Ø beam @ focus [µm]	max intensity [W/cm^2]
diode - LASERLINE LDM 200 -200	200	940	80	255	3.92E+05
fibre - SPI C-100 W	100	1035	160	23	2.41E+07

Table 4-1 Laser and optical equipment used in experiments.

Both the fibre laser and diode laser can be controlled by the scan-head software (Raylase). Typically, a value for the output power is set in the software and the laser is enabled by using the software. Both laser systems follow changes in set power precisely in a range of ± 0.5 W, as it was measured with a power meter at the work piece position. In the following, the power values are those specified in the software. Additionally the fibre laser output can be modulated at frequencies of up to 10 kHz, providing pulses of down to 10 µs. Figure 4-3 displays the pulse characteristics measured by photodiode positioned in the collimated beam path. The photodiode is connected to an oscilloscope. At the beginning of the pulse the laser typically slightly "overshoots" the set ouput power.

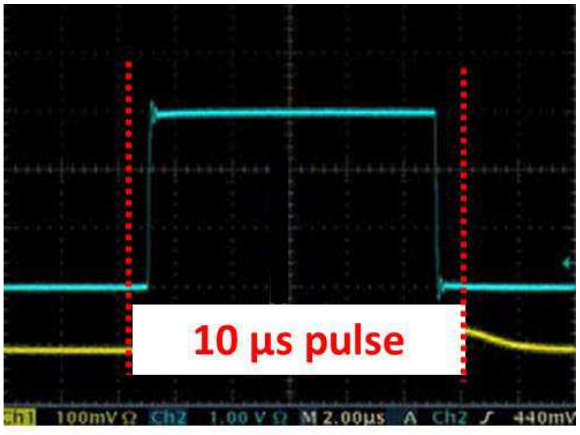

Figure 4-3 Pulse characteristics using the fibre lasers power modulation for 10 µs pulse.

The SLM experimental setup is designed to imitate features found on commercial SLM systems ([70]; Figure 4-4). A vertical stage allows adjustment relative to the focal plane. On top of the stage an aluminium table with a cut-out, sitting on 4 pillars, is mounted. A second vertical stage is mounted between table and the lower stage, holding a brass piece that is able to slide inside the cut-out of the aluminium block, simulating a standard powder bed mechanism but at a small scale. The brass piece will drop inside the aluminium block according to the movement of the second vertical stage, to precisely set the height of the brass piece relative to the aluminium block.

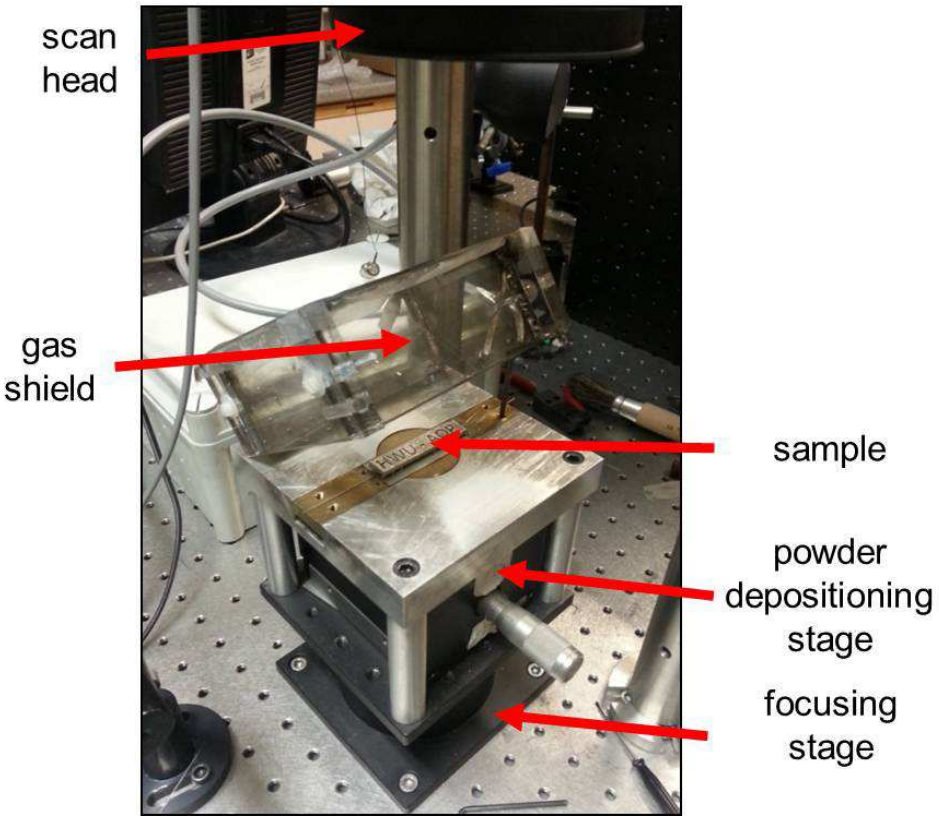

Figure 4-4 Experimental setup for SLM experiments. Base is a vertical stage for control aluminium top-plate relative to the focal plane. A second vertical stage controls the height of the brass platform. Gas shielding can additionally be applied.

A gas shield box is placed on top to provide atmospheric encapsulation. The glass on top of the shield is transparent for the laser ($\lambda \sim 1\ \mu m$). Gas in-lets allow gas to flow inside the chamber. The shield does not hermetically seal the specimen from the environment however the inflowing gas will displace the oxygen over time within the box. In preliminary experiments argon flows of about 0.5 $l*min^{-1}$ were found to be sufficient to prevent any noticeable oxidation effect.

Substrates are clamped into a recess machined into the brass bar. SS 316 sheets are laser cut to fit into this recess. SS 316 powder is deposited between the aluminium block's boundaries on top of the SS 316 sheet (Figure 4-5). The studies are carried out using gas-atomised SS 316 powder, sieved with particle sizes smaller than 40 µm. After the SLM process, the specimens can be readily removed and replaced with a new substrate.

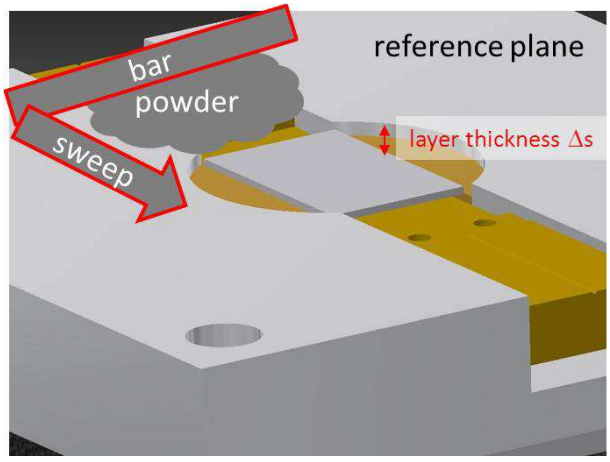

Figure 4-5 Illustration of powder deposition process.

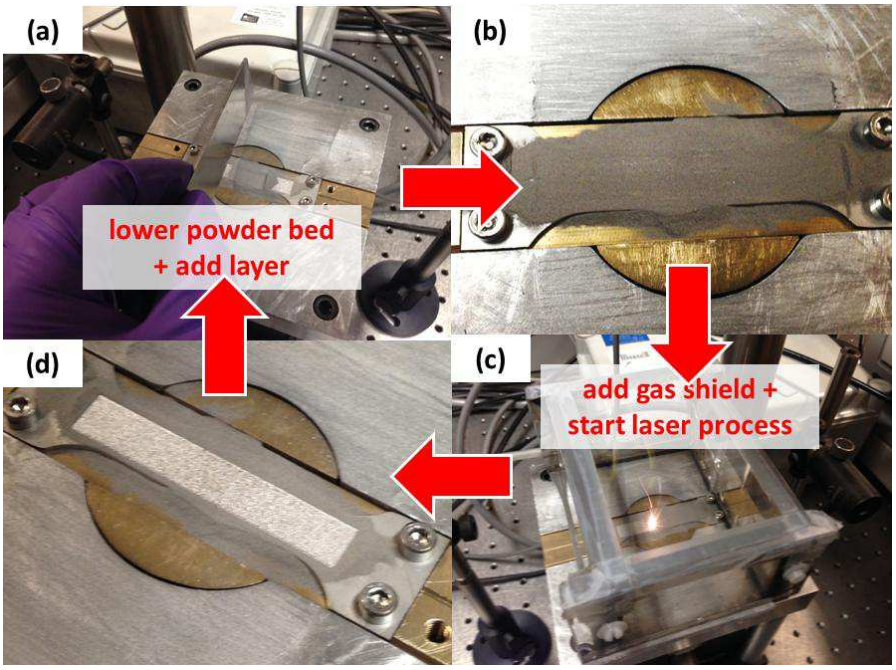

Figure 4-6 Procedure for applying layers on SS 316 substrates by SLM. The substrate is clamped onto the brass recess, powder is deposited (a & b). After applying gas shielding the laser process is started (c). The gas shield is removed after laser scanning is completed, the powder bed is lowered and another layer can be applied (d).

The cycle for applying powder layers is illustrated in Figure 4-6. After clamping the substrate on the brass piece and depositing the first powder layer the gas shield is applied and the laser process is started. After processing the gas shield is removed and either the specimen is removed from the holder or further layers are applied using the same principle.

This small-scale setup allows speedy investigation of numerous different parameters. Spot diameters can easily be changed by adjusting the lower vertical stage's position, single layer tests for identifying suitable speed, power or hatching parameters can be conducted quickly while only consuming little amounts of gas and powder. The system is also easily transferred between different laser systems. Compared to commercial SLM systems powder consumption is significantly reduced (mm^3 instead of dm^3).

4.2 Calorimetric assessment

To embed optical fibres, the SLM process main objectives have to be maintained, with the fibre in place, it is necessary to melt the nickel coating, intermixing it with SS 316 to form a solid bond whilst minimising the heat input into the fibre. If the fibre reaches too high a temperature, the FBG will decay, also the large differences in thermal expansion between the glass and metal will cause high stresses, possibly inflicting structural damage to the fibre. It is useful to consider the heat conduction mechanisms that will lead to increase temperatures in the fibre's environment during the SLM process.

According to EQN 7 in an adiabatic system, the temperature of a given volume of material increases linearly with incident energy. The laser beam moves along its path with a set feeding speed typically in the range of a few hundred millimetres per second. The width of each solidified path is similar to the spot size and to ensure that dense objects are manufactured, subsequent paths typically overlap previous paths by at least half this width. Given that spot sizes are only about a few hundred micrometres at the most, the time to fuse e.g. a single rectangular layer of dimensions 15 * 30 mm^2 (size of SS 316 specimen's used in experiments is 20 * 50 mm^2) requires extended time periods (e.g. 45s for 100 µm hatching at 100 $mm*s^{-1}$) and leads to significant heat input into the specimen, increasing its temperature. Naturally, the system is not adiabatic and heat will dissipate mostly via conduction, so a longer process time whilst maintaining the energy input will clearly result in a lower temperature. The SLM process offers

variables to accomplish this, e.g. insular scanning in not connected areas or simply inducing breaks into the process.

Modulation of the laser source output-power opens up further potential to prolong the process. Power on times need to be long enough that the energy delivered is sufficient to solidify the powder material and to solidly bond it to substrate and fibre coating. Laser off times need to be sufficient long enough for the heat energy to dissipate.

Powders have a higher absorptivity for the incident laser light, leading to increased melt pool width when processing powders. Below the powder is solid material (e.g. SS 316 or nickel coated fibre). The heat energy absorbed by the powder is conducted through the powder into the solid material. In case the amount of heat energy is sufficient to melt the substrate underneath. a secondary melt pool below the powder in the solid substrate occurs, typically narrower than the powder melt pool (Figure 4-7). The narrower melt pool width in the substrate, in comparison to the width in the powder, allows 1-dimensional solutions of the heat equation to be used to approximate the heat conduction in the solid material [66, 67].

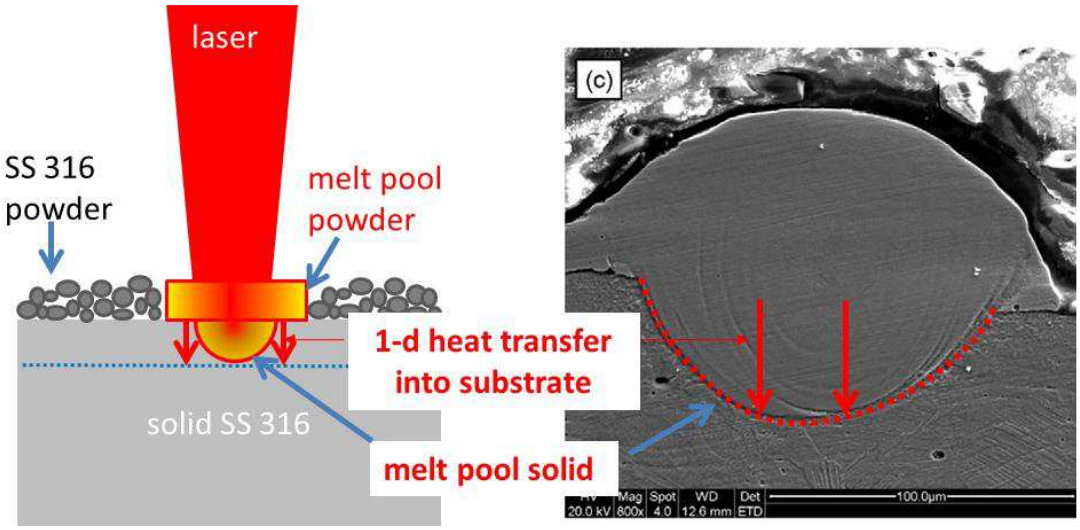

Figure 4-7 Schematic illustration of occurring melt pools in SLM processes (left). Cross-section analysis of SS 316 powder fused to solid substrate (right from [72]).

In the following model the differences in thermal diffusity of powder and solid material are not addressed, since the main concern of this research is heat conducting through either solid nickel or SS 316 which is possibly damaging the fibre. To model the

thermal penetration of a power-modulated process when melting solid SS 316, a one-dimensional solution of the heat equation is chosen which is applicable when melt pool widths do not exceed the beam diameter and heat is only transferred via conduction [66, 67]. The solution states the change in temperature over time and distance to the heat source ($\Delta T_{(z,t)}$):

$$\Delta T_{(z,t)} = \frac{8 \cdot A \cdot P_{Laser}}{\lambda \cdot d \cdot \pi} \cdot \sqrt{\alpha \cdot t} \cdot ierfc\left(\frac{z}{\sqrt{4 \cdot \alpha \cdot t}}\right) \qquad \text{EQN15}$$

Nickel and SS 316 have quite similar thermal diffusities (α_{SS316} = 1.1 x 10^{-5} ; α_{Ni} = 1.6 x 10^{-5}). For the following estimates the diffusity of SS 316 is used assuming constant laser power (P_{laser}), absorption coefficient A and spot size (d). The error function denominator is described in literature as the thermal penetration depth [66]

$$\delta_{th} = \sqrt{4 \cdot \alpha \cdot t} \qquad \text{EQN16}$$

which provides an rough estimate how far heat induced by a remote source travels over time (Figure 4-8). The thermal diffusity is part of the radicand, which means that differences in thermal diffusity of nickel and SS 316 change the result by less than 20 %[65].

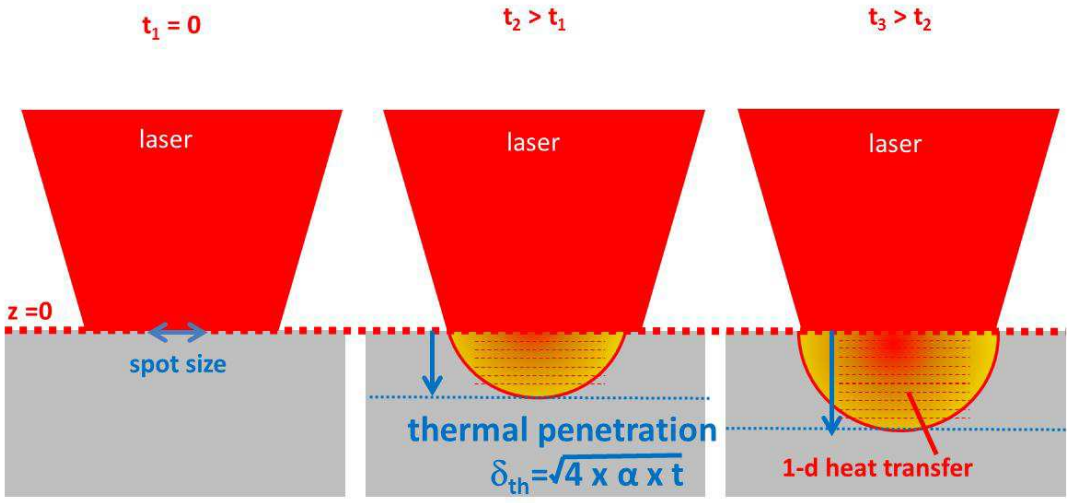

Figure 4-8 Schematic illustration for the thermal penetration of heat induced into a specimen for different times, assuming that the laser is a point source for heat.

The thermal penetration depth of solid SS 316 is displayed in Figure 4-9. In the conducted experimental studies, the powder layer particles size is below 37 µm. From Figure 4-9 it follows that the illumination time for the heat to penetrate to a depth of 75 µm in solid SS 316 is about 150 µs. The threshold of 2 times the powder size is arbitrary. However, it is assumed that at least the thickness of one powder particle is molten and that also further heat is necessary to partially melt the substrate to a similar depth to facilitate bonding between both, powder and substrate.

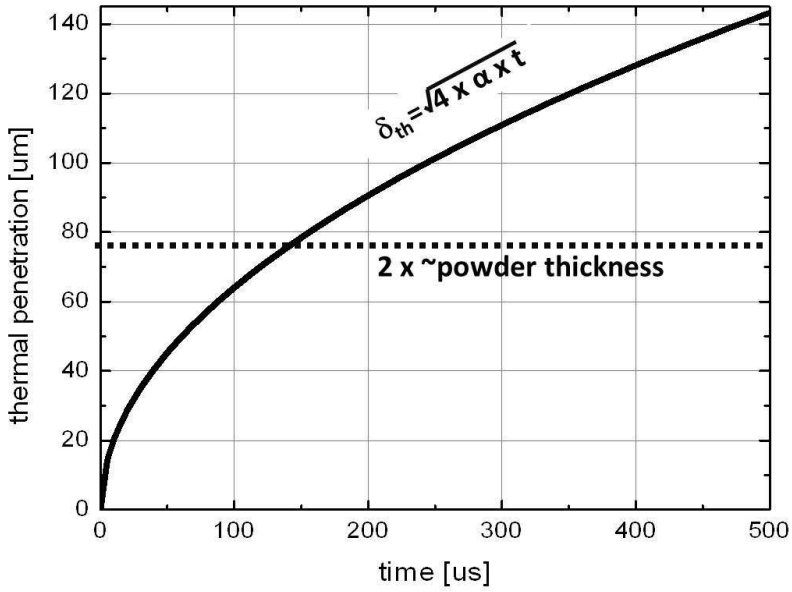

Figure 4-9 Plot for the thermal penetration of SS 316 as a function of time.

The higher the intensity of the power modulated laser beam, the sooner that the melting temperature will be reached at a certain depth, allowing the laser to be switched of so that the sample can cool down. Figure 4-10 displays estimates for the temperature over time and various depths. Two different cases are investigated, both representing specifications of available experimental equipment. In both cases the laser power represents 80 % of the laser maximum output power. The diode laser (right) has a ten times larger spot diameter than the fibre laser (left). In both cases the laser on time is set such that the process reaches melting temperature at a depth of 75 µm. In cases where temperatures exceed melting or vaporisation temperature, the model can simply be extended by adding summands ($-H_x/c_p$) for melt ($H_{m,steel}$ = 300 kJ/kg) and vaporisation ($H_{V,steel}$ = 7600 kJ/kg) enthalpy of steel. The model provides a good estimate at which time at which depth melting temperature is reached.

The high intensity of the fibre laser allows a much more rapid heating of the material (Figure 4-10 left). About 50 µs after the laser on-time, the melting temperature is reached at a depth of 75 µm. 25 µm deeper into the material, the predicted temperature is still about 600 °C whilst at a depth of 250 µm the temperature change is minimal. After stopping the energy input the material cools rapidly since only 4 mJ in total was deposited into the specimen.

The diode laser provides a much lower intensity due to the increased spot size (Figure 4-10 right). It takes about 400 µs for the material to reach melting temperature at a depth of 75 µm. This prolonged time allows the heat to travel much further into the material. At that time, the temperature at 250 µm depth is already 150 °C. Also cooling occurs much slower, since 20x more energy (80 mJ) compared to the fibre laser was deposited during the process.

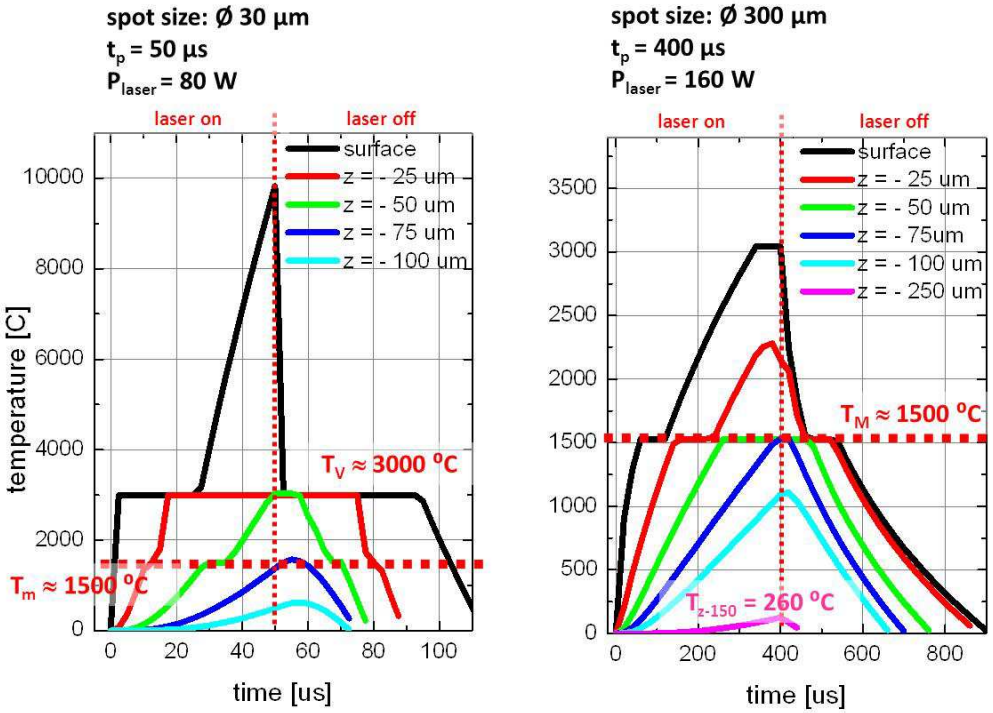

Figure 4-10 Simulated results for temperatures as a function of time for different depths. Two different cases representing different available equipment.

Figure 4-10 indicates that the intensity of the fibre laser is too high when using the minimum spot size. It is of concern that predicted temperatures almost reach 10000 °C at the specimen's surface. Vaporisation will occur which is disadvantageous for SLM

processes, leading to distortion and irregularities in the process [71] and can lead to the occurrence of micro-porosity due to entrapment of gases by the re-solidifying vaporised material provided that large aspect ratios are achieved [109]. Two possible solutions exist to tackle this issue. Either the laser power is reduced, or the spot size is increased by de-focusing the laser. De-focusing is more promising since the full laser out power is utilised and also the speed of the SLM process is increased with larger spot-sizes. For embedding SMF-28 fibres (OD 125 um + coating material) 80 µm feature sizes are considered small enough.

In Figure 4-11 simulation for a case is presented where the spot size is 80 µm. Laser power is 80 W. Heating occurs fast and melting temperature is reached after about 100 µs at a depth of 75 µm. No significant temperature increase is predicted at a depth of 250 µm. Vaporisation temperature is not exceeded. After another 100 µs the induced heat energy (8 mJ) has almost completely dissipated into the environment.

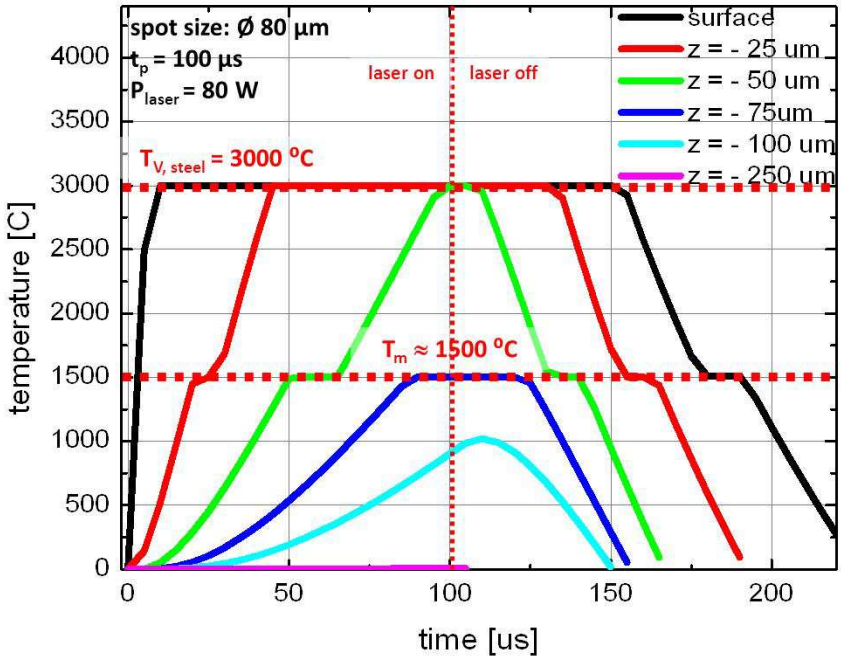

Figure 4-11 Predicted temperatures as a function of time for different depths for case with increased spot diameter of 80 µm.

The results from the model indicate that modulating the laser source is a useful method to prolong the process, ensuring that the energy deposited by the laser beam has dissipated into the environment before the next laser pulse is delivered. The dissipated energy will however remain within the specimen increasing the overall temperature.

This can easily be mitigated by adding further delays into the SLM process itself. Furthermore, the model shows that higher intensities lead to steeper temperature gradients, resulting in rapid heating and less heat conduction into more remote areas. The use of the high brightness fibre laser with its high intensities at small spot sizes is desirable to minimise the energy conducting into the environment and in particularly the optical fibre. Therefore, in the experimental studies described below, a particular focus there was on studying the SLM process using the fibre laser using time modulation of the laser power.

4.3 Experimental results

4.3.1 Fibre Laser - SPI 100 W

As described above a high brightness light source is much more likely to achieve the objective of embedding optical fibres with minimised coating thickness and without fibre damage. The high quality of the laser ($M^2 < 1.1$) allows a spot size down to about 25 µm to be easily used. The Rayleigh-range of the focused beam is about 1.4 mm. In the following a study using this laser system for processing SS 316 solid and powder material is conducted.

No powder

Figure 4-12 displays cross-sectional and etch analysis of a parameter study conducted for different energy inputs and at different focal positions on a bare SS 316 substrate. Melt seams of 10 mm length were applied using the laser and subsequently substrates were cut (perpendicular to seam direction at half the seam length), polished, etched ("Aqua Regina") and analysed using microscopy.

From analysis of the results presented, it is clear that the melt pool width is more or less constant when changing the focus position in-between ± 1 x the Rayleigh range. If the feed speed or power is changed, the melt pool width changes, as a result of the energy input. The depth of the melt pool and therefore the cross-sectional area of molten material volume, significantly vary with focal position. With high power levels (100 W) and long-interaction times, vaporisation occurs, forming a "Key-Hole" and due to multiple reflection inside the trough caused by vaporisation, the overall absorption is significantly increased leading to a significant increase of the volume of molten material

hence high efficiencies of the melting process. This increase in molten material leads to a deeper penetration depth and does not cause any significant increase in width of the seam, hence the aspect ratio depth over width increases.

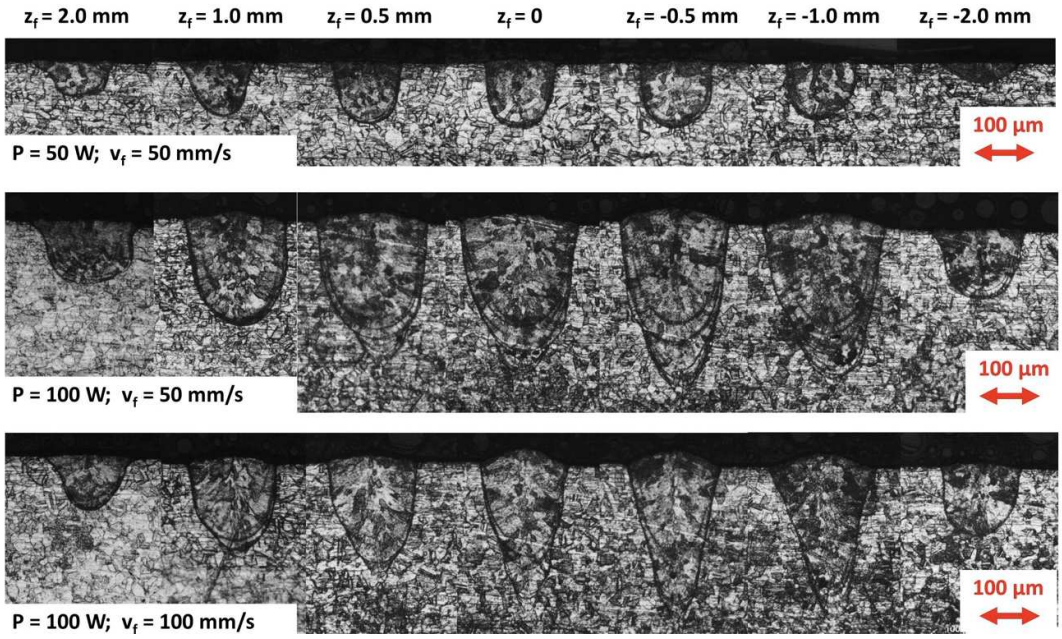

Figure 4-12 Cross-section analysis of welds applied to SS 316 sheet with varying feeding speed and power.

With Powder

Powder layers (SS 316) of 50 µm thickness are applied to a SS 316 substrate and solidified by single lines scanning under argon atmosphere. The laser beam is travelling with a speed of a 100 mm*s^{-1}. If no modulation is applied and the laser is emitting continuously (cw-mode; Figure 4-13 left), a homogenous line of added material is fused to the substrate. The dimensions of the line are about 100 µm in width and 120 µm in height, where the width is measured at the interface between substrate and the melt height is measured from the bottom of the melt pool to the top of the melt bead. When power modulation is applied (100 µs laser on & off: 50 % "duty-cycle") a homogenous line of similar height is still produced, but the width is significantly reduced by about 50 % to 85 µm (Figure 4-13 right).

As predicted by the model, modulating the laser can be used to minimise the heat input during the SLM process. During laser off times heat is dissipated leading to

solidification of the melt pool which is indicated by lines in the cross-sectional analyses, showing that the melt pool solidified 5 times. At a speed of 100 mm*s^{-1} and 80 W power the seam width is about 80 µm. Each individual segment along the beam path is processed 4-5 times leading to melting and solidification of the material, resulting in lines shown in Figure 4-13 (right). The height of the added material is almost unchanged. The seam produced during the cw-process is significantly wider since more time is available for heat energy to penetrate the material deeper and wider.

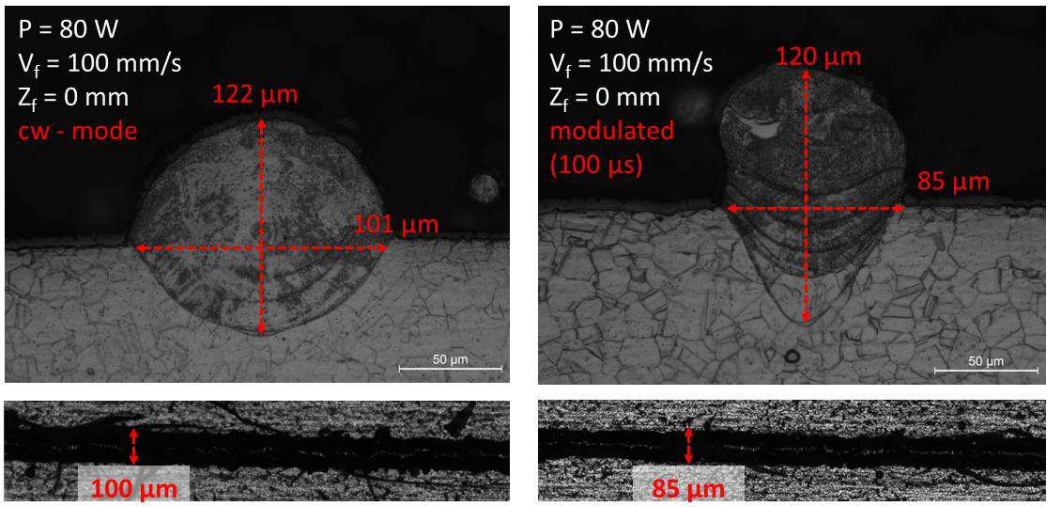

Figure 4-13 Cross-section analysis and view from above of etched SLM seams for processes with cw (left) or modulated laser.

To identify a suitable process window for single-track formation with the given equipment and powder material, sets of experiments were designed, conducted and examined, similar to many studies reported in the literature. Examination was conducted by microscopic examination of the seams from above and in cross-sectional analyses.

Figure 4-14 displays the cross-sectional and etched analysis of single lines of 50 µm thick powder layers molten to the SS 316 substrate for different powers and speeds using a power modulated laser beam with 50 % DC. Within one Rayleigh length into both directions of the focal plane the process works reasonably well and not only the powder is molten but also the energy input is sufficient to partially melt the substrate allowing intermixing both of substrate and powder materials. For focus positions further away than one Rayleigh length from the focal point, the spot size is too large and energy at the beam's edges is only dissipated without melting the material. Also, in this

regime, molten material does not properly bond to the substrate and surface tension causes contraction and therefore leads to the balling-effect (Figure 4-14; e.g. top left). The bonding in this regime can be improved by increasing the laser energy but this leads to significantly larger feature sizes due to the larger spot size.

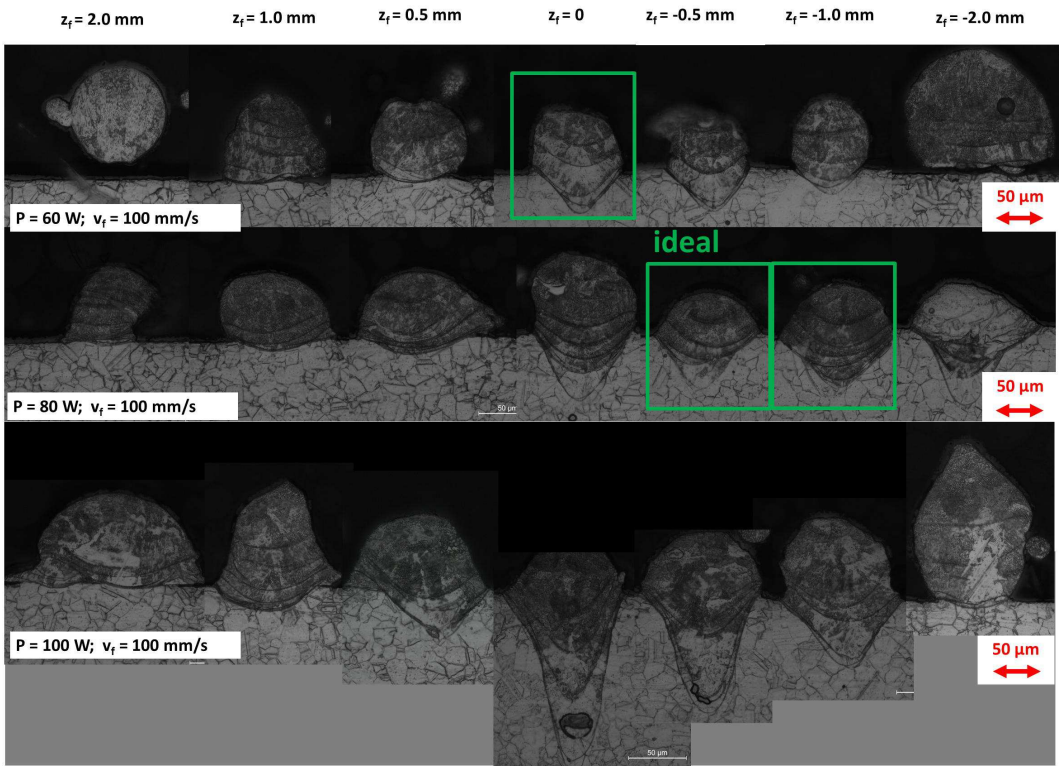

Figure 4-14 Cross-section analysis of lines of added material of SS 316 powder onto a SS 316 substrate for varying laser powers and constant feeding speed.

Typically for the investigated parameter range the width of the line of added material is about 80 – 100 µm. At high intensities, the penetration depth of the melt pool reaches deep into the substrate (200 µm) due to "key-hole" formation. This regime is considered unsuitable for the SLM process because gas entrapment can lead to the occurrence of porosity (Figure 4-14; bottom). For embedding fibres, this is not acceptable when fabricating overlapping features or in case a coated optical fibre is underneath. More ideal is the regime where the focal point is slightly below the surface of the substrate (z = - 0.5 – z = - 1.0). Intensities are high enough over a wide range not only to sufficiently melt the powder material but also to melt the substrate up to a depth of about 50 µm (depending on energy input). Ideally, the seam of added material is fused to the substrate over its whole cross-sectional width. Then, a half spherical melt pool extends into the substrate leading to a penetration depth typically half the seam

width [71]. The powder is properly bonded to the substrate and also the penetration depth into the substrate is deep enough to re-melt the previously added layer, overall minimising the occurrence of porosity when stacking individual seams together to fabricate 3D components.

4.3.2 Diode Laser – Laserline LDM 200 – 200 W

Trials were conducted to establish the diode laser as a secondary system. The system's maximum output power is 200 W which might be beneficial when trying to melt thicker powder layers. Lines of SS 316 powder melted to the SS 316 substrate with varying feeding speeds and different initial powder thicknesses are displayed in (Figure 4-15;left). The laser beam diameter is about 260 µm. The thickness of the initial powder layer is about 400 µm and the laser power is set to 200 W. At feeding speeds of about 30 mm/s uniformly shaped lines are formed. Cross-sections of these lines (Figure 4-15; middle) show hemispherical formed agglomeration of material. The width of each line is about 500 µm and the height is roughly 400 µm. At feeding speeds exceeding 50 mm/s balling occurs, because energy input per unit length is not high enough to overcome the influence of the melt pools surface tension. In cross-sections almost spherically formed agglomeration of material are observed.

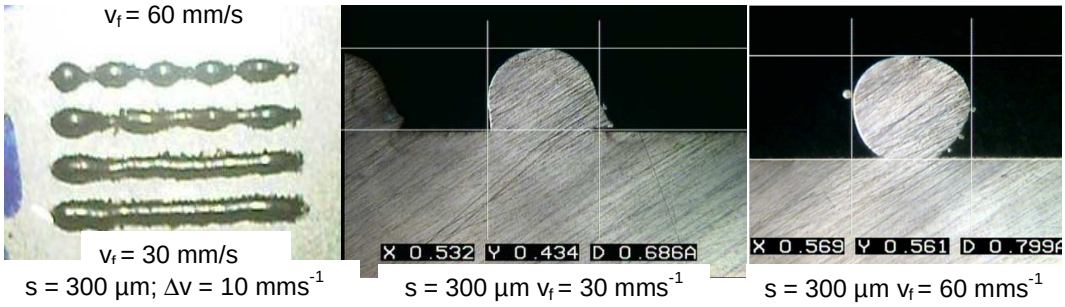

Figure 4-15 Analysis of SS 316 material added to substrate using diode laser. Left: Top view on single lines of added SS316 to a SS316 substrate using the diode laser system; middle & right: Cross-sections of these lines (dimensions in [mm]).

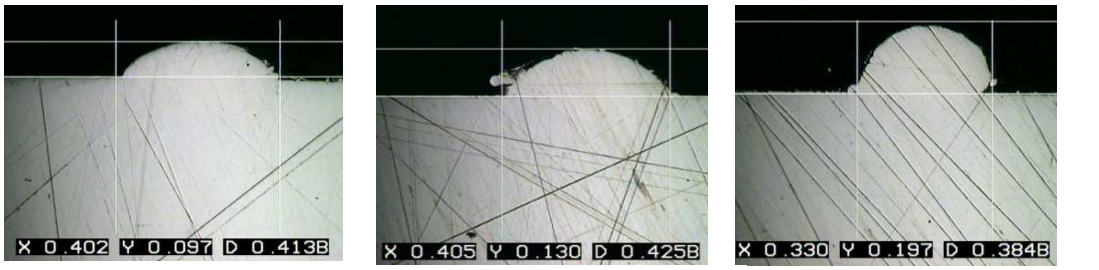

s = 100 µm P = 200 W; v_f = 20 mms^{-1} s = 100 µm P = 200 W; v_f = 60 mms^{-1} s = 100 µm; P = 200 W v_f = 100 mms^{-1}

Figure 4-16 Cross-section analysis of SS 316 material added to substrate by using the diode laser. Development of the balling effect for varying feeding speeds (dimensions in [mm]).

Thinner powder layers allow less energy input to be used. The development of the balling effect for a layer thickness of 100 µm can be seen in

Figure 4-16. For a laser power of 200 W and over a wide range of feeding speeds up to 60 mm*s^{-1}, layers with a width of about 400 µm and a height of about 100 µm are produced. Above a feeding speed of 60 mm*s^{-1} the height of the deposited material is significantly increased while the width is reduced. At a feeding speed of 100 mm*s^{-1}, the added material forms a sphere with the section headed toward the substrate becoming thinner.

The results indicate that the minimum feature width is typically in the range of 1.5 × the laser spot size of 300 µm, i.e. a minimum feature width of 400 µm. This is not ideal for embedding fibres of 125 µm in outer diameter.

4.3.3 Fabricating components by Selective Laser Melting

In the previous section parameters suitable for melting single lines of SS 316 powders onto SS 316 substrates were identified. When applying these single lines with small spacing next to each other and when additional layers of powder are added, dense components can be fabricated. The fibre laser is focused about 0.7 mm into the substrate leading to a spot size on the surface of about 80 µm. Feeding speed is set 100 mm*s^{-1} and laser power is set to 80 W. Argon is used for an inert atmosphere.

Figure 4-17 shows a cross-sectional and etched example of 2 layers of added material using these parameters. The first layer is applied in direction perpendicular to the cross-sectional plane. The line to line distance is set to 50 µm, and given that each individual line width is ~85 µm this provides a line to line overlap of about 40 – 50 %. Scanning

is conducted bi-directional from both sides and after the first layer is solidified the powder bed is lowered by 50 µm and another layer of powder is deposited. For processing the second layer the direction of the bi-directional scanning pattern is changed by 90^0 prevent the occurrence of macro-porosity and reduce residual stresses. In the first layer, applied perpendicular to the cross-sectional plane, no porosity is obvious. The line to line spacing is close enough to partially re-melt lines applied before and the penetration depth into the substrate is about 35 µm, facilitating good bonding of the added material to previous layers.

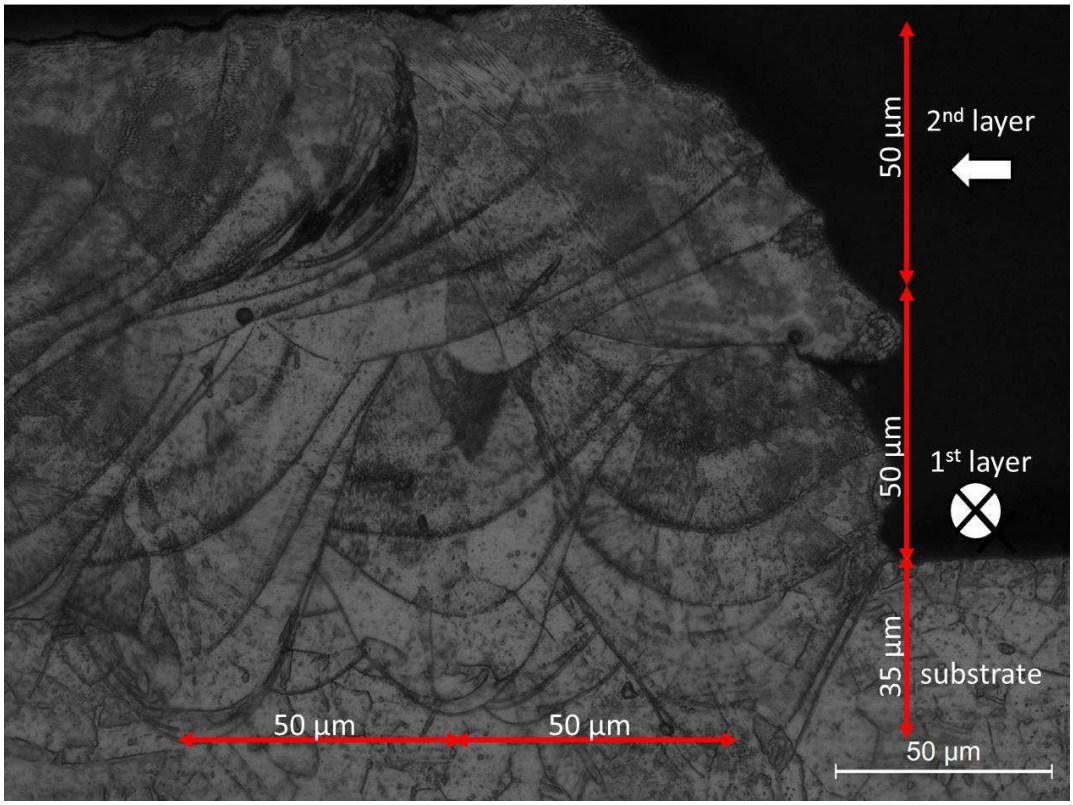

Figure 4-17 Cross-section analysis of two layers of SS 316 deposited changing direction of scanning by 90^o.

The second layer is initiated just above the centre line of the most outer line of the first layer in a direction perpendicular to it. For about the first 50 µm, equivalent to about 0.5 ms, the process has not reached equilibrium, indicated by the gradual increase in penetration depth. More layers (Figure 4-18 (5 layers) & Figure 4-19 (10 layers)) can be applied in a similar manner. Rotating the scanning pattern by 90^0 after each layer components with straight walls and no obvious macro porosity are built.

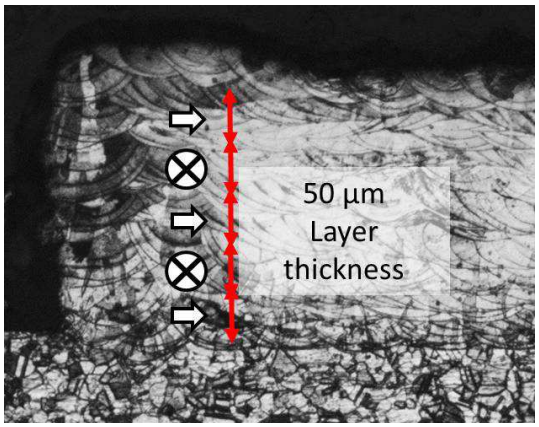

Figure 4-18 Cross-section analysis of 5 layers applied by SLM.

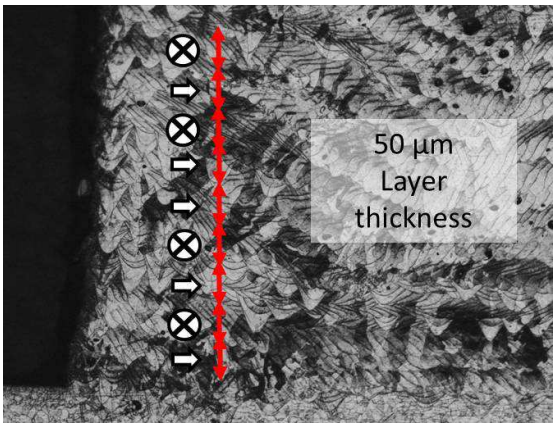

Figure 4-19 Cross-section analysis of 10 + layers applied by SLM.

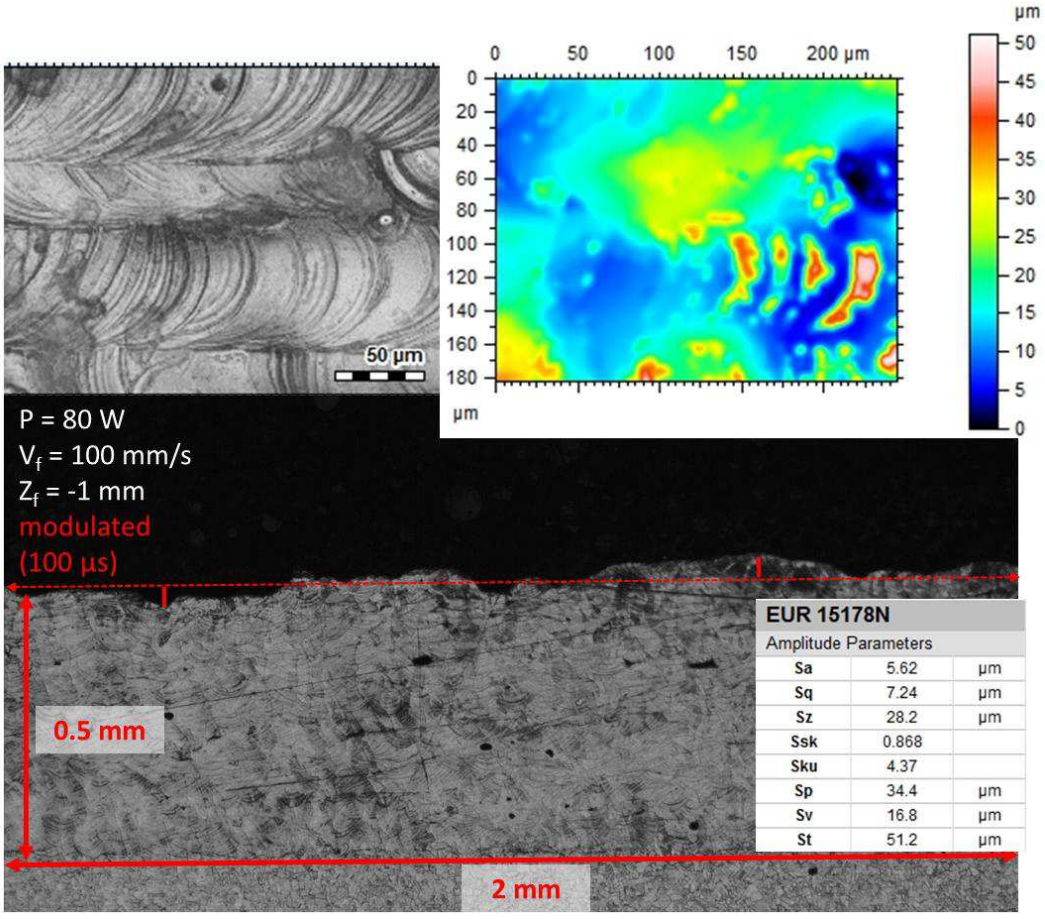

Figure 4-20 Microscopic, surface and cross-sectional analysis highlighting the surface roughness of SS 316 material added onto a substrate by SLM.

A larger cross-sectional area of another sample with SLM added SS 316 material solidified to a substrate is displayed in Figure 4-20. After adding 0.5 mm the surface roughness is about 6 µm with a peak-to-valley roughness of about 35 µm which is equal to the powder size.

Figure 4-21 illustrates the feasibility for fabricating features with overhanging geometries with no supporting material underneath. After applying one layer the area where the process is applied is offset by certain steps. When choosing a step size of 50 µm the component follows the geometry of the applied building process on both sides, the supported side (left) and unsupported (right) with no powder underneath.

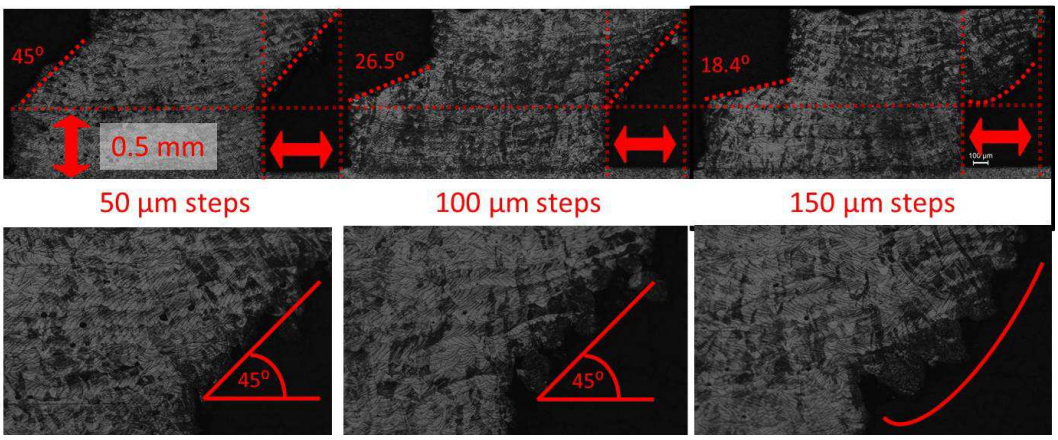

Figure 4-21 Cross-section analysis of different overhanging geometries fabricated by SLM. In case the step size exceeds the line width of the SLM process accuracy of overhanging surfaces is significantly reduced.

The angle on both sides is about 45^0, as expected when using a layer thickness and step size of 50 µm. Increasing the step size to 100 µm and the geometry of the overhanging structure does not follow the geometry of the building process. The angle of the overhanging feature remains at about 45 % and the surface is much rougher. The supported geometry follows the geometry of the actual built process. Further increases in step size lead to similar poor results in accuracy on surfaces which are not supported by solid material.

In case the step size exceeds the single line width of the SLM process (~ 85 µm) and the laser is processing powder with no solid material underneath, the melt pool extends

much further into the powder leading to poor surface characteristics of overhanging geometries. This is to be considered when fabricating internal voids.

4.4 Conclusion & Discussion

The feasibility of adding SS 316 powder material to SS 316 substrates using a home-built SLM setup is demonstrated. Laser radiation is absorbed by the powder and at sufficient laser energy not only the powder melts, also the surface of the substrate melts allowing intermixing of both materials and strong bonds to form. Different process parameters such as spot size, speed and power were investigated to identify the most suitable parameters allowing building porosity-free components with relatively high accuracy (down to ±10 µm).

Furthermore it is theoretically and empirically established that using a high brightness fibre laser with high intensities has numerous advantages compared to using a diode laser system with relatively larger spot size. Using the fibre laser and spot sizes of approximately 80 µm features with sufficient accuracy are fabricated which allows the fabrication of features such as grooves or voids to precisely matching the dimension of round coated optical fibres. High intensities while using power modulation reduce significantly the energy that is conducted into the surrounding material volume.

Chapter 5

Embedding optical fibre sensors with Selective Laser Melting

The aim of this chapter is to identify possible ways to embed nickel coated optical fibres by SLM. When building components layer-by-layer, inserting coated fibres into the SLM process causes a disturbance, especially in cases where the dimensions of the coated fibre are thicker than the powder layers that are applied (schematic in Figure 5-1). The fibre is an obstacle for deploying powder material. In this chapter approaches are explored to embed coated fibres without interfering with the powder delivery and to identify best practices for reliable and repeatable embedment.

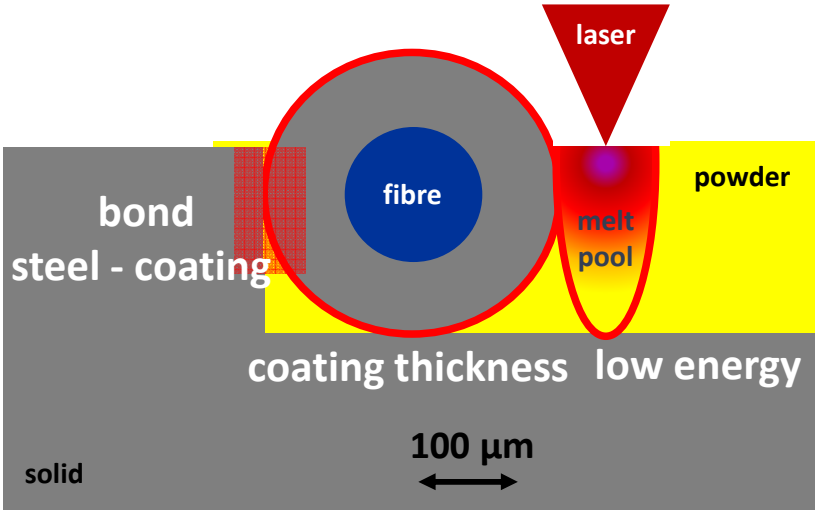

Figure 5-1 Objectives for embedding coated optical fibres into powder based SLM process. The main objective is to achieve proper bonding between the fibre coating and steel surround and to adjust the energy input of the SLM process such that the optical fibre's structural integrity is preserved. Ideally the coating thickness is minimised to reduce the influence of its mechanical properties.

An additional requirement for the embedding process is to achieve a proper bonding between the fibre, its coating and the fabricated steel component, in order that strain and temperature changes applied to the SLM fabricated structure are transferred into the fibre and measured. Thus, the necessity of creating a bond between SS component and fibre coating leads to the requirement that the energy input of the SLM process is high enough not only to melt the powder but also to partially melt the coating material,

ideally inter-mixing both materials. Pure nickel and SS 316 should easily form such a bond since nickel and carbon steels can easily go in solution with each other.

The induced laser energy for melting the powder material must be minimised to avoid damaging the optical fibres. As reported in Chapter 4, parameters for the SLM process were established to minimise the heat input during the process. A key objective of this work is to identify the minimum coating thickness necessary to protect the optical fibre to minimise the influence onto the physical properties of the SLM fabricated component.

5.1 Experimental setup fibre embedment

The SLM setup from Chapter 4 is extended with features that enhance the positioning and constraining of coated optical fibres during the SLM process (Figure 5-2). The coated optical fibres have a number (typically 3) of sections of different outer diameters since the polymer coating is only stripped from the section to be embedded. The 3 sections are, (i) the nascent polymer-only coated part (always OD 250 μm), (ii) fibre plus metal coating and (iii) polymer-coated fibre with metal coating (see also Chapter 3). A range of substrate holders with V-grooves of different dimensions was machined to hold fibres with different coating thicknesses. The fibres are held on the substrate holder by using small clamps. Ideally, the fibre is only loosely clamped so that it is only laterally and not axially constrained, to allow thermal expansion of the coated fibres during the embedding process. On both ends, fibres are pulled with a force of about 2 N to overcome the friction in the clamping mechanism and guide the movement of the expanding fibre during the SLM process. The force is typically applied by guiding the fibre over a rounded corner and attaching a mass of up to 200 g onto the free floating fibre (Figure 5-2; top left)

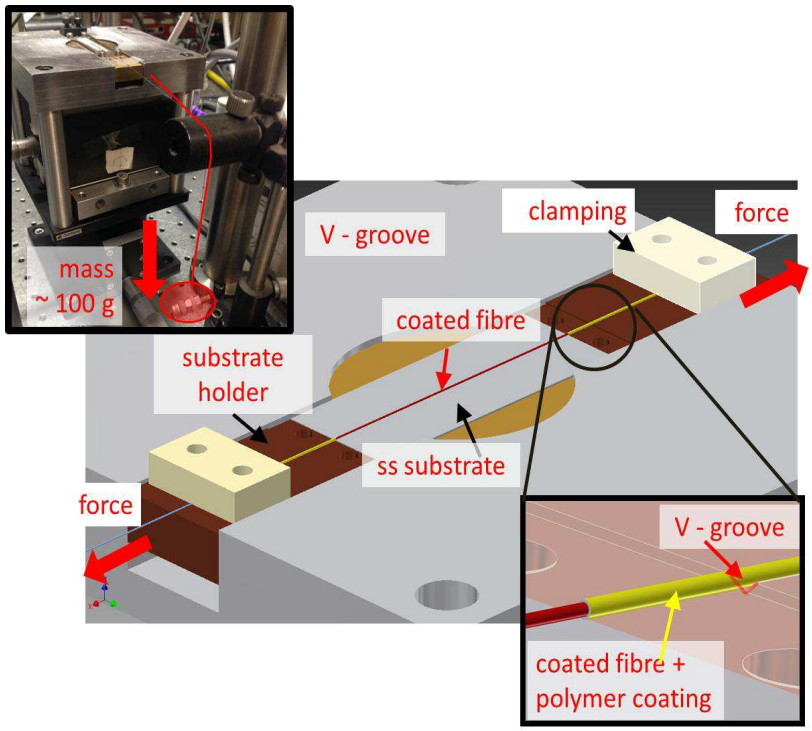

Figure 5-2 Experimental setup for embedding nickel coated optical fibres. Coated fibres are positioned in V-shaped grooves. Groove sizes are tailored to position the polymer stripped but nickel coated section directly on the surface of the SS substrate. Additional clamping can be applied to hold fibres in position.

5.2 Techniques for embedding nickel coated optical fibres into stainless steel.

Using SLM technology, the implantation of coated fibres with thicknesses of at least several hundred micrometres is an obstacle for powder delivery. Additionally, a particular challenge arises from preventing the fibres movement due to thermal stresses during the SLM process. Laser induced melt pools in vicinity of fibres locally induces thermal energy into the fibres, causing expansion and therefore bending and misalignment. The length of the coated fibres is typically 7 to 8 cm. The nickel material is very flexible and easily bends. Properly fixing and clamping the fibres is a major obstacle on the way to embedding and in the following sections the most practical solution for achieving embedment in a repeatable and precise manner are discussed.

5.2.1 Welding coated fibres to steel substrates

One straight forward way to attach nickel coated fibres to the steel substrate is to firstly to use the laser of the SLM system to partially melt the fibre coating and hence locally weld it to the substrate (

Figure 5-3). The fibre can then be subsequently encapsulated by applying powder next to the fibre and continuing the SLM process. The advantage of attachment by welding the coating to the substrate prior to encapsulation is that the fibre's position is firmly fixed over the section which is to be embedded. Then, the position of the fibre is more easily accessable, to tailor the parameters of the embedding process in respect to the fibre. Additionally, welding the coating to the substrate prior to encapsulation allows a thorough assessment of the bond.

The maximum output power of the fibre laser is 100 W allowing melting layer thicknesses of up to 400 µm. To develop the process nickel wires of 400 µm diameter were initially used in place of the nickel coated-fibres. The wires were clamped onto SS 316 substrates, and either spot welds or line welds generated using the laser (Figure 5-4). Various parameter settings are investigated by changing power from 50 W to 100 W and the illumination timer per spot or the feeding speed is varied respectively. The beam was focused about 100 µm above the SS 316 substrate to guarantee intensities high enough to facilitate melting over a wide range along the beam path. The camera system is used to precisely locate the laser spot relatively to the wire. However, reliable bonding between the wire and substrate could not be achieved.

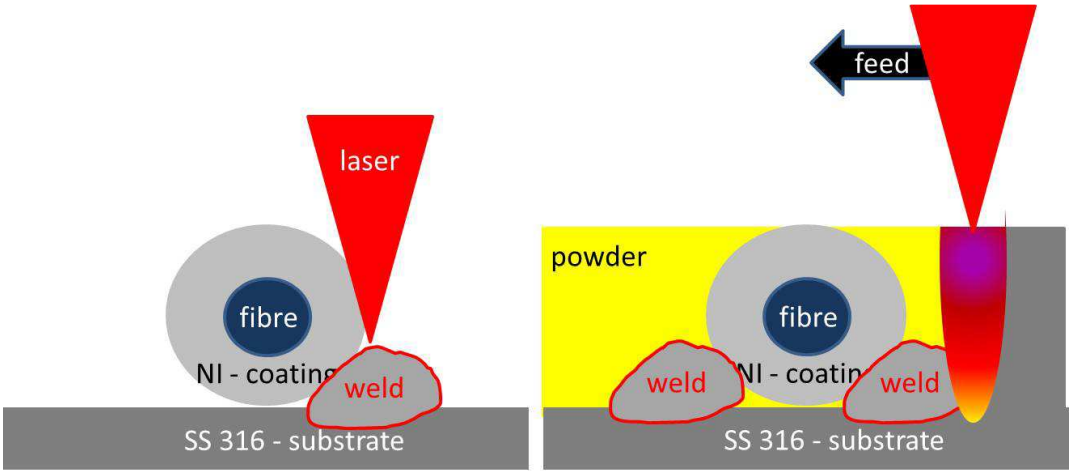

Figure 5-3 Schematic illustration for attaching the nickel coated fibre to the SS substrate using laser melting (left) and subsequent encapsulation by continuing the SLM process (right).

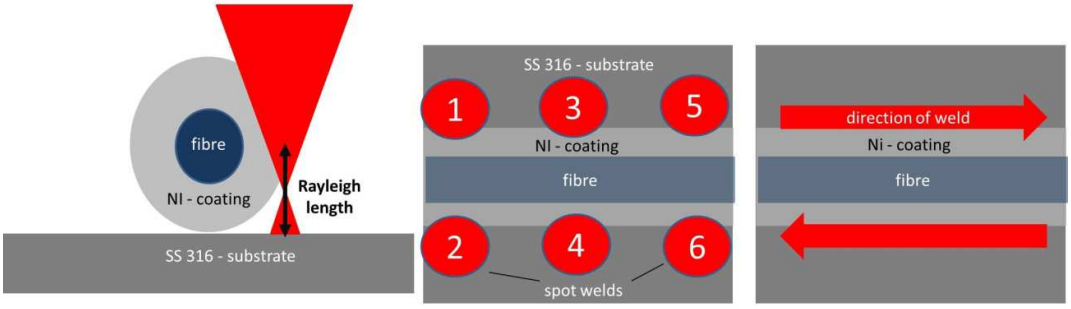

Figure 5-4 Left: Schematic illustration of geometric interdependencies between the curvature of fibre and Rayleigh length of optical system. Middle and right: schematic illustration of spot welding and line scanning approaches to attach coated fibres to substrate by using laser welding.

This is because despite the clamping mechanism the wire bends significantly when heated by the laser, resulting in movements in the range of several tens of micrometres. Figure 5-5 illustrates a model for estimating the bend angle when applying a spot weld, for a laser spot size of 80 µm half of which is incident on the fibre. The laser on-time is 100 µs, and after finishing the illumination, the melting temperature is reached at a depth of 100 µm into the wire. Given that the wire is 400 µm in diameter, the heat induced by the laser on the one side will not have reached the other side at this time (thermal penetration depth @ t = 100 µs: ~150 µm; see model in 4.2) leading to a large temperature gradient from one side to the other. Differential thermal expansion therefore occurs, leading to an increase in length of the outer surface of about 4 µm, assuming that melting temperature is reached at a depth of 100 µm and that expansion occurs in both directions away of the heating point. As a result, just after processing the wire is angled by about 1°. Over a length of 1 cm this angle corresponds to a miss-alignment of the wire by about 150 µm which is about 33 % of the wire diameter.

Applying stronger tensile forces is the only way to compensate for the miss-alignment. The necessary force to straighten the wire would need to exceed the Yield Strength of the nickel (150 MPa) in order to sufficiently strain the wire. For a wire diameter of 400 µm this represents a force of about 20 N. If applying such force onto the optical fibre it would lead to stress levels of about 1.6 GPa within the uncoated sections of the fibre, which is an issue since it is close to the tensile strengths of ideally treated silica-dioxide fibres (~ 2 GPa). Also, nickel is an extremely brittle material (HV ~ 600 N) and its Yield strength (150 MPa) and tensile strength (~190 MPa) are quite similar. Therefore, partially melting the wire during the process seems not be possible with the

comparatively large melt pool dimension (~50 µm) generated by the laser. Also the wire's cross-sectional area might be reduced during the melting process and forces applied by the clamping mechanism will increase tensile stresses further. A further problem is that the cylindrical shape of the wire means that it is difficult to achieve strong attachment between the coating and the substrate.

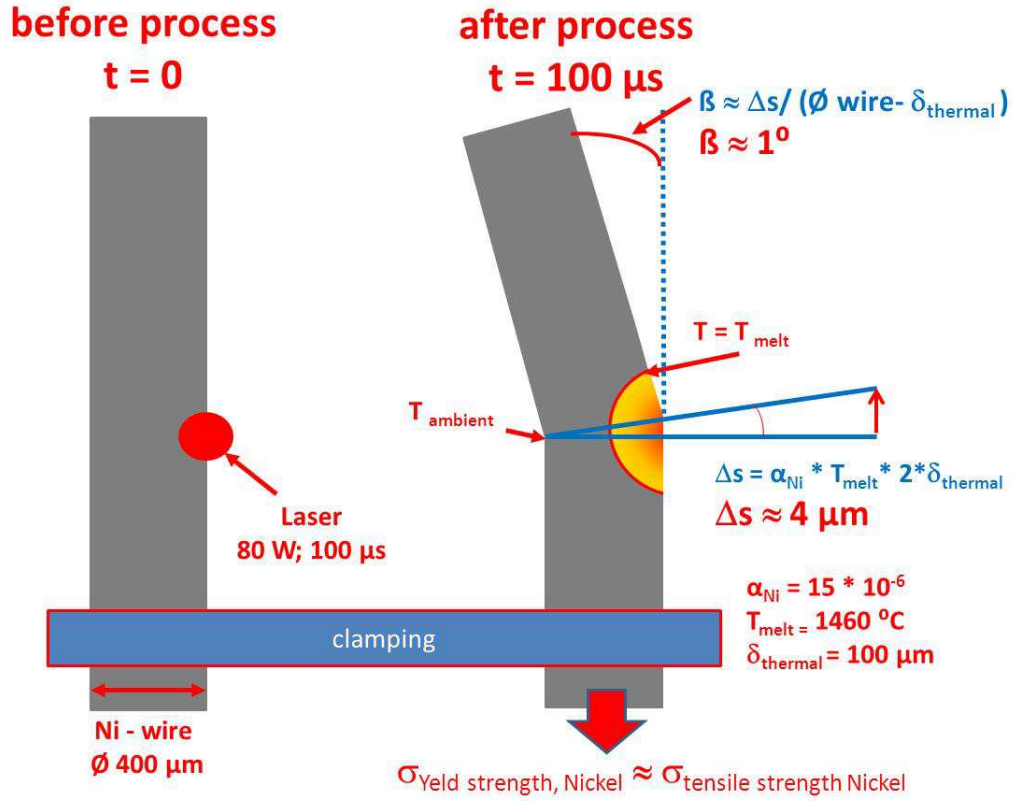

Figure 5-5 Schematic illustration for estimating the occurring forces and expansions when single-sided heating nickel wires up to melting temperatures. Large temperature gradients cause bending of the fibre leading to miss-alignment in subsequent processes.

It should be noted that partially laser melting and joining of metal components with dimension similar to the used nickel wires is commonly conducted for e.g. in integrated circuit packaging applications. This is accomplished e.g. by using rectangular shaped bonds and high forces (50 N) by applying localised clamping [110]. Neither obtaining rectangular shaped coating of fibres nor developing a clamping mechanism sophisticated enough to apply such forces without interfering with the powder delivery system or damaging the incorporated optical sensor was investigated in this thesis. Both concepts would require substantial engineering effort with possibly unknown outcome in terms of feasibility and practicability.

5.2.2 Attaching fibres to substrate using additive material

An alternative approach is to attach the fibre prior to encapsulation by using the powder material of the SLM process itself, as additive filling material. The powder material is used to fill the gap between the coated fibre and substrate, overcoming the geometric issues of welding a cylindrical fibre to a flat substrate. Furthermore, the added material allows the laser spot to be placed further away from the coating, reducing the amount of heat that is induced into the fibre/coating system. Molten powder material bonds to the coating by wetting rather than trying to directly melt the coating with the laser.

Deposition of a powder layer and subsequent deployment of the optical fibre into it, is considered not feasible. The distortion in the powder layer caused by insertion of the fibre is too significant. Therefore, the fibre has to be deployed first and the powder is deposited thereafter. Three different approaches to deposit powder layers next to the coated fibres were identified (Figure 5-6):

i. Thin powder layers are deposited independently either side of the fibre (left).

ii. Powder is deposited next to the fibre powder using a blade with a cut out for the fibre (middle).

iii. The fibre is completely covered by a powder layer of similar thickness to the coated fibre (right).

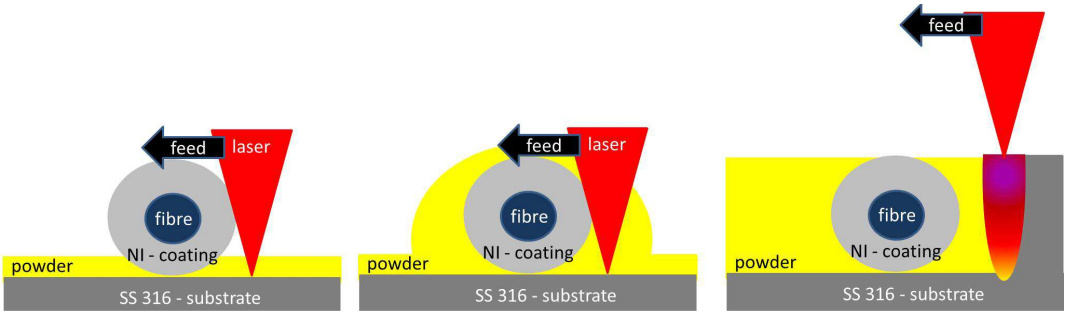

Figure 5-6 Schematic illustration for methods to attach coated optical fibres to steel substrates. Either by depositing a thin powder layer next to the fibre (left), by using blade with a cut out for the fibre (middle) or covering fibre with powder layer of similar thickness (right).

Particular challenges arise with approach (i), since the powder wiper needs to be perfectly aligned to the substrate which is particularly difficult if it is only supported from one end. Aligning the angle of the device in a way that its surface is parallel to the surface of the substrate requires much engineering effort, especially when applying layers of less than 50 µm thickness. Additionally, the wiper needs to be well-aligned to the fibre.

Approach (ii) is more straightforward. In this case the blade is supported from both sides, significantly improving the precision of the deposition. To allow free movement between wiper and coated fibre, the cut-out needs to be slightly larger than the diameter of the coated fibre. Therefore the fibre is not only covered with a small powder layer but also powder of significant thickness is accumulated next to the fibre (Figure 5-7, left).

To investigate the feasibility of this approach a series of tests were conducted, where powder layers of 100 µm thickness are homogeneously deposited next to OD 400 µm nickel wire to simulate the coated fibre. A shaped blade with a half spherical cut out of about 500 µm in width is used to deposit the powder. The wire is then joined to the substrate by applying spot-welds along the wire in alternating pattern (Figure 5-7, right). Over the series of tests it was established that the alternating pattern prevents significant wire movement due to induced thermal stresses during the process. The diode laser system is used due to its high output power allowing the melting of powder layers with thicknesses exceeding 400 µm. The beam is focused on the substrate and targeting at the powder, half a spot size away from the wire's surface. In the test series a laser on time for each spot of about 800 µs with a laser output power of 140 W was identified as the most suitable settings. Using these settings the energy input is sufficient to partially melt the wire and substrate and fully melt the powder material. Spot to spot distance along the wire axis is set to 1 mm reducing the thermal heat input into the wire.

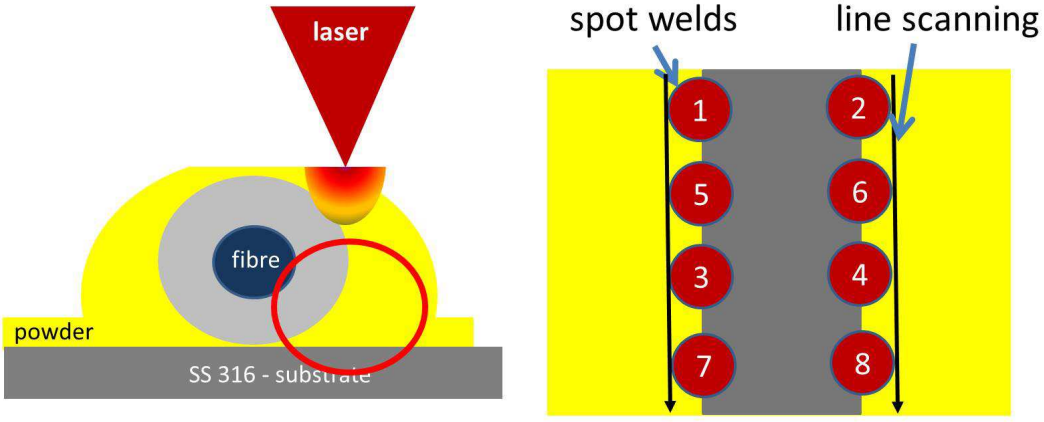

Figure 5-7 Left: Schematic illustration for applying powder with a shaped blade in vicinity of the coated optical fibre. Right: Illustration for the applied pattern of spot welds and line scanning that is used to weld the fibre to the substrate.

Subsequently, the laser spot is linearly scanned along the fibre to generate continuous joints between the spot welds. The best results were achieved with a laser power of 100 W at a processing speed of 50 mm/s and the lines are placed 100 µm further away from the fibre than the spot welds (Figure 5-7 right), in order to minimise the heat energy that is deposited into the fibres. After welding, the wire is still intact and cross-sectioning and etching indicates that the wire is partially molten and intermixing has occurred between wire and added material (Figure 5-8).

However, when substituting the nickel wire with a nickel coated fibre of similar diameter the energy input is too high and the coating partially delaminates from the fibre, due to surface tension (Figure 5-9). This is a serious problem, as the silica fibre would therefore be directly exposed to the heat energy of a subsequent encapsulation process and is most likely to be damaged.

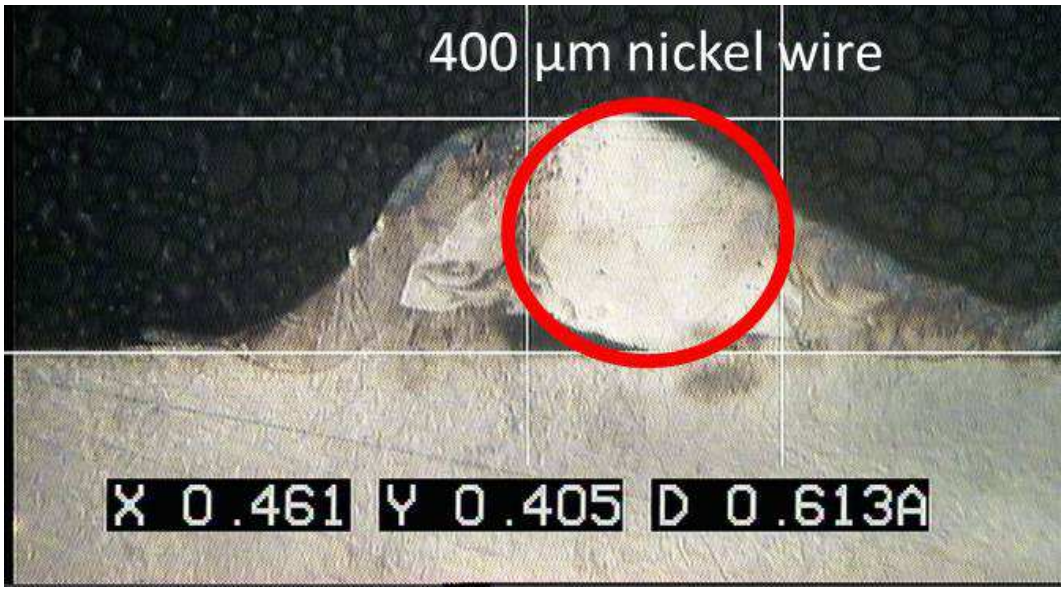

Figure 5-8 Cross-section analysis of nickel wire welded onto SS 316 substrate with the scheme illustrated in Figure 5-7 (right).

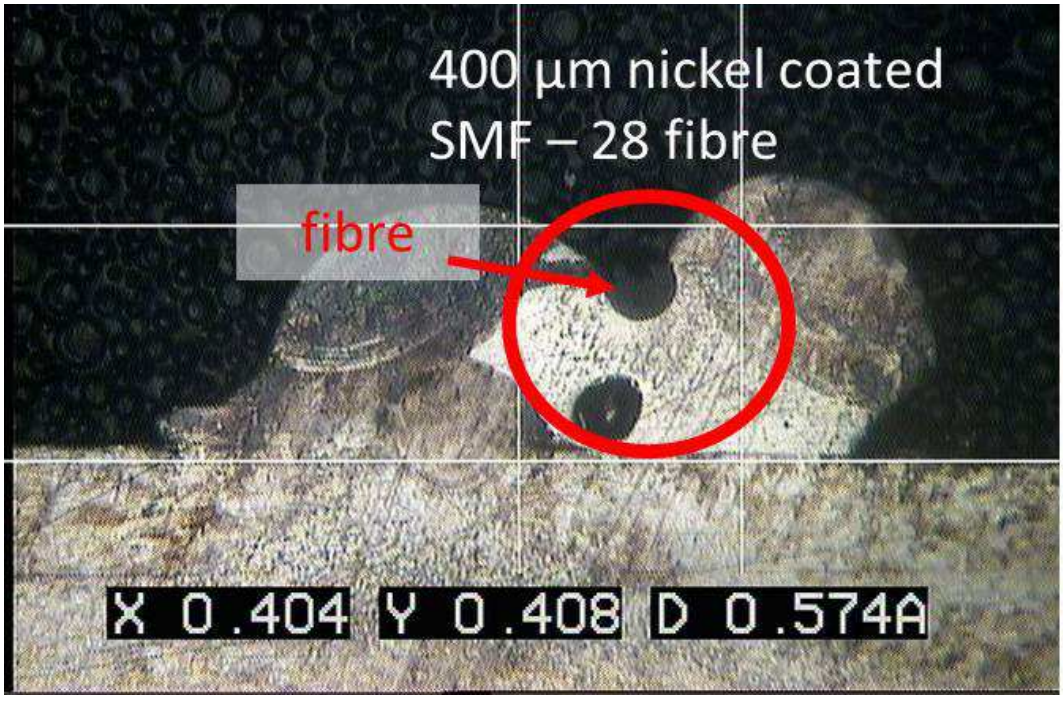

Figure 5-9 Cross-section analysis of nickel coated SMF-28 fibre (OD 400 µm) welded onto SS 316 substrate with the scheme illustrated in Figure 5-7 (right).

Increasing the diameter of the nickel coated fibre to further protect the fibre is not feasible. More laser power would be required to penetrate the powder and melt the substrate therefore increasing the energy input into the fibre further.

Approach (iii) is to cover the fibre completely with a powder layer that is thicker than the optical fibre. To reduce the heat input into the coated fibre, the area of the coated fibre itself is not illuminated for the initial layer. This has the advantage that the melt pool is established remote from the fibre and the heat input into the fibre can be regulated by determining the offset of the scanning pattern with respect to the fibre (Figure 5-10).

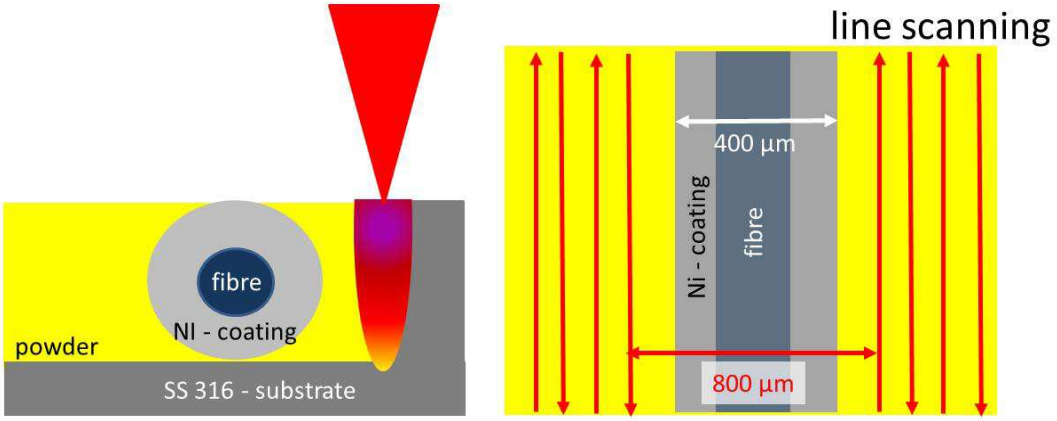

Figure 5-10 Schematic illustration for embedding coated optical fibres with powder layers of similar thickness to the metal coating. For embedment line scanning is conducted parallel to the fibre sparing out the area directly above the coated fibre.

The coated optical fibre with an outer diameter of 400 µm is placed on the substrate and is clamped down on both sides (according to Figure 5-2). Powder is deposited next to the fibre on the plate with a thickness of about 450 µm. The powder layer has to be slightly thicker than the coated fibre to prevent the fibre being touched by the wiper. The diode laser system is used due to its high output power, and parameters for the SLM process are set to 200 W laser power and 50 mm/s feeding speed. The powder is solidified in a scan pattern with lines parallel to the coated fibre. Line to line separation is set to 100 µm in order to build dense components. The offset to the midpoint of the optical fibre is set to 400 µm. A melt line width of about 500 µm should provide partial melting of the fibres coating. After the initial layer has been deposited, the fibre is attached to the substrate indicating a good bond between coating and added material. Subsequently, further powder layers can be applied, fully encapsulating the optical fibre into stainless steel (Figure 5-11).

Following the embedding process, cross-sectional analysis (Figure 5-11) indicates that the fibre is embedded and the structural integrity of the fibre in its coating is preserved. About 75 % of the fibre circumference is bonded to the steel surround. However, the bonding of the added material to the substrate is poor indicating that the laser power is in-sufficient to fuse such a thick layer of powder to the substrate. When injecting light through the fibre no light is transmitted indicating that structural damage must have occurred with the fibre, somewhere along the embedded length. This experiment was conducted several times, also for two times for coated fibres with an slightly larger OD of 450 µm. In none of the total 8 trials light was transmitted through the fibre after the SLM process.

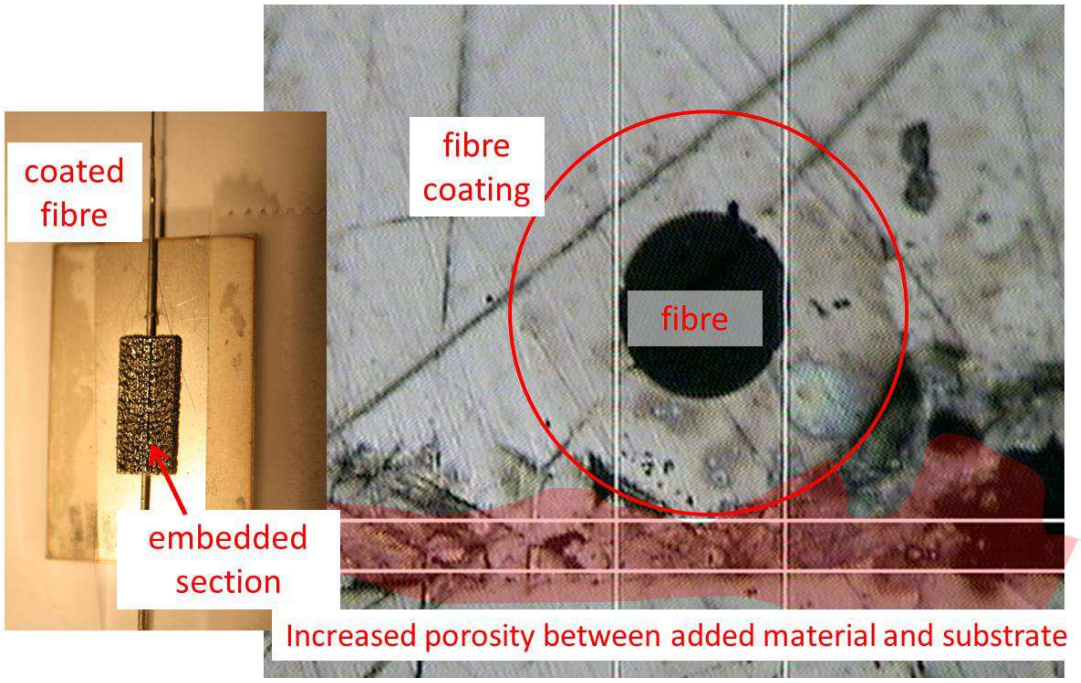

Figure 5-11 Left: Picture of specimen with fibre embedded by applying thick powder layers next to the fibre. Right: Cross-sectional analysis of the embedded fibre indicates good bonding on the sides and top and extremely poor bonding between added material and substrate.

In summary the approaches discussed above all suffer from a requirement for high-energy input to melt a relatively large volume of powder next to the fibre. Hence, significant layer thicknesses are required for thermal protection, adding to the dilemma between minimisation of the embedded sensor component and achieving embedment with the fibre's physical and optical properties prevailed.

5.2.3 Pre-fabricated groove

The high brightness fibre laser system can produce components much more precisely and accurately than the diode laser system due to its small spot size. This allows pre-fabrication of grooves with dimensions approximating the curved coated fibres with outer diameters of a few hundred micrometres. Embedding the fibre into a pre-fabricated groove offers the advantage that the position of the fibre is determined by the groove itself and also the fibre is laterally more constrained, allowing only movements vertically and axially when processing, generally improving the positioning of the fibre (Figure 5-12 left). Coated fibres are then embedded by simply continuing the SLM process (Figure 5-12 right). The disadvantage of this approach is that typically the fibre coating is only attached at the top to the larger steel structure. Since the fibre with its nickel coating is a discontinuity in the material anyway, not contributing to the mechanical strength of the component, only partially bonding around the circumference is considered acceptable, as long the bond is strong enough to transfer strain and temperature changes into the coating and fibre. Furthermore, there is the possibility to apply additional steps to improve the bonding on the sides and underneath of the fibre.

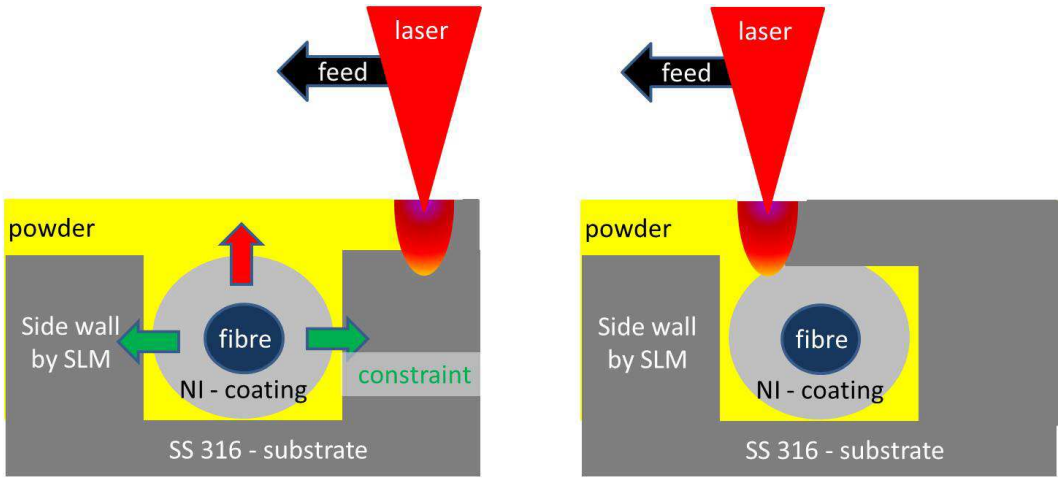

Figure 5-12 Embedding of coated optical in prefabricated U-grooves. U-grooves are built with high brightness fibre laser to fabricate small feature size. The fibre placed in groove is better constrained than the other approaches (left). Fibre is encapsulated by continuing the SLM process (right).

This approach for fibre embedding is divided into three steps. Firstly (Figure 5-13), material is added to stainless steel (SS-316) substrates (50×20×1.2 mm^3) by SLM. A 'U'-shaped groove is produced during the SLM process that is tailored to the dimension of the coated optical fibres. Typically, the width of each single line produced by the

SLM process with the selected parameters is about 80 µm. Therefore, the width of the groove scanned by the scanning program is about 80 µm wider than the diameter of the coated optical fibre.

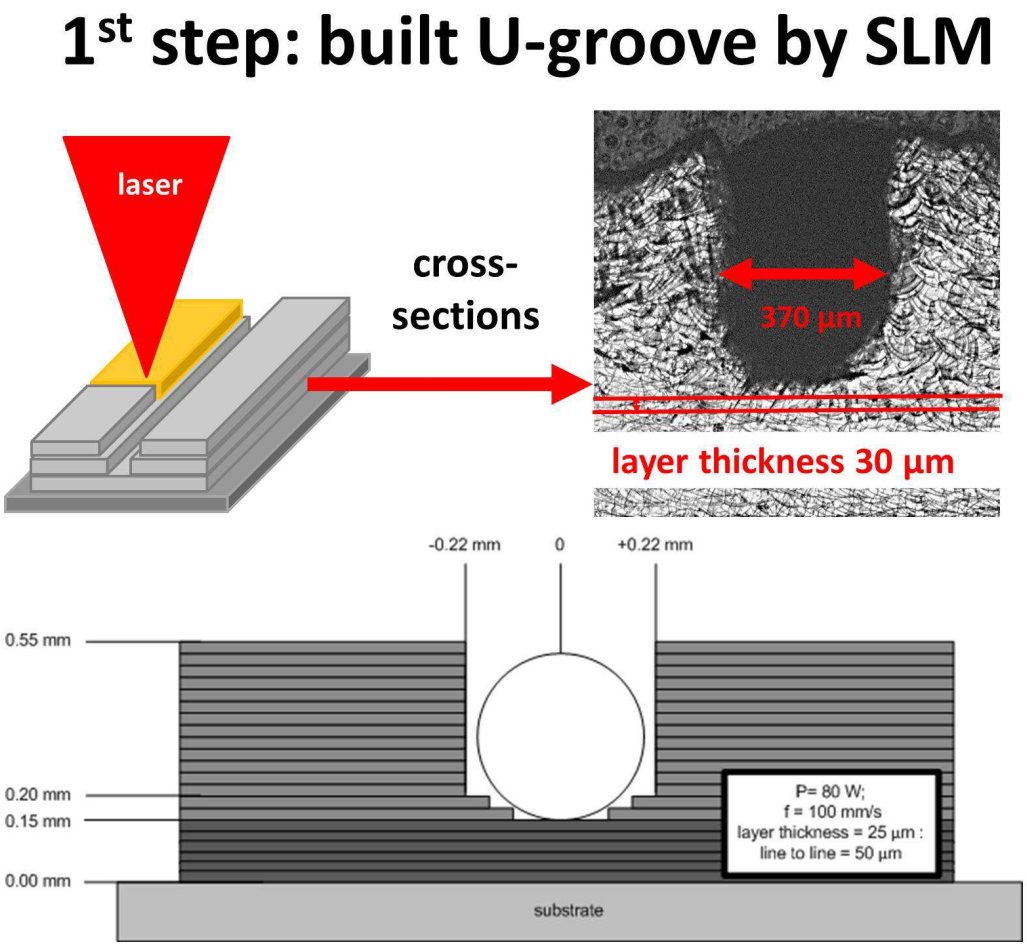

Figure 5-13 First step for embedding an optical fibre in a pre-fabricated groove. Small layer thickness allow the cross-section to match that of the coated fibre.

The parameters of the SLM process have been selected such that for each layer the re-melt depth into the substrate is in excess of 100 % of the topmost layer thickness, eliminating porosity and guaranteeing proper bonding between supporting layers (Chapter 4). The laser is used in a modulated pulsed mode with 50 % DC further minimising the energy requirements. The focal point of the optical system is about 1 mm below the powder bed surface leading to a spot size of about 80 µm on top of the powder bed. This guarantees sufficient intensity not only to melt the powder but also the steel substrate. A feeding speed of 100 $mm*s^{-1}$ and an output power of 80 W are

selected, with reference to the results presented in Chapter 4. The small layer thickness and overall minimisation of the energy input enhances the precision of the U-shaped groove, enabling the manufacture of a groove with a cross-sectional profile matching that of the fibre (cross-section Figure 5-13).

In the second step, metal jacketed fibres are inserted into the groove (Figure 5-14), clamped and a tensile load of 2 N is applied. Following this attachment, the fibres are encapsulated by continuing the SLM process on top of the fibre. In the encapsulation stage, the powder is melted in a controlled manner using a laser beam that is scanned perpendicular to the direction of the fibre. In this way, the powder bonds to itself, forming a homogenous solid layer and it also bonds to the substrate and the nickel coated fibre. Scanning is conducted towards the unclamped end of the fibre allowing the guide the expanding fibre by the applied tensile force (2N). Further applications of powder layers and laser processing allow fabricating solid metal component with layer-by-layer control of features.

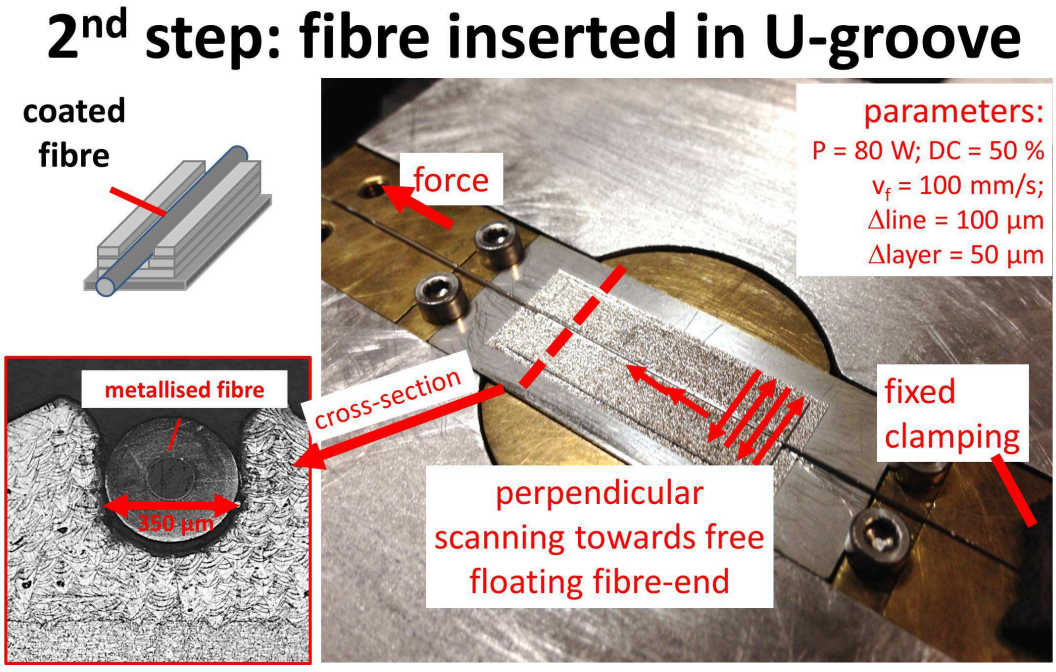

Figure 5-14 Second step of the embedding process. The fibre is placed in the groove and powder is applied on top of the fibre. The fibre is encapsulated by using parameters similar to those of the SLM process.

The laser properties must be carefully selected to ensure that the powder layer is melted without damaging the coated optical fibres. A cross section of a fibre encapsulated in this manner is shown in Figure 5-15. In this example about 30 % of the circumference of the nickel coated fibre is well bonded to the surrounding steel environment. Imperfections in encapsulation remain at the sides and underneath-side of the coated fibre. Two mechanisms cause this gap, surface roughness of the groove (R_a ~ 6 µm; R_p ~ 40 µm) and debris of the SLM process remaining in the groove.

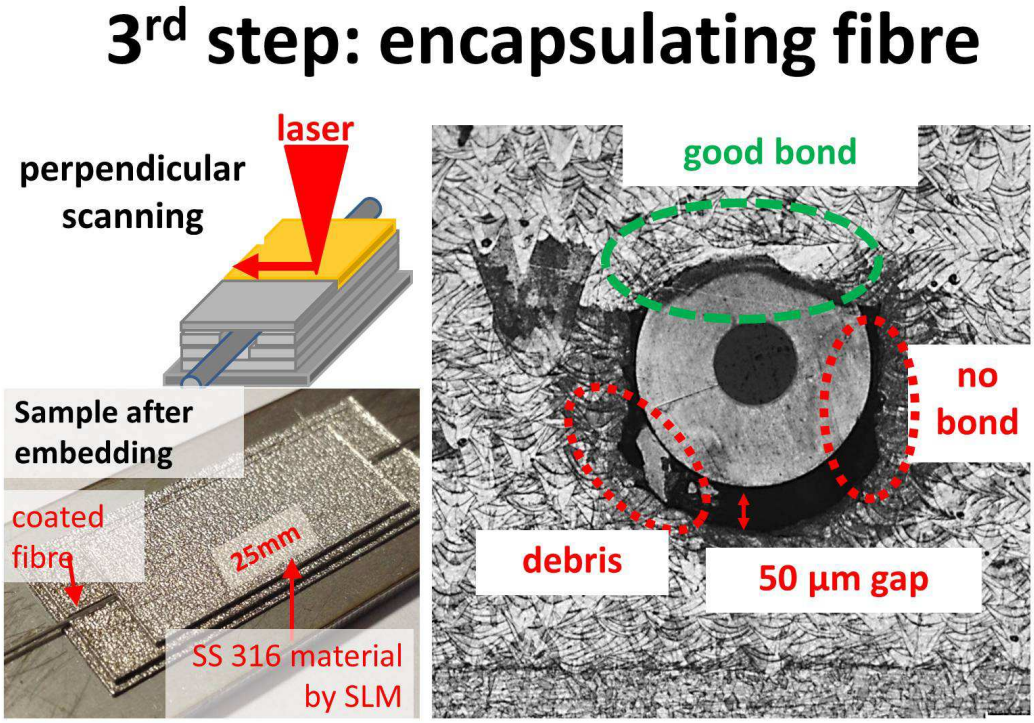

Figure 5-15 Third step of the encapsulation process, continuing the SLM process on top of the fibre. Cross-sectional analysis shows that coated fibres are well bonded on the top but no bonding on the side and underneath.

Embedding optical fibres in pre-fabricated grooves has several advantages. The grooves themselves can be tailored with respect to the dimensions of the coated optical fibres without altering the parameters of the SLM process. By deploying the fibre in the groove the position of the fibre is precisely (< 10 µm) determined and also during the encapsulation process the fibre is constrained by the side walls.

5.2.4 Best practice for embedment

Sections 5.2.1 to 5.2.3 describe the investigation of concepts to reliably embed optical fibres with small coating thicknesses into SS 316 components. The final approach described, in which the fibre is placed in pre-fabricated grooves, was found to be the most reliable and repeatable. In the other approaches, where fibres were clamped onto the substrate and powder material is molten next to the fibre, the fibres can significantly move due to thermal stresses. Also, when melting powder layers of similar thicknesses to the fibre itself, too much thermal energy is transferred into the fibre causing damage.

Deploying the fibre in pre-fabricated grooves meanwhile locates the fibre in respect to the substrate, within the accuracy of the SLM system (~10 µm in our case). As a result, the fibre can only move upwards during encapsulation. No prior attachment of the fibre to the substrate is necessary due to the constraints given by the groove itself. Furthermore, the laser power required for encapsulation is significantly reduced, since the powder layer thickness for encapsulating the fibre is independent of the fibre diameter.

5.3 Damage threshold embedding coated fibres in pre-fabricated grooves

In this section the SLM parameters for encapsulating the coated fibre placed in U-grooves are in investigated. However, the process parameters laser power (80 W), feeding speed (100 $mm*s^{-1}$) and duty cycle 50 % (100 µs laser on/off times) are unchanged to ensure that continuous lines are molten on to the substrate material and that the energy is sufficient to partially re-melt previously added material or the coating of the fibre underneath. Fibre transmission is monitored for a range of different parameters, during the embedding process.

By changing the layer thickness, the line to line spacing and scanning direction during the fibre's encapsulation, it is possible to significantly vary the energy input into the substrate and therefore influence the thermal stresses induced into the optical fibre underneath while maintaining the ability to fabricate parts which are free of porosity. For the first encapsulation layer, a wider line-to-line spacing can be chosen to reduce the actual process time and therefore also reduce fibre heating (Figure 5-16). By increasing the line-to-line spacing to 80 µm, dense components with very limited amount of macro-porosity can be fabricated while significantly reducing the process

time by about 50 % compared to the standard SLM parameters. In addition, increasing the layer thickness can help to shield the fibre from the deposited laser energy.

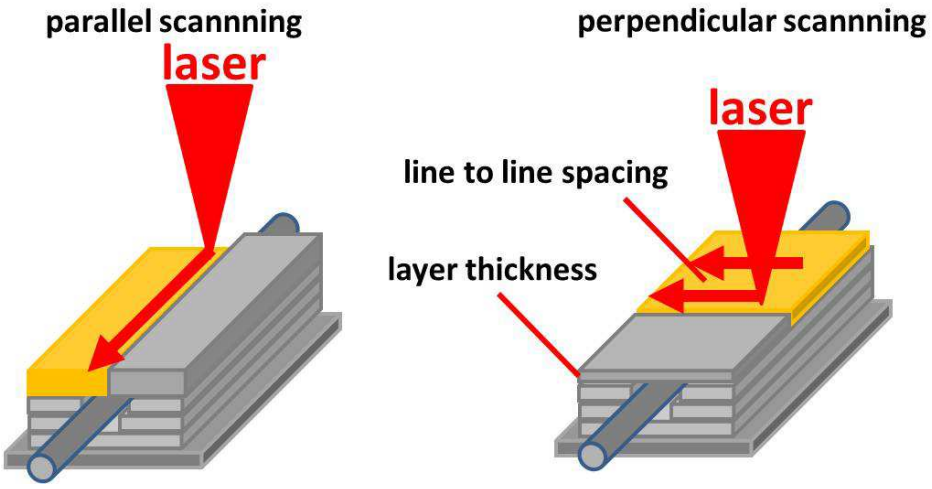

Figure 5-16 For the third step of the encapsulation process three parameters can be varied, line-to line spacing, layer thickness and the scanning direction (parallel and perpendicular). Other parameters like scanning speed or laser power are fixed to at least ensure that continuous lines are molten.

5.3.1 Layer thickness and scanning strategy

To investigate the influence of different parameters for the encapsulation process four example sets of parameters were identified and tested (Table 5-1). In all cases, the fibres were first of all RF sputtered with chromium (1 hr; 200 W) and subsequently electroplated with nickel to coating diameters of about 350 µm. U grooves were built according to the scheme illustrated in Figure 5-17 with steps of 25 µm precision to approximate the curvature of the coated fibre. The thickness of the first encapsulation layer is chosen to be slightly larger to ensure that the fibre is fully covered with powder since the fibre might not sit perfectly flat on the bottom of the groove.

case [#]	description [-]	layer thickness [um]				line to line [um]				scan direction [-]			
		1	2	3	4	1	2	3	4	1	2	3	4
A	SLM parameters from chapter 4	50	25	25	25	50	50	50	50	ppf	ppf	ppf	par
B	lower energy input - larger layer thickness	100	50	25	25	50	50	50	50	ppf	ppf	ppf	par
C	low energy input - wider line to line spacing	50	25	25	25	100	70	50	50	ppf	ppf	ppf	par
D	very low energy input	100	50	25	25	100	70	50	50	ppf	ppf	ppf	rpp

ppf = perpendicular towards free floating end
par = parallel to fibre
rpp = perpendicular scanning -reversed direction

Table 5-1 Set of parameters which are investigated for applying the encapsulation layer on a fibre lying in a U-shaped groove.

In case A, a coated optical fibre placed in the U-groove is encapsulated by simply continuing the SLM process using standard parameters as developed in Chapter 4.3.1. In case B the thermal input to the fibre is reduced by increasing the layer thickness whereas this is done in case C by using a wider line-to-line spacing. In both cases the relevant parameter is changed back to the value of the standard SLM process in a series of steps. Case D is the case with the lowest energy input, where the initial parameters have the largest line-to-line distance and layer thickness. In all cases the first three layers are applied by scanning perpendicular to the fibre towards unclamped end. In preliminary trials it was found that parallel scanning along the fibre deposits too much thermal energy into the fibre causing it to break.

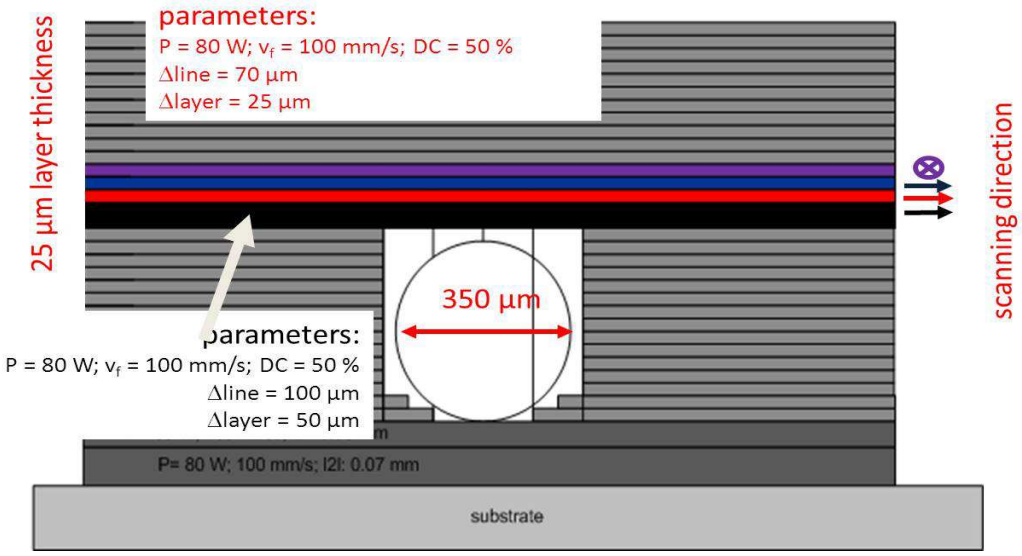

Figure 5-17 Example illustration of the process strategy to encapsulate coated optical fibres deployed in U-groove shaped features.

The fibre transmission is monitored by splicing APC connectors to both ends of the optical fibre and connecting one side to a broadband source (centre wavelength: 1550 nm) and the other side to an optical spectrum analyser (OSA). The length of the embedded section is about 3 cm. A picture of the experimental setup is shown in Figure 5-18.

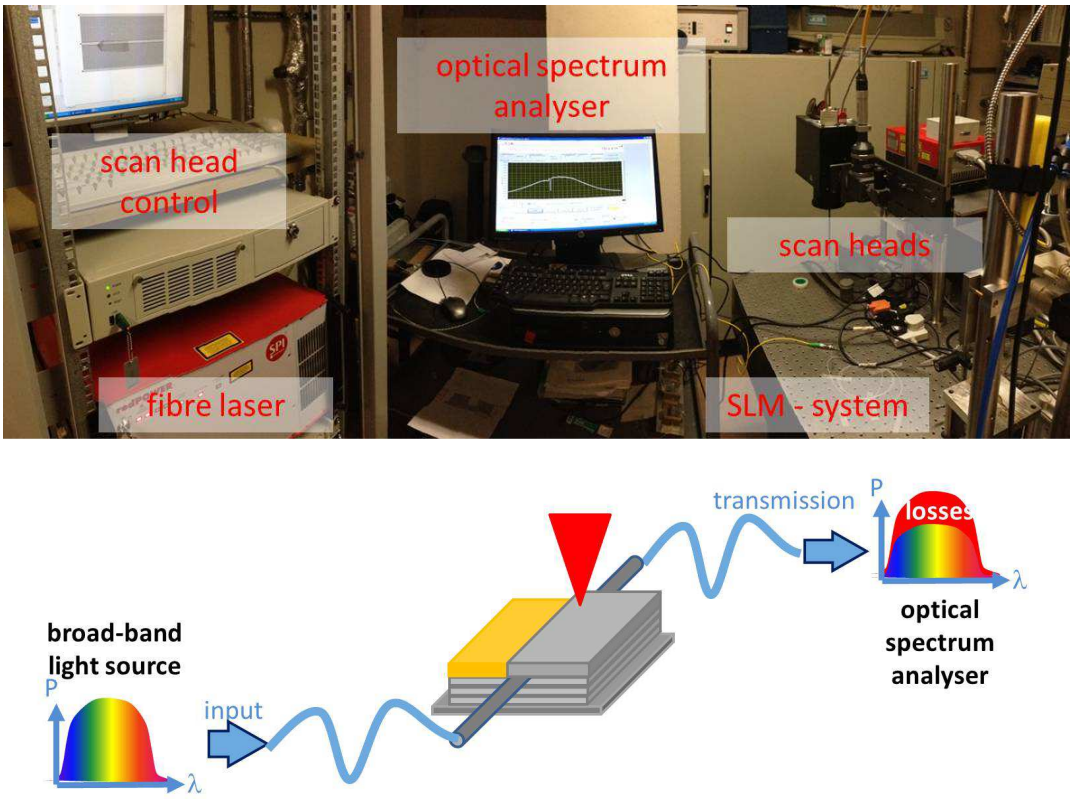

Figure 5-18 Photo and schematic illustration of the experimental setup for measuring transmission through the optical fibre when encapsulating fibres by SLM.

For selected cases from Table 5-1, the fibre transmission (intensity measured at a wavelength of 1550 nm) for the first 4 layers of the encapsulation process is displayed in Figure 5-19. Using standard SLM parameters for encapsulation (A) a significant drop in transmission (75 %) is observed. Varying either powder layer thickness (B) or line-to-line spacing (C) mitigates these losses significantly (only 30 – 40 % loss). Only small losses (~10 %) occur when increasing both layer thickness and line-to-line spacing (D). Typically, as displayed in Figure 5-19, for any encapsulation strategy, the majority of losses in transmission occur for the first 3 layers. As subsequent layers are applied, the transmission characteristics changes only incrementally, as expected since the re-melt depth of the SLM process which is typically not more than 50 µm into the substrate.

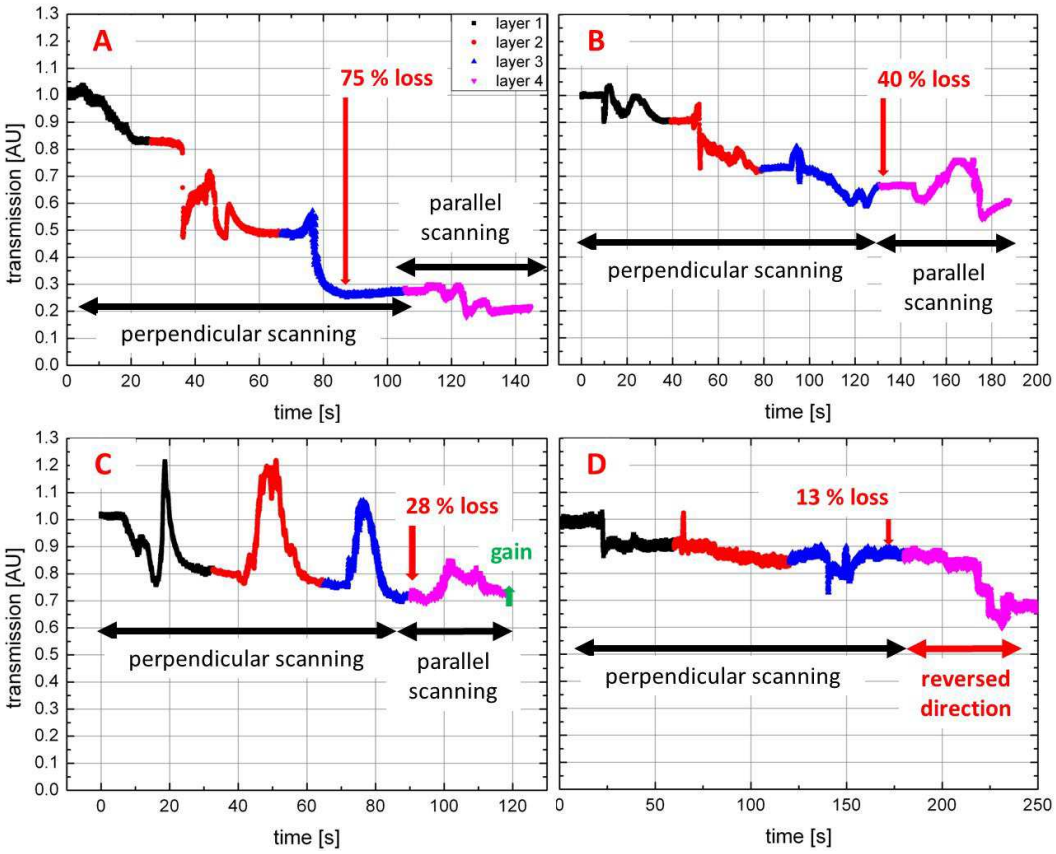

Figure 5-19 Fibre transmission (measured at 1550 nm) for the first four layers when encapsulating optical fibres according to the cases displayed in Table 5-1.

In case A the largest losses in transmission occur, therefore this case is the most interesting and more thoroughly discussed here. The general trend should be applicable to the other cases too. When applying the first layer in case A, the intensity of the transmitted light gradually drops throughout the process by about 18 %, despite a slight increase by about 3 % at the beginning of the process. A magnified version of the measured transmission for the first two layers of case #A is displayed in Figure 5-20 (top). This is quite a complex trace, and the most likely explanations for the changes with time are proposed below.

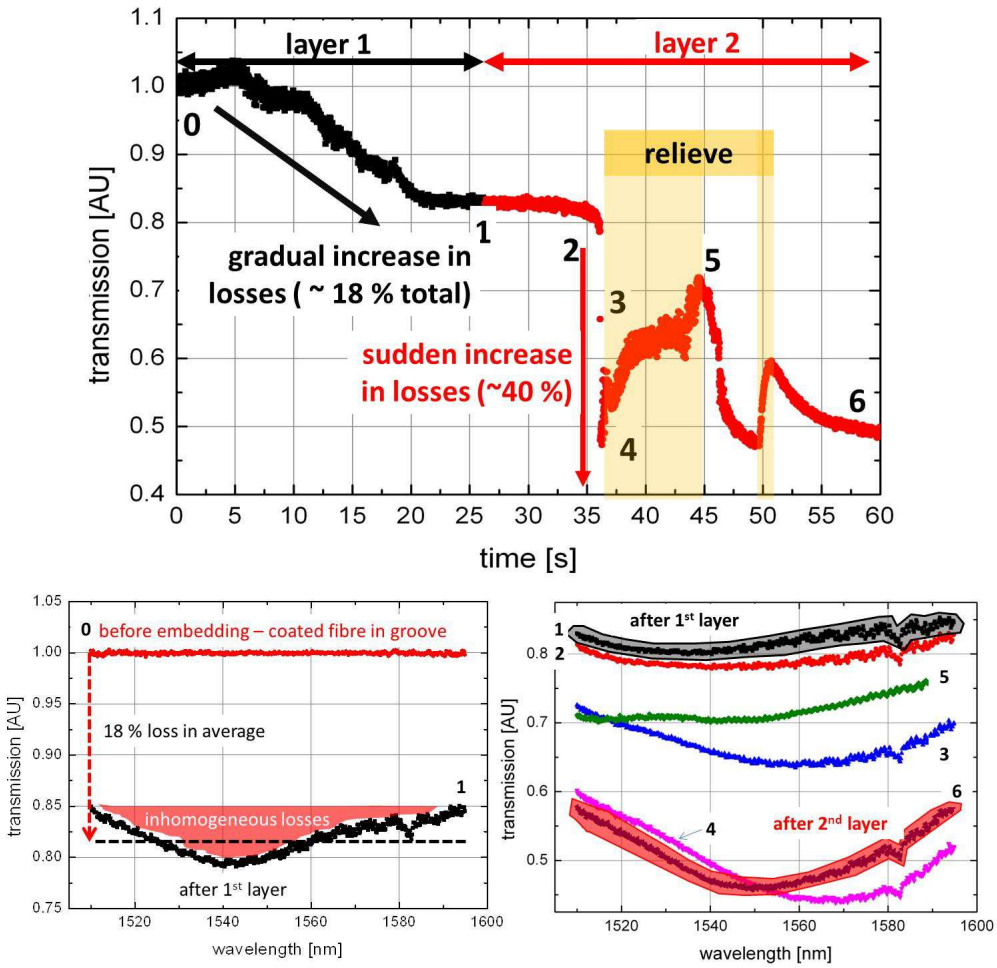

Figure 5-20 Top: Transmission measurements for the first two layers of case #A. Bottom: Normalised transmission spectra for selected times.

One possible explanation for the increase in transmission at the beginning of the process (Figure 5-20; top; ~5 s) is reduced micro-bending of the fibre due to thermal expansion of the U-groove. Before encapsulation, the fibre with coating is squeezed into the U-groove. The groove width is tailored to tightly match the coated fibres outer diameter. The U-groove however, has a comparatively rough surface roughness (R_p ~ 40 µm) and its peaks will induce stresses into the nickel coating (Figure 5-21). These stresses will be transferred into the fibre and cause losses in transmission due to micro-bending. During the process the U-groove gradually becomes wider due to thermal expansion caused by the heat energy provided by the laser and this expansion gradually releases the stresses caused by the surface roughness and hence the losses due to micro-bending.

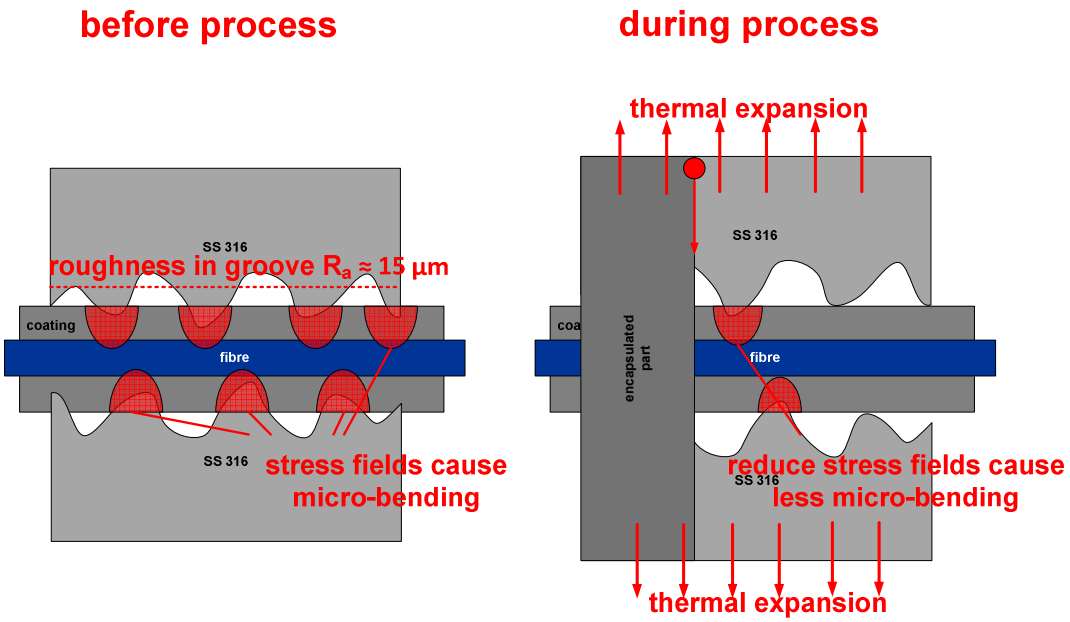

Figure 5-21 Schematic illustration for the occurrence of micro-bending for the non encapsulated fibre placed in U-groove (view from above). When applying the first layer the groove is expanding due to the heat induced by the laser counteracting the losses due micro-bending.

However, at some point during the application of the first layer, the increase in transmission due to less micro-bending caused by the groove's side wall roughness is overcome by the micro-bending induced by the stresses on top of the fibre due to the SLM process (Figure 5-22). The SLM process incrementally induces stress fields on top of the fibre with a periodicity equalling the line-to-line spacing of the scanning strategy.

Figure 5-20 (bottom) displays the normalised transmission spectra at times of interest for the first two layers of case A. After the first layer is applied (time #1), not only was the average intensity of the transmission dropped by 18 %, also the losses are in-homogenously distributed over the spectral range of the measured spectrum. The in-homogenous distribution of losses is attributed to a loss band due to micro-bending which is super-imposed onto the fibre's transmission characteristics. The loss band is highly dependent on the periodicity of the stress field caused by the scanning strategy. The peak of the loss band is centred on a wavelength of about 1540 nm. Sakata [28] reports similar loss characteristics in single-mode fibres where stress fields with periodicities in the range of 50 – 100 µm cause micro-bends along the fibre.

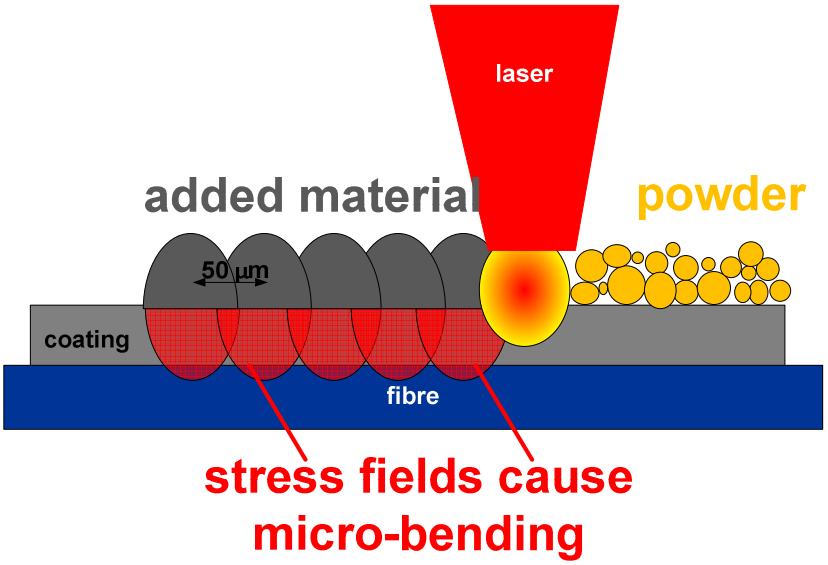

Figure 5-22 Schematic illustration for stress fields induced by SLM leading to losses in transmission due to micro-bending (cross-sectional view).

When applying the second layer, initially the intensity of the transmission continues to gradually drop until time #2. Within 30 ms (measurements #2; #3; #4) losses in transmission (worth 40 % of the initial transmission) occur. Spectra recorded at these times indicate that until time #2 only the intensity dropped with no changes in the imposed loss-band. Between measurements #3 and #4 an instantaneous drop occurs. The spectrum measured at time #3, apart from the average losses, shows increased losses centred around 1560 nm and at time #4 these losses are even more defined centred around 1565 nm.

The sudden drop in transmission is only explainable by structural damage of the fibre. The penetration depth of the SLM process might be sufficient to partially re-melt the first layer but the fibre is solidly embedded over a length of 3 cm and the melt pool width is less than 100 µm. Therefore, when applying the second layer, the fibre with its coating is solidly attached to the metal component, at all times. During the SLM process of the second layer, the specimen is expanding and the fibre is additionally strained by the high thermal expansion coefficient of steel, 30× that of the fibre. This axial stress in combination with further lateral stresses induced by the SLM process leads to cracks and therefore eventually to sudden losses in transmission.

Following the sudden drop the induced losses are gradually relieved until a maximum is reached at time #5. Then, the measured spectrum is more homogenous, indicating that the expanding steel causes less micro-bending of the fibre. The average transmission rises by 75 % compared to time (#4) just after the sudden drop occurred. The increase in fibre transmission is within the same magnitude of the incremental losses (excluding the sudden drop at times #2-4) caused by the process so far. These losses are eased by the rapid thermal expansion of the metal due to further energy input of the SLM process. The losses which occurred during the sudden drop (cracking) are irreversible. Following this both mechanism increased losses due to further applied stresses by the SLM process and easing stresses by the increased temperature results in alternately increasing and decreasing losses. After the end of the process (@50s), the transmission exponentially plateaus, since the energy input of the SLM process has stopped. The specimen gradually cools down, shrinks with the thermal expansion coefficient of steel and leads to increased losses due to increased micro-bending.

In cases B and D larger layer thicknesses of about 100 µm are applied on top of the fibre for the first encapsulating layer. This concept seems to sufficiently dissipate the heat induced by the SLM process, and hence reduce transmission loses. However, increased porosity is observed in vicinity of the encapsulating layers (Figure 5-23). In case B, a large layer thickness is chosen while maintaining a narrow line-to-line spacing. Cross-sectional analyses disclose that a dense layer, apart from some minor occurrence of porosity is added to the fibre. However, no proper bond between fibre and added material is formed indicating that the layer thickness is too thick and that the process energy was in-sufficient to partially melt the coating.

In case D, not only is a larger layer thickness chosen but also a wider line-to-line spacing. This causes a significant increase in porosity in the vicinity of the encapsulation plane. In both cases B and D, optical fibres were embedded, however the poor bonding between fibre coating and metal surround and also the occurrence of porosity are of concern.

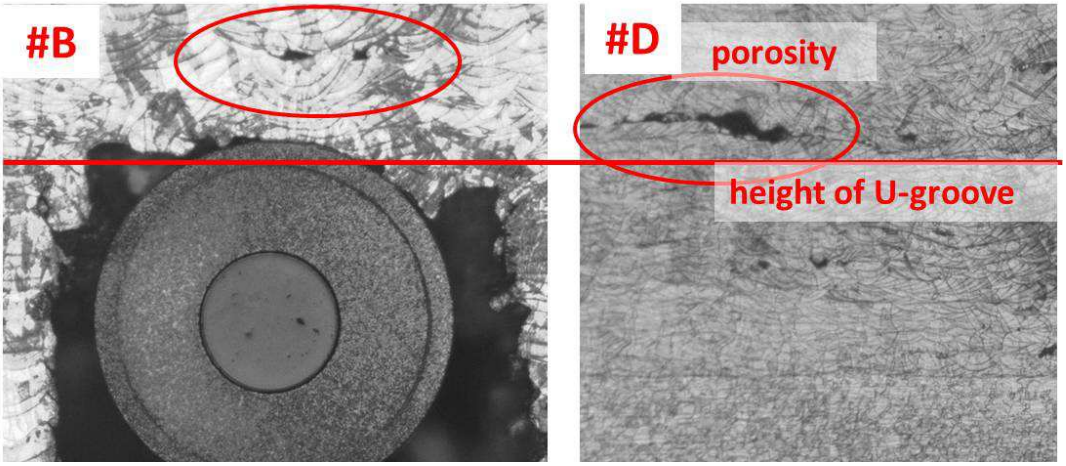

Figure 5-23 Cross-section analysis for fibres embedded according to the approach for case #B (left) and case #D (right) from Table 5-1.

More ideal is the approach applied in case C (Figure 5-24). The layer thickness for encapsulating the coated optical fibre is maintained constant, whilst ensuring that before encapsulation the fibre is fully covered with powder material. Line-to-line spacing was increased to 80 µm. The wider spacing seems to induce less localised stresses into the fibre. In particular this case, the fitting between fibre diameter and U-groove dimension is extremely tight (Figure 5-25) leading to significant losses due to micro-bending before the process. During the process, thermal expansion of the U-groove results in significant spikes in the fibre transmission.

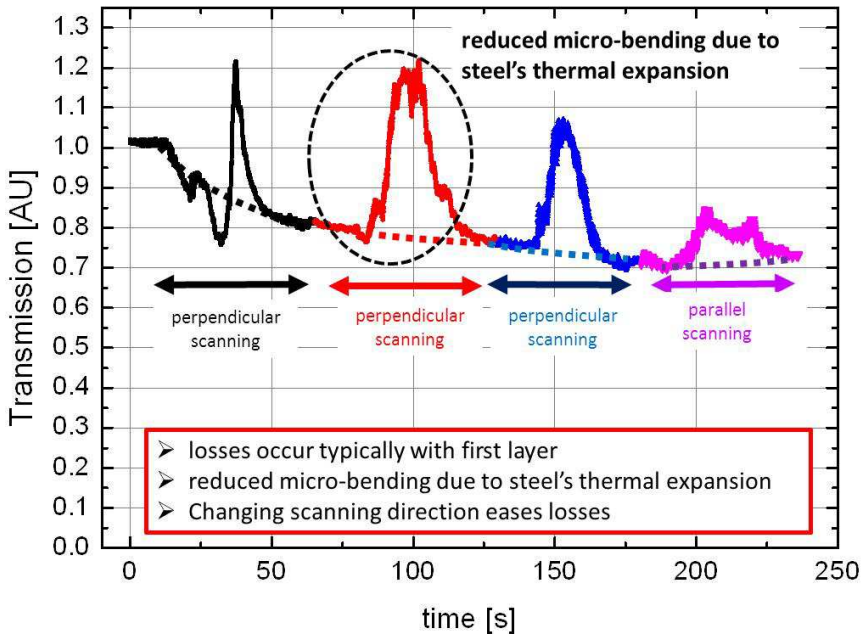

Figure 5-24 Transmitted intensity for case C (Table 5-1). Increased transmission due to reduced micro-bending. Only minor losses occur after applying the first layer.

Cross-sectional analysis of coated fibres embedded according to the recipe in C are displayed in Figure 5-25. The penetration depth of the melt pool is sufficient enough to partially melt the fibre coating by about 25 µm. On the top of the coating, etching demonstrates that both the nickel and steel, are properly intermixed, indicating a good bond capable of transferring strain and temperature changes induced into the steel component. This is backed up by SEM and EDX analysis showing movement of chromium from the steel into the nickel coating.

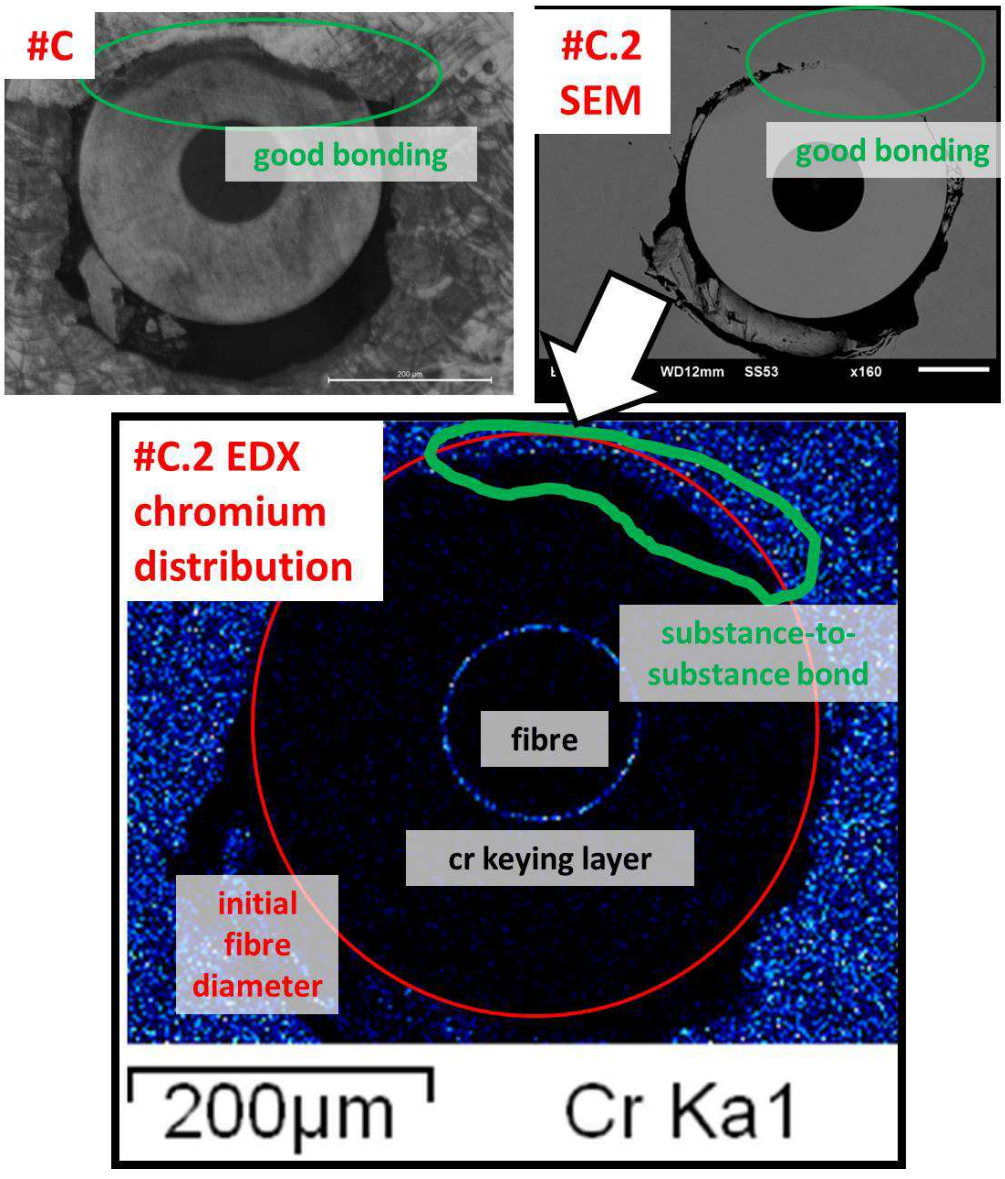

Figure 5-25 Cross-section analysis (top left), SEM analyses (top right) and EDX analyses (bottom) for fibres embedded according to the recipes for case C.

Embedding according to case C provides the best result in terms of combination of bond strength and low induced loss. The resulting bond between the fibre and coating is better than cases where the layer thickness is substantially increased. The increased line-to-line spacing significantly reduces the thermal load into the fibre counteracting losses due to micro-bending while maintaining the ability to fabricate dense components.

5.3.2 Coating thickness

A further variable of the process, the thickness of the nickel coating, is of particular interest since one objective of this work is minimisation of the coated fibre.

Any material between fibre and melt pool tends to protect the fibre from stresses induced by the SLM process. Therefore larger coating thicknesses reduce micro-bending that leads to losses in embedded fibres. The strategy for encapsulating coated fibres in pre-fabricated grooves is easily adjusted for various coating thicknesses by applying an SLM strategy that tailors the dimensions of the fabricated groove to approximate the width and underside of the coated optical fibre (Figure 5-26).

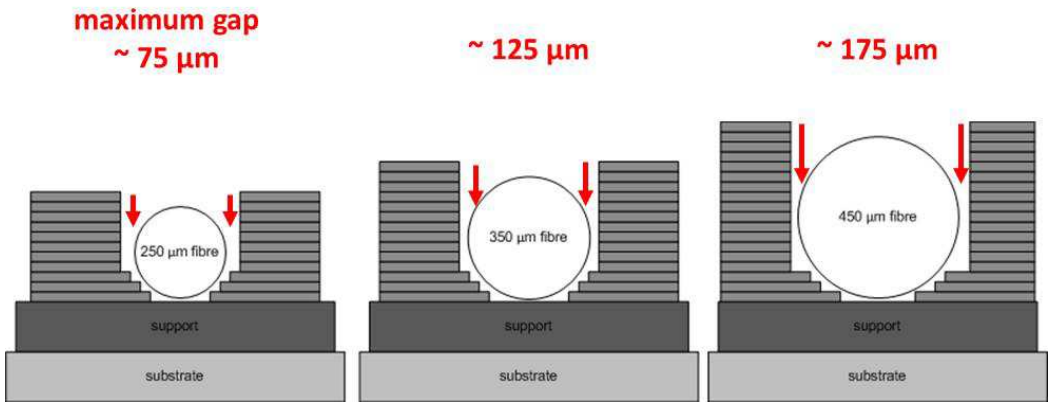

Figure 5-26 Schematic illustration for adjusting the process for fibre embedment for various coating thicknesses. The thicker the fibre coating, the more difficulties arise in achieving a proper bonding along the coated fibres circumference.

Nickel coated fibres with different coating thicknesses are embedded according to the recipe described in the previous section (case C). Groove dimensions are tailored according to the outer dimensions of the coated optical fibres. In this manner, nickel coated optical SMF-28 fibres are embedded while preserving their mechanical integrity

and optical properties. Figure 5-27 displays transmission losses (measured at 1550 nm) for nickel coated SMF-28 fibres for various coating thicknesses after completion of the embedding process. Typically, for outer diameters less than 335 µm, successful embedding could not be achieved, with fibre transmission dropping to zero in all these cases. For outer diameters in the range of 350 to 500 µm, losses are in the range of 60 % down to 10 %, lower for larger coating thicknesses (for an embedding length of 3 cm). For nickel coated fibres with an outer diameter >500 µm losses are below 10 %.

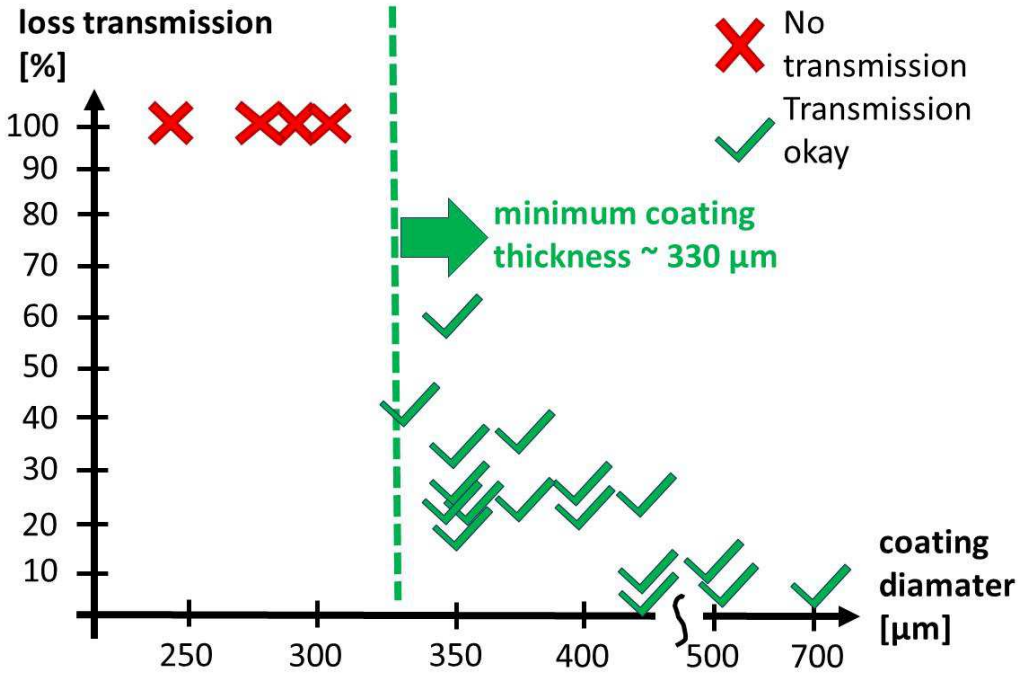

Figure 5-27 Summary of transmission losses for embedded fibres as a function of coating thickness. Coating thickness of more than 350 µm are required for successful embedment of optical fibre with the approach developed above.

Analysis of samples with outer diameter of less than 350 µm suggests that the heat input during the encapsulation process causes cracking or complete melting and delamination of the coating. Locally induced stresses, due to the heat input of SLM process, causes in-homogenously distributed stress levels along the coating, leading to cracks in the coatings. Also, when the heating exceeds certain thresholds, the majority of the coating instantaneously melts, leading to contraction of the molten coating material most likely due to surface tensions (Figure 5-28 bottom). This ultimately leads to exposure of the optical fibre to the incident laser radiation of the SLM process and hence damage.

Outer diameters of at least 350 µm are therefore considered essential to allow successful embedment of SMF-28 (OD 125 µm) optical fibres with the chosen SLM parameters.

With larger outer diameters however, the difficulties arise are associated with bonding issues at the top of the fibre. The larger diameter means that there are larger gaps between the fibre coating and the plane of the first encapsulation layer (Figure 5-26). The penetration depth in powder with the given SLM parameters is about 100 µm. Two possible solutions exist to tackle this issue. One way is to change the energy input of the SLM process to provide larger penetration depths in these areas of concern. However, this causes the dilemma that increasing energy input of the SLM process reduces the advantages of larger coating thicknesses to buffer the fibre from the heat of the SLM process.

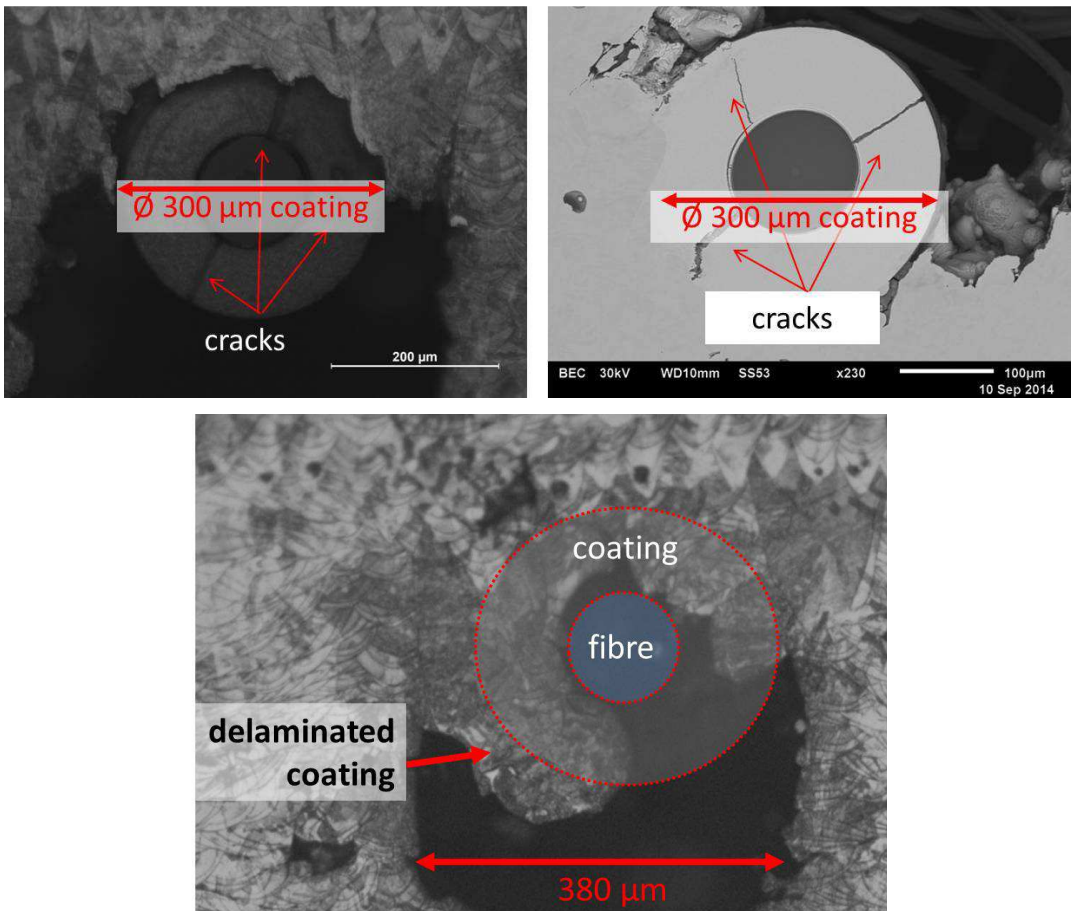

Figure 5-28 Cross-section analysis for embedded fibres with small coating thicknesses. With outer diameters of less than 350 µm the coating is too thin and either cracks (top) or completely delaminates from the fibre (bottom).

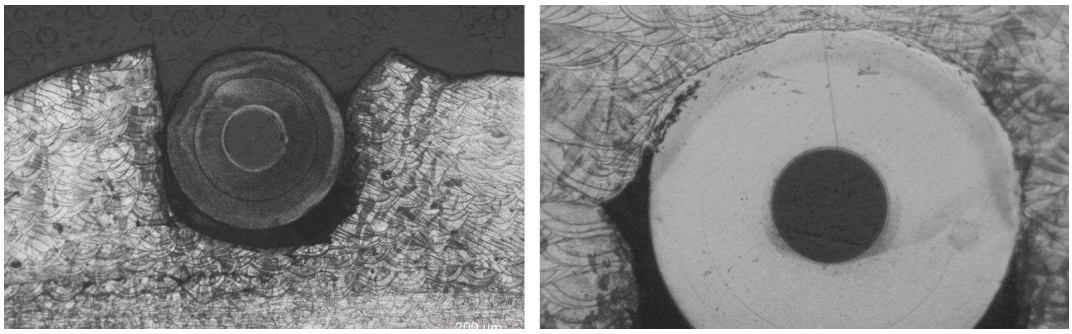

Figure 5-29 Cross-section analysis of coated fibre (OD 450 µm) placed in U-groove. Height of U-groove was reduced by 50 µm to minimise amount of powder material between fibre and U-groove resulting bonding over about 40 % of the fibres upper circumference.

Another simpler technique is to reduce the height of the side-walls of the groove, according to the coating thickness and penetration depth of the SLM process. In Figure 5-29 (left) an outer diameter 450 µm coated fibre is displayed, sitting in a U-shaped-groove that was designed in a way that the side walls are 50 µm below the top of the coated optical fibre sitting in the groove. In reality the edge of the SLM fabricated U-groove is typically slightly higher due to powder consolidation for initial line scans. When the encapsulation process is continued proper bonding between fibre and stainless steel can be observed over an extended area of the fibre circumference. Etch analysis of the cross-sectional sample suggests that the coating is bonded to the SLM structure over approximately 40 % of the coatings circumference. This approach has the advantage that the standard SLM parameters are used and furthermore providing a better bonding over a wider area between fibre coating and metal surround.

5.4 Improved Embedding

In the previous sections of this chapter, the approach of embedding optical fibres in pre-fabricated U-grooves was identified to deliver most reliable and repeatable results. The disadvantage of this approach is that typically only bonding between fibre coating and metal surround is achieved on the top of the optical fibre (Figure 5-30).

In the following section two possible ways for improved embedding are investigated. To achieve better bonding on the sides of the coated fibre in the U-groove, deep penetration laser welding can be applied after the first few layers of material have been

applied on top of the fibre. The bonding underneath the fibre can be improved by deploying a layer of easily diffusing low melting temperature "met-glass" underneath the fibre.

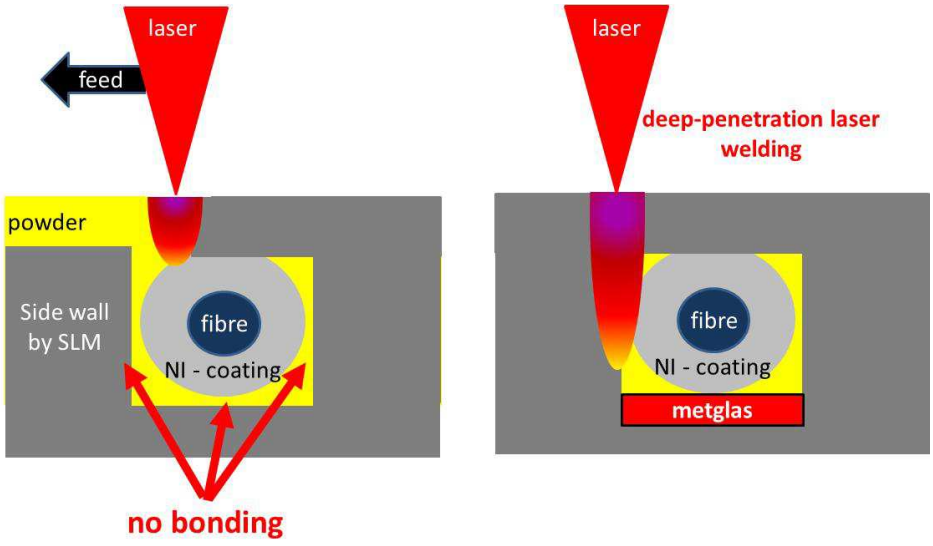

Figure 5-30 Schematic illustration for strategies to improve bonding for coated fibres embedded in U-shaped grooves.

5.4.1 Additional "deep-penetration" welding

To improve the overall bonding between the fibre coating and the adjusted steel walls, deep penetration laser welding is a feasible approach. It could be used to re-melt the edges of the coated fibre and groove, and fuse them together after the coated fibre was encapsulated. Coated optical fibres (OD 350 µm) are encapsulated in U-shaped grooves according to the recipe described above. After applying 4 powder layers on top of the fibre (~100 µm material) deep penetration laser welds are applied in a direction parallel to the fibre (Figure 5-31), whilst monitoring fibre transmission. The parameters of the deep penetration welds are chosen according to the results in (Chapter 4). The focus of the fibre laser system is positioned on the top of the surface to achieve the deepest possible penetration. Laser power is set to 100 W at a full duty cycle. Feed speed is set at 75 $mm*s^{-1}$ to minimise the lateral heat affected zone whilst maintaining a high penetration depth.

With these parameters the weld seam typically reaches a width of about 100 µm and a penetration depth of 250 to 350 µm. Various weld seams are positioned parallel to the

optical fibre in distances of 150, 200 and 300 µm. An example cross-sectional analysis is shown in Figure 5-32.

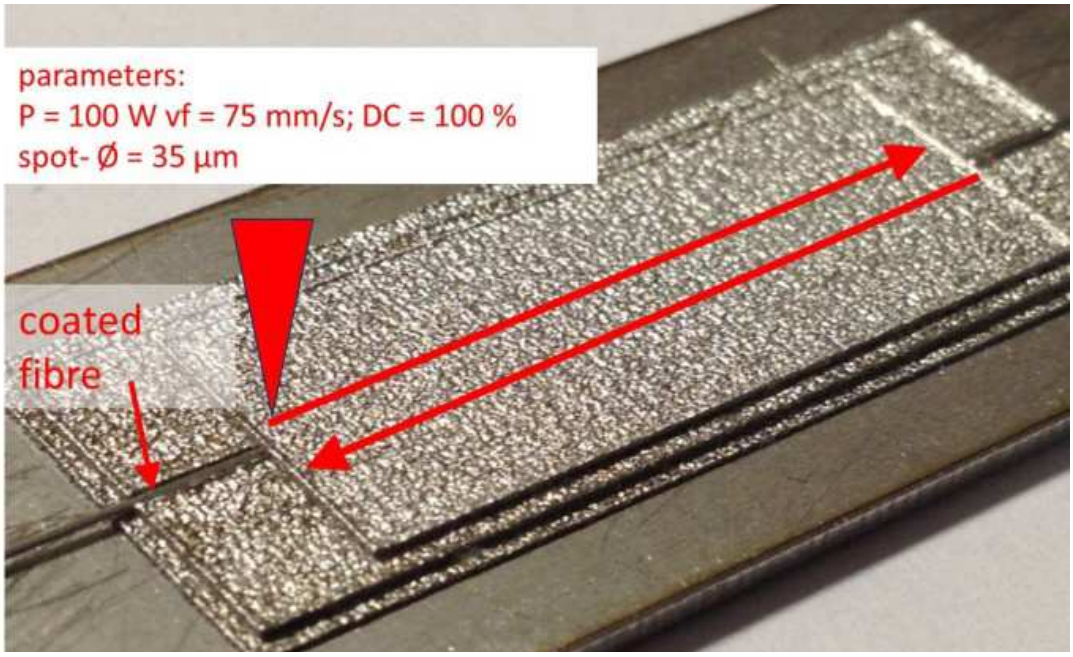

Figure 5-31 Schematic illustration for applying deep-penetration weld seems to improve bonding between coated fibre and side-wall of U-grooves.

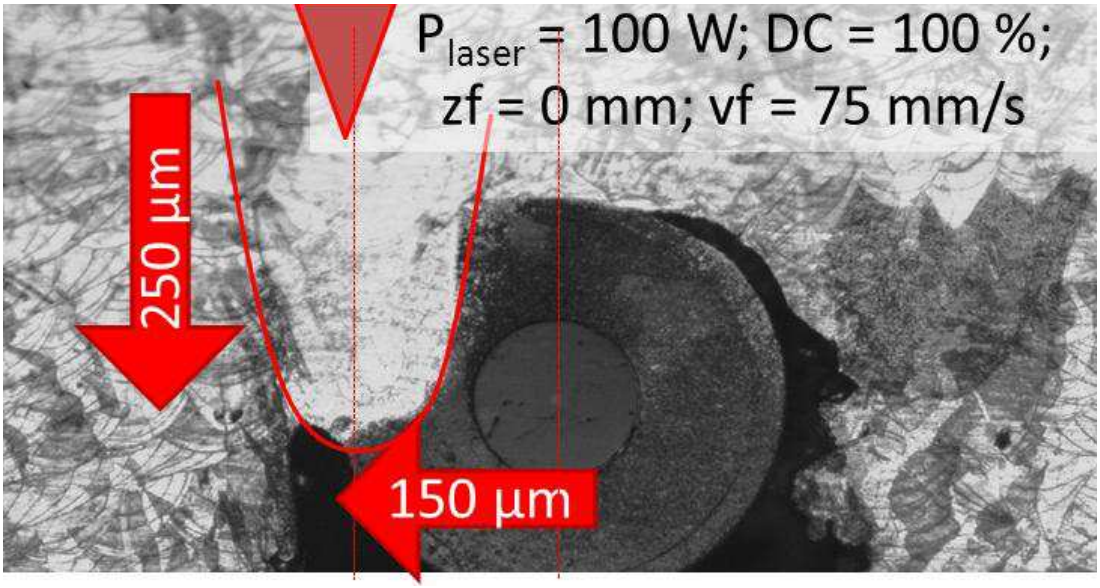

Figure 5-32 Cross-section analysis of the embedded fibre with the weld seam placed 150 um apart from the fibre. No transmission was measured after applying this weld, indicating the fibre was structurally damaged during the process.

The weld at 150 µm has severely penetrated the fibre coating. Etching indicates that the nickel has easily gone into solution with the steel material, forming a strong bond between coating and metal surround. Unfortunately, however, the fibre did not survive the welding process. As soon as the process started the transmission dropped to zero.

When applying the weld 50 µm further away, the fibre survives the embedding process but severe losses in the transmitted intensity occur (Figure 5-33). When measuring the transmitted intensity during the process, the recording shows typical behaviour for fibres that experience thermal overload (see above). At the beginning the transmitted intensity is increased due reduced micro-bending caused by thermal expansion of the U-groove. Shortly thereafter, (~3 s) the transmitted intensity suddenly and severely starts to drop by about 90 %.

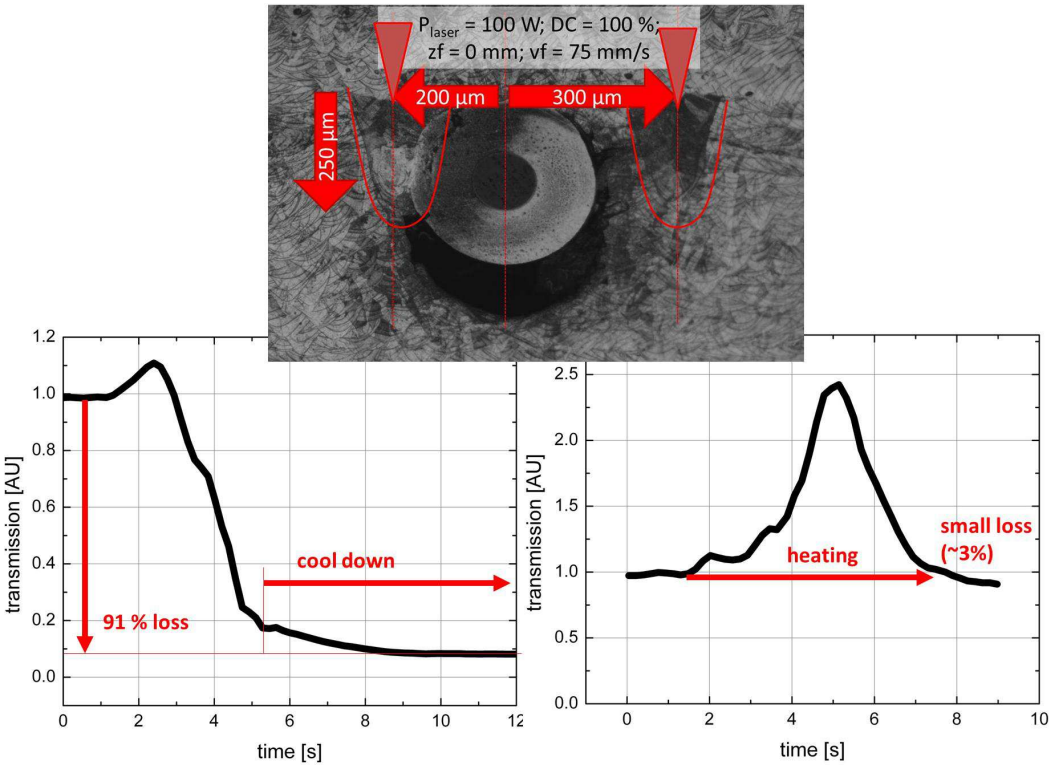

Figure 5-33 Cross-section analysis of embedded coated fibre with deep-penetration welds applied to the sides (top). Transmitted intensity through the fibre for both applied welds (bottom).

Placing the weld about 350 µm away significantly reduces the heat input into the fibre, almost no losses in transmission occur, indicating that the material between fibre and melt pool is a sufficient thermal protection. Transmission measurements show during the process significant increases by reduced micro-bending of the heated SLM structure

but only small losses after process end (~3 %). However, this is too far away to improve the bonding between fibre and metal surrounding since the coated fibre only has a diameter of only 350 µm.

In conclusion deep-penetration welding offers the potential to significantly improve the bonding of the coated fibre, provided that the weld seam is at least 350 µm away from the mid-point of the fibre to preserve the spectral properties of the fibre during the process. Taking into account the results for the embedding, the indication is strong that the fibre will survive a welding process as long as either sufficient coating material or added material is buffering the heat input into the fibre. With larger laser power only the aspect-ratio of the deep-penetration weld seam is increased, without increasing the width of the weld seam. In theory a fibre with 600 – 700 µm OD nickel coating could be embedded and subsequently laser welded to the sides by applying roughly about 300 W laser power to the side. However this indicates a dilemma in terms of minimisation of the embedded sensor component.

5.4.2 Met-glass

Met-glasses are nickel-based alloys with low melting temperatures due to their significant boron or phosphor contents (both 1 to 10 %; [111]). At elevated temperatures both boron and phosphor easily diffuse into surrounding metals and also lower their melting temperature [111]. Therefore, the bonding of the fibre can easily be improved by depositing met-glass underneath the coated fibre. After embedment, the specimen is deployed in an oven and heated up to melting temperature of the met-glass.

To investigate the feasibility of adding met-glass into the process the embedding process is expanded by making the U-groove deeper (Figure 5 34; top). . This allowed met-glass foil to be placed in the bottom of the groove before adding the optical fibre. The met-glass foil (MBF 20; Tm ~ 1030 C; 25 µm thick [112]) was laser cut (SPI G4 20 W MS pulsed laser (*parameters: 20 W; prf: 0; 50 mm/s*)) into slides of approximately 350 µm in width. Two layers of met-glass were deposited on top of each other in the U-groove. A nickel coated fibre of 450 µm was subsequently placed in the groove and embedded. Finally, the specimen was put into a furnace and baked at 1100 °C for 30 min.

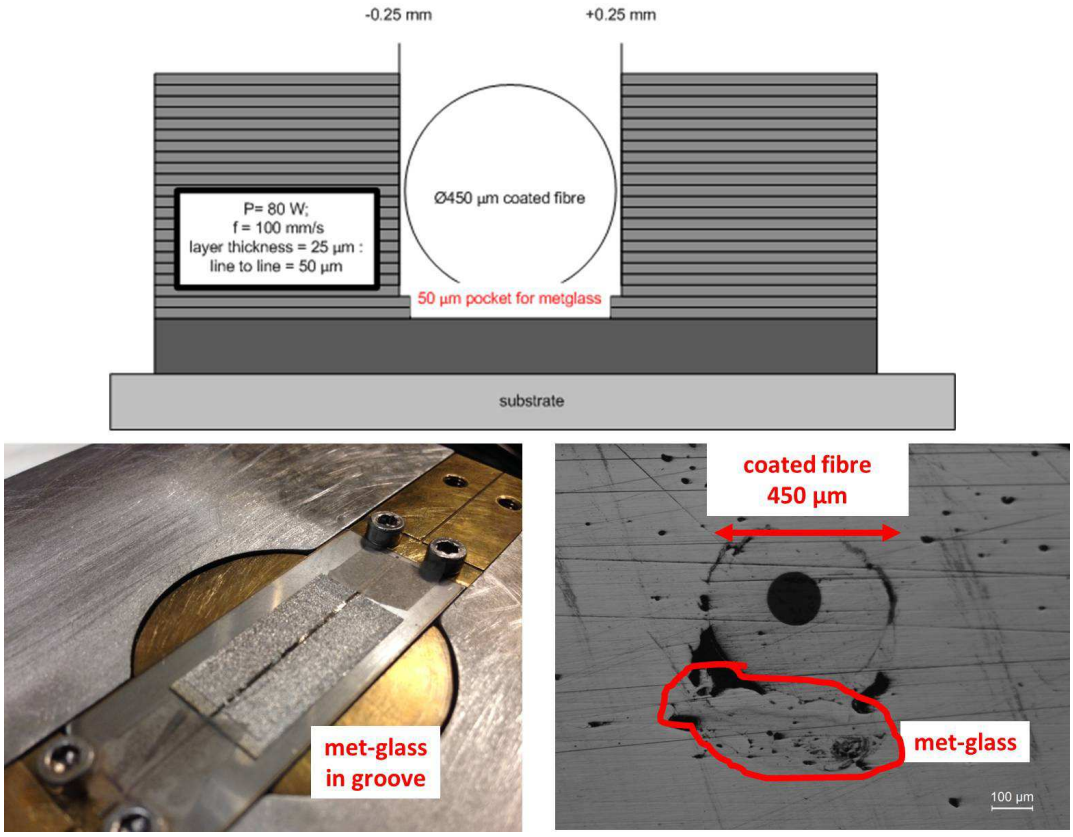

Figure 5-34 Schematic illustration for approach for improved embedding of nickel coated fibres with met-glass. Height of U-groove is increased by 50 µm and to layers of met-glass are deployed underneath the optical fibre in the groove.

Cross-sectional analysis of the sample indicates that the met-glass foil melted sufficiently during the temperature process and achieved a bond between the groove surface and metal coating (Figure 5-34; bottom right). This is a promising indicator that by simply applying met-glass foil this technique hence shows promise to significantly improve the bonding to the fibre.

5.5 Chapter review

This chapter provides an overview on different approaches and strategies to embed a coated optical fibre into a metal component with SLM technology. The most successful technique was to place the fibre into SLM-fabricated U-grooves. Only minor modifications to the SLM parameters for the encapsulation process are necessary to guarantee reliable embedment of optical fibres with minimised transmission losses. The line-to-line distance was increased when scanning perpendicular to the optical fibre for the first layers. Having established the fibre embedding process, the next step was to embed fibres containing sensing elements, as described in chapter 6.

Additional steps, such as deep penetration welding close to the fibre or the introduction of met-glass into the process, can easily be accomplished with minor changes of the SLM process. The capability that deep penetration welding can significantly increase the area of bonding is demonstrated. However the optical fibre has to be properly shielded from the welding process, increasing the requirement for larger coating thicknesses. Met-glass can easily be introduced into the process and shows good potential to provide a bonding between the underside of the coated optical fibre and the steel substrate.

Chapter 6

Embedded Sensing

In this chapter, the methods developed for embedding optical fibres (described in Chapter 5) are utilised to embed Fibre Bragg Gratings (FBG). These FBGs not only offer potential for in-situ structural health monitoring of strain and temperatures changes of SLM fabricated components, they can also provide information about the SLM process itself.

This chapter is divided in three sub-sections. At first in section 6.1, the embedding process of FBGs is described and investigated. The following two sub-chapters evaluate the feasibility for using SS 316 embedded FBG for strain (6.2) and temperature measurements (6.3).

6.1 Embedding Fibre Bragg gratings

The bare optical fibres used in previous experiments are replaced with photosensitive germanosilicate fibres containing FBG. The fibres were H_2-loaded prior to FBG inscription to enhance their high temperature performance (see section 2.1.6). The FBG's length is about 10 mm and fibres are typically embedded over a length of about 4 cm (Figure 6-1) with the FBG positioned in the centre of the embedded section. FBGs are RF sputtered with chromium and subsequently electroplated with nickel. The Bragg wavelength negatively shifts by about 0.5 nm to shorter wavelengths after electroplating. No significant birefringence in the gratings spectral response is observed after coating. The negative shift in Bragg wavelength is caused by the nickel's high thermal expansion coefficient, compared to glass, and the elevated temperature of the plating bath. When placing the chromium coated fibre in the plating bath, glass dominates the thermal expansion since the chromium layer thickness is only a few µm. Nickel is then electroplated in much larger quantities onto the fibre at a temperature of 50 °C; when the nickel coated fibre is removed from the plating bath the thermal coefficient of nickel dominates, yielding compressive stress onto the FBG (see section 2.1.5).

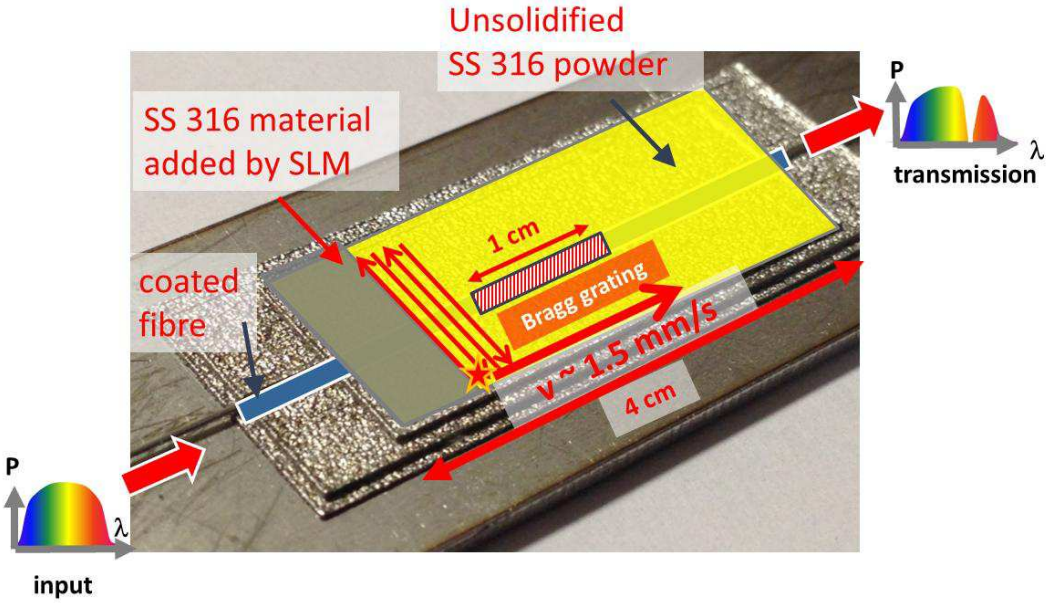

Figure 6-1 Schematic illustration for position and interrogation of Fibre Bragg Grating sensor during embedding by Selective Laser Melting.

A substrate containing a U-groove was fabricated by SLM and a coated FBG (OD 420 µm) was placed in the groove and encapsulated (see Chapter 5). A high frequency interrogator (IBSEN) was used for interrogating the FBG. Powder is deposited on top of the fibre and scanning the SLM process is conducted perpendicular to the direction of the optical fibre typically for the first three layers (Figure 6-1). The width of the embedded section is typically about 7 mm. The SLM progresses at a speed of 100 mm*s^{-1} and the line-to-line spacing is set to 100 µm for the first layer with narrower spacing is used for subsequent layers (see section 1.1.1; case #C). The overall speed by which the SLM process moves along the fibre is about 1.5 mm*s^{-1} for the first layer.

6.1.1 Applying the first layer

The transmission spectra of the deployed FBG are recorded at 10 µs intervals. The spectra for the first 9s after starting the process are plotted together in Figure 6-2. When starting the SLM process no significant change in the spectrum is observed. Five seconds into the process, the SLM process is still about 10 mm away from the FBG, and Bragg wavelength and spectral profile of the grating are almost unchanged. The closer the laser spot gets to the FBGs location, the longer the Bragg wavelength, indicating that the temperature of the grating increases. About 9s after starting the process, the

SLM process has travelled by about 15 mm and is almost on top of the grating. The Bragg wavelength has shifted by about 950 pm (red line). For a nickel coated FBG this shift indicates a temperature increase of about 50 °C (see section 6.3.2). The grating width (FWHM) also increases, caused by a temperature gradient along the grating. The side of the grating facing the SLM process is warmer than the opposed side. Therefore, along the grating, the grating pitch length is not homogenously strained, leading to a broadening of its spectral response.

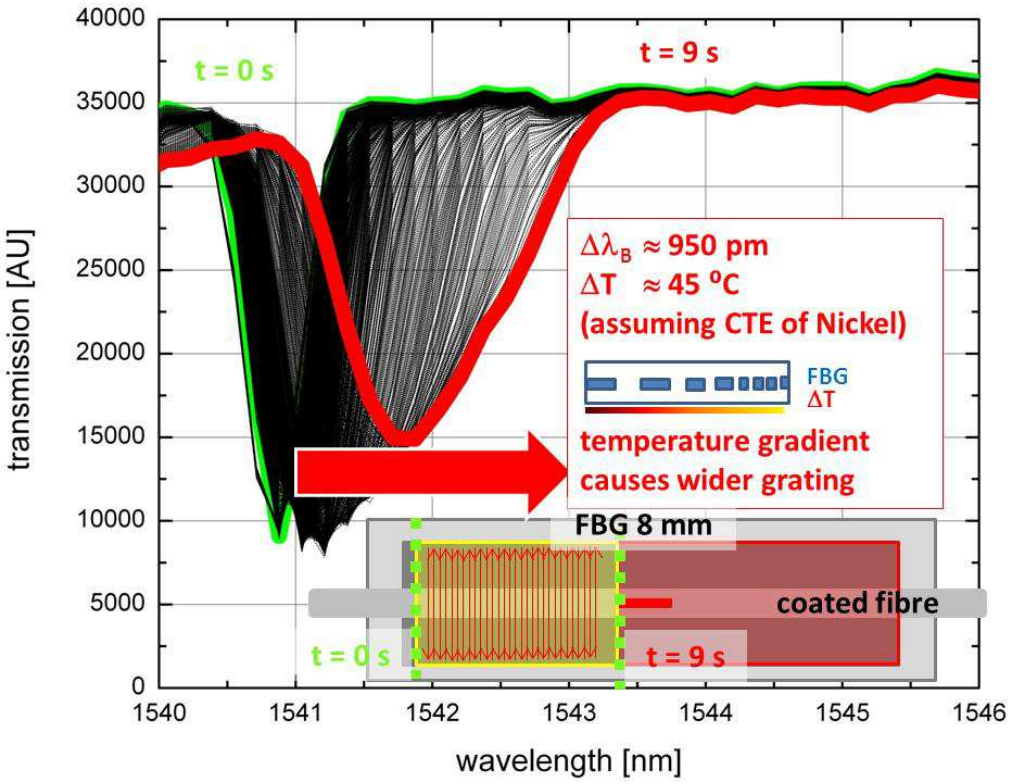

Figure 6-2 Transmission spectra for the first 9 s of the encapsulation process. The Bragg wavelength gradually shifts to longer wavelengths due to proximity of the melt pool. Temperature gradients along the grating lead to widening of the grating.

While scanning directly above the grating, the Bragg wavelength increases further, indicating a further increase in temperature (Figure 6-3). The highest Bragg wavelength is reached just when the laser spot has moved to the far end of the FBG. At this point, the Bragg wavelength has shifted by about 3.5 nm, which indicates an increase in temperature by about 200 °C. The grating spectral width at this point is slightly larger than at the start of this process (green line). The spectral profile of the grating indicates a reversed direction of the temperature gradient along the FBG. When the laser spot is

at the centre of the grating the spectrum is more symmetric, indicating equal temperature gradients in both directions of the fibre (blue line). The double peaking that is observed is caused by in-homogenous stress distribution across the cross-sectional plane. The two peaks are separated by about 700 pm which indicates a transversal load of about 35 MPa (see section 2.1.5;[46]).

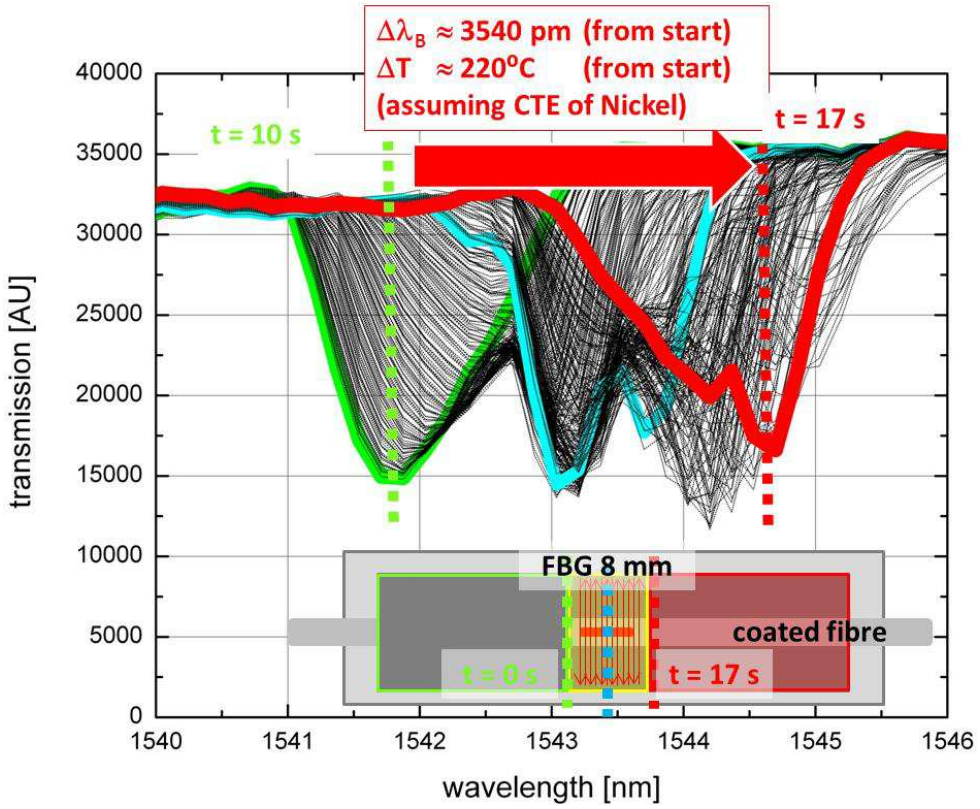

Figure 6-3 Transmission spectra when the SLM process is directly above the FBG. The grating reaches its maximum temperature of about 220 °C indicated by a large shift in wavelength of about 4.8 nm (red line). The grating width remains almost constant. However, double peaks indicate the occurrence of birefringence due to transverse loading.

Once the SLM process has sintered the powder above the grating, the Bragg wavelength gradually starts to move to shorter wavelengths again, as the grating cools down (Figure 6-4 left). Significant residual heat of the SLM process remains at the grating's location for more than 5 s after processing the area. At that time, the laser spot is already more than 8 mm away from the grating.

As the processing laser moves further away, the spectra narrows again and the Bragg wavelength moves to a shorter wavelength due to cooling and decreasing temperature

gradients. Once the SLM process has stopped (orange line in Figure 6-4 right), the Bragg wavelength continues to shift towards shorter wavelengths, until the sample cools to ambient temperature which takes about 120s.

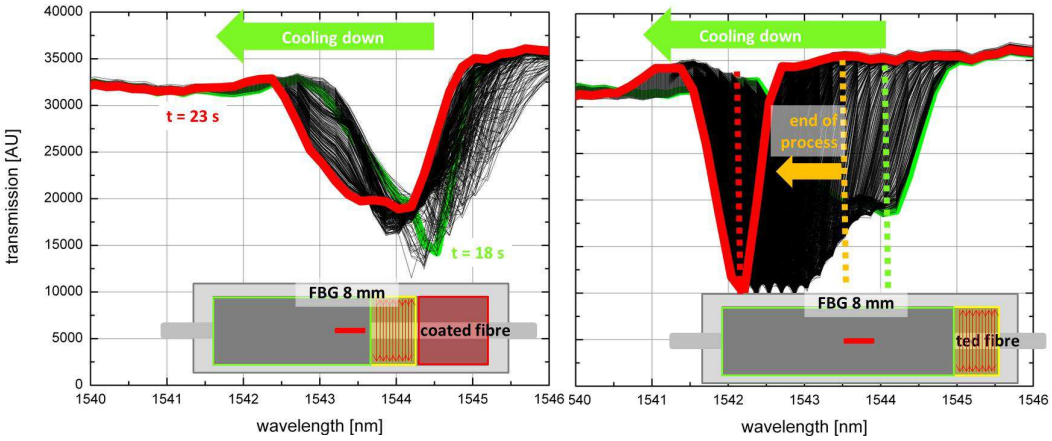

Figure 6-4 Transmission spectra recorded shortly after the grating has been encapsulated and the process zone of the SLM process is moving away from the now embedded FBG.

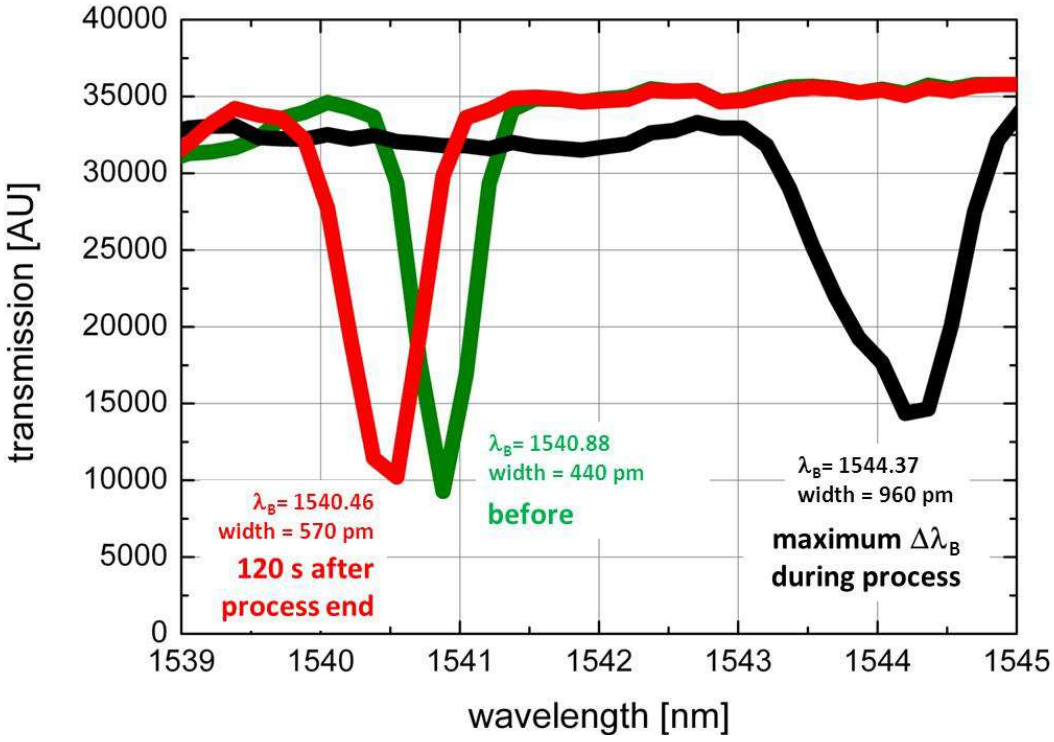

Figure 6-5 Transmission spectra of the SLM embedded FBG recorded before (green), at maximal shift during process (black) and 120 s after the end of the SLM process.

After applying the first layer, no losses in transmitted intensity occur, demonstrating that nickel coatings with an outer diameter of 420 µm are sufficient to prevent losses due to micro-bending (Figure 6-5). The grating width (FWHM) is increased from 440 pm before embedding to 570 pm after embedding (~ 30 % increase), and the Bragg wavelength has shifted by about 420 pm to shorter wavelengths.

When encapsulating the fibre with the first layer, the FBG is gradually heated before the SLM process creates a solid bond between the coated FBG and the SS 316 surround. During this heating, the nickel coated FBG expands according to the thermal expansion of nickel which is slightly smaller than the thermal expansion of SS 316 (CTE_{nickel} ~15×10^{-6}; CTE_{SS316} ~17×10^{-6}). During this process the grating reaches temperatures of about 250 ^{0}C (derived from spectrum in Figure 6-3 and data from section 6.3.2) when a bond between nickel and SS 316 is formed. Once a proper bond between nickel and the SS 316 is formed and the first layer is complete, the nickel-coated FBG's shrinkage is dominated by the slightly higher CTE of the SS 316, generating a compressive stress into the embedded FBG. Given the CTE values and the temperature measured by the grating, the optical fibre is theoretically compressed by about 400 µε when the temperature drops back to ambient which results in a negative shift in Bragg wavelength of about 450 pm, matching well with the experimental value of about 420 pm.

The widening of the grating when applying the first layer is caused by temperature gradients along the grating during the SLM process. The grating is heated up during the SLM process, and temperature gradients from the process zone to the ambient environment cause in-homogenous straining of the grating along the fibre, leading to wider spectral profiles of the grating. The SLM process above the section with the FBG takes a comparatively long time (~ 6s for 10 mm) to form a solid bond between fibre, its coating and metal surround. Continuous energy input varies the temperature of not yet bonded sections, so that in-homogenously straining FBG is preserved by incrementally attaching the grating to the metal surround.

The results obtained with an FBG with a thinner coating (OD 352 µm) are shown in Figure 6-6. The black trace is the transmission spectrum after depositing in a tailored, pre-fabricated U-groove, but before embedding. The figure also shows the transmission

spectra after each of the first five layers have been applied by SLM and after adding more than 14 layers. The spectral width (FWHM) of the nickel coated grating before embedding is 663 pm and no indication of significant birefringence is observed in the spectrum.

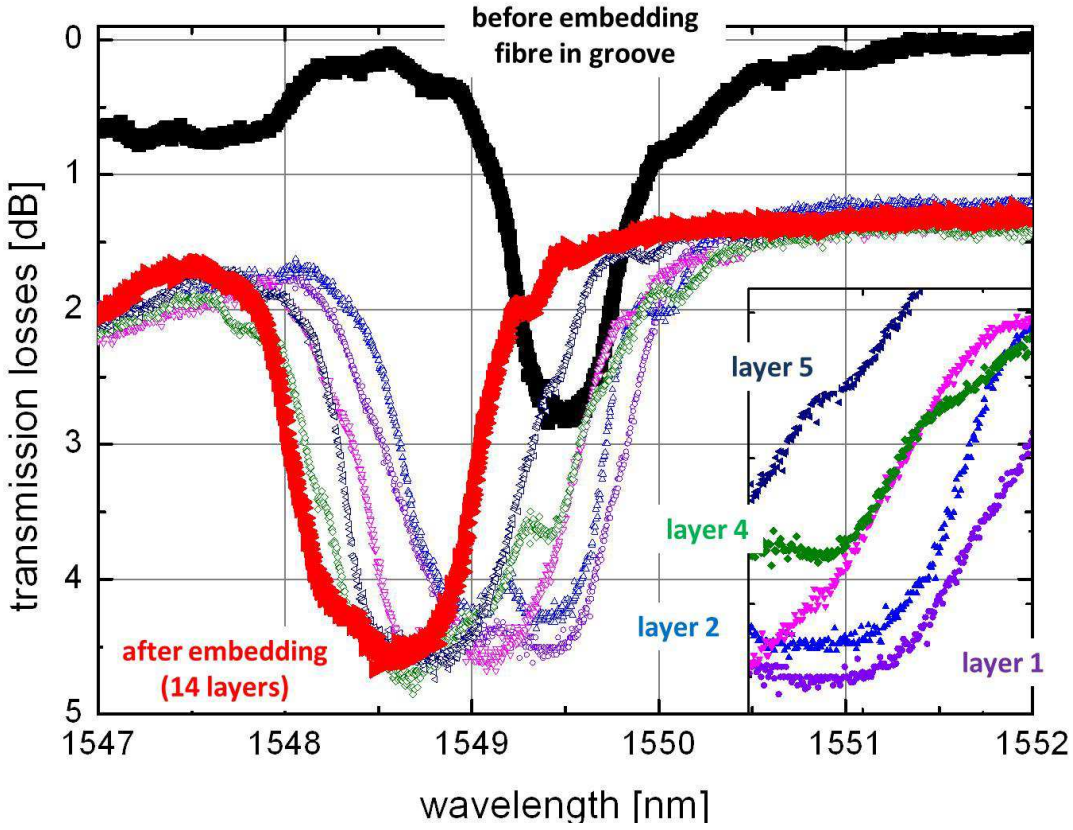

Figure 6-6 Transmission spectra of FBG recorded after applying layers of stainless steel powder on top of the fibre with FBG.

After applying the first layer by SLM, the grating width almost doubles to 1.183 nm which is a significantly larger increase compared to the grating with thicker coating which width only increased by 25 %. Similar to the fibre described earlier, the Bragg wavelength similarly shifted by about 0.4 nm, however in this case losses in transmitted intensity of about 1 dB occur. Reduced coating thicknesses hence lead to widening of the grating's spectrum and losses in transmission after embedding. Less material is available to buffer the FBG from the heat energy of the SLM process, leading to steeper temperature gradients within the optical fibre and therefore wider gratings. The negative shift in Bragg wavelength due to different thermal expansion coefficients after applying the first layer is not affected by different coating thicknesses.

6.1.2 Applying further layers

Applying the first three layers, the grating width remains almost constant after the initial increase due to the 1st layer (see Figure 6-6; and also Figure 6-7 top). From the fourth layer onwards the scanning strategy alternates between parallel and perpendicular scanning to the optical fibre. Applying the fourth layer by scanning parallel to the fibre, the grating width is further increased by about 200 pm. Subsequent scanning in the direction perpendicular to the optical fibre reverses the widening. However, after applying six or more layers, changes in width become less distinguishable and the grating width plateaus at around 0.95 nm.

Accumulation of material between (~ 100 µm after 3 layers) fibre coating and SLM process shields the grating from further changes. If the polarisation of the injected light is changed following the SLM process, the spectral characteristics at the peak wavelength slightly change, indicating the occurrence of Birefringence due to non-axisymmetric tensile stresses over the fibres cross-sectional plane (Figure 6-7 right). Double peaking occurs, with the peaks separated by about 400 pm which indicates a transverse load onto the FBG of about 25 MPa (Figure 2-11; [46]).

The Bragg wavelength shifts to shorter wavelengths when adding more layers of material on top of the fibre. The shift follows an exponential decay function and plateaus after having added 7 or more layers. Once the SLM process is finished, after adding 14 layers the Bragg wavelength is at 1458.54 nm, corresponding to a shift of about 920 pm compared prior embedding (Figure 6-6). The negative shift indicates that the grating is under compressive stress. Translating the shift in Bragg wavelength into compression using a sensitivity of 1 pm*$\mu\varepsilon^{-1}$ and using the Young Modulus of fused silica (72 GPa), this indicates that after 14 layers the fibre is under a compressive stress of about 70 MPa.

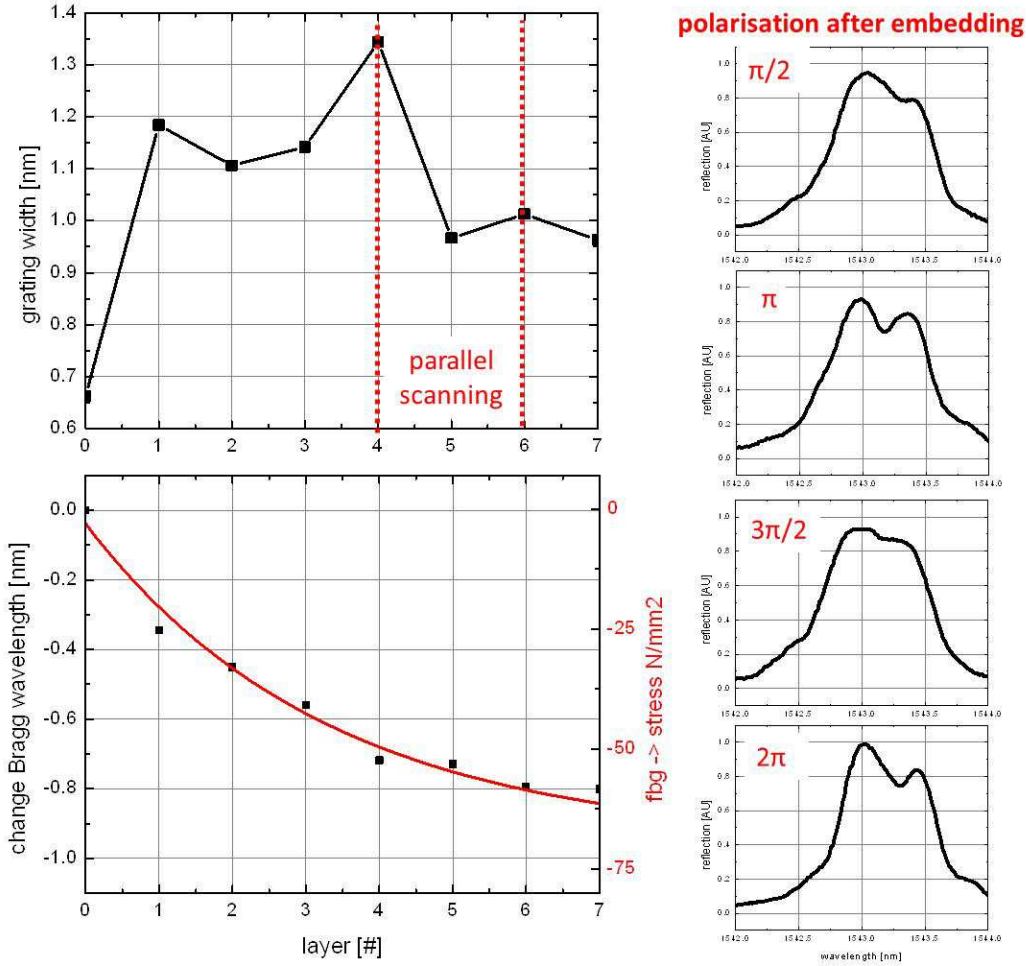

Figure 6-7 Plot grating width (top left) and change in Bragg wavelength (bottom left) as a function of applied layers. Grating spectrum for different polarisation angles (right).

6.1.3 Residual Stresses

Residual stresses built up during the SLM process explain both the change in grating width and the negative shift of the grating when adding more than one layer. When applying subsequent layers, the penetration depth of the SLM process does not extend sufficiently deep to re-melt the bond between nickel coating and steel. Melt pool dimensions are only in the range of ten µm whereas the length of the FBG is ~10 mm, so when applying subsequent layers, the FBG is always solidly attached to the SS 316 surround, no further yield in compressive stress can occur due to differences in thermal expansion coefficients.

Shiomi was among the first to develop a model to describe the layer-by layer built up of residual stresses during SLM processes [86]. This model was applied to the experiments described above to determine the expected distribution of residual stresses in the axis of building up the component. The model indicates that in the plane where the FBG is located, compressive stresses of about 120 MPa occur (Figure 6-8). Indeed, once the SLM process is complete, stresses of about 75 MPa have been measured by the FBG when translating the wavelength shift of the FBG into stress (red line in Figure 6-7 bottom left). About 40 % of the measured stress in the fibre (400 pm wavelength shift after 1st layer ≈ 400 με ≈ 35 MPa) is caused by differential thermal expansion coefficients between nickel and steel (see section 6.1.1). Assuming that FBG and SS 316 are strained similarly and considering the almost three times higher Young Modulus of SS 316 (205 GPa), the remaining stress within the optical fibre (about 40 MPa) corresponds to a stress of about 110 MPa in the surrounding metal, indicating that the compressive stresses predicted by the model are in good agreement with the experimental results measured by the embedded FBG.

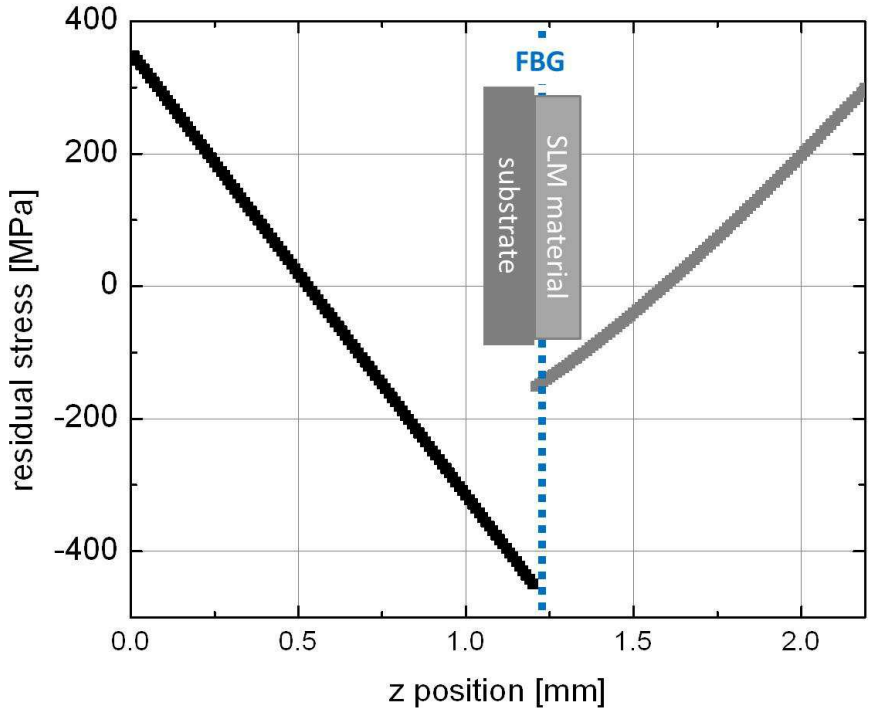

Figure 6-8 Plot for simulated residual stress as a function of position within the specimen for both substrate & SLM added material. The model predicts compressive residual stresses of about 120 MPa in plane where the optical fibre is located.

To hold the sample in position during the process the rectangular shaped sample is clamped down in each corner by screws. When removing the clamping mechanism of the fabricated component the specimen bends. Residual stresses are responsible for this bending. When un-clamping the specimen, these residual stresses lead to rapid bending of the component, adding further compressive stress onto the FBG, indicated by a further negative shift in Bragg wavelength of about 1.1 nm (Figure 6-9). Assuming again, that both FBG and SS 316 are strained similarly and that the SS 316 is relaxing linear-elastically, the change in stresses within the SS 316 is about 300 MPa. This is close to the Yield Strength of the material and correlates well with the model which predicts high residual stresses as high as such, in planes close to the surface of the specimen or at the interface between substrate and added material.

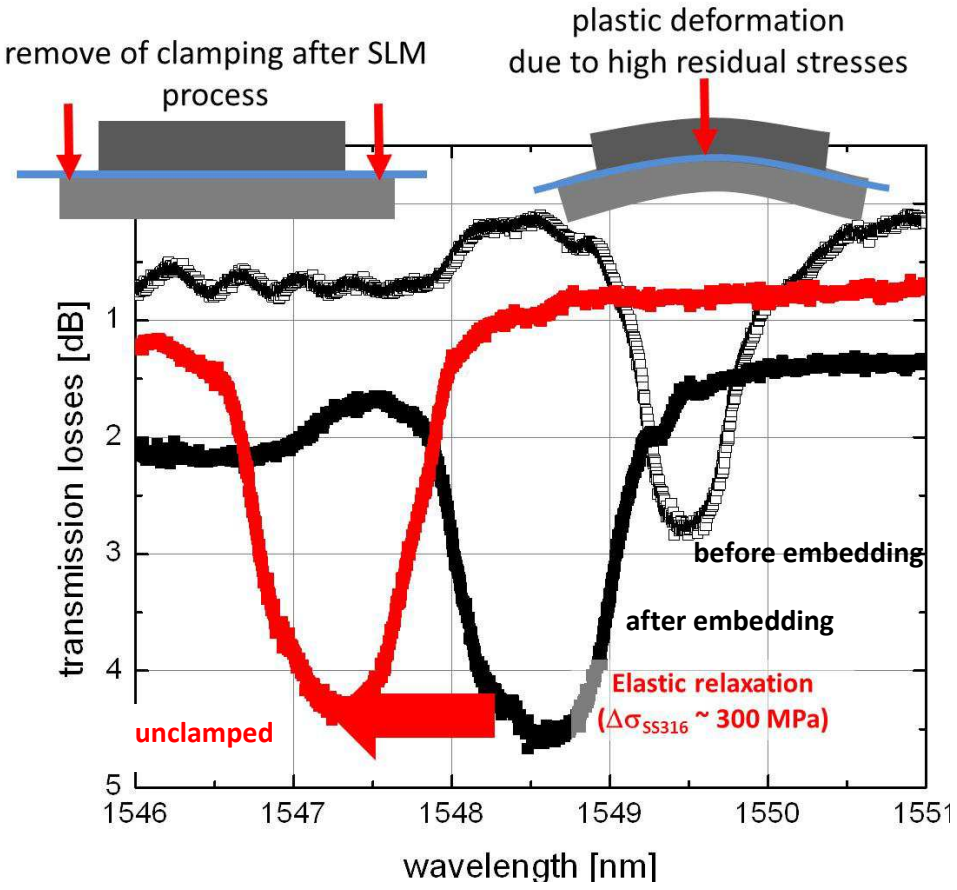

Figure 6-9 Embedded FBG spectrum recorded after specimen is removed from clamping mechanism. The Bragg wavelength negatively shifts by more than 1.2 nm indicating elastic relaxation of the steel material as high as the material's Yield Strength (300 MPa).

The overall distribution of residual stresses is highly complex in a 3D manner and the distribution is highly influenced by other varying parameters, such as ambient temperature or scanning strategy of the SLM process. The changes in grating width when changing the scanning direction of the SLM process indicates that a much more complex distribution of residual stresses occur when process parameters are changed.

To verify the observations from above and further investigate phenomena occurring when embedding FBGs, two more gratings with thin nickel coatings (~OD 350 µm) and shorter grating lengths are embedded. The grating length is only about 3 mm, therefore leading to weak grating characteristics (grating strength ~1 dB). The gratings were written "in-house" during preliminary studies by our research group (Jinesh Matthew) into photosensitive H_2 loaded germanosilicate fibres using a copper-vapour laser and phase mask (see section 2.1.3). Different writing times lead to different fluence, causing different grating strengths (Figure 6-10). The grating written with at higher fluence (left) is stronger than the one with less fluence (right). Due to the weak initial grating strength of both gratings, the occurrence of perturbations along the grating is easier to distinguish.

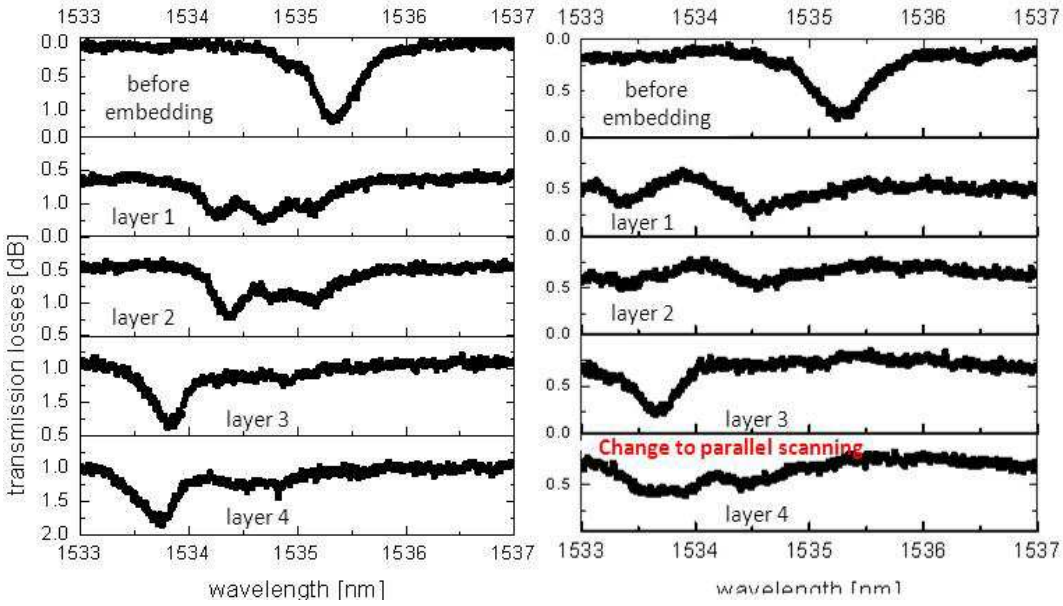

Figure 6-10 Transmission spectra for two FBGs of shorter length (3 mm). Gratings lacking the strength of longer gratings. Short grating length and strength increase gratings sensitivity for perturbations induced by the SLM process.

In both cases, after the first layer is applied on top of the fibre, the Bragg wavelengths shifts towards shorter wavelength and significantly widens. A periodicity occurs in the spectral profiles of both gratings, and in case of the weaker grating (right) the amplitude of this periodicity is as strong as the grating itself. Losses in transmission occur after applying the first layer (~0.5 dB). In both cases the transmission spectra remain almost constant when applying the second layer, albeit a slight shift to shorter wavelengths occurs. When applying the third layer, both gratings narrow again, indicating a more homogenous stress distribution along the fibre. The Bragg gratings spectrum again approximates in both cases a Gaussian profile. The narrower line-to-line spacing of the SLM process when applying the third layer leads to more heat energy accumulated in the specimen. High speed interrogation of the gratings during application of the third layer with only half the line-to-line distance (50 µm) show positive wavelength shifts of about 6 -7 nm. This wavelength shifts indicates temperatures within the optical fibre of about 400 – 500 °C for typically more than 5 s, albeit already more than 100 µm of SS 316 material deposited in-between fibre coating and SLM process. Temperatures exceeding 500 °C are considering high enough to relieve SLM fabricated steel components from residual stresses and hence the FBG spectral profile becomes narrower.

For the 4th layer the scanning strategy is varied. When continuing the SLM process by scanning perpendicular to the direction of the optical fibre (Figure 6-10 left) the grating slightly (<100 pm) shifts towards shorter wavelengths preserving its Gaussian profile and grating width. In case where the scanning is conducted parallel to the fibre (Figure 6-10 right) the, gratings spectrum is significantly influenced by the change in scanning direction. The gratings spectrum has significantly widened, barely distinguishable from the perturbations in spectrum, indicating that changing scanning direction makes the distribution of residual stresses significantly more complex.

6.2 Strain sensing

One major application for embedded sensing is measuring strain changes of SLM fabricated components induced by stress. The optical sensor is deployed directly in the heart of the metal component allowing to follow strain changes in-situ from within the component. In this section the feasibility is explored and evaluated, in order to follow the development of elastic and plastic strain changes with embedded FBG sensors.

To stress the sample sufficiently to reach the Yield Strength of SS 316 (~290 MPa), loads of several thousand Newton are applied. Therefore, additional space has to be provided on the substrate to allow it to be clamped in the tensile testing machine. The rectangular shaped samples used in other experiments only have lengths of 5 cm. Using 1 cm on each side for clamping in the tensile testing machine, the remaining length is too short to provide a homogenous distribution of the applied stresses. Finite Element Simulation (FEM) reveals for stresses reaching SS 316's Yield Strength that the specimen in the remaining 3 cm is only homogeneously strained over a length of about 2 cm (Figure 6-11). In particular the SLM added material located outside the plane where the load is applied is strained very in-homogenously. The embedded FBGs typically have lengths of about 1 cm and the length of the "clip-on" extensometer is about 2 cm. Longer samples are hence required.

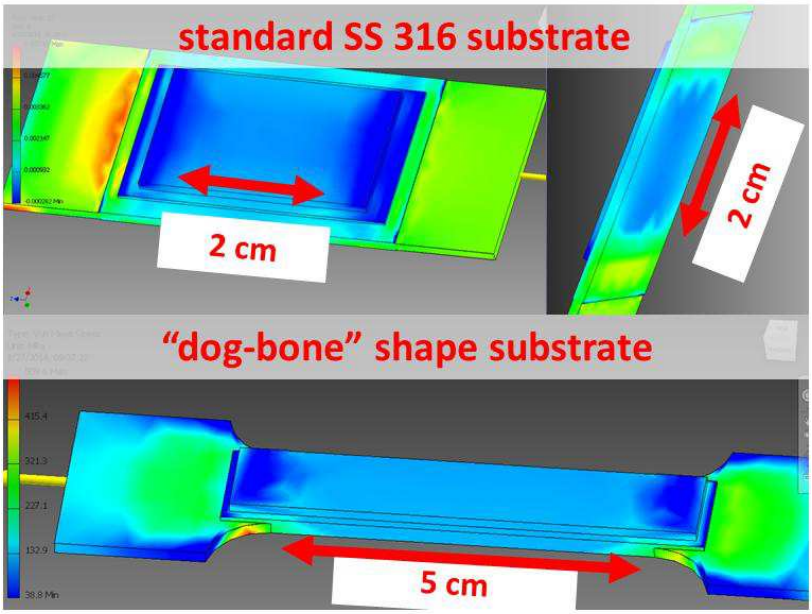

Figure 6-11 FEM analysis for conventional rectangular SS 316 substrates (top) and "dog-bone" shaped substrates (bottom).

The dimensions of the RF sputtering process for deploying the chromium keying-layer unit generally limit the length available for embedding. Chromium keying-layers can be applied for lengths of only up to about 8 cm. Suitable "Dog-bone" shaped substrates were therefore designed according to current standards. The tapered profile significantly reduces the cross-sectional area in sections where material is added by SLM. In this case homogenous distribution of stress and strain should be achieved over a longer area (about 5 cm).

A sample with an embedded FBG on a dog-bone shaped substrate (Figure 2; top left) is fabricated with SLM. The sample is mounted on a tensile testing rig. The experimental setup includes optical spectrum analyser (Micron-Optic 125) for interrogating the embedded FBG and digital readouts for both tensile testing machine and FBG interrogation. Signals, from load cell, extensometer and optical interrogator are recorded and correlated using LABVIEW software. The actual strain of the specimen is measured by an extensometer (Instron "axial clip-on" Type 2630) clamped onto the rear side of the SS 316 substrate. Strain is applied by moving one clamping mechanism of the tensile testing machine at very slow speeds (1 $\mu m*min^{-1}$). The load cell of the tensile testing machine provides corresponding values for the applied force.

Results for tensile tests conducted with bare specimens without added material are displayed in Figure 6-13. The bare SS 316 specimen's results are well within the specifications for this austenitic stainless steel. Firstly, the material linear-elastically deforms when increasing the sample's load. Above stress levels of about 210 MPa (2500 N) the material plastically deforms. The yield strength (0.2 % permanent deformation) of the material is reached at about 290 MPa, in our case at a load of about 3500 N. The Young's-Modulus for the material is calculated to about 208 GPa. When releasing the load the material linear-elastic contracts and in subsequent load cycles, where load levels do not exceed previously applied load levels, the material elastically follows changes in load with the Young's Modulus.

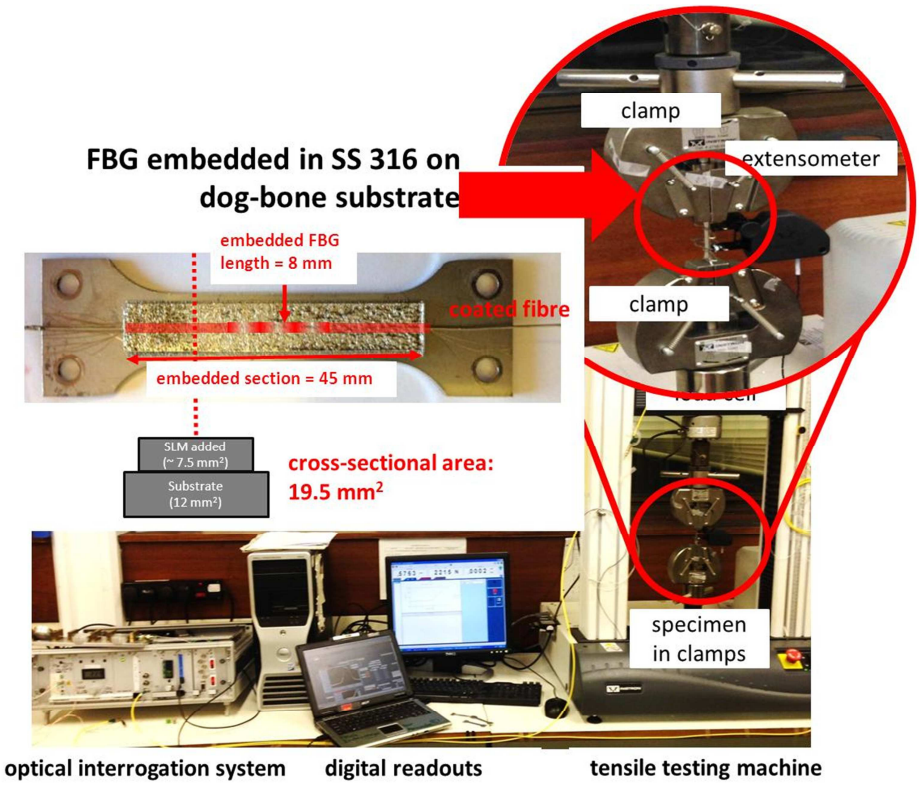

Figure 6-12 **Experimental setup for strain testing of SLM embedded FBG sensors. SLM substrates are dog-bone shaped to facilitate homogenous stress levels during tensile straining. Specimens are clamped into tensile testing machine, an "clip-on" extensometer measures physical elongation of the sample. LABVIEW software is used for recorded and correlating sensor data from extensometer, load cell and interrogated FBG.**

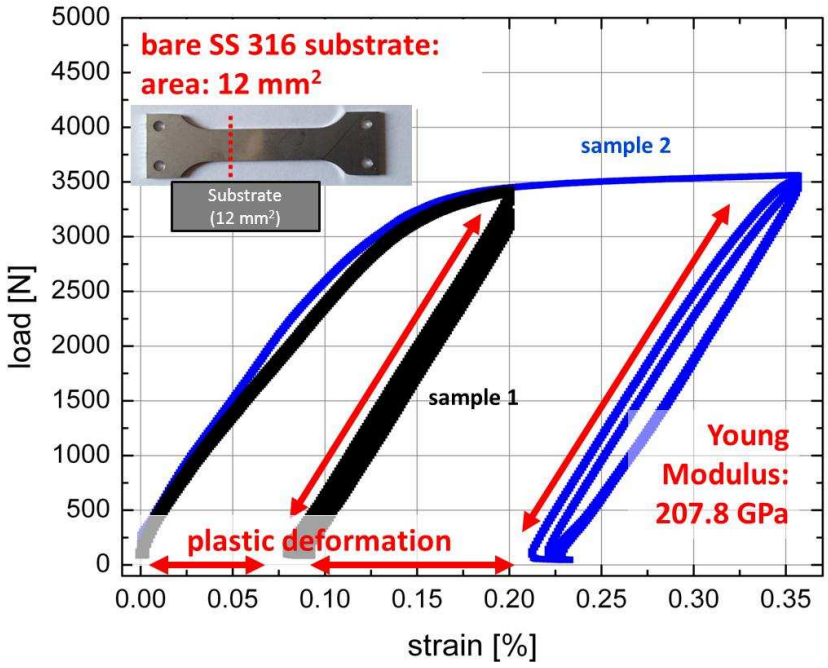

Figure 6-13 **Plots for load as a function of applied strain showing tensile tests conducted with bare SS 316 specimen.**

6.2.1 Measuring plastic deformation

The specimen with the SLM added material shows significantly different behaviour compared to the bare SS 316 sample (Figure 6-12). Despite the increased cross-sectional area of the SLM sample, the material is much more easily strained. The bare sample reaches about 0.07% elongation at a load level of about 2000 N. At the same load, the SLM sample reaches much more elongation (0.1 %). No pure linear elastic behaviour is observed for the SLM specimen even when applying small loads. When releasing the load from the SLM specimen the sample repeatedly linear-elastically relaxes with a Young's Modulus of about 205 MPa.

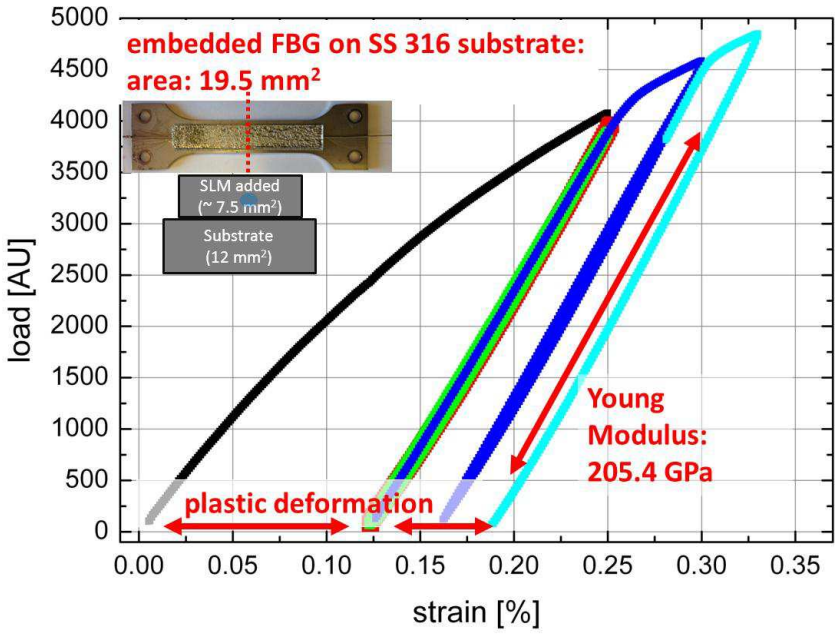

Figure 6-14 Plot for load as a function of applied strain for tensile tests substrate with SLM added material and embedded fibres. Despite its larger cross-sectional area the sample with SLM embedded fibre is more ductile.

After the SLM process the SS 316 material appears to be more ductile. A possible explanation for the increased ductility are residual stresses and anisotropies induced by the SLM process [113]. The substrate only has a relatively small volume due to small thickness (1.2 mm). High residual stresses of several hundred MPa are predicted by models and are also measured from embedded FBGs, confirming the model (see section 6.1). High tensile residual stresses are particularly observed in planes close to the specimen surfaces, both in the substrate and the SLM added material. Residual stresses easily exceed the material's Yield Strength and lead to plastic deformation. The

specimen is already tensile stressed to levels up to the Yield Strength and therefore any additional tensile stress will instantaneously lead to plastic deformation. Anisotropies in the mechanical properties induced by different scanning directions perhaps also add to the more ductile behaviour of the SLM fabricated specimens. When tensile testing and plastic deformation occurs, the material is strain hardened and subsequently linearly and elastically relaxes with a Young Modulus of about 205 GPa [114]. Subsequent straining of the sample, where applied load levels not exceed levels of previous cycles, does not cause further plastic deformation of the material.

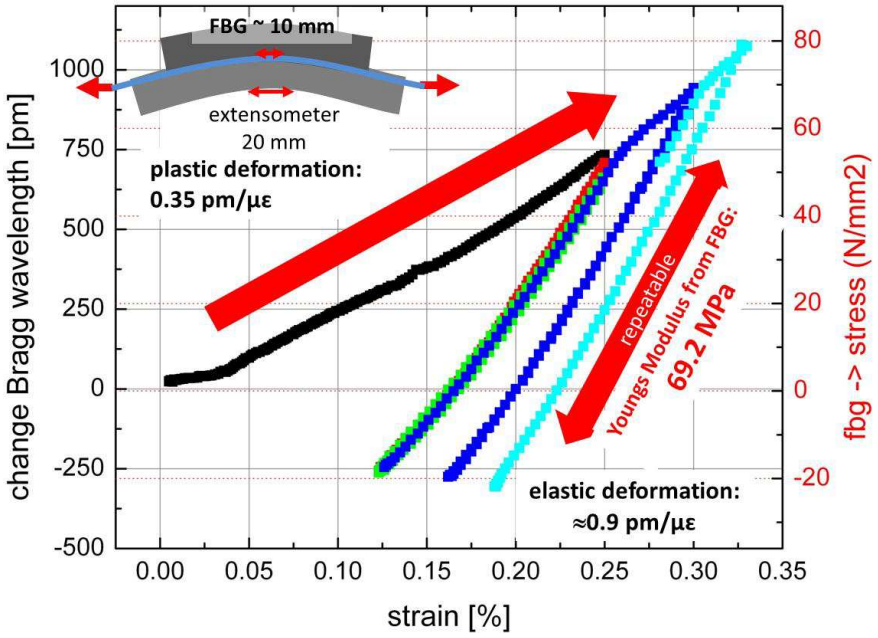

Figure 6-15 Change in Bragg wavelength recorded as a function of applied strain. Residual stresses within the specimen lead in-homogenous straining of FBG and extensometer during plastic deformation.

The data for the embedded FBG is displayed in Figure 6-15. When straining the sample for the first time and therefore plastically deforming the specimen, the FBG shows a sensitivity of about 0.35 pm*$\mu\varepsilon^{-1}$. At the beginning of the strain cycle, the response is slightly reduced due to the bending of the sample during the SLM process. When the applied load is reduced, the FBG repeatedly follows elastic deformation of the sample with a sensitivity of about 0.9 pm*$\mu\varepsilon^{-1}$, leading to compression once the sample is released from the load, indicated by an negative shift in Bragg wavelength of about 250 pm. In subsequent load cycles, where load levels do not exceed the levels of previous cycles the FBG follows the linear-elastic deformation repeatedly with 0.9 pm $\mu\varepsilon^{-1}$. In

case load levels exceed previously applied levels, instantaneously, the sample continues to plastically deform and the response of the FBG decreases to about 0.35 pm*με^{-1}.

The reduced sensitivity of SLM embedded during plastic deformation is possibly explained by high residual stresses and anisotropies within the specimen. Model and data from embedded FBGs indicate high compressive residual stresses in the plane where the FBG is located. When taking the specimen out of the clamping mechanism after the SLM process, the sample bends and the Bragg wavelength shifts by more than 2 nm compared to before embedding. This shift represents a compression of the fibre of about 2 mε. FBG data from the tensile test demonstrates existence of a proper bonding between fibre, coating and SS 316. In section 3.3 it was established that the bonding mechanism between fibre and coating is suitable for enduring the occurring stresses in strain measuring applications at ambient temperature. And indeed, the data suggest homogenous staining of the FBG when linearly increasing the load. Any occurrence of "stick-slip-effects" caused by weak bonding strength would result in pronounced discontinuities in the gratings response, which are clearly not observed. Therefore it is assumed when tensile straining the specimen, due to complex residual stress distribution and anisotropies, the specimen is in-homogenously strained over its cross-sectional area, mitigating the FBGs sensitivity during plastic deformation. Cold hardening during the plastic deformation results in homogenous straining of the sample over its cross-sectional area during subsequent elastic strain cycles. Then, the FBG in the centre and the extensometer on the outside of the specimen are strained equally.

6.2.2 Elastic-strain measurements

To investigate the long-term stability of SLM embedded FBGs in the linear elastic-regime of SS 316, a sample is strain cycled at smaller load levels. A maximum load of 2 kN was chosen which is equivalent to a stress level in the coupon of about 100 MPa. When reaching the maximum load of 2 kN, the tensile testing machine was set to reverse to relieve the strain at the same speed. To compensate for temperature sensitivity of the embedded FBG, a thermocouple is glued onto the test coupon and the temperature measured. Subsequently the FBG response is compensated for ambient temperature changes. LABVIEW software is used to record and correlate both data streams from FBG interrogation and tensile testing machine. Recorded data for measured strain and interrogated FBG covering about an day after initial plastic

deformation and slippage in the clamping mechanism had eased are displayed in Figure 6-16.

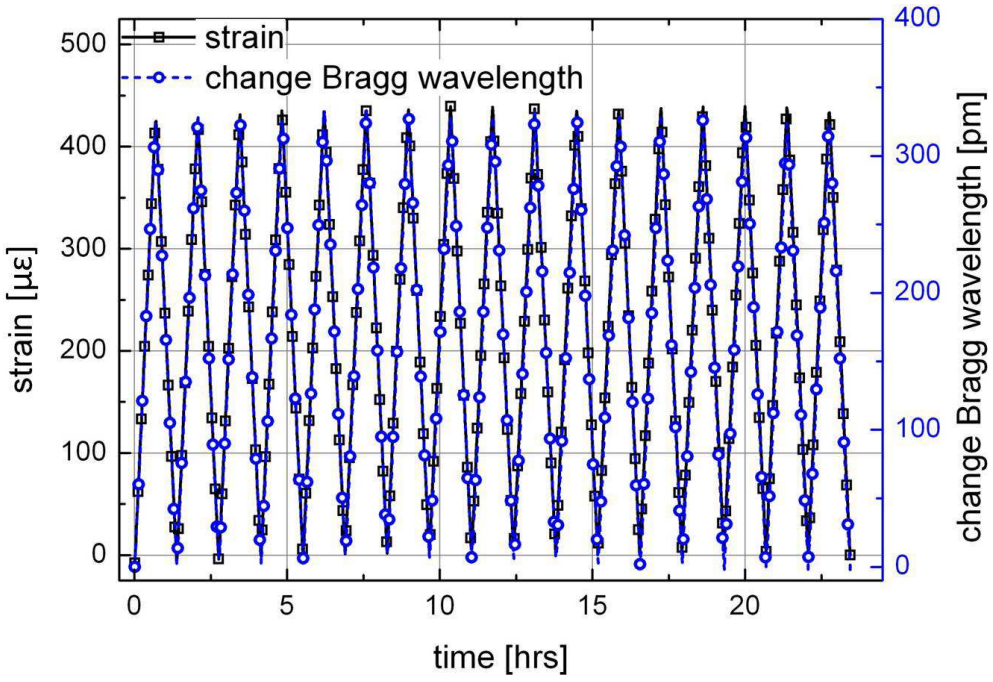

Figure 6-16 Plot for strain and change in Bragg wavelength as a function of time for elastic strain cycling of the SS 316 specimen with SLM embedded optical fibre

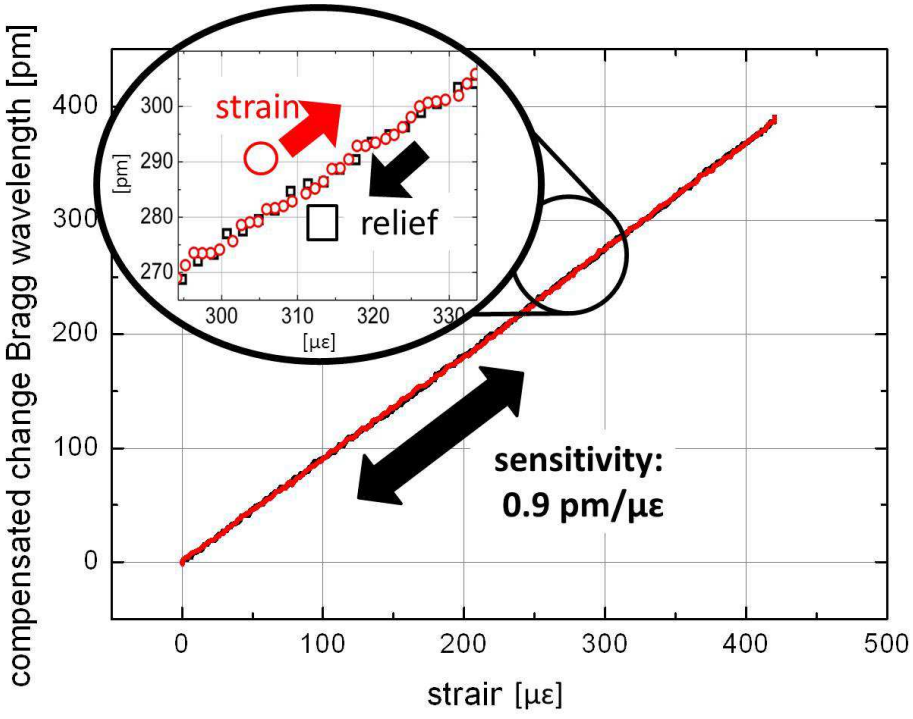

Figure 6-17 Change in Bragg wavelength over applied strain for one cycle after more than 500 cycles have been applied to the specimen.

In this manner, the sample was strain tested in an elastic dynamic mode for more than 3 weeks where apart from the first initial cycles no permanent plastic deformation of the component is observed. The temperature compensated change in Bragg wavelength over applied strain for one cycle of straining and relieving after more than 500 cycles is illustrated in Figure 6-17.

Linear fitting to the plot in determines the sensitivity of the embedded FBG to strain of about 0.92 pm*$\mu\varepsilon^{-1}$ which is slightly less than the 1.0 pm*$\mu\varepsilon^{-1}$ predicted for a bare SMF-28 fibre with similar grating properties. This deviation is to some extent explainable through axial misalignment between the plane where the fibre is located and the plane in which the axial stress is induced. Residual distribution of the measured Bragg wavelength about this fit is spread within a band of ± 3 pm*$\mu\varepsilon^{-1}$. For individual cycles of straining and relieving, data sets are within 2 pm of each other, indicating the reliability of the conducted measurements.

6.3 Temperature sensing

This section explores the feasibility of using SLM embedded FBGs for high temperature applications. For comparison reasons, specimens of bare, nickel coated and embedded FBGs were separately investigated. Specimens were placed in a high temperature (t_{max} ~ 1200 ^{0}C) tube furnace (CARBOLITE) for temperature cycling, to assess their temperature sensing characteristics. Test specimens were packaged together with K-type thermocouples. Typically, the furnace is programmed to change temperatures at slow speed (1 K*min^{-1}) to mitigate temperature gradients in the furnace. A Micron Optic interrogator system (SM 125) is being used to interrogate the FBGs. LabVIEW software is used to record and correlate data from both the FBG interrogator and thermocouple. A 2nd order polynomial peak fit is applied to the spectrum of back-reflected light from the grating, for accurate determination of the location of the Bragg peak. The reflected power (also referred to as strength) of the grating is determined by the peak reflectivity at the Bragg wavelength.

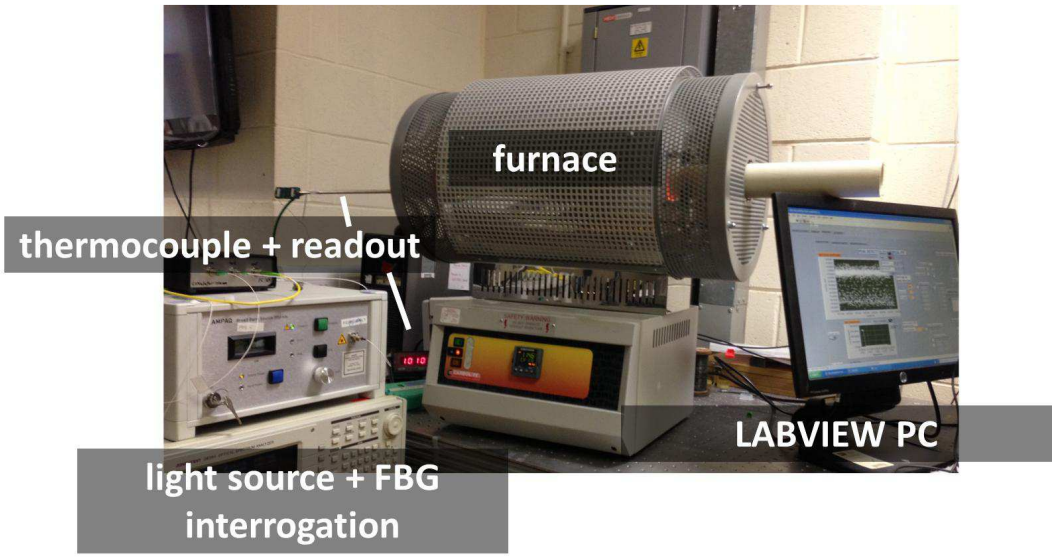

Figure 6-18 Experimental setup for temperature testing of FBGs. Specimens and thermocouples are deployed in a high temperature furnace. Data from FBG and thermocouple is correlated using LABVIEW software.

6.3.1 Characterising bare optical fibre

In this sub-section techniques for reliably measuring temperature with bare non coated FBGs are established. After mechanically stripping from their polymer coating, optical fibres containing FBGs were put into the furnace and interrogated.

Figure 6-19 displays the recorded data for thermocouple temperature, peak intensity for back-reflected light at Bragg wavelength and Bragg wavelength. Firstly, the furnace was set to cycle two times between 100 °C and 500 °C and then subsequently three times between 100 °C and 700 °C and finally heated up to 850 °C, at which the grating completely decays. The reflected power was adjusted for the spectral profile of the light source.

When the temperature was cycled between 100 °C and 700 °C, the gratings gradually lose strength at temperatures above 600 °C. However, the Bragg wavelength reliably tracks the temperature changes. Ultimately, if the temperature is increased further to about 850 °C the grating rapidly loses strength until it completely vanishes.

Plotting the Bragg wavelength as a function of temperature, the grating's sensitivity for temperature changes is typically about 7.5 $pm*K^{-1}$ for the case when the fibre is heated up for the first time. In subsequent temperature cycles where temperatures do not exceed previous maximum temperatures the grating follows temperature changes with a sensitivity of about 11.5$pm*K^{-1}$ at 400 °C. The theoretical value for the used fibre is 11.35 $pm*K^{-1}$ so experimental data conducted in this study corresponds well with results found in literature (see section 2.1.5), confirming the reliability of the experimental setup.

The lower sensitivity when heating the FBG for the first time is explained by the cross-sensitivity of the Bragg wavelength for spacing and strength of the refractive index changes. According to EQN 3 the Bragg wavelength negatively shifts with weaker gratings. The grating's weakening during initial temperature cycles is caused by annealing effects [52].

This section establishes temperature measurements with bare uncoated Fibre Bragg gratings. After the initial annealing effects have been completed, typically after heating the fibre for the first time, the fibre Bragg grating follows temperature changes with approximately 11.5 $pm*K^{-1}$ in average. At elevated temperatures of above 500 °C, the gratings written into H2-doped germanosilicate fibres suffer from accelerated decay (as described in section 2.1.6). At temperatures above 700 °C the grating decays even more rapidly and completely vanishes at a temperature at about 850 °C.

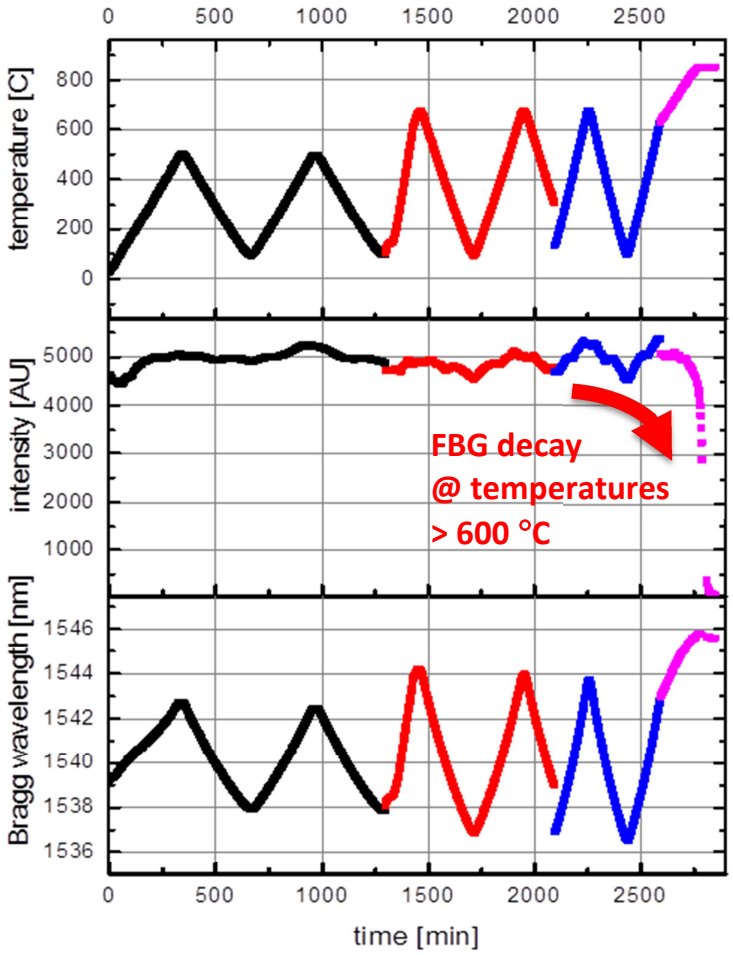

Figure 6-19 **Recorded data for temperature measurements with an bare untreated (mechanically stripped) FBG over time, data from thermocouple place next to fibre (top), intensity (strength) of the applied Gaussian peak fitting function (middle) and central position of the peak fitting (bottom).**

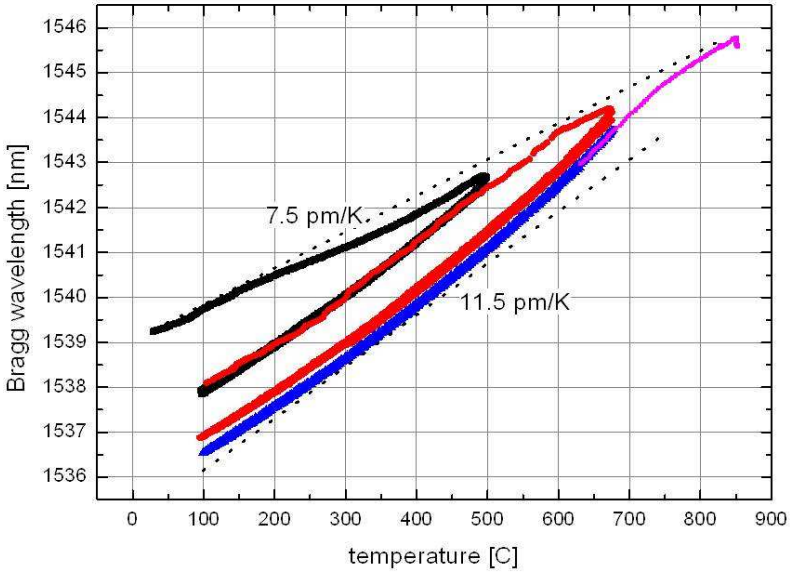

Figure 6-20 **Plot for measured Bragg wavelength from a bare uncoated fibre as a function of thermocouple temperature.**

6.3.2 Characterising nickel coated optical fibre

In this section the temperature characteristics of nickel coated FBGs are established. The experimental setup and procedure is similar to that used in the previous section where bare uncoated fibres are tested. A fibre containing a FBG is RF sputtered with chromium and nickel electroplated to an outer diameter of about 350 µm. The coated fibre is placed next to a K-type thermocouple in the furnace. For temperature testing the furnace is programmed such that the maximum temperature increases by 100 °C after 3 cycles, whereby the starting temperature is set to 300 °C. Figure 6-21 displays the measured Bragg wavelength as a function of temperature measured by the thermocouple.

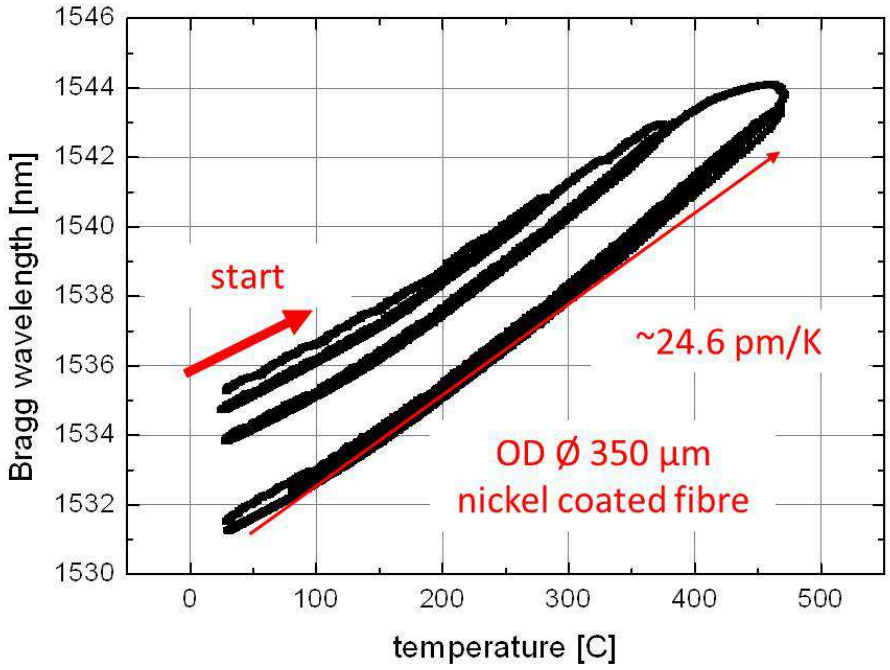

Figure 6-21 Plot for measured Bragg wavelength from a RF sputtered and nickel coated FBG as a function of thermocouple temperature.

Similar to the bare uncoated fibre, the sensitivity of the coated fibre is decreased the first time it is heated up to a temperature that has not been applied before. Provided that previous applied temperatures are not exceeded, the fibre follows temperature changes with a sensitivity of about 24.6 pm*K^{-1} (@ 300 °C). This is more than twice the sensitivity of an uncoated FBG and similar to the results reported for nickel embedded fibres by Li (~24 pm*K^{-1}; [44]). The increased sensitivity is explained by the significantly higher thermal expansion coefficient of the nickel coating compared to the

fused silica. The cross-sectional area of the nickel coating is significantly larger than that of the one of the fused silica or the chromium interlayer. Provided that the coating thickness exceeds 50 µm the fused silica should follow the thermal expansion coefficient of the surrounding material [43].

If temperatures are increased further, the grating further decays until it completely vanishes at about 780 °C. Figure 6-22 shows the reflected power (intensity) and position (Bragg wavelength) of the applied peak fitting. When increasing the temperature even further to about 880 °C in this particular case the Bragg grating reappeared, it is regenerated (see section 2.1.6). The grating continues to follow temperature changes with similar sensitivity. The gratings reflectivity achieves about 15 % (@400 C) of the reflectivity prior to regeneration.

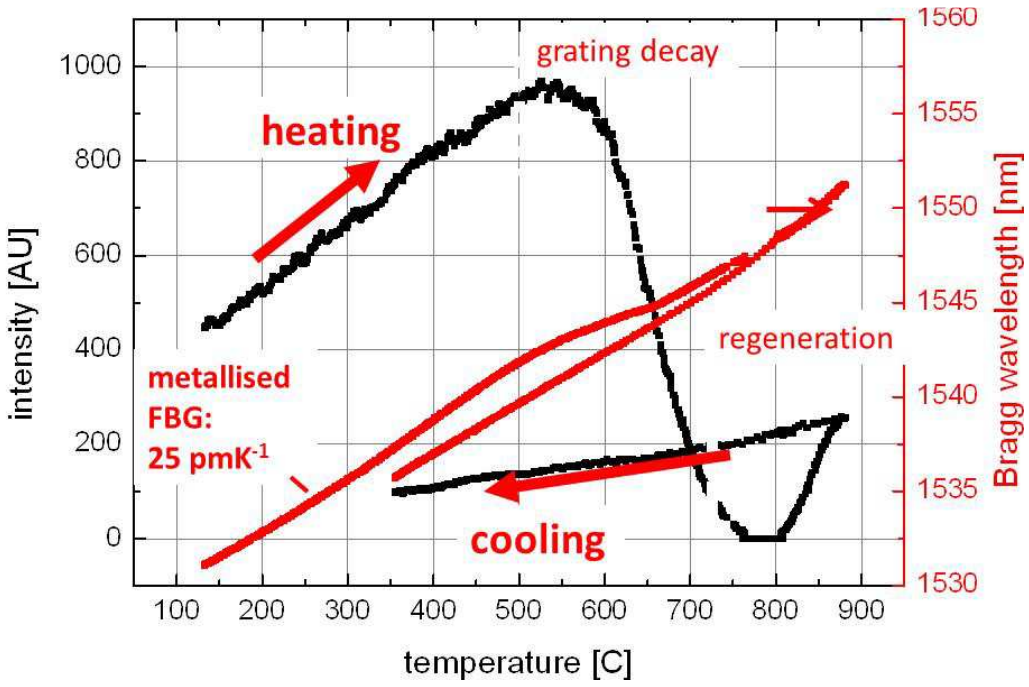

Figure 6-22 Regeneration of nickel coated FBG. At about 800 °C the previously annealed and completely decayed starts to regenerate.

During the cooling phase the coated fibre broke, probably just inside the coating leading to the generation of a cavity whose back reflections overlapped the back reflected light from the FBG, making it difficult to distinguish the FBG signal. Further attempts to reproduce the regeneration inside nickel coated fibres failed. It may be that stresses induced into the optical fibre by the higher thermal expansion coefficient of the nickel

cause fatigue in the fibre leading to structural disintegration. Experimental studies to investigate the physical strength of SMF 28 fibres show that poor handling and elevated temperatures significantly reduce the mean endurable strength of optical fibres [24].

6.3.3 Fibre Bragg Gratings embedded into Stainless Steel 316

FBGs are coated and embedded according to the procedure described in section 6.1. The outer diameter of the coated fibres is in the range of 350 - 400 μm. A typical temperature profile applied to SLM embedded FBGs is displayed in Figure 6-23 (lower plot). Heating to a set temperature occurs fairly quickly over a period of 10-15 minutes. The specimen was allowed cool down after reaching the set temperature. Between successive cycles the set temperature was increased by 100 °C. The grating response to the temperature profile over time is displayed in Figure 6-23. (upper plot). For the displayed temperature profile two discontinuities in the gratings response are observed. The first occurs after the grating has been heated from 100 °C (previous data not shown in figure) to 200 °C and the temperature was held at that level for three hours. The Bragg wavelength remains constant for the first 150 min but then suddenly drops by about 1.5 nm. The second discontinuity occurs when heating up the specimen to 500 °C. At about 440 °C (@ 1150 min) the measured Bragg wavelength again spontaneously drops by about 2 nm.

The Bragg wavelength follows temperature changes with a 2^{nd} order polynomial function, whereby the 1^{st} order slope, the sensitivity, is about 32 pm*K^{-1}, which is about three times the sensitivity of an uncoated FBG. In Figure 6-24 the Bragg wavelength is plotted over temperature with the data from Figure 6-23. Following the discontinuities in wavelength, the sensitivity to further increasing temperature is reduced to ~ 10 pm*K^{-1}, which is typically close to the sensitivity of an uncoated FBG. However, when the specimen is cooling, the sensitivity is always about 32 pm*K^{-1}. After applying this temperature treatment, the Bragg wavelength at ambient temperature has reduced by about 8 nm to about 1542 nm compared to the initial value of 1550 nm prior temperature cycling, indicating that the grating is under significant compressive stress.

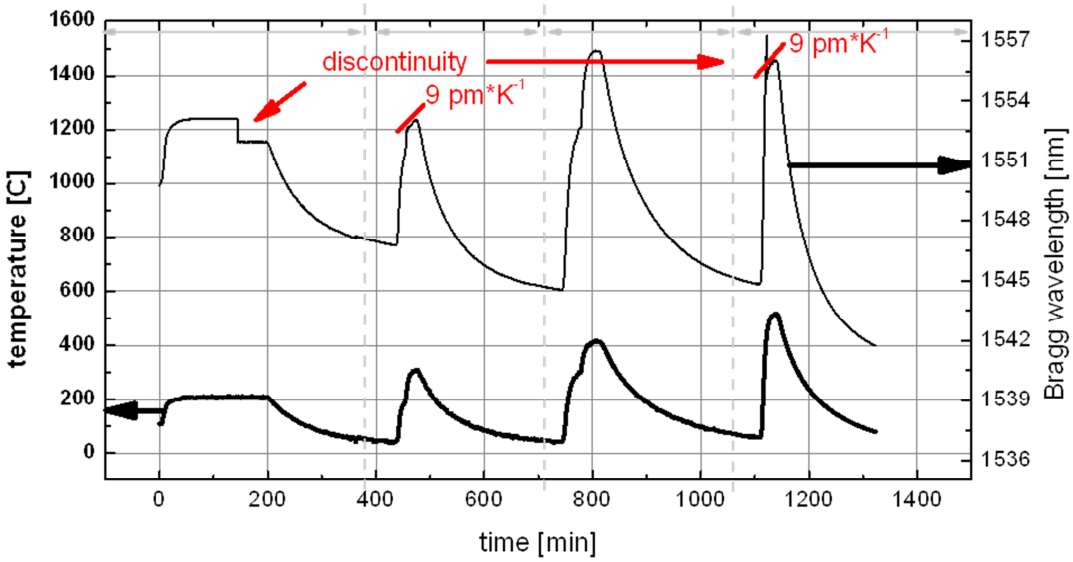

Figure 6-23 **Temperature profile applied to SLM embedded FBGs. Discontinuities occur in the gratings response leading to rapid relaxation of the fibre indicated by a sudden drop in Bragg wavelength.**

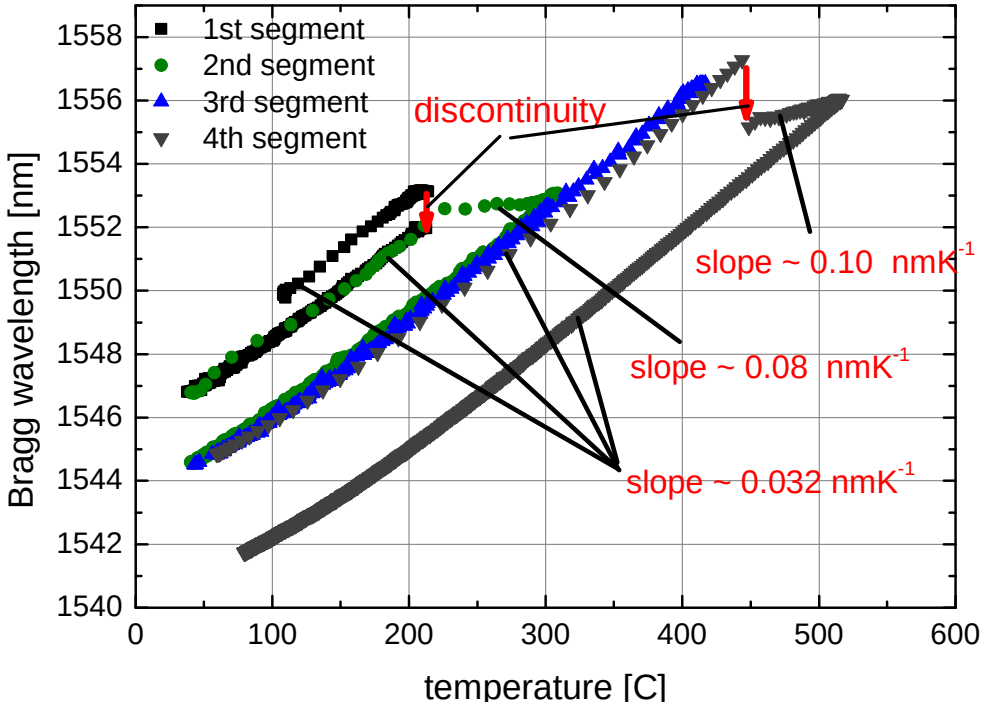

Figure 6-24 **Plot for Bragg wavelength as a function of temperature. Discontinuities occur two times when cycling this SLM embedded grating between ambient temperature and 500 °C.**

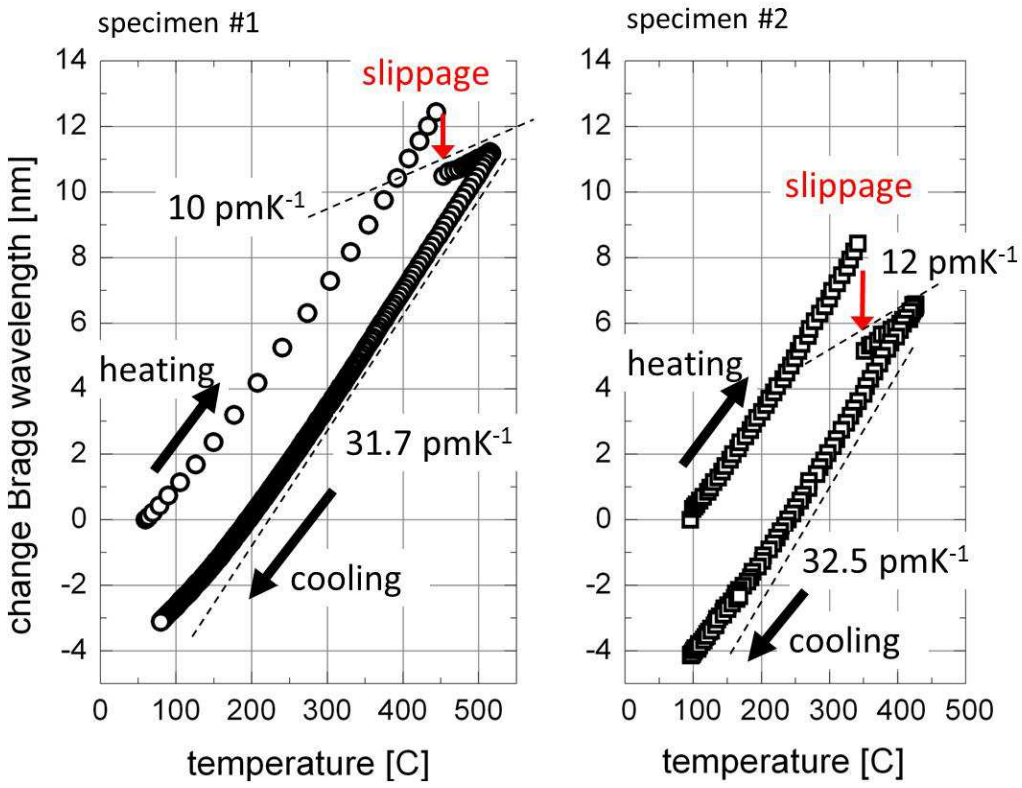

Figure 6-25 Plots for change in Bragg wavelength as a function of temperature for 2 specimens where slippage has occurred.

Repeating these measurements with similarly embedded FBGs (Figure 6-25) indicates that this phenomenon repeatedly occurs at temperatures above 200 ^{0}C, whereby the discontinuity displayed in Figure 6-24 (@200 ^{0}C) was observed at the lowest temperature in the conduct experiments.

The occurring discontinuities must be caused by delamination of the embedded fibre from its metal environment due to significant differences in thermal expansion. At a temperature of 500 ^{o}C the estimated size of the lateral gap between nickel coating and silica fibre due to differences in CTE at 500 ^{0}C is more than 300 nm (Figure 6-26). Also, the fibre is axially strained with the 30 times larger CTE of SS 316. During delamination the strained fibre spontaneously relaxes, resulting in an immediate drop in Bragg wavelength. The exact point when delamination occurs is difficult to predict, but possibly handling of the fibres before coating (stripping, cleaning etc.) has an impact on the endurable stresses of the glass-metal bond. At a temperature of 500 ^{0}C the fibre is additionally strained by the more rapidly expanding SS 316 by about 7.5 mε which corresponds to a wavelength shift of about 7 nm. Therefore it is obvious that the fibre

only partially slips and the slippage is best understand considering a “stick-slip-effect” due to weak adhesive bonding between glass and metal (see section 3.3).

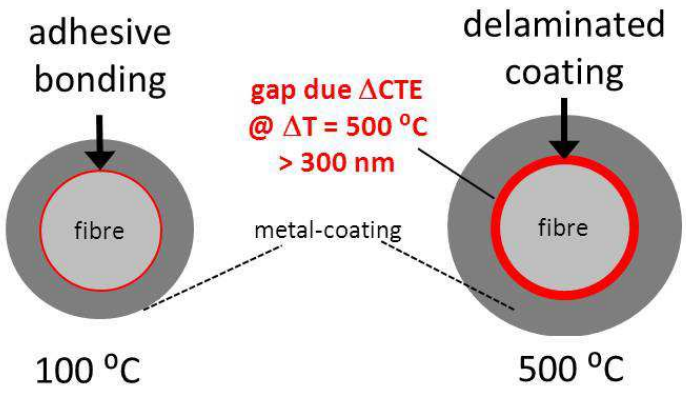

Figure 6-26 Schematic explanation of the occurring delamination at elevated temperatures.

The argument that fibre partially delaminates from the metal at high temperatures is supported by the significantly reduced sensitivity of the FBG after a discontinuity occurs, dropping from ~32 pm K^{-1} to 11 pm K^{-1}, which is the response of a free-floating FBG to temperature changes. In this case the fibre is free floating within the metal component, which is expanding much more rapidly than the fibre. When cooling the specimen, the grating instantaneously follows the steel’s contraction again. As a result, when the specimen is further heated following delamination, the compression at ambient temperature is dependent on the temperature increase after delamination. In Figure 6-25 (left) the temperature after delamination is increased by 70 °C resulting in a negative wavelength shift of 2.5 nm at ambient temperature. A temperature increase after delamination by a 100 °C yields a 4 nm negative wavelength shift.

The recorded reflection spectrum of a FBG after the occurrence of slippage is displayed in Figure 6-27. After embedding the Bragg wavelength shifted to shorter wavelength and broadened. After slipping the grating width is again similar again to the width before embedding. This is another indicator that during the slippage the fibre is detached from its metal surround since the additional spectral features that were induced during the embedding have vanished.

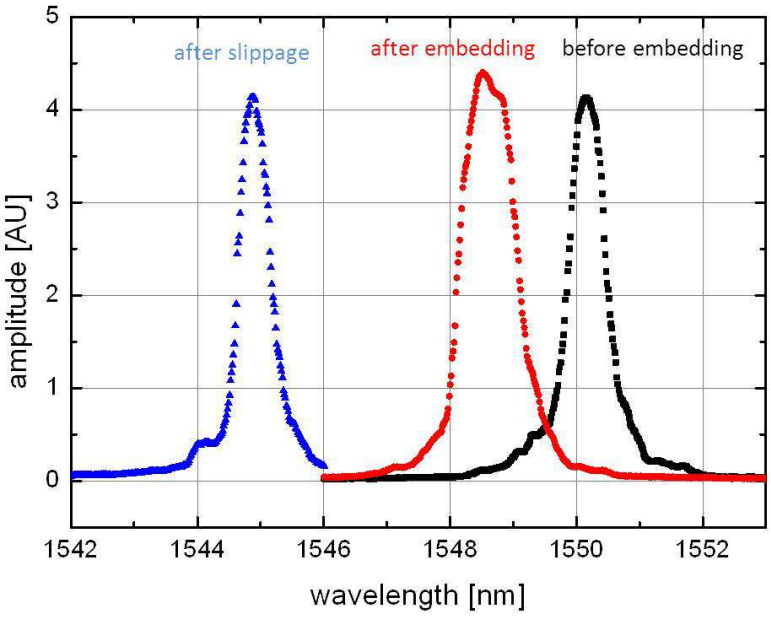

Figure 6-27 Spectra of SLM embedded FBG before and after embedding. After applying temperatre treatment to the specimen such that slippage occurred the FBG's reverts to that measured before embedding, indicating that the grating while slipping completely delaminated from the metal and hence stresses induced during the embedding process vanish.

The increased temperature sensitivity of embedded FBGs of 31.7 pm*K^{-1} corresponds to a thermal expansion coefficient (CTE) of 15.8*10^{-6} K^{-1}, which is close to the CTE of SS-316 (16.2*10^{-6} K^{-1}). The axial stress between the fibre and its metal coating linearly increases with temperature due to significant differences in CTE of silica (5.5*10^{-7} K^{-1}) and steel. At 400 °C the stress level induced by differential CTEs corresponds to an axial strain of about 6 mε (Figure 6-28). This is well below the theoretical limits for fused silica fibres (~ 30 mε), however, increased temperatures and manual handling of fibres (etc. stripping, coating) can significantly reduce the tensile strength of such fibres [24]. Therefore the stresses induced by differential thermal expansion are of concern for possible applications at temperatures exceeding 700 °C. Regeneration of the embedded FBGs was not observed in any of these experiments. Typically, at temperatures above 700 °C the grating vanishes and transmission through the fibre is interrupted indicating structural failure of the fibre. The tensile strength of the used optical fibres is not sufficient to support the occurring axial stresses due to the large thermal expansion of the surrounding metals.

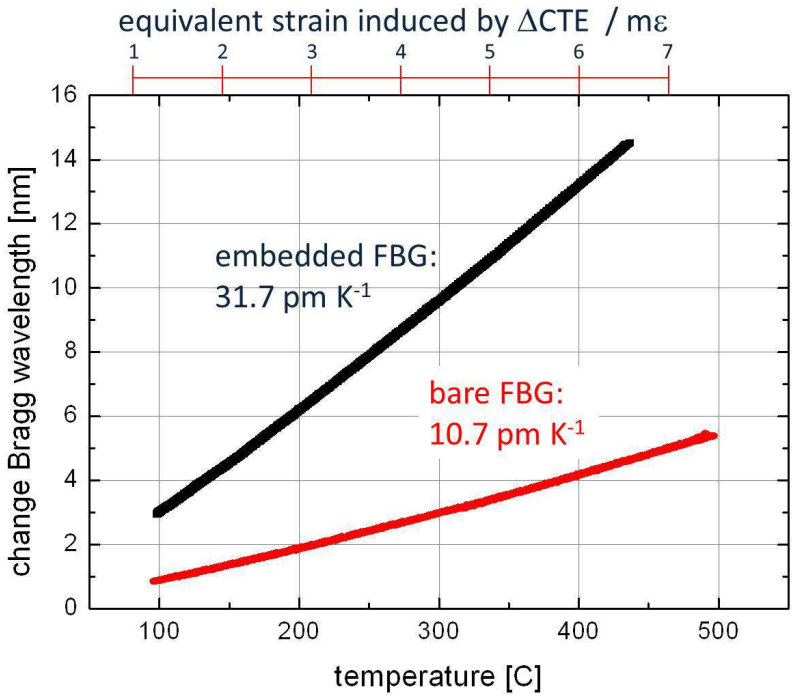

Figure 6-28 Plot for change in Bragg wavelength as a function of temperature for SLM embedded FBG and bare uncoated FBG. The significant higher thermal expansion coefficient of SS 316 causes straining of the embedded optical fibre.

Cross-sectional analyses of a temperature treated sample are shown in Figure 6-29. The outer diameter of the nickel coated FBG before embedding is 355 µm, with no obvious imperfections. After embedding the specimen is temperature cycled with temperatures up to 1200 °C. The cross-section in Figure 6-29 (right) shows that the outer diameter of the nickel coating has shrunk significantly by about 10 % to about 328 um. Cracks occur along the coatings circumference, reaching deep into the coating material.

SEM analysis of the sample disclose further cracks to appear on-top of the nickel coating where a solid bond was created by the SLM process. Nickel diffused into SS 316 material. Phosphor-sulphate from the nickel-plating bath is trapped between deposited nickel particles. At elevated temperatures the sulphate is outgassing leading to shrinkage of the coating material and hence cracks to appear. The deterioration of the coating material at elevated temperatures might be of concern but in the experimental studies the FBG always vanished or the fibre broke before any conclusions about the long-term stability of the glass-metal bond at high temperatures could be made.

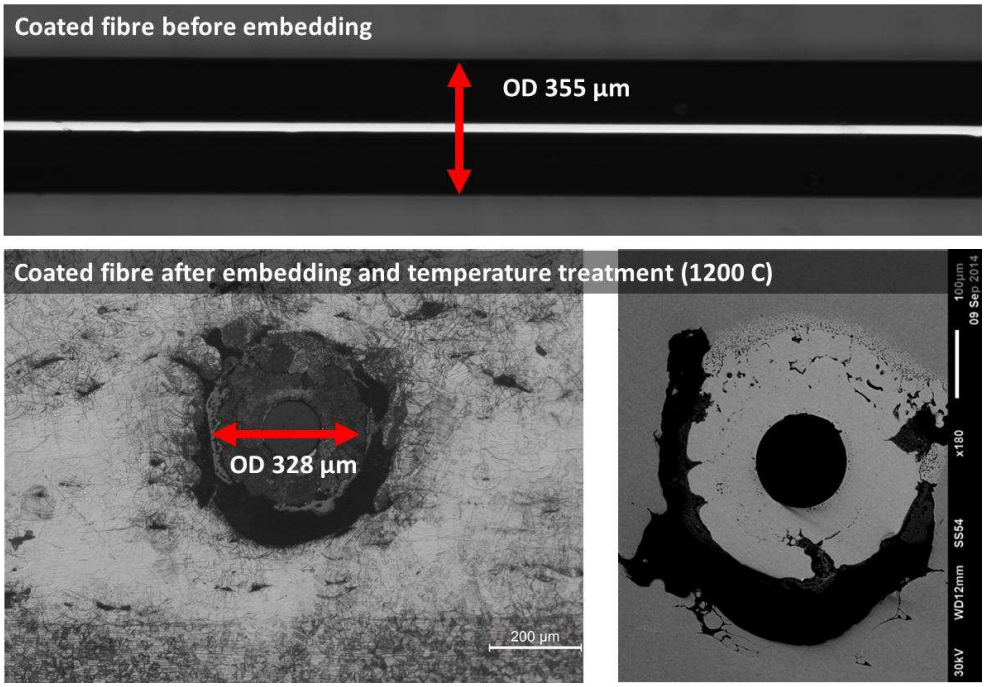

Figure 6-29 Image of coated optical with FBG before embedding (top). Cross-sectional and SEM analysis after FBG is embedded and heated up to temperatures of up to 1200 °C.

6.4 Chapter review

Fibre Bragg Gratings have been integrated successfully using bespoke powder bed SLM technology into SS 316 components whilst preserving their spectral properties. Interrogating gratings during the process shows incremental built-up of residual stresses, layer-by-layer during the process. Measured residual stresses by the FBG are in good agreement with predictions by models. Deploying an FBG in vicinity of the SLM process can contribute in-situ information of the build-up of residual stresses in AM fabricated components. They hence have great promise as tools to investigate and understand the residual stresses in such components.

Repeatable strain measurements with high dynamic elastic stress levels have been demonstrated. Plastic deformations are equally tracked by embedded FBG, however high residual stresses and anisotropies in the components significantly influence the results, adding complexity. For temperature sensing applications at elevated temperatures issues occur with the glass metal bonding. Eventually, the fibre slips inside the metal due to insufficient bonding strength between glass and metal as a result of the more rapid expansion of metals caused by large differences in thermal expansion.

However, provided that temperatures remain sufficiently low (~ 500 °C), embedded fibres can provide in-situ temperature measurements from within the component. At higher temperatures the grating starts to decay. Furthermore, the research indicates that the occurring axial stresses due to differences in thermal expansion between glass and metal exceed the fibres tensile strength, leading to structural damage and ultimately to destruction of the fibre.

Chapter 7

Conclusion and Future Work

7.1 Conclusion

In this thesis the feasibility of embedding and encapsulating fibre optic sensors into SS 316 components during the Selective Laser Melting additive manufacturing process is demonstrated. To achieve this objective, it was first all necessary to acquire techniques for jacketing optical fibres with metals and procedures for Selective Laser Melting processes; these were reproduced from literature. Nickel coatings are applied onto optical fibres with micrometre accuracy for the coating diameter. Laser melting processes of SS 316 are analysed and parameters optimised for reduced energy input (to protect fibre) are identified. Both technologies for fibre coating and SLM are combined to integrally embed optical fibres into solid SS 316 components.

Different approaches for fibre incorporation by SLM are investigated. Only the approach of deploying the nickel-coated fibre in SLM pre-fabricated U-grooves was found to reliable and repeatable incorporate coated fibres into SS 316. The other approaches suffer from increased energy input of the SLM process, which is necessary to facilitate melting of larger powder volumes. Ultimately, when operated in vicinity of the optical fibre, this increased energy input leads to damage of the deployed optical fibres. The U-groove approach is only a compromise. The coated fibre is only fused to the surrounding metal structure at its upper side.

Using met-glass and additional deep penetration welding for improved attachment of the coating over its whole circumference is possible. Trials demonstrate that laser “key-hole” welding can significantly improve the bonding of the coated fibre on the sides. Positioning nickel-based “met-glass alloys” underneath the fibre enables bonding on the underside. Both innovative approaches potentially allow improved joining of the embedded coated optical fibre along its whole circumference with the metal structure. Achieving a proper bond along the whole circumference of the coated fibre is naturally desirable to avoid having voids inside a component. However, the embedded fibre is a

foreign inclusion anyway, and if considered as an element of zero strength in a stress analysis then should not necessarily pose a structural problem. Considering the fibre as a non-load-bearing part, the occurrence of gaps can be accepted.

Using the U-groove approach for fibre embedment significantly reduces the obstruction that the integration of the sensor causes for the SLM process, compared to techniques reported prior to this work (see chapter 2.5). The SLM process is only temporally interrupted, and the fabricated component can remain within the SLM machine and the sensor is deployed for embedding. Furthermore, the fibre sensor is constrained by the SLM fabricated U-groove allowing embedment with high precision (~ ±10 µm - determined by the accuracy of the pre-fabricated groove) and only small changes to the process parameters of the SLM process (wider line-to-line spacing) are necessary to encapsulate the fibre optic sensor.

The use of high brightness fibre lasers also allows the dimensions of the embedded sensor to be minimised. Detailed experimental studies using fibres with a range of different coating thicknesses identified that a nickel coating thickness of about ~350 µm outer diameter is sufficient to protect the fibre sensor during embedment. With such coatings only small losses in fibre transmission (~ 25 %) are caused by micro-bending mechanisms. These losses are due to stresses induced by the SLM embedding and the results presented show that they are caused by micro-bending mechanisms, induced by two phenomena, surface roughness of the U-groove and induced stresses by partially melting the fibre coating on the top during embedding. These losses reduce to zero if nickel coatings exceeding > 420 µm outer diameter are used. This represents a reduction in size of a factor of 6 compared to work reported by Li prior to this thesis, leading to minimised obstruction of the SLM fabricated component's physical properties.

Optical properties of FBG's are preserved during the embedding process, enabling in-situ measurements of strain and temperature changes. High-speed interrogation of embedded FBGs during SLM process provides temperature information in close vicinity (e.g. 400 °C measured ~200 µm apart) to the SLM process. This opens up further potential for SLM process control using fibre optic sensing. Embedded FBGs also allow monitoring of the build-up of residual stresses during the SLM processes.

Residual stresses increase incrementally as additional layers are added to the component and are precisely measured by the embedded FBG. Also, the FBG's spectral response is sensitive to the scanning direction of the SLM process potentially helping to investigate the occurrence of anisotropies of AM manufactured components. E.g. if the laser scanning direction is changed by 90° spectral profile of the grating is widened indicating a more complex distribution of residual stresses.

In-situ strain measurements with high dynamic stress levels have been demonstrated with embedded FBGs. The embedded sensor follows elastic deformations reliably and precisely. Long term elastic strain cycling (~500 cycles) was conducted and no deterioration of the embedded sensor functionality was observed. The embedded fibre sensor follows elastic strain changes up to half the Yield Strength (100 MPa) of the component precisely with a sensitivity of 0.92 pm*μe^{-1}. Measuring plastic deformation is more complex due to the occurring residual stresses and anisotropies in the SLM fabricated components. However, results indicate that plastic deformation is equally measured to elastic deformation from within the component by the embedded fibre optic sensor, but residual stresses within the specimen superimpose the measurements of the fibre sensor during plastic deformation.

At high temperatures delamination of the fibre from the metal occurs. The weak glass-metal bonding causes discontinuities in the embedded sensor signal. After the sensor slips within the surrounding metal no further discontinuities are observed provided that temperatures do not exceed previous temperature levels applied to the sensor. A specimen which showed such slippage at a temperature of about 450 °C was subsequently temperature cycled more than 50 times between ambient and 430 °C. Changes in temperature were reliably tracked by the embedded FBG with high precision (± 3pm*K^{-1}). However, at temperatures above 500 °C the gratings suffer from severe losses in grating strengths and also fibres broke due to high axial stresses caused by the thermal expansion of the surrounding metal.

7.2 Future Work

The observation of the silica fibre slipping inside the metal component at elevated temperatures and ultimately the damage of such fibres is a cause of concern for the implementation of SLM embedded FBGs as practical and reliable sensors in high

temperature applications. A potential solution for the problems arising from high axial stress levels at elevated temperatures is the use of sapphire optical fibres. Sapphire fibres can endure much higher stresses compared to silica based fibres. A study conducted with nickel coated sapphire fibres shows that such fibres can exhibit tensile strengths of about 2.5 GPa after annealing them at 1300 °C [115]. This is a factor of 5 higher than the tensile strength observed in silica fibres. The approach developed in this thesis for fibre embedding can easily be adjusted to facilitate sapphire fibres (commercially available with similar dimensions). And more importantly the CTE of sapphire is about 10x higher ($CT_{sapphire} = 6*10^{-6}\ K^{-1}$) compared to silica, reducing the stresses induced due to differences in thermal expansion between sapphire and metal significantly when deployed in high temperature environments. However, sapphire fibres are extremely costly and more difficult to handle in terms of connecting them to other optical devices (splicing).

The developed processes for coating and embedding of silica fibres still hold promise for further improvements. Promising research has already started to tackle the issues discovered in this thesis, concentrating on mitigating the observed phenomena of fibre slippage at elevated temperatures and ensuring the fibre sensor is used in a regime capable for long-term operations at elevated temperatures.

Replace mechanical with chemical stripping of the fibre before coating

One way to improve the glass-metal bonding and also to preserve the fibres strength is to strip the fibre more carefully from its plastic coating and also guaranteeing the glass-surface is properly cleaned prior metal jacketing. In a small study, three FBG sensors were chemically stripped and more thoroughly cleaned using an ultrasonic-bath and a mixture of isopropanol and acetone rinsing. Chemically stripping reduces the chance of damaging the fibre surface and hence the fibre strength [116]. Two of the sensors showed slippage similar to the results described (see section 6.3.3), however one of the sensors successfully tracked a temperature increase from ambient temperature up to 850 ^{0}C (Figure 7-1).

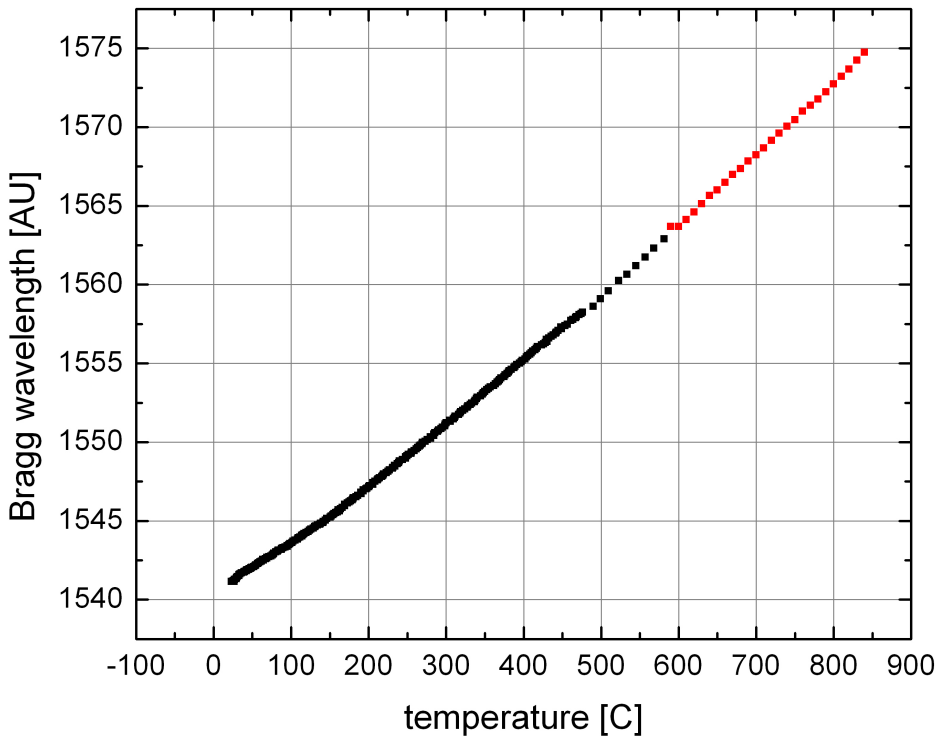

Figure 7-1 Plot for Bragg wavelength as a function of temperature for SLM embedded FBG in SS 316. Fibre was chemically stripped and rinsed using a ultrasonic-bath with isopropanol and acetone.

This behaviour was only observed for temperature testing of a single sample and therefore is presented here and was not included into the main experimental chapter. No slippage occurred and the fibre endured axial stresses of almost 1 GPa without breaking. Astonishingly, the Bragg wavelength exceeded the spectral range of the used interrogation system. At temperatures above 500 °C the FBG position was tracked manually and above 600 °C another optical spectrum analyser with a wider spectral range was quickly connected to the temperature tested embedded FBG. Above 850 °C the grating strength deteriorated rapidly. The grating strength soon became too weak for tracking the Bragg wavelength any further. Regeneration of the grating was not observed and fibre transmission ceased, indicating that the fibre was potentially destroyed due to high axial stresses induced by the expanding metal. This one-off results indicates that embedded silica fibres might be potentially suitable for high temperature measurements if treated more carefully (e.g. developing a fully automated process with minimised manual handling for careful stripping and coating).

Variable diameter fibres

A method to improve the stress transfer from metal to glass is by embedding optical sensors with varying outer diameter (Figure 7-2). A silica fibre containing a FBG with outer diameter 125 µm is spliced on both ends two silica fibre with an outer diameter of 80 µm and after electroplating the outer diameter of the nickel coating is 400 µm and 350 µm respectively (Figure 7-2). When embedded the sections with smaller diameter act as a clamping mechanism, ideally mitigating shear stresses in the bonding between fibre and metal at elevated temperatures.

All preliminary attempts to embed such fibres with SLM have failed so far. Preliminary results show that the interface where fibres with different outer diameter are spliced is a particular weak-point and fail during the embedding process. In all cases where such fibres were embedded, fibre transmission abruptly ceased after a few seconds into the process, when processing above the section with varying outer diameter. Potentially the strength of such fibres could be increased by conducting further research to improve the splicing process and also by applying larger coating thicknesses.

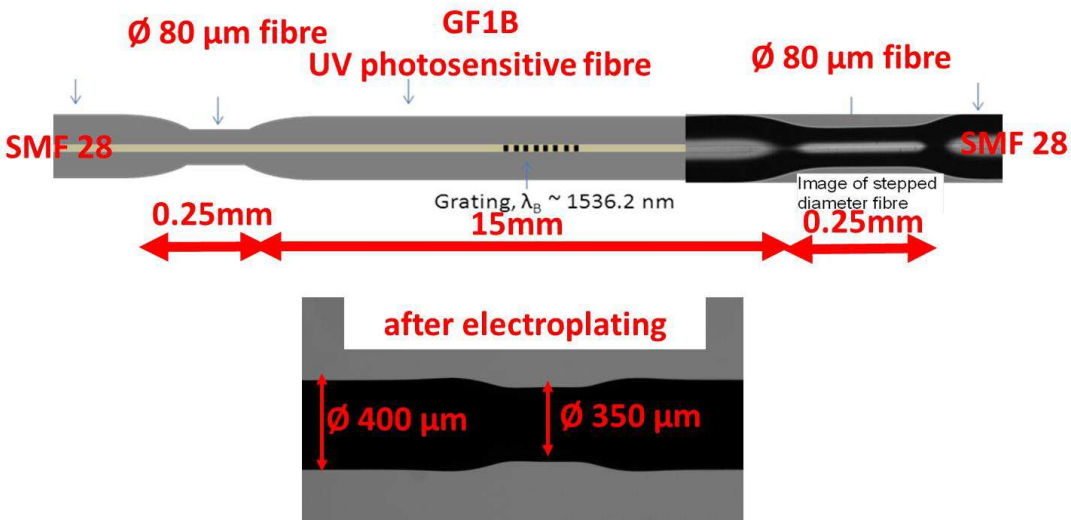

Figure 7-2 Schematic illustration for fibres with varying outer diameter for improved transfer of axial stresses (top) and microscopic view of nickel coated section with varying outer diameter.

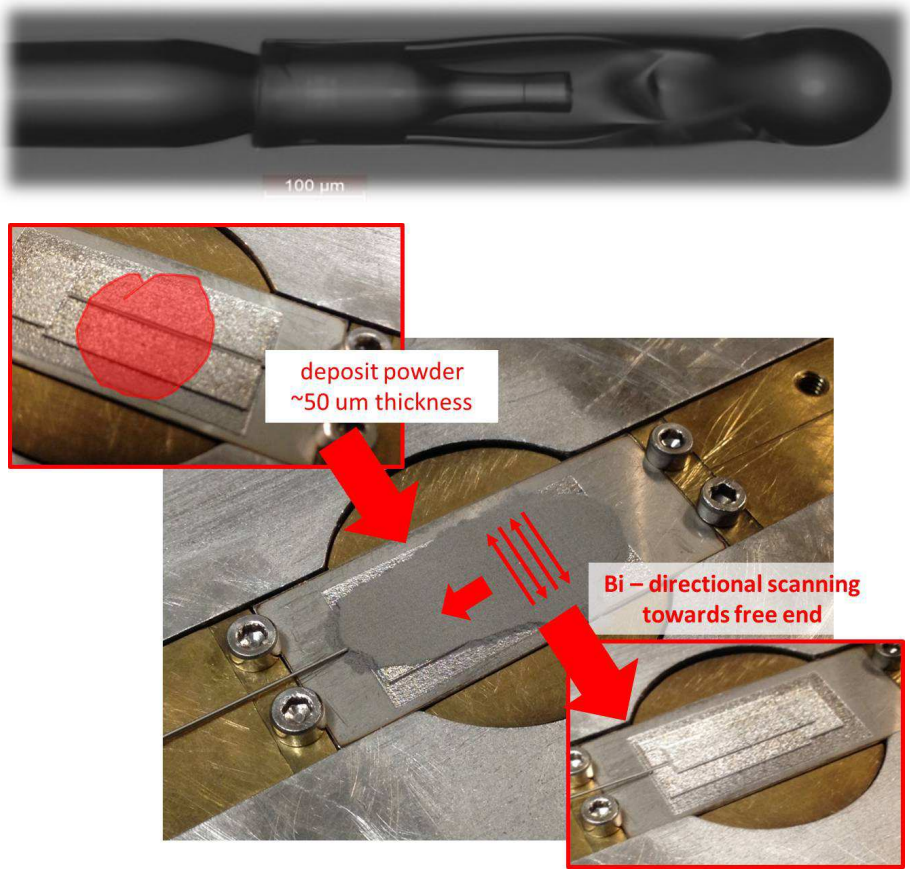

Figure 7-3 Top: Microscopic of image of FP-sensor free floating in silica capillary. Bottom: Approach for embedding of single-ended fibre sensors.

Strain isolation using silica capillary tube

Another approach is to place the fibre sensor inside a larger diameter silica capillary in order to strain isolate the fibre and stopping it from becoming axially stressed at elevated temperatures due to differences in thermal expansion between glass and metal (Figure 7-3 top). By nature, this type of sensor only allows to measure temperature. Ideally, the fibre is free-floating and stresses from the expanding metal capillary are not transferred into the fibre sensor. Preliminary studies were conducted to validate the feasibility of embedding such capillaries into SS 316 using similar methods from above (Figure 7-3 bottom)

Results indicate the embedment of single ended nickel coated silica capillaries is feasible and that subsequently a single ended fibre optic sensor can be inserted in such

embedded capillary. Research is under way either to place FBGs inside these capillaries or, more promising, deploy high temperature suitable Fabry-Perot based optical sensors. Such sensors are currently developed by the research group (Jinesh Matthew and Dimitrios Polyzos) and are by nature single ended. A study on the necessary steps for SLM embedding of single ended sensors has been conducted and successfully proven the feasibility.

Embedding at elevated temperatures

Another approach is to conduct the embedding at elevated temperatures in order to provide compression of the embedded FBG at ambient temperature. The component containing an optical fibre, cooled down after the embedding process, will shrink with the much more rapid rate of the metal. Subsequent temperature increases will initially relieve the compression of the fibre and only when temperatures exceed the temperature of the embedding process the fibre will be axially strained. The higher the temperature during the embedding process the smaller the actual straining of the embedded fibre due to differences in thermal expansion. Estimates for using embedding temperatures of about 500 °C show, that such embedded fibres can be used in subsequent applications with temperatures of up to 1000 °C within their tensile strength.

Additionally the energy input of the SLM process necessary for melting the metal powder will be reduced (smaller ΔT; see EQN 7), allowing to potentially increasing the speed of the SLM process. Also, smaller temperature gradients between ambient and melting temperature of the metal will occur, potentially reducing the coating thickness of the embedded fibre. However, conducting such high temperature SLM processes is highly complex and the necessary engineering work to address issues arising at such temperatures (thermal expansion of components, insertion of the fibre, thermal shielding, safety) was initiated based on the results of this thesis.

Applications

Despite the observed issues at elevated temperatures the approach developed for embedding fibre optic sensors into metals already opens up huge potential for a wide range of applications. The pre-fabricated U-groove approach significantly reduces the

obstruction on the SLM process caused by the fibre embedding compared to the approach by Li [44]. The long-term aim of the work conducted in this thesis is to transfer the embedding process onto commercial SLM systems. Based on the work presented in this thesis one of our collaborators (INSPIRE AG) is currently working to implement the necessary functionalities on a commercial SLM system (Figure 7-4)

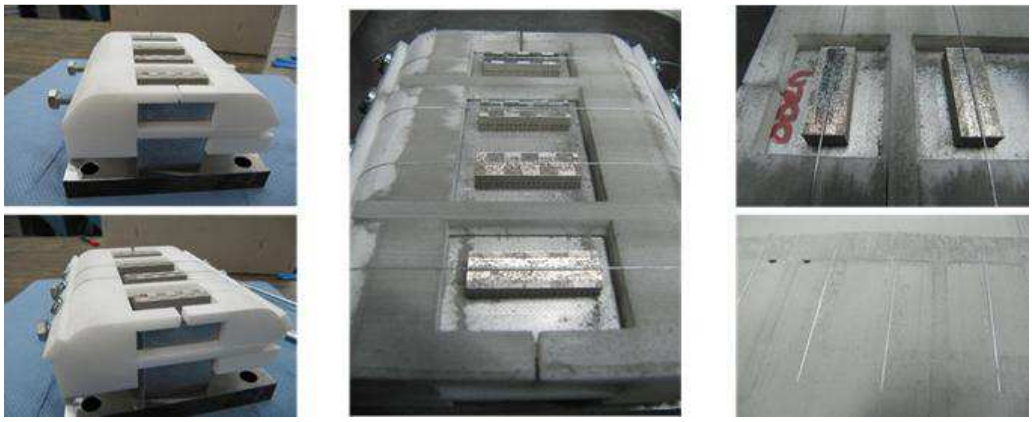

Figure 7-4 In-lets for adaption of the fibre embedding process in an commercial SLM machine. (from Inspire AG)

At the moment a particular challenge is implementing the necessary features for the positioning of the fibre into the SLM machine (e.g. clamping, pulling mechanism) in a way that these features are not interfering with the powder delivery system. Furthermore, some further obstacles remain when integrating coated optical fibres into the SLM process e.g. breaking of the inert atmosphere for fibre insertion or quality of the powder deposition above sections with U-grooves and coated fibres.

Currently work is also underway to implement SLM embedded FBG for initial proof of feasibility applications in oil and gas industry where temperatures do not exceed 200 °C. SLM embedded sensors into SS 316 will be potentially placed in locations with poor accessibility and high pressure (oil dwells), enhancing asset-management and leading to more economic use of assets.

References

[1] I. Gibson, D. W. Rosen, and B. Stucker, *Additive Manufacturing Technologies: Rapid Prototyping to Direct Digital Manufacturing. [eBook]*: Boston, MA : Springer US, 2010., 2010.

[2] R. Hague, I. Campbell, and P. Dickens, "Implications on design of rapid manufacturing," *Proceedings of the Institution of Mechanical Engineers Part C-Journal of Mechanical Engineering Science,* vol. 217, pp. 25-30, 2003.

[3] "3D printing scales up," *The Economist,* vol. Technology Quarterly, Sep 7 2013.

[4] G. A. O. Adam and D. Zimmer, "Design for Additive Manufacturing—Element transitions and aggregated structures," *CIRP Journal of Manufacturing Science and Technology,* vol. 7, pp. 20-28, // 2014.

[5] D. Wang, Y. Yang, R. Liu, D. Xiao, and J. Sun, "Study on the designing rules and processability of porous structure based on selective laser melting (SLM)," *Journal of Materials Processing Technology,* vol. 213, pp. 1734-1742, 10// 2013.

[6] J. P. Kruth, L. Froyen, J. Van Vaerenbergh, P. Mercelis, M. Rombouts, and B. Lauwers, "Selective laser melting of iron-based powder," *Journal of Materials Processing Technology,* vol. 149, pp. 616-622, 6/10/ 2004.

[7] K. Kunze, T. Etter, J. Grässlin, and V. Shklover, "Texture, anisotropy in microstructure and mechanical properties of IN738LC alloy processed by selective laser melting (SLM)," *Materials Science and Engineering: A,* vol. 620, pp. 213-222, 1/3/ 2015.

[8] J. Kruth, M. Leu, and T. Nakagawa, "Progress in Additive Manufacturing and Rapid Prototyping," *CIRP Annals - Manufacturing Technology,* vol. 47, pp. 525-540, 1998.

[9] M. Matsumoto, M. Shiomi, K. Osakada, and F. Abe, "Finite element analysis of single layer forming on metallic powder bed in rapid prototyping by selective laser processing," *International Journal of Machine Tools and Manufacture,* vol. 42, pp. 61-67, 1// 2002.

[10] P. Hanzl, M. Zetek, T. Bakša, and T. Kroupa, "The Influence of Processing Parameters on the Mechanical Properties of SLM Parts," *Procedia Engineering,* vol. 100, pp. 1405-1413, // 2015.

[11] X. Li and F. Prinz, "Metal Embedded Fiber Bragg Grating Sensors in Layered Manufacturing," *Journal of Manufacturing Science and Engineering,* vol. 125, p. 577, 2003.

[12] Raylase. (2015). *Miniscan II - Data sheet.* Available: http://www.raylase.de/fileadmin/downloads/public/RAYLASE_MINISCAN_II_en.pdf

[13] T. C. Sidler, "High efficiency laser resonators for high brightness beam generation, with application to micro-material processing and non linear processes.," *Laser Resonators and Beam Control V,* vol. 4629, pp. 49-57, 2002.

[14] W. Schulz, D. Becker, J. Franke, R. Kemmerling, and G. Herziger, "Heat-Conduction Losses in Laser Cutting of Metals," *Journal of Physics D-Applied Physics,* vol. 26, pp. 1357-1363, Sep 14 1993.

[15] F. Mitschke, *Fiber optics : physics and technology*. Berlin ; London: Springer, 2009.

[16] O. A. Hill and G. Meltz, "Fiber Bragg grating technology fundamentals and overview," *Journal of lightwave technology,* vol. 15, p. 14, 1997.

[17] K. T. V. Grattan and T. Sun, "Fiber optic sensor technology: an overview," *Sensors and Actuators A: Physical,* vol. 82, pp. 40-61, 5/15/ 2000.
[18] H. Alemohammad, E. Toyserkani, and C. Paul, "Fabrication of smart cutting tools with embedded optical fiber sensors using combined laser solid freeform fabrication and moulding techniques," *Optics and Lasers in Engineering,* vol. 45, pp. 1010-1017, 2007.
[19] D. Barrera, V. Finnazi, J. Villatoro, S. Sales, and V. Pruneri, "Performance of a high-temperature sensor based on regenerated fiber Bragg gratings," presented at the 21st International Conference on Optical Fiber Sensors, 2011.
[20] Y. Zhao and Y. Liao, "Compensation technology for a novel reflex optical," *Optics Communications,* vol. 215, p. 6, 2003.
[21] M. L. Wang, J. P. Lynch, and H. Sohn, *Sensor technologies for civil infrastructures*.
[22] M. Majumder, T. K. Gangopadhyay, A. K. Chakraborty, K. Dasgupta, and D. K. Bhattacharya, "Fibre Bragg gratings in structural health monitoring—Present status and applications," *Sensors and Actuators A: Physical,* vol. 147, pp. 150-164, 2008.
[23] M. J. Matthewson, C. R. Kurkjian, and J. R. Hamblin, "Acid stripping of fused silica optical fibers without strength degradation," *Lightwave Technology, Journal of,* vol. 15, pp. 490-497, 1997.
[24] Y. Tu and S. T. Tu, "Tensile strength of silica optical fibers for high-temperature sensing applications," in *Recent Advances in Structural Integrity Analysis - Proceedings of the International Congress (APCF/SIF-2014)*, L. Ye, Ed., ed Oxford: Woodhead Publishing, 2014, pp. 158-162.
[25] K. Furuya and Y. Suematsu, "Random-bend loss in single-mode and parabolic-index multimode optical fiber cables," *Applied Optics,* vol. 19, pp. 1493-1500, 1980/05/01 1980.
[26] K. Petermann, "Microbending loss in monomode fibres," *Electronics Letters,* vol. 12, pp. 107-109, 1976.
[27] N. K. Pandey and B. C. Yadav, "Embedded fibre optic microbend sensor for measurement of high pressure and crack detection," *Sensors and Actuators A: Physical,* vol. 128, pp. 33-36, 3/31/ 2006.
[28] H. Sakata and T. Iwazaki, "Sensitivity-variable fiber optic pressure sensors using microbend fiber gratings," *Optics Communications,* vol. 282, pp. 4532-4536, 12/1/ 2009.
[29] A. J. Rogers, V. A. Handerek, M. Farhadiroushan, R. Feced, T. R. Parker, and F. Parvaneh, "Advances in distributed optical fibre sensing," 1998, pp. 5-10.
[30] J. Liu, J. Zhang, X. Li, and Z. Zheng, "Study on Multiplexing Ability of Identical Fiber Bragg Gratings in a Single Fiber," *Chinese Journal of Aeronautics,* vol. 24, pp. 607-612, 10// 2011.
[31] K. O. Hill, Y. Fujii, D. C. Johnson, and B. S. Kawasaki, "Photosensitivity in optical fiber waveguides: Application to reflection filter fabrication," *Applied Physics Letters,* vol. 32, p. 647, 1978.
[32] Grattan, "Fiber optic sensor technology " *Sensors and Actuators* vol. 2000, p. 21, 1999.
[33] R. Kashyap, *Fiber bragg gratings*. San Diego ; London: Academic Press, 1999.
[34] A. Othonos and K. Kalli, *Fiber Bragg gratings : fundamentals and applications in telecommunications and sensing*. Boston, Mass. ; London: Artech House, 1999.
[35] C. Smelser, S. Mihailov, and D. Grobnic, "Formation of Type I-IR and Type II-IR gratings with an ultrafast IR laser and a phase mask," *OPTICS EXPRESS,* vol. 13, p. 10, 2005.

[36] Y. Zhan, S. Xue, Q. Yang, S. Xiang, H. He, and R. Zhu, "A novel fiber Bragg grating high-temperature sensor☆," *Optik - International Journal for Light and Electron Optics*, vol. 119, pp. 535-539, 2008.
[37] D. Lam and B. Garside, "Characterization of single-mode optical fiber filters," *Applied Optics*, vol. 20, p. 6, 1981.
[38] M. Lancry, N. Groothoff, S. Guizard, W. Yang, B. Poumellec, P. G. Kazansky, *et al.*, "Femtosecond laser direct processing in wet and dry silica glass," *Journal of Non-Crystalline Solids*, vol. 355, pp. 1057-1061, 2009.
[39] E. Lindner, C. Chojetzki, S. Brückner, and H. Bartelt, "Thermal regeneration of fiber Bragg gratings in photosensitive fibers," *OPTICS EXPRESS*, vol. 17, p. 9, 2009.
[40] S. P. Ugale and V. Mishra, "Modeling and characterization of fiber Bragg grating for maximum reflectivity," *Optik - International Journal for Light and Electron Optics*, vol. 122, pp. 1990-1993, 2011.
[41] H. Kogelnik, "Filter Response of Nonuniform Almost-Periodic Structures," *Bell Systems Technical Journal*, vol. 55, p. 18, 1976.
[42] X. Li, F. Prinz, and J. Seim, "Thermal behavior of a metal embedded fiber Bragg grating sensor," *Smart Materials and Structures*, vol. 2001, p. 6, 2000.
[43] A. P. Zhang, "Sensitivity Analysis of Fiber Bragg Grating Sensors coated by metal films produced by the laser-assisted Maskless Microdeposition Process," presented at the ICALEO, Orlando, Florida, 2011.
[44] X. Li, "Embedded Sensors in Layered Manufacturing," Doctor of Philosophy PhD, Mechanical Enginnering, Stanford University, Stanford, 2001.
[45] S. J. A. Capouilliet, D. J. Smith, G. S. Walter, G. E. Glaesmann, and R. D. Kohnke. *A Fiber Bragg grating Measurement system for monitoring of optical fiber strain*. Available: http://www.corning.com/docs/opticalfiber/tr3680.pdf
[46] B.-J. Peng, Y. Zhao, J. Yang, and M. Zhao, "Pressure sensor based on a free elastic cylinder and birefringence effect on an FBG with temperature-compensation," *Measurement*, vol. 38, pp. 176-180, 9// 2005.
[47] J. Canning, S. Bandyopadhyay, P. Biswas, and M. Aslund, "Regenerated fibre bragg gratings," in *Frontiers in Guided Wave Optics and Optoelectronics*. vol. 2010, ed: INTECH, 2008, p. 22.
[48] G. Brambilla, V. Pruneri, L. Reekie, C. Contardi, D. Milanese, and M. Ferraris, "Bragg gratings in ternary SiO2 : SnO2 : Na2O optical glass fibers," *Optics Letters*, vol. 25, pp. 1153-1155, Aug 15 2000.
[49] J. Canning, K. Sommer, and M. Englund, "Fibre gratings for high temperature sensor applications," *Meas. Sci. Technol.*, vol. 12, p. 4, 2001.
[50] J. Canning and N. Groothoff, "Enhanced type IIA gratings for high-temperature operation," *OPTICS LETTERS*, vol. 29, p. 3, 2004 2004.
[51] E. Lindner, J. Canning, C. Chojetzki, S. Brückner, M. Becker, M. Rothhardt, *et al.*, "Thermal regenerated type IIa fiber Bragg gratings for ultra-high temperature operation," *Optics Communications*, vol. 284, pp. 183-185, 2011.
[52] J. Canning, M. Aslund, and M. Stevenson, "Canning - Thermal stabilization of Type I FBG for operations up to 600C," *OPTICS LETTERS*, vol. 35, p. 3, 2010.
[53] J. Canning, "A study of regenerated gratings produced in germanosilicate fibers by high temperature annealing," *OPTICS EXPRESS*, vol. 19, p. 9, 2010.
[54] J.-J. Zhu, A. P. Zhang, B. Zhou, F. Tu, J.-T. Guo, W.-J. Tong, *et al.*, "Effects of doping concentrations on the regeneration of Bragg gratings in hydrogen loaded optical fibers," *Optics Communications*, vol. 284, pp. 2808-2811, 2011.
[55] Seo and Paek, "Melt coating of TIn on Silica Optical Fiber," *Journal of lightwave technology*, vol. 16, p. 10, 1998.

[56] B. J. Anderson, "Thermal stability and lifetime estimates of a high temperature epoxy by Tg reduction," *Polymer Degradation and Stability,* vol. 98, pp. 2375-2382, 2013.
[57] S.-W. Kim, M.-S. Jeong, I. Lee, I.-B. Kwon, and T.-K. Hwang, "Effects of mechanical and geometric properties of adhesive layer on performance of metal-coated optical fiber sensors," *International Journal of Adhesion and Adhesives,* vol. 47, pp. 1-12, 2013.
[58] S. Sandlin, T. Kinnunen, J. Ramo, and M. Sillanpaa, "A simple method for metal re-coating of optical fibre Bragg gratings," *Surface and Coatings Technology,* vol. 201, pp. 3061-3065, 2006.
[59] Y. Li, Z. Hua, F. Yan, and P. Gang, "Metal coating of fiber Bragg grating and the temperature sensing character after metallization," *Optical Fiber Technology,* vol. 15, pp. 391-397, 2009.
[60] C. E. Lee, W. N. Gibler, R. A. Atkins, J. J. Alcoz, and H. F. Taylor, "Metal-embedded fiber-optic Fabry-Perot sensors," *Opt Lett,* vol. 16, pp. 1990-2, Dec 15 1991.
[61] L. Rickenbacher, T. Etter, S. Hövel, and K. Wegener, "High temperature material properties of IN738LC processed by selective laser melting (SLM) technology," *Rapid Prototyping Journal,* vol. 19, pp. 282-290, 2013.
[62] K. Lucas, *Thermodynamik die Grundgesetze der Energie- und Stoffumwandlungen*, 7., korr. Aufl. ed. Berlin Heidelberg: Springer, 2008.
[63] A. Blom, P. Dunias, P. van Engen, W. Hoving, and J. de Kramer, "Process spread reduction of laser micro-spot welding of thin copper parts using real-time control," *Photon Processing in Microelectronics and Photonics Ii,* vol. 4977, pp. 493-507, 2003.
[64] H. Hügel and T. Graf, *Laser in der Fertigung Grundlagen der Strahlquellen, Systeme, Fertigungsverfahren*, 3., überarb. und erw. Aufl. ed. Wiesbaden: Springer Vieweg, 2014.
[65] K. Klages, *Laserstrahl-Mikroschweißen ungleicher Metalle durch Nahtschweißen mit gepulsten Nd:YAG-Lasern*. Aachen: Shaker, 2006.
[66] R. Poprawe, *Tailored light 2 : laser application technology*. Heidelberg: Springer, 2011.
[67] W. M. Steen and J. Mazumder, *Laser material processing*, 4th ed. ed. London: Springer, 2010.
[68] F. Schmitt, *Laserstrahl-Mikroschweißen mit Strahlquellen hoher Brillanz und örtlicher Leistungsmodulation.* Aachen: Shaker, 2012.
[69] S. Katayama, "Handbook of laser welding technologies Preface," *Handbook of Laser Welding Technologies,* pp. Xxi-Xxii, 2013.
[70] F. Abe, K. Osakada, M. Shiomi, K. Uematsu, and M. Matsumoto, "The manufacturing of hard tools from metallic powders by selective laser melting," *Journal of Materials Processing Technology,* vol. 111, pp. 210-213, 2001.
[71] I. Yadroitsev, A. Gusarov, I. Yadroitsava, and I. Smurov, "Single track formation in selective laser melting of metal powders," *Journal of Materials Processing Technology,* vol. 210, pp. 1624-1631, 2010.
[72] R. Li, Y. Shi, Z. Wang, L. Wang, J. Liu, and W. Jiang, "Densification behavior of gas and water atomized 316L stainless steel powder during selective laser melting," *Applied Surface Science,* vol. 256, pp. 4350-4356, 4/15/ 2010.
[73] M. Averyanova, E. Cicala, P. Bertrand, and D. Grevey, "Experimental design approach to optimize selective laser melting of martensitic 17-4 PH powder: part I – single laser tracks and first layer," *Rapid Prototyping Journal,* vol. 18, pp. 28-37, 2012.

[74] M. Rombouts, J. P. Kruth, L. Froyen, and P. Mercelis, "Fundamentals of Selective Laser Melting of alloyed steel powders," *CIRP Annals - Manufacturing Technology*, vol. 55, pp. 187-192, // 2006.

[75] C. Hauser, T. H. C. Childs, K. W. Dalgarno, and R. B. Eane, "Atmospheric control during direct selective laser sintering of stainless steel 314S powder.," *Solid Freeform Fabrication Proceedings, August 1999*, pp. 265-272, 1999.

[76] H. Asgharzadeh and A. Simchi, "Effect of sintering atmosphere and carbon content on the densification and microstructure of laser-sintered M2 high-speed steel powder," *Materials Science and Engineering: A*, vol. 403, pp. 290-298, 2005.

[77] L. E. Murr, E. Martinez, J. Hernandez, S. Collins, K. N. Amato, S. M. Gaytan, *et al.*, "Microstructures and Properties of 17-4 PH Stainless Steel Fabricated by Selective Laser Melting," *Journal of Materials Research and Technology*, vol. 1, pp. 167-177, 2012.

[78] I. Yadroitsev and I. Smurov, "Surface Morphology in Selective Laser Melting of Metal Powders," *Physics Procedia*, vol. 12, pp. 264-270, 2011.

[79] D. Gu and Y. Shen, "Balling phenomena in direct laser sintering of stainless steel powder: Metallurgical mechanisms and control methods," *Materials & Design*, vol. 30, pp. 2903-2910, 2009.

[80] K. A. Mumtaz and N. Hopkinson, "Selective Laser Melting of thin wall parts using pulse shaping," *Journal of Materials Processing Technology*, vol. 210, pp. 279-287, Jan 19 2010.

[81] R. Morgan, C. J. Sutcliffe, and W. O'Neill, "Density analysis of direct metal laser re-melted 316L stainless steel cubic primitives," *Journal of Materials Science*, vol. 39, pp. 1195-1205, Feb 2004.

[82] *X. C. Wang, T. Laoui, J. Bonse, J. Kruth, B. Lauwers*, and *L. Froyen*, "Direct Selective Laser Sintering of Hard Metal Powders," *Advanced Manufacturing Technology*, vol. 19, p. 7, 2002.

[83] E. Abele, H. A. Stoffregen, M. Kniepkamp, S. Lang, and M. Hampe, "Selective laser melting for manufacturing of thin-walled porous elements," *Journal of Materials Processing Technology*, vol. 215, pp. 114-122, 1// 2015.

[84] K. Guan, Z. Wang, M. Gao, X. Li, and X. Zeng, "Effects of processing parameters on tensile properties of selective laser melted 304 stainless steel," *Materials & Design*, vol. 50, pp. 581-586, 9// 2013.

[85] L. Thijs, M. L. Montero Sistiaga, R. Wauthle, Q. Xie, J.-P. Kruth, and J. Van Humbeeck, "Strong morphological and crystallographic texture and resulting yield strength anisotropy in selective laser melted tantalum," *Acta Materialia*, vol. 61, pp. 4657-4668, 7// 2013.

[86] M. Shiomi, K. Osakada, K. Nakamura, T. Yamashita, and F. Abe, "Residual Stress within Metallic Model Made by Selective Laser Melting Process," *CIRP Annals - Manufacturing Technology*, vol. 53, pp. 195-198, 2004.

[87] M. H. Lee, J. J. Kim, K. H. Kim, N. J. Kim, S. Lee, and E. W. Lee, "Effects of HIPping on high-cycle fatigue properties of investment cast A356 aluminum alloys," *Materials Science and Engineering: A*, vol. 340, pp. 123-129, 1/15/ 2003.

[88] P. Fu and C. Jiang, "Residual stress relaxation and micro-structural development of the surface layer of 18CrNiMo7-6 steel after shot peening during isothermal annealing," *Materials & Design*, vol. 56, pp. 1034-1038, 4// 2014.

[89] J. M. Robinson, B. A. Van Brussel, J. T. M. De Hosson, and R. C. Reed, "X-ray measurement of residual stresses in laser surface melted Ti-6Al-4V alloy," *Materials Science and Engineering: A*, vol. 208, pp. 143-147, 4/15/ 1996.

[90] M. L. Griffith, M. E. Schlienger, L. D. Harwell, M. S. Oliver, M. D. Baldwin, M. T. Ensz, *et al.*, "Understanding thermal behavior in the LENS process," *Materials & Design*, vol. 20, pp. 107-113, 6/1/ 1999.

[91] K. S. C. Kuang, R. Kenny, M. P. Whelan, W. J. Cantwell, and P. R. Chalker, "Embedded fibre Bragg grating sensors in advanced composite materials," *Composites Science and Technology*, vol. 61, pp. 1379-1387, 2001.

[92] R. R. J. Maier, W. N. MacPherson, J. S. Barton, M. Carne, M. Swan, J. N. Sharma, *et al.*, "Embedded Fiber Optic Sensors Within Additive Layer Manufactured Components," *Ieee Sensors Journal*, vol. 13, Mar 2013.

[93] T. K. M. Gangopadhyay, C. Paul; Bjerkan, Leif, "Fiber-optic sensor for real-time monitoring of temperature on high voltage (400KV) power transmission lines," in *The 20th International Conference on optical fibre Sensor (OFS-20)*, Edinburgh, 2009, pp. M-1-4.

[94] Y. Li, W. Liu, Y. Feng, and H. Zhang, "Ultrasonic embedding of nickel-coated fiber Bragg grating in aluminum and associated sensing characteristics," *Optical Fiber Technology*, vol. 18, pp. 7-13, 2012.

[95] Y. Yang, G. D. Janaki Ram, and B. E. Stucker, "Bond formation and fiber embedment during ultrasonic consolidation," *Journal of Materials Processing Technology*, vol. 209, pp. 4915-4924, 6/1/ 2009.

[96] P. Marshall, *Austenitic stainless steels : microstructure and mechanical properties*. London: Elsevier Applied Science, 1984.

[97] P. M. Dickens, P. Erasenthiran, and W. N. Su, "Investigation of fully dense laser sintering of tool steel powder using a pulsed Nd:YAG (neodymium-doped yttrium aluminium garnet) laser," *Proceedings of the Institution of Mechanical Engineers, Part C: Journal of Mechanical Engineering Science*, vol. 217, pp. 127-138, 2003.

[98] Heraeus-Quarzglas. (2014, October). *Thermal properties of fused silica*. Available: http://heraeus-quarzglas.com/en/quarzglas/thermalproperties/Thermal_properties.aspx

[99] D. M. Mattox, *Handbook of physical vapor deposition (PVD) processing : film formation, adhesion, surface preparation and contaimination control*. Westwood, N.J.: Noyes Publications, 1998.

[100] G. K. Narula, K. S. Narula, and V. K. Gupta, *Materials Science*: Tata McGraw-Hill, 1989.

[101] Y. Mikami, K. Yamada, A. Ohnari, T. Degawa, T. Migita, T. Tanaka, *et al.*, "Effect of DC bias voltage on the deposition rate for Ni thin films by RF–DC coupled unbalanced-magnetron sputtering," *Surface and Coatings Technology*, vol. 133–134, pp. 295-300, 11// 2000.

[102] U. A. Bakshi and V. U. Bakshi, *Basic Electrical Engineering*: Technical Publications, 2009.

[103] G. R. Jones, M. A. Laughton, and M. G. Say, *Electrical engineer's reference book*, 15th ed. Oxford ; Boston: Butterworth-Heinemann, 1993.

[104] Y. Kilinc, U. Unal, and B. E. Alaca, "Residual stress gradients in electroplated nickel thin films," *Microelectronic Engineering*, vol. 134, pp. 60-67, 2/20/ 2015.

[105] M. Schlesinger and M. Paunovic, *Modern electroplating*, 5th ed. ed. Oxford: Wiley-Blackwell, 2010.

[106] H. Berns and W. Theisen, *Ferrous Materials: Steel and Cast Iron. [eBook]*: Berlin, Heidelberg : Springer Berlin Heidelberg, 2008., 2008.

[107] V. Guilbaudmassereau, A. Celerier, and J. Machet, "Study and Improvement of the Adhesion of Chromium Thin-Films Deposited by Magnetron Sputtering," *Thin Solid Films*, vol. 258, pp. 185-193, Mar 15 1995.

[108] J. E. Shigley, C. R. Mischke, N. S. Prasad, M. S. Shunmugam, and S. Krishnamurthy, *Mechanical engineering design*: Boston: McGraw-Hill, 2001. 6th ed., 2001.
[109] C. Weingarten, D. Buchbinder, N. Pirch, W. Meiners, K. Wissenbach, and R. Poprawe, "Formation and reduction of hydrogen porosity during selective laser melting of AlSi10Mg," *Journal of Materials Processing Technology,* vol. 221, pp. 112-120, 7// 2015.
[110] B. Mehlmann, E. Gehlen, A. Olowinsky, and A. Gillner, "Laser Micro Welding for Ribbon Bonding," *Physics Procedia,* vol. 56, pp. 776-781, // 2014.
[111] A. Rabikin. (2015). *Brazing foil manual*. Available: http://www.metglas.com/assets/pdf/lit/ibsc_2003_text.pdf
[112] Metglas. (2015, 20/5/2015). *Metglas - Brazing Foil MBF 20* [Product data sheet (PDF)]. Available: http://www.metglas.com/assets/pdf/mbf20_data_sheet.pdf
[113] B. Song, S. Dong, Q. Liu, H. Liao, and C. Coddet, "Vacuum heat treatment of iron parts produced by selective laser melting: Microstructure, residual stress and tensile behavior," *Materials & Design,* vol. 54, pp. 727-733, 2// 2014.
[114] E. J. Mittemeijer, *Fundamentals of materials science : the microstructure-property relationship using metals as model systems*. Heidelberg ; London: Springer, 2010.
[115] D. E. Hajas, T. Gebhardt, H. Chen, and J. M. Schneider, "Tensile Strength of Ni45Al45Cr7.5Ta2.5-Coated Sapphire Fibers," *Journal of the American Ceramic Society,* vol. 91, pp. 4009-4015, 2008.
[116] J.-R. Lee, D. Dhital, and D.-J. Yoon, "Investigation of cladding and coating stripping methods for specialty optical fibers," *Optics and Lasers in Engineering,* vol. 49, pp. 324-330, 2011.